University of Udine

Polytechnic Department of Engineering and Architecture

Ph.D. Program in Industrial and Information Engineering

Cycle XXXI

Ph.D. Thesis

Modeling and control of flexible-link robotic systems

Ph.D. Candidate:
Lorenzo Scalera

Supervisor:
Prof. Alessandro Gasparetto

Course Coordinator:
Prof. David Esseni

October, 2018

Modeling and control of flexible-link robotic systems

Abstract:

The scientific activity presented in this Ph.D. thesis deals with the modeling and control of flexible-link robotic systems. Nowadays, the industrial demand for high performances, high speeds and low energy consume has highlighted the need to develop lightweight manipulators and robots. However, their design and control result more difficult and challenging with respect to traditional rigid-link robotic systems mainly due to the flexibility of the arms.

In the first part of my Ph.D., the research activity has been focused on the modeling and simulation of flexible-link mechanism, using an Equivalent Rigid-Link System (ERLS) formulation. In recent years, the ERLS approach, firstly implemented together with a Finite Element Method (FEM) formulation, has been extended through a modal approach and, in particular, a Component Mode Synthesis (CMS) technique. This novel formulation allows a reduced-order system of equations to be maintained even when a fine discretization is needed. After an analysis of the state of the art about dynamic modeling of flexible-link mechanisms, a numerical comparison between the ERLS-FEM and the ERLS-CMS approaches has been conducted. A benchmark manipulator has been implemented and the results have been compared in terms of accuracy and computational effort under different input conditions. The discretization of the mechanism and the number of considered vibrational modes have been as well discussed.

In the CMS approach, a classical Craig-Bampton reduction has been adopted. However, this is not the only technique capable of reducing the number of degrees of freedom of flexible-link mechanisms. For this reason, further developments of the work have seen the implementation and comparison of different Model Order Reduction Techniques, which can be applied to different benchmark robotic systems in order to highlight their advantages and disadvantages.

The second part of this thesis is focused on cable-driven parallel robots, which are a special class of flexible-link mechanisms in which flexible cables, rather than rigid links, are employed to actuate the end-effector. A particular class of cable-driven robots is given by cable-suspended parallel robots, which rely on gravity to maintain the cables taut. These mechanisms are characterized by large workspaces, high velocities and payload-to-weight ratios and can be employed for several different tasks such as handling and moving loads, pick-and-place and building tasks.

In collaboration with University of Trieste (Italy), a novel design of cable-suspended parallel robot based on variable radius drums has been developed and experimentally validated. A variable radius drum is characterized by the variation of the radius along the spool. This device is used in the cable-driven manipulator to move the end-effector through a planar working area, using just two actuated joints. Experimental results demonstrate a good agreement with the theoretical model.

Another example of cable-driven robot has been studied during the months that I

spent at the Wearable Robotic Systems (WRS) Laboratory, Department of Mechanical Engineering, Stevens Institute of Technology (Hoboken, NJ, USA). The device consists of a 3-degree-of-freedom, under-actuated, pendulum-like robot. The mechanism is capable of performing planar point-to-point motions in its dynamic workspace by means of two actuated joints only, using parametric excitation in a way similar to playground swings. The control system is based on a feedback linearization that allows the dynamics of the variable-length pendulum to be decoupled from the dynamics of the rotation of the end-effector. Adaptive Frequency Oscillators have been introduced to estimate the phase of the pendulum-robot in real-time and without delay. The device has been experimentally validated showing the feasibility of the design and good performances of the control architecture.

Keywords: flexible multibody systems, Equivalent Rigid-Link System, model order reduction, cable-driven robot, under-actuated robot

Modellazione e controllo di sistemi robotici a membri flessibili

Riassunto:

L'attività scientifica presentata in questa tesi di Dottorato affronta le tematiche della modellazione e del controllo di meccanismi a membri flessibili. Al giorno d'oggi, la richiesta industriale di elevate performances, alte velocità e bassi consumi energetici ha evidenziato la necessità di sviluppare manipolatori e robot sempre più leggeri. Tuttavia, la progettazione e il controllo di questo tipo di meccanismi risulta più difficile e complesso rispetto ai sistemi robotici a link rigidi tradizionali, principalmente a causa della flessibilità dei membri che li compongono.

Nella prima parte del mio Dottorato, l'attività di ricerca è stata focalizzata sulla modellazione dinamica e sulla simulazione di meccanismi flessibili, utilizzando una formulazione basata su un sistema rigido equivalente (Equivalent Rigid-Link System, ERLS). Recentemente, l'approccio ERLS, inizialmente implementato in combinazione con un metodo agli elementi finiti (FEM), è stato esteso mediante l'utilizzo di una formulazione modale, la Component Mode Synthesis (CMS). Questo nuovo approccio permette di utilizzare un sistema di equazioni di ordine ridotto anche nei casi in cui la discretizzazione richiesta è fine. Dopo un'analisi dello stato dell'arte sulla modellazione dinamica di meccanismi a membri flessibili, è stata condotta una comparazione numerica tra i due approcci ERLS-FEM ed ERLS-CMS. I modelli sono stati implementati utilizzando un meccanismo di rifermento e i risultati numerici sono stati comparati in termini di accuratezza ed onere computazionale sotto diverse condizioni. La discretizzazione del sistema e il numero di modi di vibrare considerati sono stati ugualmente discussi.

Nell'approccio CMS è stata adottata la classica riduzione modale di Craig-Bampton. Tuttavia, questa non è l'unica tecnica capace di ridurre il numero di gradi di libertà di un meccanismo a link deformabili. Per questo motivo, gli sviluppi successivi del lavoro hanno visto l'implementazione e il confronto di diverse tecniche di riduzione modale, che possono essere applicate a diversi sistemi meccanici di riferimento allo scopo di valutare i loro rispettivi vantaggi e svantaggi.

La seconda parte di questa tesi è stata focalizzata sui robot paralleli a cavi, che costituiscono una speciale classe di meccanismi a membri deformabili nei quali l'organo terminale è attuato tramite cavi flessibili, invece che mediante link rigidi. Una classe particolare di robot a cavi è costituita dai robot paralleli sospesi a cavi, nei quali la tensione dei cavi è garantita dalla forza di gravità. Questi meccanismi sono caratterizzati da grandi spazi di lavoro, alte velocità e alti rapporti carico utile / peso proprio e trovano numerose applicazioni come, ad esempio, in operazioni di movimentazione carichi e costruzione.

In collaborazione con l'Università di Trieste (Italia), è stato sviluppato e validato sperimentalmente un nuovo design di robot sospeso a cavi, basato su pulegge a raggio variabile, caratterizzate dalla variazione del raggio lungo la spoletta. Questo tipo di dispositivo è utilizzato per muovere l'end-effector entro un'area di lavoro planare, utilizzando solamente due giunti attuati. I risultati sperimentali hanno dimostrato un ottimo accordo

con il modello teorico.

Un secondo esempio di robot a cavi è stato studiato durante il periodo che ho trascorso all'estero presso il Wearable Robotic System (WRS) Laboratory, Dipartimento di Ingegneria Meccanica, allo Steven Institute of Technology (Hoboken, NJ, USA). Il dispositivo consiste in un robot-pendolo a 3 gradi di libertà, sotto-attuato. Il meccanismo consente di realizzare un moto punto-a-punto nello spazio di lavoro dinamico utilizzando solamente due giunti attuati e sfruttando l'eccitazione parametrica, in maniera simile all'altalena. Il sistema di controllo è basato su una linearizzazione in retroazione che permette di disaccoppiare la dinamica del pendolo a lunghezza variabile da quella della rotazione dell'end-effector. Per la stima della fase del pendolo in tempo reale e senza ritardi sono stati introdotti oscillatori a frequenza adattativa. Il dispositivo è stato validato sperimentalmente dimostrando la fattibilità del design proposto e ottime performances del sistema di controllo.

Parole chiave:
sistemi a membri flessibili, sistema equivalente a membri rigidi, riduzione modale, robot a cavi, robot sotto-attuati

Contents

List of Figures

List of Tables

Introduction

Robotic systems and manipulators are becoming more and more pervasive and required in several industrial fields. Robots are employed in a large number of tasks, including pick-and-place, assembling, soldering, welding, testing, but also handling loads, spray painting and coating. Their widespread application arises from the fact that robotic systems allow to operate with high precision and speed, to remove humans from hazardous environments, and to produce higher volumes of goods at relative low costs. The constant increasing of the worldwide annual supply of industrial robots can be seen in the report of IFR World Robotics 2016, reported in Figure 1, where the trend of number of units per years is estimated to be +13 % on average in the next years.

In this context, the production cost of manufacturing operations is heavily affected by the cost of the electric energy that is needed to operate industrial robots and machines, in particular when high volumes of goods need to be processes at low costs. For this reason, energy saving and conservation is becoming an important topic in the industry and economic sectors, as it is testified by the scientific community [6, 7, 8, 9], as well as by the directions set by the European Union policy, which designs a reduction of the energy consumption up to 30 % by 2030 [10].

Several strategies can be applied in order to limit and reduce the energy consumption of robotic systems with both hardware and software solutions. The hardware approach achieves this objective through the optimal design of new systems as well as by replacing components of existing system. For example, the selection of more energy-efficient mechatronic and robotic systems, the substitution of parts with lighter components or the adoption of energy recovery and storage systems, such as regenerative drives. From the software point of view, several strategies can be implemented to minimize the required energy, such as optimization of the trajectories, redesign of the motion planning, rescheduling of operations and task sequences [8].

This dissertation is focused on the study and analysis of robotic systems composed of lightweight links and structures, which not only allows to reduce the costs connected to the power and energy consumption, but are also usually required for high speed operations and high performances in several industrial applications. To achieve high speed is, indeed, a recurrent target in the design and operation of an industrial robotic system, for obvious economic reasons. Furthermore, a lighter structure allows to minimize the inertia load during the motion and to maximize the payload to weight ratio, with direct benefits on the manufacturing process.

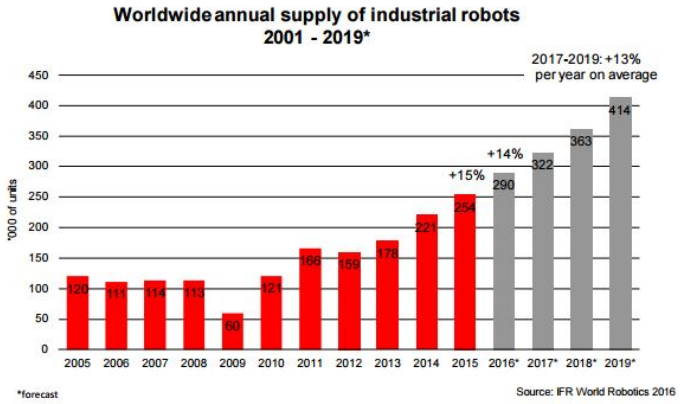

Figure 1: Worldwide annual supply of industrial robots, IFR World Robotics 2016.

The light weight and the reduced dimensions of the structure usually introduce high flexibility in the links of this kind of manipulators, in which, differently from traditional rigid-link mechanisms and robots (such as the KUKA and the FANUC industrial robots shown in Figure 2), the elastic deformation plays an important role in their design and control and, therefore, has to be taken into account. The flexibility of the links, if neglected or poorly controlled, can lead to errors in the positioning and motion accuracy but also to mechanical stresses and instability of the system. Therefore, in order to study and control flexible-link robotic systems, appropriate mathematical descriptions of the dynamics (dynamic models) have to be investigated and implemented [11].

The dynamic modeling of flexible multibody systems can then be applied for numerical simulations, in which the dynamic behavior of the system can be predicted by software, without the requirement of real working prototypes. In the recent years, the development of numerical simulators has been facilitated by the increasing of computational power, which allows to simulate the dynamics of mechanical systems in a fast and efficient way. The numerical models need to require low computational time and, at the same time, to achieve good accuracy in the description of the dynamic behavior: it yields in the research of a trade-off between computational effort and precision of the solutions.

This work focuses on the dynamic modeling and control of flexible-link mechanisms. Examples of flexible-link robotic systems are mechanical systems in which the arms are constituted by deformable bodies, or robots in which the end-effector is controlled by means of flexible-cables, rather than by structural elements. While the first group is composed of traditional serial-link or closed-chain structures that present deformations of the bodies (an example can be given by the delta robot Adept Quattro reported in Fig. 3(a)), the second group consists of a special class of flexible robots, in which the traditional links are substituted by cables, inherently flexible (an example of cable-robot is shown in Fig. 3(b)).

The main advantages of cable-driven robots, over traditional ones, are the possibility of extending over larger workspace, their modularity and reconfigurability, as well as the possibility of achieving higher velocities and accelerations due to the lower inertia loads. The main drawback of this class of manipulators is that cables can be pulled but not

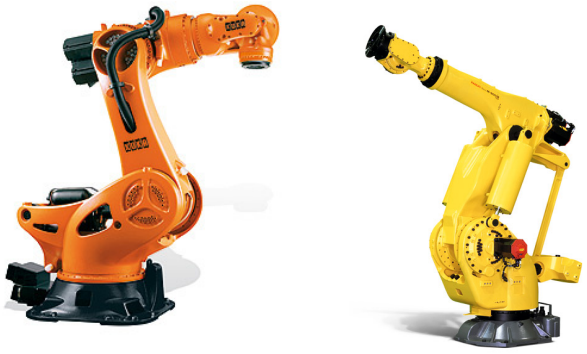

(a) KUKA KR 1300 titan PA.

(b) FANUC M-900iB/700.

Figure 2: Examples of traditional rigid-link industrial robots.

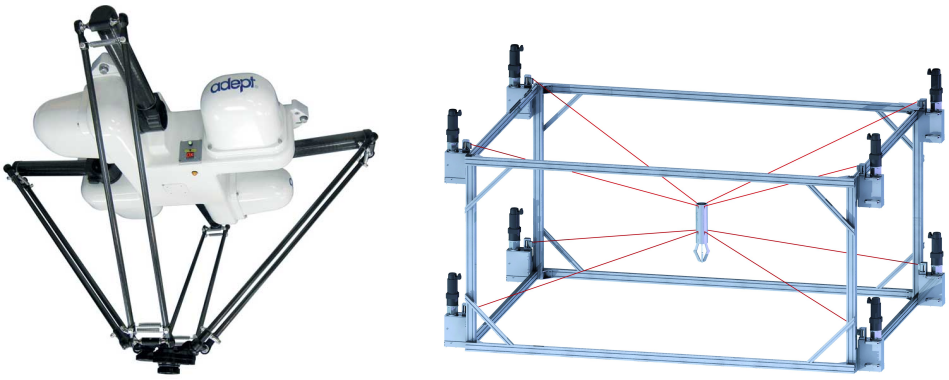

(a) Delta robot Adept Quattro.

(b) Cable-driven parallel robot.

Figure 3: Examples of flexible-link manipulators.

pushed and, therefore, only tension forces can be applied on the end-effector, and redundant solutions have often to be implemented in order to achieve the desired kinematics. Moreover, interferences between the cables and the environment have to be taken into account.

Nevertheless, the possibility of reducing the required energy and of operating in large workspaces with high speed and performances have made cable-driven robots an open field of investigation in both industry and academia. In particular, several designs of cable-based robots have been studied over the years, especially for control purposes, dynamic modeling and trajectory planning.

The work presented in this Ph.D. thesis deals with the modeling and control of flexible-link robotic systems. In the case studies reported in the dissertation, not only theoretical modeling but also numerical simulations, control, experimental tests and validations have been carried out. In the following, an overview on the different aspects that are taken into account in the chapters of this dissertation is presented and the contributions of the author dealing with the topics described in this thesis are reported as references.

Contributions and summary of the work

The first four chapters of this dissertation deal with the dynamic modeling and simulation of flexible multibody systems. The main contribution of this part of the work is the *comparison* of different approaches for modeling the dynamics of deformable mechanisms and of different techniques capable of reducing the computational effort of the numerical models, by maintaining a good accuracy in the description of the dynamic behavior.

- Chapter 1 reports an introduction about the dynamic modeling of flexible multibody systems and recalls the Equivalent Rigid-Link System (ERLS) formulation for flexible-link mechanism, based on the Finite Element Method (FEM) [1];
- Chapter 2 reports the kinematic and dynamic model of the Equivalent Rigid-Link System (ERLS) formulation for flexible-link mechanism, based on a modal approach (i.e. the Component Mode Synthesis, CMS) for the simulation of the dynamics of deformable-link mechanisms, previously published in [12];
- Chapter 3 presents a comparison between the ERLS-FEM and the ERLS-CMS approaches for flexible-link robots. Numerical simulations on a benchmark mechanisms are presented and the results analyzed and discussed in terms of computational time and accuracy in both the time and frequency domains [2];
- Chapter 4 presents a comparison of Model Order Reduction techniques using the ERLS formulation for flexible-link robots. The results of different numerical simulations are presented and compared in terms of computational time, accuracy in frequency domain and modal vector correlation parameters [3].

The second part of the thesis deals with cable-driven robots, which are a special class of flexible-link robotic systems. The main contribution of this research activity is the *design* of novel cable-driven mechanisms and their *experimental validation*.

- Chapter 5 gives an introduction on cable-driven robots. In particular, the classes of cable-driven parallel robots and cable-suspended parallel robots are analyzed and described;
- Chapter 6 presents a novel design of cable-suspended parallel robot based on variable radius drums, capable of moving the end-effector throughout a planar workspace with just two degrees of freedom. The kinematic model and an experimental prototype are presented and validated with interesting results [4];
- Chapter 7 deals with a particular class of cable-suspended parallel robots: pendulum-like robots. The dynamic modeling and the non-linear control of an under-actuated, 3-DOF pendulum-robot is presented and experimentally validated by means of a prototype capable of performing point-to-point motion in its dynamic workspace [5];
- Chapter 8 reports the conclusions of this work and some possible future developments.

The work presented in this Ph.D. thesis includes theoretical modeling, numerical implementation and simulation, control, experimental tests and validation. This wide range of research activities has been possible thank to a collaboration with several universities and international institutes, in particular with:

- Free University of Bolzano-Bozen (Italy): I worked with prof. Renato Vidoni on the introduction to the ERLS formulation, the understanding of the modal approach (Chapter 2), the comparison between the ERLS-FEM and ERLS-CMS approached (Chapter 3) and the comparison of Model Order Reduction techniques (Chapter 4);
- University of Trieste (Italy): I worked with prof. Paolo Gallina and Dr. Stefano Seriani on the kinematic development of the variable radius drum and the fabrication of the experimental prototype of cable-suspended robot presented in Chapter 6;
- Stevens Institute of Technology (USA): during my visiting period abroad, I worked with prof. Damiano Zanotto on the design and experimental validation of the 3-DOF, under-actuated, pendulum-like, cable-driven robot described in Chapter 7.

Chapter 1

Dynamic modeling of flexible multibody systems

Nowadays, industrial mechanisms and robotic systems are demanded to be lightweight, easy maneuverable and capable of high speed operations. These features result in multibody systems in which the flexibility of the links has to be taken into account. Therefore, not only the kinematics, but also the dynamic modeling and simulation of such systems has becoming a more and more challenging field of investigation in both industry and academia.

In this chapter, an introduction about the dynamic modeling of flexible multibody systems is presented. Then, a dynamic model, that have been developed at University of Udine (Italy) in the last decades, is recalled and described in its evolution [1]. The model is based on the Equivalent Rigid-Link System (ERLS) approach and it is suitable in the case of large displacements and small elastic deformations.

1.1 Modeling the vibration of flexible-link robots

In the last decades, high speed operations of robotic and mechatronic systems have become more and more demanded in industry and, therefore, the study of dynamic models for the simulation and control of flexible multibody systems has represented a challenging field of research in applied mechanics for machinery and robotics. In this context, several authors have been studying single flexible-link mechanisms, then planar robots and machines, and finally 3D flexible systems. The area is still an open field of research and investigation [13, 14, 15, 16, 17]; this interest can be evaluated by looking at the increasing trend of the number of documents by year dealing with *flexible multibody systems*, as reported in Figure 1.1 (source Scopus®).

Flexible multibody dynamics emerged as a new field of research and investigation in the early seventies, as a response to the need to simulate many industrial and technological systems, in which the deformation can not be neglected. Examples of physical and mechanical systems that can be modeled as flexible multibody systems are ground and space vehicles, machines, mechanisms, space structures and components. In particular, in the last decades, the research activities on flexible multibody have been motivated by the

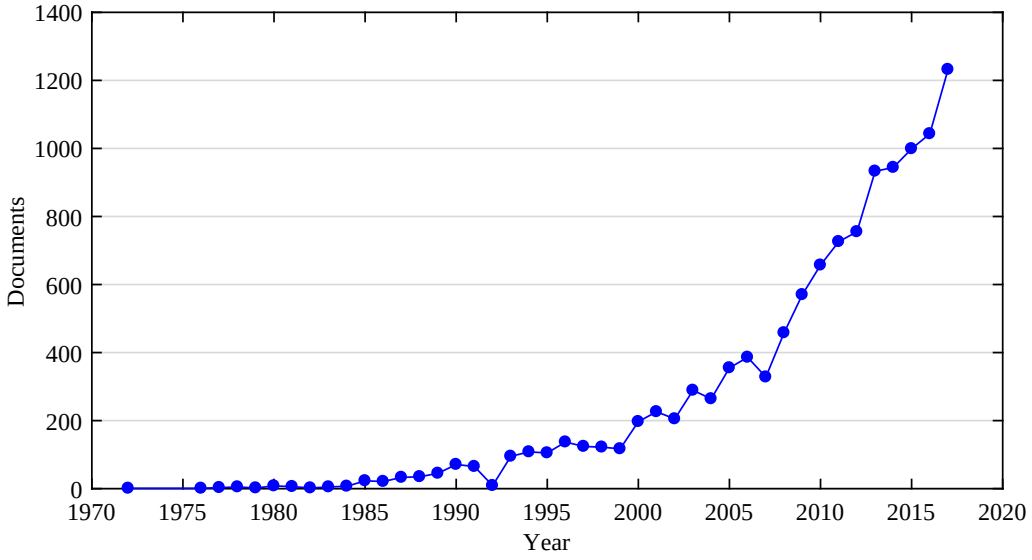

Figure 1.1: Documents by year dealing with *flexible multibody systems* (source Scopus®).

development of new lightweight manipulators and robots, characterized by high operating speeds and performances.

Flexible multibody dynamics is the subject concerned with the computer modeling and analysis of constrained deformable bodies that undergo large displacements, including large rotations [15]. A flexible multibody system usually consists of elastic and rigid components which are connected by means of joints and/or force elements such as springs, dampers and actuators (Figure 1.2). Joint constraints force the displacements of the bodies to be dependent to each other. Furthermore, in addition to large rotations and constraints problems, the elasticity of the bodies can have a significant effect on the way the large rotation problem and joint constraints are formulated.

An approach for the modeling of deformable-links mechanisms is based on the rigid-body model of the robot, to which the deformations due to its elastic properties are added in order to take the flexibility of the links into account. The dynamic equations of the deformable bodies that undergo large rigid body displacements are highly non-linear and, therefore, the number of coordinates required to obtain a reasonable mathematical model for flexible multibody systems can be very large as compared to the number of coordinates used in traditional rigid-body systems. This approach yields a coupled set of non-linear partial differential equations. In order to provide a set of ordinary differential equations from this system of partial differential equations, two different approaches have been developed and adopted in the Literature. These two methodologies are the *nodal* and the *modal* formulations [18, 19, 20, 21, 22, 23, 24, 25].

The nodal approach involves the *Finite Element Method* (FEM), emerged in the early sixties as a powerful tool for the analysis of deformations. In the FEM, the infinite dimension problem is discretized by using some FEM models: one of the most popular is the Euler-Bernoulli beam elements. The use of Timoshenko beams is less frequent, since it allows to better describe the dynamics of flexible-link manipulators only for the cases with

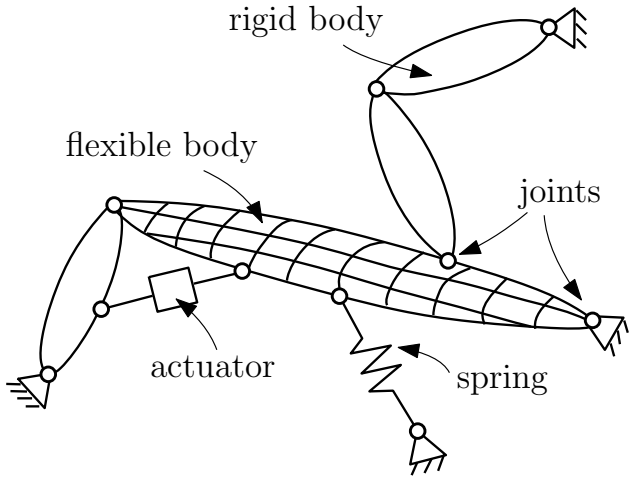

Figure 1.2: Graphical example of flexible multibody system.

short links. In the Euler-Bernoulli approach, each element is composed of a fixed number of nodes, which define the number of degrees of freedom (DOF) of the flexible system. In this manner, the forces applied to the nodes can be related to the nodal displacements and accelerations through the mass and stiffness matrices. Because of the non-linearity and large dimensionality, a drawback of the FEM approach is that the degrees of freedom of the flexible multibody system have to be kept low, if a low computational time is needed (i.e. for fast simulations or real-time control applications).

On the other hand, the modal approach, i.e. the *Assumed Mode Method* (AMM), is based on the representation by a truncated finite modal series of the link flexibility. Although very popular, the latter methodology has the disadvantage to yield a system of coupled differential equations with no separation between the rigid-body motion and the elastic deformation.

In the case of large displacements (or rotations) and small flexible deformations, the most famous and adopted formulation is the *Floating Frame of Reference* (FFR), introduced by Shabana [15, 26]. The formulation of the FFR was originally presented in the aerospace literature and it is currently the most widely used method in computer simulation. In particular, it is implemented in several commercial multibody tools like SIMPACK, MSC ADAMS™ and LMS Virtual Lab. In this formulation the motion of a flexible body is separated into a usually non-linear motion of the reference frame and a linear elastic deformation with respect to this reference frame. The small elastic deformations are described with the linear finite element method and represented by a second order differential equation [15, 26]. The main difficulties that arise when using the floating frame of reference formulation are associated with the selection of the reference frame of the deformable body, the definition of modal shape functions, and the formulation of the coupled kinetic energy.

Another formulation for flexible-link robots, suitable in the case of large and small deformations, is the *Absolute Nodal Coordinate Formulation* (ANCF). In this non-linear finite element formulation, no infinitesimal or finite rotations are used as nodal coordinates,

instead absolute displacements and global slopes are used as element coordinates [27, 28]. The locations and deformations of the material points on the finite element are defined in the global coordinate system using the element shape function and the nodal coordinates. The Absolute Nodal Coordinate Formulation allows to efficiently describe not only the large deformations of flexible multibody systems but can also be employed in the analysis of curved structures and to obtain the mass moment and inertia of complex structures, since the rigid body inertia can be exactly modeled.

Other approaches to the dynamic modeling of flexible multibody systems, which can be considered as derivations of the above mentioned basic approaches, are the *linear theory of elastodynamics*, and the *large rotation vectors formulation* [15].

Finally, alternative formulations to the dynamic analysis and characterization of planar and spatial robotic systems can be found in [29, 30].

In the following, a particular formulation for flexible multibody dynamics based on an Equivalent Rigid-Link System and suitable for the case of large rigid displacements and small elastic deformation is described in its evolution.

1.2 A dynamic model based on an Equivalent Rigid-Link System

In the first part of this dissertation, a novel and alternative approach to model flexible multibody systems under the condition of large displacements and small elastic deformations has been adopted. This formulation is based on the concept of Equivalent Rigid-Link System (ERLS) and it has been investigated and experimentally validated at University of Udine throughout a period of almost 30 years.

The idea of the ERLS has been firstly introduced by Chang and Hamilton for the study of the kinematics of robotic manipulators with flexible links [31] and by Turcic *et al.* [32, 33, 34] for the dynamic analysis of elastic mechanism systems. The model based on the ERLS formulation enables the kinematic equations of the equivalent rigid-link system to be decoupled from the compatibility equations of the displacements at the joints.

The original formulation of the model (in the two-dimensional case) has been developed by Giovagnoni *et al.* in the 1980s [35, 36]. The ERLS theoretical formulation has been experimental validated for a 4-link flexible mechanism by Giovagnoni in 1994 [37].

Further developments have seen the validation of the model for a 5-link flexible mechanical system by Gasparetto [38] and its linearization in the state-space form, necessary for the application to the synthesis of control systems [39].

Subsequently, the linearized ERLS-based model has been applied to different controllers, such as PID regulators, optimal controllers, model predictive controllers, delayed reference controlled, as well as hybrid controllers, in order to reduce the vibration of mechanical systems. Examples can be found in the works of Boscariol *et al.* [40, 41, 42], Boschetti *et al.* [43], Caracciolo *et al.* [44, 45], Gallina *et al.* [46] and Trevisani [47].

In more recent years, other examples of control systems for flexible-link mechanisms can be found in the works of Gasparetto *et al.* [48], where the vibration reduction in a

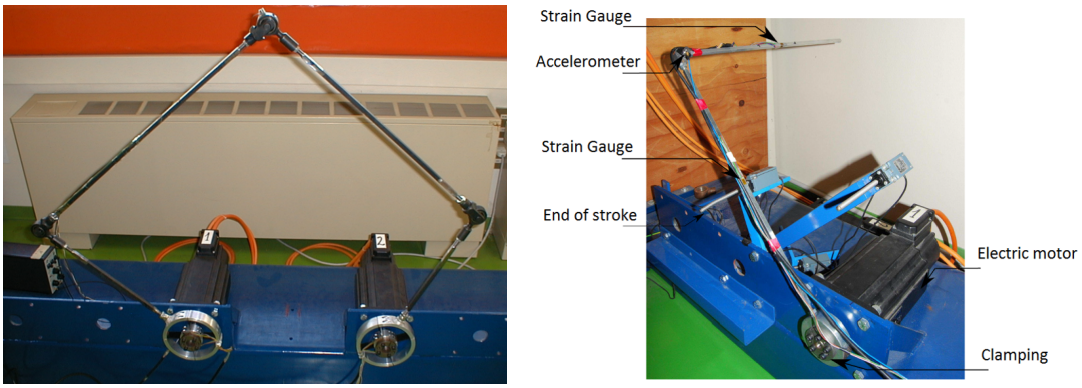

(a) 4-link flexible mechanism.

(b) L-shaped flexible system.

Figure 1.3: Examples of flexible-link mechanisms at University of Udine.

flexible-link mechanism through the synthesis of an optimal controller is presented, and of Zanotto *et al.* [49], where the model has been employed with the Hardware-in-the-Loop simulation technique.

Furthermore, the ERLS formulation has been extended by Vidoni *et al.* to three-dimensional flexible systems, which better describe the case of industrial machines based on spatial mechanisms [50, 51]. The extension to the 3D system has been implemented by collocating several reference frames along the kinematic chain, according to the Denavit-Hartenberg rules, and by defining the transformation matrices between any two consecutive frames. The 3D model has been validated by means of experimental tests, by comparing the measured accelerations and deformations with those provided by numerical simulations [52].

In more recent years, the Equivalent Rigid-Link System formulation has been extended through a modal approach, by using the Component Mode Synthesis (CMS) technique, in order to obtain a more flexible solution based on a reduced-order system of equations [12]. The modal formulation has been validated by comparing the results of the simulator with those provided by ADAMS-Flex™ software for the same benchmark mechanism (a spatial L-shaped link with one rigid degree of freedom).

The evolution of the ERLS-based dynamic model has been described in [1], whereas examples of flexible-link benchmark mechanisms for the application of control systems based on the ERLS model are reported in Figure 1.3, where a 4-link flexible mechanism and a L-shaped spatial system are shown.

In its recent developments, presented in this dissertation, a comparison between the ERLS-FEM and the ERLS-CMS formulations has been carried out, in order to evaluate the advantages and disadvantages in terms of computational time and accuracy in the description of the dynamic behavior of the two approaches [2].

Furthermore, different Model Order Reduction techniques have been investigated and compared in [3], choosing a L-shaped manipulator as a benchmark mechanism. These techniques allow to reduce the computational effort and to open the application of the

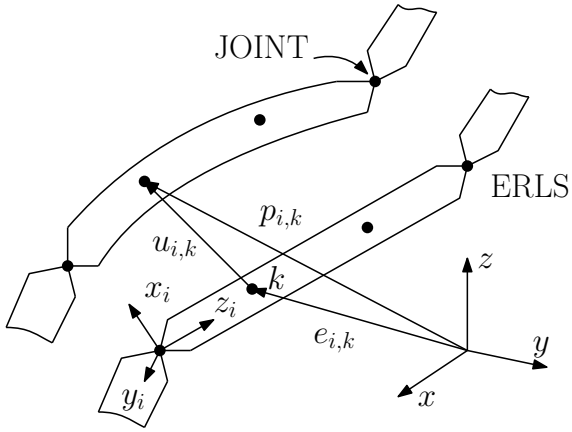

Figure 1.4: Kinematic model of the system and definition of the main vectors [2].

modal formulation to fast numerical simulations and real-time vibration control systems, as it is explained in the next chapters.

1.3 The ERLS-FEM dynamic formulation

In this section the 3D formulation of the ERLS-FEM dynamic model, extensively described by Vidoni *et al.* in [50, 51], is briefly recalled.

The definitions of the main vectors involved in the kinematic analysis can be described with respect to Figure 1.4, where $\{x, y, z\}$ indicates a fixed global reference frame. In particular, $\boldsymbol{u}_i$ represents the nodal displacement vector of the i-th link, $\boldsymbol{e}_i$ defines the nodal position vector for the i-th element of the ERLS and $\boldsymbol{p}_i$ the absolute nodal position vector of the generic point inside the i-th finite element, calculated as:

$$\boldsymbol{p}_i = \boldsymbol{e}_i + \boldsymbol{u}_i \tag{1.1}$$

The index i spans from 1 to l, where l is the number of links of the robotic system. $\{x_i, y_i, z_i\}$ indicates a local reference frame, which follows the motion of the ERLS. This reference frame can be expressed with respect to the ERLS adopting a set of generalized coordinates $\boldsymbol{\theta}$, the m rigid degrees of mobility of the mechanism, by exploiting the Denavit-Hartenberg notation that can be introduced to describe the kinematics of the ERLS. The i-th components $\boldsymbol{e}_i$ can be grouped together into a unique vector $\boldsymbol{e}$, which describes the position and orientation of the whole ERLS.

The dynamic equations can be obtained by applying the principle of virtual works and computing the inertial, elastic, gravity and external generalized forces terms as follows

$$\begin{aligned} &\delta \boldsymbol{W}^{inertia} + \delta \boldsymbol{W}^{elastic} = -\delta \boldsymbol{W}^{external} \\ &\sum_i \int_{v_i} \delta \boldsymbol{p}_i^T \ddot{\boldsymbol{p}}_i \rho_i dv + \sum_i \int_{v_i} \delta \boldsymbol{\epsilon}_i^T \boldsymbol{D}_i \boldsymbol{\epsilon}_i dv = \sum_i \int_{v_i} \delta \boldsymbol{p}_i^T \boldsymbol{g} \rho_i dv + \left(\delta \boldsymbol{u}^T + \delta \boldsymbol{e}^T\right) \boldsymbol{f} \end{aligned} \tag{1.2}$$

where ρ_i, $\boldsymbol{D}_i$ and $\boldsymbol{\epsilon}_i$ are the mass density, the stress-strain matrix and the strain vector for the i-th finite element, respectively. $\boldsymbol{g}$ is the gravitational acceleration vector, and $\boldsymbol{f}$ is the vector of the concentrated external forces and torques. $\delta\boldsymbol{u}$ and $\delta\boldsymbol{e}$ refer to all the nodes of the model.

The nodal elastic virtual displacements $\delta\boldsymbol{u}$ and the virtual displacements of the Equivalent Rigid-Link System $\delta\boldsymbol{e}$ are completely independent. Thus, two set of equilibrium equations, i.e. local nodal equilibrium and global equilibrium equations, can be obtained from (1.2) by zeroing alternatively the nodal elastic virtual displacements and the virtual displacements of the ERLS.

The following system of differential equations can be written

$$\boldsymbol{M}(\ddot{\boldsymbol{e}} + \ddot{\boldsymbol{u}}) + 2(\boldsymbol{M}_{G1} + \boldsymbol{M}_{G2})\dot{\boldsymbol{u}} + (\boldsymbol{M}_{C1} + 2\boldsymbol{M}_{C2} + \boldsymbol{M}_{C3})\boldsymbol{u} + \boldsymbol{K}\boldsymbol{u} = \boldsymbol{f}_g + \boldsymbol{f} \tag{1.3}$$

$$\boldsymbol{J}^T\boldsymbol{M}(\ddot{\boldsymbol{e}} + \ddot{\boldsymbol{u}}) + 2\boldsymbol{J}^T(\boldsymbol{M}_{G1} + \boldsymbol{M}_{G2})\dot{\boldsymbol{u}} + \boldsymbol{J}^T(\boldsymbol{M}_{C1} + 2\boldsymbol{M}_{C2} + \boldsymbol{M}_{C3})\boldsymbol{u} = \boldsymbol{J}^T(\boldsymbol{f}_g + \boldsymbol{f}) \tag{1.4}$$

where $\boldsymbol{M}$ is the mass matrix, $\boldsymbol{M}_{G1}$ and $\boldsymbol{M}_{G2}$ are the Coriolis terms, $\boldsymbol{M}_{C1}$, $\boldsymbol{M}_{C2}$ and $\boldsymbol{M}_{C3}$ the centrifugal stiffness terms, $\boldsymbol{K}$ the stiffness matrix, and $\boldsymbol{J}$ the Jacobian matrix. $\boldsymbol{J}$ allows to express the $\delta\boldsymbol{e}$ virtual displacements with respect to the $\delta\boldsymbol{\theta}$ independent generalized coordinates. $\boldsymbol{f}_g$ the vector of the equivalent nodal loads due to gravitational force.

After the substitution of the second order differential kinematics equations of the ERLS, the dynamic equations can be grouped and rearranged in matrix form

$$\begin{bmatrix} \boldsymbol{M} & \boldsymbol{M}\boldsymbol{J} \\ \boldsymbol{J}^T\boldsymbol{M} & \boldsymbol{J}^T\boldsymbol{M}\boldsymbol{J} \end{bmatrix} \begin{bmatrix} \ddot{\boldsymbol{u}} \\ \ddot{\boldsymbol{\theta}} \end{bmatrix} = \begin{bmatrix} -2\boldsymbol{M}_{G12} & -\boldsymbol{M}\dot{\boldsymbol{J}} & -\boldsymbol{M}_{C123} - \boldsymbol{K} \\ -\boldsymbol{J}^T 2\boldsymbol{M}_{G12} & -\boldsymbol{J}^T\boldsymbol{M}\boldsymbol{J} & -\boldsymbol{J}^T\boldsymbol{M}_{C123} \end{bmatrix} \begin{bmatrix} \dot{\boldsymbol{u}} \\ \dot{\boldsymbol{\theta}} \\ \boldsymbol{\theta} \end{bmatrix} + \begin{bmatrix} \boldsymbol{M} & \boldsymbol{I} \\ \boldsymbol{J}^T\boldsymbol{M} & \boldsymbol{J}^T \end{bmatrix} \begin{bmatrix} \boldsymbol{f}_g \\ \boldsymbol{f} \end{bmatrix} \tag{1.5}$$

where

$$\boldsymbol{M}_{G12} = \boldsymbol{M}_{G1} + \boldsymbol{M}_{G2} \tag{1.6}$$

and

$$\boldsymbol{M}_{C123} = \boldsymbol{M}_{C1} + 2\boldsymbol{M}_{C2} + \boldsymbol{M}_{C3} \tag{1.7}$$

The complete development of the model is reported in [50] and [51].

A Rayleigh damping model can be eventually taken into account and introduced in the dynamic model to deal with real flexible-link systems.

Chapter 2

Equivalent Rigid-Link System, Component Mode Synthesis model

In this chapter, the Equivalent Rigid-Link System approach, extended through a modal formulation, is presented and described. With respect to the previous approach of the dynamic model, in which the ERLS has been applied together with a Finite Element Method (FEM), the formulation here proposed is developed in combination with a Component Mode Synthesis (CMS) technique. The ERLS-CMS formulation for flexible-link robots allows to obtain a reduced-order system of equations even when a fine discretization of the system is needed. The approach is suitable for large displacements and small elastic deformations and it allows the kinematics equations of motion to be decoupled from the compatibility equations of the displacements at the joints. After the description of the kinematics of the ERLS, the equation of motions are derived and, finally, the differences between the ERLS-CMS and the Floating Frame of Reference (FFR) are highlighted.

The ERLS-CMS model described in this chapter has been previously presented in [12].

2.1 Kinematics of the ERLS-CMS

In this section, the description of the kinematics of the Equivalent Rigid-Link System, extended through a Component Mode Synthesis formulation, is presented.

With respect to Fig. 1.4, where $\{x, y, z\}$ is a fixed global reference frame, it can be useful to recall the kinematic definitions of the main vectors. $\boldsymbol{u}_i$ represents the nodal displacement vector of the i-th link, $\boldsymbol{e}_i$ defines the nodal position vector for the i-th element of the ERLS and $\boldsymbol{p}_i$ the absolute nodal position vector of the generic point inside the i-th finite element, where $\boldsymbol{p}_i = \boldsymbol{e}_i + \boldsymbol{u}_i$.

In order to rewrite the system with a modal approach, the nodal displacements $\boldsymbol{u}_i$ of the i-th link have to be expressed as functions of a given number of eigenvectors $\boldsymbol{U}_i$ and modal coordinates $\boldsymbol{q}_i$:

$$\boldsymbol{u}_i = \boldsymbol{U}_i \boldsymbol{q}_i \tag{2.1}$$

The eigenvectors and eigenvalues can be obtained according to the chosen modal reduction

strategy (Chapter 4). In terms of modal coordinates, the joint displacement belonging to two subsequent links i and $i+1$ can be expressed by $\hat{\boldsymbol{u}}_i = \boldsymbol{S}_i \boldsymbol{U}_i \boldsymbol{q}_i$ and $\hat{\boldsymbol{u}_{i+1}} = \boldsymbol{S}_{i+1} \boldsymbol{U}_{i+1} \boldsymbol{q}_{i+1}$ respectively, where the matrices $\boldsymbol{S}_i$ and $\boldsymbol{S}_{i+1}$ are introduced just to extract the proper joint displacements from all the nodal ones. The compatibility condition at the i-th joint can be written using the following expression: $\hat{\boldsymbol{u}_{i+1}} = \boldsymbol{T}_{i+1} \hat{\boldsymbol{u}}_i$, where $\boldsymbol{T}_{i+1}(\boldsymbol{\theta})$ is a local-to-local transformation matrix between two consecutive reference frames associated to the two subsequent links. The transformation matrices are function of the joint coordinates:

$$\boldsymbol{\theta} = \{\theta_1 \quad \theta_2 \quad ... \quad \theta_n\}^T \tag{2.2}$$

The compatibility equation at the i-th joint can be expressed as

$$\boldsymbol{S_{i+1} U_{i+1} q_{i+1}} = \boldsymbol{T_{i+1,i}}(\boldsymbol{\theta}) \boldsymbol{S_i U_i q_i} \tag{2.3}$$

or, in matrix form, as:

$$\begin{bmatrix} -\boldsymbol{T_{i+1,i}}(\boldsymbol{\theta}) \boldsymbol{S_i U_i} & | & \boldsymbol{S_{i+1} U_{i+1}} \end{bmatrix} \begin{bmatrix} \boldsymbol{q_i} \\ \boldsymbol{q_{i+1}} \end{bmatrix} = \boldsymbol{0} \tag{2.4}$$

By writing the previous equation for all the links and assembling them into a matrix, a comprehensive compatibility equation can be described by

$$\boldsymbol{C}(\boldsymbol{\theta}) \boldsymbol{q} = \boldsymbol{0} \tag{2.5}$$

where

$$\boldsymbol{C}(\boldsymbol{\theta}) = \begin{bmatrix} \boldsymbol{S_i U_i} & \boldsymbol{0} & ... & ... & \boldsymbol{0} \\ -\boldsymbol{T_{1,2}}(\boldsymbol{\theta}) \boldsymbol{S_i U_i} & \boldsymbol{S_2 U_2} & ... & ... & \boldsymbol{0} \\ \boldsymbol{0} & -\boldsymbol{T_{2,3}}(\boldsymbol{\theta}) \boldsymbol{S_2 U_2} & \boldsymbol{S_3 U_3} & ... & \boldsymbol{0} \\ \boldsymbol{0} & \boldsymbol{0} & ... & ... & \boldsymbol{0} \\ \boldsymbol{0} & \boldsymbol{0} & ... & -\boldsymbol{T_{n-1,n}}(\boldsymbol{\theta}) \boldsymbol{S_{n-1} U_{n-1}} & \boldsymbol{S_n U_n} \\ \boldsymbol{0} & \boldsymbol{0} & \boldsymbol{0} & \boldsymbol{0} & -\boldsymbol{T_{n,n+1}}(\boldsymbol{\theta}) \boldsymbol{S_n U_n} \end{bmatrix} \tag{2.6}$$

The matrix $\boldsymbol{C}(\boldsymbol{\theta})$ only depends on the joint parameters. The vector $\boldsymbol{q}$ comprehends both the rigid and the elastic modal coordinates

$$\boldsymbol{q} = \begin{bmatrix} \boldsymbol{q}_1^T & \boldsymbol{q}_2^T & ... & \boldsymbol{q}_n^T \end{bmatrix}^T \tag{2.7}$$

The total number of degrees of freedom of the mechanical system without the constraints m is related to the total number of DOF of the Equivalent Rigid-Link System n through the following expression

$$m - v = n \tag{2.8}$$

where v indicates the number of constraints imposed by the joints. It has to be noticed that the number of raws of matrix $\boldsymbol{C}(\boldsymbol{\theta})$ is equal to v. The number of columns corresponds to $m + d$, where m is the number of the rigid-body modal coordinates and d is the

number of elastic modal coordinates. The dimension of matrix $\boldsymbol{C}$ can be calculated as $v \times (m+d) = (m-n) \times (m+d)$. Therefore, (2.5) represents an under-determined linear system with a solution in the form of ∞^{n+d}.

The rigid-body modal coordinates and the elastic modal ones can be grouped into two separate vectors, namely $\boldsymbol{q}_r$ and $\boldsymbol{q}_d$. In this manner, (2.5) can be rewritten as:

$$\boldsymbol{C}_r \boldsymbol{q}_r + \boldsymbol{C}_d \boldsymbol{q}_d = \boldsymbol{0} \tag{2.9}$$

The sub-matrices $\boldsymbol{C}_r$ and $\boldsymbol{C}_d$ have dimensions $(v \times m)$ and $(v \times n)$ respectively. The number of unknowns is greater than the number of equations, since $(v < m)$.

Equation (2.9) can be solved with respect to $\boldsymbol{q}_r$, by using the right pseudo-inverse matrix [53]:

$$\boldsymbol{C}_r^{+} = \boldsymbol{C}_r^T (\boldsymbol{C}_r \boldsymbol{C}_r^T)^{-1} \tag{2.10}$$

The elastic modal coordinates $\boldsymbol{q}_d$ can be then represented as function of the rigid-body modal coordinates and joint parameters

$$\boldsymbol{q}_r = \boldsymbol{D}(\boldsymbol{\theta}) \boldsymbol{q}_d \tag{2.11}$$

where the matrix $\boldsymbol{D}(\boldsymbol{\theta})$ is defined as:

$$\boldsymbol{D}(\boldsymbol{\theta}) = -\boldsymbol{C}_r^{+}(\boldsymbol{\theta}) \boldsymbol{C}_d(\boldsymbol{\theta}) \tag{2.12}$$

The rigid-body modal coordinates are function of $\boldsymbol{\theta}$ and $\boldsymbol{q}_d$ only. In particular, if all the links of the mechanism are considered as rigid bodies, the remaining DOF are those of the ERLS.

2.2 Derivative terms

The velocities and accelerations terms are derived as functions of $\boldsymbol{\theta}, \boldsymbol{q}_d$ and their derivatives, in order to implement the dynamic analysis of the complete flexible multibody system.

First, (2.5) is differentiated with respect to time. The following expression is obtained

$$\dot{\boldsymbol{C}} \boldsymbol{q} + \boldsymbol{C} \dot{\boldsymbol{q}} = \boldsymbol{0} \tag{2.13}$$

which can be written as

$$\sum_k \frac{\partial \boldsymbol{C}}{\partial \theta_k} \boldsymbol{q} \dot{\boldsymbol{\theta}}_k + \boldsymbol{C} \dot{\boldsymbol{q}} = \boldsymbol{0} \tag{2.14}$$

By defining

$$\boldsymbol{E}(\boldsymbol{\theta}, \boldsymbol{q}) = \begin{bmatrix} \dfrac{\partial \boldsymbol{C}}{\partial \theta_1} \boldsymbol{q} & \ldots & \dfrac{\partial \boldsymbol{C}}{\partial \theta_n} \boldsymbol{q} \end{bmatrix} \tag{2.15}$$

it is possible to easily obtain

$$\boldsymbol{E} \dot{\boldsymbol{\theta}} + \boldsymbol{C} \dot{\boldsymbol{q}} = \boldsymbol{0} \tag{2.16}$$

By substituting (2.9), it holds

$$\boldsymbol{E}\dot{\boldsymbol{\theta}} + \boldsymbol{C}_d\dot{\boldsymbol{q}}_d + \boldsymbol{C}_r\dot{\boldsymbol{q}}_r = \boldsymbol{0} \tag{2.17}$$

By exploiting the pseudo-inverse matrix $\boldsymbol{C}_r^+$, the previous equation can be solved with respect to $\dot{\boldsymbol{q}}_r$

$$\dot{\boldsymbol{q}}_r = -\boldsymbol{C}_r^+\boldsymbol{C}_d\dot{\boldsymbol{q}}_d - \boldsymbol{C}_r^+\boldsymbol{E}\dot{\boldsymbol{\theta}} \tag{2.18}$$

By introducing the matrix

$$\boldsymbol{G}(\boldsymbol{\theta}, \boldsymbol{q}) = -\boldsymbol{C}_r^+\boldsymbol{E}(\boldsymbol{\theta}, \boldsymbol{q}) \tag{2.19}$$

the relationship between the velocities of the rigid-body modal coordinates and the velocities of the independent variables can be found

$$\dot{\boldsymbol{q}}_r = \boldsymbol{D}(\boldsymbol{\theta})\dot{\boldsymbol{q}}_d + \boldsymbol{G}(\boldsymbol{\theta}, \boldsymbol{q})\dot{\boldsymbol{\theta}} \tag{2.20}$$

The previous equation can be rewritten in terms of virtual displacements as well

$$\delta\boldsymbol{q}_r = \boldsymbol{D}(\boldsymbol{\theta})\delta\boldsymbol{q}_d + \boldsymbol{G}(\boldsymbol{\theta}, \boldsymbol{q})\delta\boldsymbol{\theta} \tag{2.21}$$

2.3 Acceleration terms

Let differentiate (2.5) with respect to time twice. It can be obtained

$$\ddot{\boldsymbol{C}}\boldsymbol{q} + 2\dot{\boldsymbol{C}}\dot{\boldsymbol{q}} + \boldsymbol{C}\ddot{\boldsymbol{q}} \tag{2.22}$$

The second derivative of the coefficient matrix can be written as

$$\ddot{\boldsymbol{C}} = \frac{d}{dt}\sum_k \frac{\partial \boldsymbol{C}}{\partial \theta_k}\dot{\boldsymbol{\theta}}_k = \sum_j\sum_k \frac{\partial^2 \boldsymbol{C}}{\partial \theta_j \partial \theta_k}\dot{\boldsymbol{\theta}}_j\dot{\boldsymbol{\theta}}_k + \sum_k \frac{\partial \boldsymbol{C}}{\partial \theta_k}\ddot{\theta}_k \tag{2.23}$$

By defining

$$\boldsymbol{h}(\boldsymbol{\theta}, \dot{\boldsymbol{\theta}}, \boldsymbol{q}) = \left(\sum_j\sum_k \frac{\partial^2 \boldsymbol{C}}{\partial \theta_j \partial \theta_k}\dot{\boldsymbol{\theta}}_j\dot{\boldsymbol{\theta}}_k\right)\boldsymbol{q} \tag{2.24}$$

and

$$\boldsymbol{c}(\boldsymbol{\theta}, \dot{\boldsymbol{\theta}}, \boldsymbol{q}) = \dot{\boldsymbol{C}}\dot{\boldsymbol{q}} = \left(\sum_k \frac{\partial \boldsymbol{C}}{\partial \theta_k}\right)\dot{\boldsymbol{q}} \tag{2.25}$$

the following equation can be obtained

$$\ddot{\boldsymbol{C}}\boldsymbol{q} = \boldsymbol{h}(\boldsymbol{\theta}, \dot{\boldsymbol{\theta}}, \boldsymbol{q}) + \boldsymbol{E}(\boldsymbol{\theta}, \boldsymbol{q})\ddot{\boldsymbol{\theta}} \tag{2.26}$$

(2.22) can be finally rewritten as

$$\boldsymbol{h}(\boldsymbol{\theta}, \dot{\boldsymbol{\theta}}, \boldsymbol{q}) + \boldsymbol{E}(\boldsymbol{\theta}, \boldsymbol{q})\ddot{\boldsymbol{\theta}} + 2\boldsymbol{c}(\boldsymbol{\theta}, \dot{\boldsymbol{\theta}}, \boldsymbol{q}) + \boldsymbol{C}\ddot{\boldsymbol{q}} = \boldsymbol{0} \tag{2.27}$$

The acceleration of rigid-body modal coordinates $\ddot{\boldsymbol{q}}_r$ can be written as function of the independent coordinates by splitting $\boldsymbol{C}$ according to (2.9)

$$\ddot{\boldsymbol{q}}_r = -\boldsymbol{C}_r^+(\boldsymbol{\theta})\boldsymbol{h}(\boldsymbol{\theta},\dot{\boldsymbol{\theta}},\boldsymbol{q}) - \boldsymbol{C}_r^+(\boldsymbol{\theta})\boldsymbol{E}(\boldsymbol{\theta},\boldsymbol{q})\ddot{\boldsymbol{\theta}} - 2\boldsymbol{C}_r^+(\boldsymbol{\theta})\boldsymbol{c}(\boldsymbol{\theta},\dot{\boldsymbol{\theta}},\boldsymbol{q}) - \boldsymbol{C}_r^+(\boldsymbol{\theta})\boldsymbol{C}_d(\boldsymbol{\theta})\ddot{\boldsymbol{q}}_d \quad (2.28)$$

By defining

$$\boldsymbol{n}(\boldsymbol{\theta},\dot{\boldsymbol{\theta}},\boldsymbol{q},\dot{\boldsymbol{q}}) = -\boldsymbol{C}_r^+(\boldsymbol{\theta})\boldsymbol{h}(\boldsymbol{\theta},\dot{\boldsymbol{\theta}},\boldsymbol{q}) - 2\boldsymbol{C}_r^+(\boldsymbol{\theta})\boldsymbol{c}(\boldsymbol{\theta},\dot{\boldsymbol{\theta}},\boldsymbol{q}) \quad (2.29)$$

The acceleration of rigid-body modal coordinates can be arranged as

$$\ddot{\boldsymbol{q}}_r = \boldsymbol{G}(\boldsymbol{\theta},\boldsymbol{q})\ddot{\boldsymbol{\theta}} + \boldsymbol{D}(\boldsymbol{\theta})\ddot{\boldsymbol{q}}_d + \boldsymbol{n}(\boldsymbol{\theta},\dot{\boldsymbol{\theta}},\boldsymbol{q},\dot{\boldsymbol{q}}) \quad (2.30)$$

2.4 Virtual work contributions

2.4.1 Virtual work of inertial forces for a link

For the sake of simplicity, in the following the index i-th, that spans from 1 to the number of links, is dropped. According to (1.1), $\boldsymbol{p}$ indicates the vector containing the global coordinates of all the nodes of the link, $\boldsymbol{e}$ the vector containing the global coordinates of all the nodes belonging to the Equivalent Rigid-Link System, and $\boldsymbol{u}$ the vector containing the nodal displacements

$$\boldsymbol{p} = \boldsymbol{e} + \boldsymbol{u} \quad (2.31)$$

The nodal displacements $\boldsymbol{u}$ can be expressed as function of modal coordinates by means of block-matrix $\bar{\boldsymbol{R}}$, which is obtained by assembling the local-to-local transformation matrices $\boldsymbol{T}_i$ on the main diagonal

$$\boldsymbol{u} = \bar{\boldsymbol{R}}\boldsymbol{U}\boldsymbol{q} \quad (2.32)$$

The nodal virtual displacements can be written as

$$\delta\boldsymbol{u} = \delta\bar{\boldsymbol{R}}\boldsymbol{U}\boldsymbol{q} + \bar{\boldsymbol{R}}\boldsymbol{U}\delta\boldsymbol{q} \quad (2.33)$$

In the same manner, the second derivative of nodal displacements is equal to

$$\ddot{\boldsymbol{u}} = \ddot{\bar{\boldsymbol{R}}}\boldsymbol{U}\boldsymbol{q} + 2\dot{\bar{\boldsymbol{R}}}\boldsymbol{U}\dot{\boldsymbol{q}} + \bar{\boldsymbol{R}}\boldsymbol{U}\ddot{\boldsymbol{q}} \quad (2.34)$$

Before computing the virtual displacements and acceleration related to the ERLS, the general formulation of velocity and acceleration of a generic point associated to the link of the ERLS has to be computed.

With respect to point $\boldsymbol{O}$ in the global reference frame, the velocity and acceleration of a point $\boldsymbol{P}$ are

$$\boldsymbol{v}_p = \boldsymbol{v}_0 - (\boldsymbol{P}-\boldsymbol{O}) \wedge \boldsymbol{\omega} \quad (2.35)$$

$$\boldsymbol{a}_p = \boldsymbol{a}_0 - (\boldsymbol{P}-\boldsymbol{O}) \wedge \boldsymbol{\alpha} + \boldsymbol{\omega} \wedge (\boldsymbol{v}_p - \boldsymbol{v}_0) \quad (2.36)$$

Let identify three different non-aligned points, with subscripts 0, 1 and 2. $\boldsymbol{v}_1 = \boldsymbol{v}_0 - (\boldsymbol{P}_1 - \boldsymbol{O}_0) \wedge \boldsymbol{\omega}$ and $\boldsymbol{v}_2 = \boldsymbol{v}_0 - (\boldsymbol{P}_2 - \boldsymbol{O}_0) \wedge \boldsymbol{\omega}$ are the velocities of the last two points with respect to the first one. In matrix notation

$$\begin{bmatrix} \boldsymbol{v}_0 \\ \boldsymbol{v}_1 \\ \boldsymbol{v}_2 \end{bmatrix} = \hat{\boldsymbol{B}} \begin{bmatrix} \boldsymbol{v}_0 \\ \boldsymbol{\omega} \end{bmatrix} \tag{2.37}$$

$\hat{\boldsymbol{B}}$ is a 9×6 matrix (see Appendix A.2).

Let split the matrix of the eigenvectors $\boldsymbol{U}$ into two blocks, one related to the rigid-body mode eigenvectors $\boldsymbol{U}_r$ and the other related to the elastic mode eigenvectors $\boldsymbol{U}_d$: $\boldsymbol{U} = \begin{bmatrix} \boldsymbol{U}_r | \boldsymbol{U}_d \end{bmatrix}$. The sub-matrix $\hat{\boldsymbol{U}}_r$ is defined as the matrix composed by the rows of $\boldsymbol{U}_r$ that correspond to the nodes 0, 1 and 2. Since $\boldsymbol{U}_r$ is composed of the mode vectors related to the rigid motion, an unknown vector $\boldsymbol{x}$ that satisfies the following equation can be found

$$\begin{bmatrix} \boldsymbol{v}_0 \\ \boldsymbol{v}_1 \\ \boldsymbol{v}_2 \end{bmatrix} = \hat{\boldsymbol{U}}_r \boldsymbol{x} \tag{2.38}$$

From (2.37) and (2.38), it can be obtained that

$$\boldsymbol{x} = \tilde{\boldsymbol{B}} \begin{bmatrix} \boldsymbol{v}_0 \\ \boldsymbol{\omega} \end{bmatrix} \tag{2.39}$$

where the left pseudo-inverse matrix $\tilde{\boldsymbol{B}} = (\hat{\boldsymbol{U}}_r^T \hat{\boldsymbol{U}}_r)^{-1} \hat{\boldsymbol{U}}_r^T \hat{\boldsymbol{B}}$ has been used. The left pseudo-inverse matrix allows to obtain the solution that minimizes the norm of the error [53].

The velocities of the nodes of the ERLS can be expressed, in the links reference frame, as a function of the velocity of node 0 and the angular velocity vector, as

$$\dot{\boldsymbol{e}} = \bar{\boldsymbol{R}} \boldsymbol{U}_r \tilde{\boldsymbol{B}} \begin{bmatrix} \boldsymbol{v}_0 \\ \boldsymbol{\omega} \end{bmatrix} \tag{2.40}$$

$\tilde{\boldsymbol{B}}$ is only defined by the geometry of the link and the eigenvectors. Therefore, it can be calculated only once prior to starting the simulations.

The accelerations of nodes 0, 1 and 2 can be expressed as the sum of two contributes

$$\begin{aligned} \boldsymbol{a}_0 &= \boldsymbol{a}_0^I + \boldsymbol{a}_0^{II} \\ \boldsymbol{a}_1 &= \boldsymbol{a}_1^I + \boldsymbol{a}_1^{II} \\ \boldsymbol{a}_2 &= \boldsymbol{a}_2^I + \boldsymbol{a}_2^{II} \end{aligned} \tag{2.41}$$

where the first terms describe the acceleration for null angular velocity, whereas the second terms depend on the angular velocity.

By knowing that $\boldsymbol{a}_0^I = \boldsymbol{a}_0$, $\boldsymbol{a}_1^I = \boldsymbol{a}_0 - (\boldsymbol{P}_1 - \boldsymbol{P}_0) \wedge \boldsymbol{\alpha}$ and $\boldsymbol{a}_2^I = \boldsymbol{a}_0 - (\boldsymbol{P}_2 - \boldsymbol{P}_0) \wedge \boldsymbol{\alpha}$,

the acceleration of the nodes for null angular velocity are

$$\ddot{\boldsymbol{e}}^{I} = \bar{\boldsymbol{R}}\boldsymbol{U}_r\tilde{\boldsymbol{B}}\begin{bmatrix}\boldsymbol{a}_0\\ \boldsymbol{\alpha}\end{bmatrix} \tag{2.42}$$

whereas the contributes to the nodal acceleration due to angular velocity is

$$\ddot{\boldsymbol{e}}^{II} = \bar{\boldsymbol{R}}\bar{\boldsymbol{\Omega}}\boldsymbol{U}_r\tilde{\boldsymbol{B}}\begin{bmatrix}\boldsymbol{0}\\ \boldsymbol{\omega}\end{bmatrix} \tag{2.43}$$

The main diagonal of $\bar{\boldsymbol{\Omega}}$ is composed of the skew-symmetric matrices $\boldsymbol{\Omega}$ given by the components of the angular velocity in the link reference frame. The relationship $\boldsymbol{\omega}\wedge(\boldsymbol{v}_p - \boldsymbol{v}_0) = \boldsymbol{\omega}\wedge[(\boldsymbol{P}-\boldsymbol{O})\wedge\boldsymbol{\omega}]$ has been applied to obtain the centripetal contribution to all the nodes of the link.

Then, we can obtain:

$$\ddot{\boldsymbol{e}} = \bar{\boldsymbol{R}}\boldsymbol{U}_r\tilde{\boldsymbol{B}}\begin{bmatrix}\boldsymbol{a}_0\\ \boldsymbol{\alpha}\end{bmatrix} + \bar{\boldsymbol{R}}\bar{\boldsymbol{\Omega}}\boldsymbol{U}_r\tilde{\boldsymbol{B}}\begin{bmatrix}\boldsymbol{0}\\ \boldsymbol{\omega}\end{bmatrix} \tag{2.44}$$

where

$$\boldsymbol{B} = \begin{bmatrix}\tilde{\boldsymbol{B}}\\ \boldsymbol{0}\end{bmatrix} \tag{2.45}$$

It can be noticed that the lower block of $\boldsymbol{B}$ is composed of a number of null rows equal to the number of elastic modal coordinates of the link that is taken into account.

By rewriting $\boldsymbol{U}_r\tilde{\boldsymbol{B}}$ as $\boldsymbol{U}\boldsymbol{B}$, the following equations can be obtained

$$\dot{\boldsymbol{e}} = \bar{\boldsymbol{R}}\boldsymbol{U}\tilde{\boldsymbol{B}}\begin{bmatrix}\boldsymbol{v}_0\\ \boldsymbol{\omega}\end{bmatrix} \tag{2.46}$$

$$\ddot{\boldsymbol{e}} = \bar{\boldsymbol{R}}\boldsymbol{U}\boldsymbol{B}\begin{bmatrix}\boldsymbol{a}_0\\ \boldsymbol{\alpha}\end{bmatrix} + \bar{\boldsymbol{R}}\bar{\boldsymbol{\Omega}}\boldsymbol{U}\boldsymbol{B}\begin{bmatrix}\boldsymbol{0}\\ \boldsymbol{\omega}\end{bmatrix} \tag{2.47}$$

The virtual displacements of the nodes of the Equivalent Rigid-Link System can be written as

$$\delta\boldsymbol{e} = \bar{\boldsymbol{R}}\boldsymbol{U}\boldsymbol{B}\begin{bmatrix}\delta\boldsymbol{P}_0\\ \delta\boldsymbol{\phi}\end{bmatrix} \tag{2.48}$$

By considering that $\delta\boldsymbol{p} = \delta\boldsymbol{e} + \delta\boldsymbol{u}$ and $\ddot{\boldsymbol{p}} = \ddot{\boldsymbol{e}} + \ddot{\boldsymbol{u}}$, the virtual displacements and the absolute accelerations are equal to

$$\delta\boldsymbol{p} = \bar{\boldsymbol{R}}\boldsymbol{U}\boldsymbol{B}\begin{bmatrix}\delta\boldsymbol{P}_0\\ \delta\boldsymbol{\phi}\end{bmatrix} + \delta\bar{\boldsymbol{R}}\boldsymbol{U}\boldsymbol{q} + \bar{\boldsymbol{R}}\boldsymbol{U}\delta\boldsymbol{q} \tag{2.49}$$

$$\ddot{\boldsymbol{p}} = \bar{\boldsymbol{R}}\boldsymbol{U}\boldsymbol{B}\begin{bmatrix}\boldsymbol{a}_0\\ \boldsymbol{\alpha}\end{bmatrix} + \bar{\boldsymbol{R}}\bar{\boldsymbol{\Omega}}\boldsymbol{U}\boldsymbol{B}\begin{bmatrix}\boldsymbol{0}\\ \boldsymbol{\omega}\end{bmatrix} + \ddot{\bar{\boldsymbol{R}}}\boldsymbol{U}\boldsymbol{q} + 2\dot{\bar{\boldsymbol{R}}}\boldsymbol{U}\dot{\boldsymbol{q}} + \bar{\boldsymbol{R}}\boldsymbol{U}\ddot{\boldsymbol{q}} \tag{2.50}$$

By defining as $\boldsymbol{M}$ the mass matrix in the local reference frame, the virtual work related to inertial forces can be computed as

$$\delta W_{inertia} = -\delta \boldsymbol{p}^T \bar{\boldsymbol{R}} \boldsymbol{M} \bar{\boldsymbol{R}}^T \ddot{\boldsymbol{p}} \tag{2.51}$$

or, by introducing the expressions for the virtual displacements $\delta\boldsymbol{p}$ and the absolute accelerations $\ddot{\boldsymbol{p}}$, as

$$\begin{aligned} \delta W_{inertia} = & \left(\delta \boldsymbol{q}^T \boldsymbol{U}^T + \boldsymbol{q}^T \boldsymbol{U}^T \delta \bar{\boldsymbol{R}}^T \bar{\boldsymbol{R}} + \begin{bmatrix} \delta \boldsymbol{P}_0 \\ \delta \boldsymbol{\phi} \end{bmatrix}^T \boldsymbol{B}^T \boldsymbol{U}^T \right) \boldsymbol{M} \\ & \times \left(\boldsymbol{U}\boldsymbol{B} \begin{bmatrix} \boldsymbol{a}_0 \\ \boldsymbol{\alpha} \end{bmatrix} + \bar{\boldsymbol{\Omega}} \boldsymbol{U}\boldsymbol{B} \begin{bmatrix} \boldsymbol{0} \\ \boldsymbol{\omega} \end{bmatrix} + \bar{\boldsymbol{R}}^T \ddot{\bar{\boldsymbol{R}}} \boldsymbol{U}\boldsymbol{q} + 2\bar{\boldsymbol{R}}^T \dot{\bar{\boldsymbol{R}}} \boldsymbol{U}\dot{\boldsymbol{q}} + \boldsymbol{U}\ddot{\boldsymbol{q}} \right) \end{aligned} \tag{2.52}$$

The terms

$$\delta \bar{\boldsymbol{R}}^T \bar{\boldsymbol{R}} = \delta \bar{\boldsymbol{\Phi}}^T \tag{2.53}$$

$$\bar{\boldsymbol{R}}^T \dot{\bar{\boldsymbol{R}}} = \bar{\boldsymbol{\Omega}} \tag{2.54}$$

$$\bar{\boldsymbol{R}}^T \ddot{\bar{\boldsymbol{R}}} = \bar{\boldsymbol{A}} - \bar{\boldsymbol{\Omega}}^T \bar{\boldsymbol{\Omega}} \tag{2.55}$$

are computed as reported in Appendix A.3.

The matrices $\bar{\boldsymbol{\Omega}}$, $\boldsymbol{A}$ and $\delta\boldsymbol{\Phi}$ are calculated as:

$$\bar{\boldsymbol{\Omega}} = \begin{bmatrix} 0 & -\omega_z & \omega_y \\ \omega_z & 0 & -\omega_x \\ -\omega_y & \omega_x & 0 \end{bmatrix}; \quad \boldsymbol{A} = \begin{bmatrix} 0 & -\alpha_z & \alpha_y \\ \alpha_z & 0 & -\alpha_x \\ -\alpha_y & \alpha_x & 0 \end{bmatrix}; \quad \delta\boldsymbol{\Phi} = \begin{bmatrix} 0 & -\delta\phi_z & \delta\phi_y \\ \delta\phi_z & 0 & -\delta\phi_x \\ -\delta\phi_y & \delta\phi_x & 0 \end{bmatrix} \tag{2.56}$$

$\delta\phi_x$, $\delta\phi_y$ and $\delta\phi_z$ are the components of the virtual rotational displacement of the link. The virtual work of inertial forces can be finally rewritten in the following form

$$\begin{aligned} \delta W_{inertia} = & -\left(\delta \boldsymbol{q}^T \boldsymbol{U}^T + \boldsymbol{q}^T \boldsymbol{U}^T \delta \bar{\boldsymbol{\Phi}}^T + \begin{bmatrix} \delta \boldsymbol{P}_0 \\ \delta \boldsymbol{\phi} \end{bmatrix}^T \boldsymbol{B}^T \boldsymbol{U}^T \right) \boldsymbol{M} \\ & \left(\boldsymbol{U}\boldsymbol{B} \begin{bmatrix} \boldsymbol{a}_0 \\ \boldsymbol{\alpha} \end{bmatrix} + \bar{\boldsymbol{\Omega}} \boldsymbol{U}\boldsymbol{B} \begin{bmatrix} \boldsymbol{0} \\ \boldsymbol{\omega} \end{bmatrix} + (\bar{\boldsymbol{A}} - \bar{\boldsymbol{\Omega}}^T \bar{\boldsymbol{\Omega}}) \boldsymbol{U}\boldsymbol{q} + 2\bar{\boldsymbol{\Omega}} \boldsymbol{U}\dot{\boldsymbol{q}} + \boldsymbol{U}\ddot{\boldsymbol{q}} \right) \end{aligned} \tag{2.57}$$

The previous equation can be expanded by computing the products between virtual displacements and inertial forces

$$\begin{aligned} & -\delta W_{inertia} = \\ & = \delta \boldsymbol{q}^T \boldsymbol{U}^T \boldsymbol{M} \boldsymbol{U}\boldsymbol{B} \begin{bmatrix} \boldsymbol{a}_0 \\ \boldsymbol{\alpha} \end{bmatrix} + \boldsymbol{q}^T \boldsymbol{U}^T \delta \bar{\boldsymbol{\Phi}}^T \boldsymbol{M} \boldsymbol{U}\boldsymbol{B} \begin{bmatrix} \boldsymbol{a}_0 \\ \boldsymbol{\alpha} \end{bmatrix} + \begin{bmatrix} \delta \boldsymbol{P}_0 \\ \delta \boldsymbol{\phi} \end{bmatrix}^T \boldsymbol{B}^T \boldsymbol{U}^T \boldsymbol{M} \boldsymbol{U}\boldsymbol{B} \begin{bmatrix} \boldsymbol{a}_0 \\ \boldsymbol{\alpha} \end{bmatrix} \end{aligned}$$

$$
\begin{aligned}
&+\delta\boldsymbol{q}^T\boldsymbol{U}^T\boldsymbol{M}\bar{\boldsymbol{\Omega}}\boldsymbol{U}\boldsymbol{B}\begin{bmatrix}\boldsymbol{0}\\ \boldsymbol{\omega}\end{bmatrix}+\boldsymbol{q}^T\boldsymbol{U}^T\delta\bar{\boldsymbol{\Phi}}^T\boldsymbol{M}\bar{\boldsymbol{\Omega}}\boldsymbol{U}\boldsymbol{B}\begin{bmatrix}\boldsymbol{0}\\ \boldsymbol{\omega}\end{bmatrix}+\begin{bmatrix}\delta\boldsymbol{P}_0\\ \delta\boldsymbol{\phi}\end{bmatrix}^T\boldsymbol{B}^T\boldsymbol{U}^T\boldsymbol{M}\bar{\boldsymbol{\Omega}}\boldsymbol{U}\boldsymbol{B}\begin{bmatrix}\boldsymbol{0}\\ \boldsymbol{\omega}\end{bmatrix}\\
&+\delta\boldsymbol{q}^T\boldsymbol{U}^T\boldsymbol{M}(\bar{\boldsymbol{A}}-\bar{\boldsymbol{\Omega}}^T\bar{\boldsymbol{\Omega}})\boldsymbol{U}\boldsymbol{q}+\boldsymbol{q}^T\boldsymbol{U}^T\delta\bar{\boldsymbol{\Phi}}^T\boldsymbol{M}(\bar{\boldsymbol{A}}-\bar{\boldsymbol{\Omega}}^T\bar{\boldsymbol{\Omega}})\boldsymbol{U}\boldsymbol{q}\\
&+\begin{bmatrix}\delta\boldsymbol{P}_0\\ \delta\boldsymbol{\phi}\end{bmatrix}^T\boldsymbol{B}^T\boldsymbol{U}^T\boldsymbol{M}(\bar{\boldsymbol{A}}-\bar{\boldsymbol{\Omega}}^T\bar{\boldsymbol{\Omega}})\boldsymbol{U}\boldsymbol{q}+2\delta\boldsymbol{q}^T\boldsymbol{U}^T\boldsymbol{M}\bar{\boldsymbol{\Omega}}\boldsymbol{U}\dot{\boldsymbol{q}}+2\boldsymbol{q}^T\boldsymbol{U}^T\delta\bar{\boldsymbol{\Phi}}^T\boldsymbol{M}\bar{\boldsymbol{\Omega}}\boldsymbol{U}\dot{\boldsymbol{q}}\\
&+2\begin{bmatrix}\delta\boldsymbol{P}_0\\ \delta\boldsymbol{\phi}\end{bmatrix}^T\boldsymbol{B}^T\boldsymbol{U}^T\boldsymbol{M}\bar{\boldsymbol{\Omega}}\boldsymbol{U}\dot{\boldsymbol{q}}+\delta\boldsymbol{q}^T\boldsymbol{U}^T\boldsymbol{M}\boldsymbol{U}\ddot{\boldsymbol{q}}+\boldsymbol{q}^T\boldsymbol{U}^T\delta\bar{\boldsymbol{\Phi}}^T\boldsymbol{M}\boldsymbol{U}\ddot{\boldsymbol{q}}+\begin{bmatrix}\delta\boldsymbol{P}_0\\ \delta\boldsymbol{\phi}\end{bmatrix}^T\boldsymbol{B}^T\boldsymbol{U}^T\boldsymbol{M}\boldsymbol{U}\ddot{\boldsymbol{q}}
\end{aligned}
\tag{2.58}
$$

Let now split the virtual work into two contributes

$$
\delta W_{inertia}=\delta W^I_{inertia}+\delta W^{II}_{inertia}
\tag{2.59}
$$

where the first groups together all the terms depending on the second derivative of the variables, the second all the remaining elements

$$
\begin{aligned}
&-\delta W^I_{inertia}=\\
&=\delta\boldsymbol{q}^T\boldsymbol{U}^T\boldsymbol{M}\boldsymbol{U}\boldsymbol{B}\begin{bmatrix}\boldsymbol{a}_0\\ \boldsymbol{\alpha}\end{bmatrix}+\boldsymbol{q}^T\boldsymbol{U}^T\delta\bar{\boldsymbol{\Phi}}^T\boldsymbol{M}\boldsymbol{U}\boldsymbol{B}\begin{bmatrix}\boldsymbol{a}_0\\ \boldsymbol{\alpha}\end{bmatrix}+\begin{bmatrix}\delta\boldsymbol{P}_0\\ \delta\boldsymbol{\phi}\end{bmatrix}^T\boldsymbol{B}^T\boldsymbol{U}^T\boldsymbol{M}\boldsymbol{U}\boldsymbol{B}\begin{bmatrix}\boldsymbol{a}_0\\ \boldsymbol{\alpha}\end{bmatrix}\\
&+\delta\boldsymbol{q}^T\boldsymbol{U}^T\boldsymbol{M}\bar{\boldsymbol{A}}\boldsymbol{U}\boldsymbol{q}+\boldsymbol{q}^T\boldsymbol{U}^T\delta\bar{\boldsymbol{\Phi}}^T\boldsymbol{M}\bar{\boldsymbol{A}}\boldsymbol{U}\boldsymbol{q}\begin{bmatrix}\delta\boldsymbol{P}_0\\ \delta\boldsymbol{\phi}\end{bmatrix}^T\boldsymbol{B}^T\boldsymbol{U}^T\boldsymbol{M}\bar{\boldsymbol{A}}\boldsymbol{U}\boldsymbol{q}\\
&+\delta\boldsymbol{q}^T\boldsymbol{U}^T\boldsymbol{M}\boldsymbol{U}\ddot{\boldsymbol{q}}+\boldsymbol{q}^T\boldsymbol{U}^T\delta\bar{\boldsymbol{\Phi}}^T\boldsymbol{M}\boldsymbol{U}\ddot{\boldsymbol{q}}+\begin{bmatrix}\delta\boldsymbol{P}_0\\ \delta\boldsymbol{\phi}\end{bmatrix}^T\boldsymbol{B}^T\boldsymbol{U}^T\boldsymbol{M}\boldsymbol{U}\ddot{\boldsymbol{q}}
\end{aligned}
\tag{2.60}
$$

$$
\begin{aligned}
&-\delta W^{II}_{inertia}=\\
&=\delta\boldsymbol{q}^T\boldsymbol{U}^T\boldsymbol{M}\bar{\boldsymbol{\Omega}}\boldsymbol{U}\boldsymbol{B}\begin{bmatrix}\boldsymbol{0}\\ \boldsymbol{\omega}\end{bmatrix}-\boldsymbol{q}^T\boldsymbol{U}^T\delta\bar{\boldsymbol{\Phi}}^T\boldsymbol{M}\bar{\boldsymbol{\Omega}}\boldsymbol{U}\boldsymbol{B}\begin{bmatrix}\boldsymbol{0}\\ \boldsymbol{\omega}\end{bmatrix}-\begin{bmatrix}\delta\boldsymbol{P}_0\\ \delta\boldsymbol{\phi}\end{bmatrix}^T\boldsymbol{B}^T\boldsymbol{U}^T\boldsymbol{M}\bar{\boldsymbol{\Omega}}\boldsymbol{U}\boldsymbol{B}\begin{bmatrix}\boldsymbol{0}\\ \boldsymbol{\omega}\end{bmatrix}\\
&+\delta\boldsymbol{q}^T\boldsymbol{U}^T\boldsymbol{M}\bar{\boldsymbol{\Omega}}^T\bar{\boldsymbol{\Omega}}\boldsymbol{U}\boldsymbol{q}+\boldsymbol{q}^T\boldsymbol{U}^T\delta\bar{\boldsymbol{\Phi}}^T\boldsymbol{M}\bar{\boldsymbol{\Omega}}^T\bar{\boldsymbol{\Omega}}\boldsymbol{U}\boldsymbol{q}+\begin{bmatrix}\delta\boldsymbol{P}_0\\ \delta\boldsymbol{\phi}\end{bmatrix}^T\boldsymbol{B}^T\boldsymbol{U}^T\boldsymbol{M}\bar{\boldsymbol{\Omega}}^T\bar{\boldsymbol{\Omega}}\boldsymbol{U}\boldsymbol{q}\\
&-2\delta\boldsymbol{q}^T\boldsymbol{U}^T\boldsymbol{M}\bar{\boldsymbol{\Omega}}\boldsymbol{U}\dot{\boldsymbol{q}}-2\boldsymbol{q}^T\boldsymbol{U}^T\delta\bar{\boldsymbol{\Phi}}^T\boldsymbol{M}\bar{\boldsymbol{\Omega}}\boldsymbol{U}\dot{\boldsymbol{q}}-2\begin{bmatrix}\delta\boldsymbol{P}_0\\ \delta\boldsymbol{\phi}\end{bmatrix}^T\boldsymbol{B}^T\boldsymbol{U}^T\boldsymbol{M}\bar{\boldsymbol{\Omega}}\boldsymbol{U}\dot{\boldsymbol{q}}
\end{aligned}
\tag{2.61}
$$

The single terms of $\delta W^I_{inertia}$ and $\delta W^{II}_{inertia}$ are computed in Appendix A.4.

2.4.2 Variation of elastic energy for a link

Let now consider the elastic energy for a single link

$$\boldsymbol{H} = \frac{1}{2}\boldsymbol{u}^T\boldsymbol{K}\boldsymbol{u} \tag{2.62}$$

The variation of $\boldsymbol{H}$ can be expressed as

$$\delta\boldsymbol{H} = \delta\boldsymbol{u}^T\boldsymbol{K}\boldsymbol{u} \tag{2.63}$$

By substituting $\boldsymbol{u} = \boldsymbol{U}\boldsymbol{q}$, it holds

$$\delta\boldsymbol{H} = \delta\boldsymbol{q}^T\boldsymbol{U}^T\boldsymbol{K}\boldsymbol{U}\boldsymbol{q} = \delta\boldsymbol{q}^T\boldsymbol{\Gamma}\boldsymbol{q} \tag{2.64}$$

$\boldsymbol{\Gamma}$ is a diagonal matrix whose components are the squares of the natural frequencies. If we define $\boldsymbol{\Gamma}_d$ the sub-matrix corresponding to the non-null eigenvalues only, the variation of the elastic energy becomes

$$\delta\boldsymbol{H} = \delta\boldsymbol{q}_d^T\boldsymbol{\Gamma}_d\boldsymbol{q}_d \tag{2.65}$$

2.4.3 Virtual work of gravitational forces for a link

Let now consider the virtual work of gravitational forces for a single link

$$\delta W_g = \delta\boldsymbol{p}^T\boldsymbol{f}_g \tag{2.66}$$

where gravity is indicated with $\boldsymbol{f}_g$.

The corresponding virtual displacement is equal to

$$\delta\boldsymbol{p} = \bar{\boldsymbol{R}}\boldsymbol{U}\boldsymbol{B}\begin{bmatrix}\delta\boldsymbol{P}_0\\ \delta\boldsymbol{\phi}\end{bmatrix} + \delta\bar{\boldsymbol{R}}\boldsymbol{U}\boldsymbol{q} + \bar{\boldsymbol{R}}\boldsymbol{U}\delta\boldsymbol{q} \tag{2.67}$$

and the gravitational force vector as

$$\boldsymbol{f}_g = \bar{\boldsymbol{R}}\boldsymbol{M}\hat{\boldsymbol{g}}_l = \bar{\boldsymbol{R}}\boldsymbol{M}(\hat{\boldsymbol{i}}_1 q_x + \hat{\boldsymbol{i}}_2 q_y + \hat{\boldsymbol{i}}_3 q_z) = \bar{\boldsymbol{R}}\boldsymbol{M}\hat{\boldsymbol{I}}\boldsymbol{g}_l \tag{2.68}$$

$\boldsymbol{g}_l$ represents the gravitational vector in the reference frame of the link and vectors $\hat{\boldsymbol{i}}_i$ depend on the nature of nodes, as explained in Appendix A.5.

δW_g can be rewritten as

$$\delta W_g = \left(\begin{bmatrix}\delta\boldsymbol{P}_0\\ \delta\boldsymbol{\phi}\end{bmatrix}^T\boldsymbol{B}^T\boldsymbol{U}^T\bar{\boldsymbol{R}}^T + \boldsymbol{q}^T\boldsymbol{U}^T\delta\bar{\boldsymbol{R}}^T + \delta\boldsymbol{q}^T\boldsymbol{U}^T\bar{\boldsymbol{R}}^T\right)\bar{\boldsymbol{R}}\boldsymbol{M}\hat{\boldsymbol{I}}\boldsymbol{g}_l \tag{2.69}$$

or as

$$\delta W_g = \begin{bmatrix}\delta\boldsymbol{P}_0\\ \delta\boldsymbol{\phi}\end{bmatrix}^T\boldsymbol{B}^T\boldsymbol{U}^T\boldsymbol{M}\hat{\boldsymbol{I}}\boldsymbol{g}_l + \boldsymbol{q}^T\boldsymbol{U}^T\delta\bar{\boldsymbol{\Phi}}^T\boldsymbol{M}\hat{\boldsymbol{I}}\boldsymbol{g}_l + \delta\boldsymbol{q}^T\boldsymbol{U}^T\boldsymbol{M}\hat{\boldsymbol{I}}\boldsymbol{g}_l \tag{2.70}$$

The first term of the previous equation can be expressed as

$$\begin{bmatrix} \delta \boldsymbol{P}_0 \\ \delta \boldsymbol{\phi} \end{bmatrix}^T \boldsymbol{B}^T \boldsymbol{U}^T \boldsymbol{M} \hat{\boldsymbol{I}} \boldsymbol{g}_l = \begin{bmatrix} \delta \boldsymbol{P}_0 \\ \delta \boldsymbol{\phi} \end{bmatrix}^T \boldsymbol{B}^T \boldsymbol{Q}_4 \boldsymbol{g}_l \tag{2.71}$$

where

$$\boldsymbol{Q}_4 = \boldsymbol{U}^T \boldsymbol{M} \hat{\boldsymbol{I}} \tag{2.72}$$

A part of the second term is

$$\boldsymbol{U}^T \delta \bar{\boldsymbol{\Phi}}^T \boldsymbol{M} \hat{\boldsymbol{I}} = \boldsymbol{U}^T \left(\delta \phi_x \bar{\boldsymbol{A}}_1^T + \delta \phi_y \bar{\boldsymbol{A}}_2^T + \delta \phi_z \bar{\boldsymbol{A}}_3^T \right) \boldsymbol{M} \hat{\boldsymbol{I}} = \delta \phi_1 \boldsymbol{Q}_1 + \delta \phi_2 \boldsymbol{Q}_2 + \delta \phi_3 \boldsymbol{Q}_3 \tag{2.73}$$

where the following matrices have been defined

$$\begin{aligned} \boldsymbol{Q}_1 &= \boldsymbol{U}^T \bar{\boldsymbol{A}}_1^T \boldsymbol{M} \hat{\boldsymbol{I}} \\ \boldsymbol{Q}_2 &= \boldsymbol{U}^T \bar{\boldsymbol{A}}_2^T \boldsymbol{M} \hat{\boldsymbol{I}} \\ \boldsymbol{Q}_3 &= \boldsymbol{U}^T \bar{\boldsymbol{A}}_3^T \boldsymbol{M} \hat{\boldsymbol{I}} \end{aligned} \tag{2.74}$$

Finally, the third term is

$$\delta \boldsymbol{q}^T \boldsymbol{U}^T \boldsymbol{M} \hat{\boldsymbol{I}} \boldsymbol{g}_l = \delta \boldsymbol{q}^T \boldsymbol{Q}_4 \boldsymbol{g}_l \tag{2.75}$$

2.4.4 Virtual work of the resultant generalized forces acting on a link

Let now consider the virtual work of the resultant generalized forces (forces or torques) $\boldsymbol{f}$ acting on a link

$$\delta W_f = \delta \boldsymbol{p}^T \boldsymbol{f} \tag{2.76}$$

The virtual displacement is written as

$$\delta \boldsymbol{p} = \boldsymbol{T} \hat{\boldsymbol{U}}_f \boldsymbol{B} \begin{bmatrix} \delta \boldsymbol{P}_0 \\ \delta \boldsymbol{\phi} \end{bmatrix} + \delta \boldsymbol{T} \hat{\boldsymbol{U}}_f \boldsymbol{q} + \boldsymbol{T} \hat{\boldsymbol{U}}_f \delta \boldsymbol{q} \tag{2.77}$$

$\hat{\boldsymbol{U}}_f$ is a sub-matrix of $\boldsymbol{U}$ whose rows are the rows related to the degrees of freedom the generalized force is applied to.

If we define $\boldsymbol{f}_l$ the generalized force vector whose components are referred to the local reference frame of the link, we can obtain $\boldsymbol{f} = \boldsymbol{T} \boldsymbol{f}_l$. The virtual work δW_f can be developed as

$$\delta W_f = \left(\begin{bmatrix} \delta \boldsymbol{P}_0 \\ \delta \boldsymbol{\phi} \end{bmatrix}^T \boldsymbol{B}^T \hat{\boldsymbol{U}}_f^T \boldsymbol{R}^T + \boldsymbol{q}^T \hat{\boldsymbol{U}}_f^T \delta \boldsymbol{R}^T + \delta \boldsymbol{q}^T \hat{\boldsymbol{U}}_f^T \boldsymbol{R}^T \right) \boldsymbol{T} \boldsymbol{f}_l \tag{2.78}$$

or

$$\delta W_f = \begin{bmatrix} \delta \boldsymbol{P}_0 \\ \delta \boldsymbol{\phi} \end{bmatrix}^T \boldsymbol{B}^T \hat{\boldsymbol{U}}_f^T \boldsymbol{f}_l + \boldsymbol{q}^T \hat{\boldsymbol{U}}_f^T \delta \boldsymbol{\Phi}^T \boldsymbol{f}_l + \delta \boldsymbol{q}^T \hat{\boldsymbol{U}}_f^T \boldsymbol{f}_l \tag{2.79}$$

where

$$\begin{aligned}&\boldsymbol{q}^T\hat{\boldsymbol{U}}_f^T\delta\boldsymbol{\Phi}^T\boldsymbol{f}_l = \\ &= \delta\phi_1\boldsymbol{q}^T\hat{\boldsymbol{U}}_f^T\begin{bmatrix}0&0&0\\0&0&1\\0&-1&0\end{bmatrix}\boldsymbol{f}_l + \delta\phi_2\boldsymbol{q}^T\hat{\boldsymbol{U}}_f^T\begin{bmatrix}0&0&-1\\0&0&0\\1&0&0\end{bmatrix}\boldsymbol{f}_l + \delta\phi_3\boldsymbol{q}^T\hat{\boldsymbol{U}}_f^T\begin{bmatrix}0&1&0\\-1&0&0\\0&0&0\end{bmatrix}\boldsymbol{f}_l\end{aligned} \tag{2.80}$$

2.5 Equation of motion

Starting from (2.21), the virtual terms of the generic i-th link, i.e. linear $\delta\boldsymbol{P}_{0i}$, angular $\delta\boldsymbol{\phi}_i$ and modal $\delta\boldsymbol{q}$, can be expressed as

$$\begin{bmatrix}\delta\boldsymbol{P}_{0i}\\\delta\boldsymbol{\phi}_i\\\delta\boldsymbol{q}\end{bmatrix} = \begin{bmatrix}\boldsymbol{V}_{\theta i}&\boldsymbol{0}&\boldsymbol{0}\\\boldsymbol{0}&\boldsymbol{V}_{qri}&\boldsymbol{0}\\\boldsymbol{0}&\boldsymbol{0}&\boldsymbol{V}_{qdi}\end{bmatrix}\begin{bmatrix}\boldsymbol{J}(\boldsymbol{\theta})&\boldsymbol{0}\\\boldsymbol{G}(\boldsymbol{\theta},\boldsymbol{q})&\boldsymbol{D}(\boldsymbol{\theta})\\\boldsymbol{0}&\boldsymbol{I}\end{bmatrix}\begin{bmatrix}\delta\boldsymbol{\theta}\\\delta\boldsymbol{q}_d\end{bmatrix} = \boldsymbol{V}_i^o\boldsymbol{N}\begin{bmatrix}\delta\boldsymbol{\theta}\\\delta\boldsymbol{q}_d\end{bmatrix} \tag{2.81}$$

$\boldsymbol{V}_i^o$ is the selection matrix for the proper elements of the i-th link, ($\boldsymbol{V}_{\theta i}$ is the selection block-matrix for the rigid DOF, $\boldsymbol{V}_{qri}$ for the rigid modal coordinates and $\boldsymbol{V}_{qdi}$ for the elastic modal ones) and $\boldsymbol{J}(\boldsymbol{\theta})$ the Jacobian matrix of the ERLS. The $\boldsymbol{V}_i^o$ matrix is block diagonal and allows to select the correct terms related to both the rigid degrees of freedom and the independent vibration modal coordinates. Also the acceleration terms (2.30), i.e. linear $\boldsymbol{a}_{0i}$, angular $\boldsymbol{\alpha}_i$ and modal $\ddot{\boldsymbol{q}}$, can be rewritten as function of the independent variables:

$$\begin{bmatrix}\boldsymbol{a}_{0i}\\\boldsymbol{\alpha}_i\\\ddot{\boldsymbol{q}}\end{bmatrix} = \boldsymbol{V}_i^o\boldsymbol{N}\begin{bmatrix}\ddot{\boldsymbol{\theta}}\\\ddot{\boldsymbol{q}}_{\boldsymbol{d}}\end{bmatrix} + \boldsymbol{V}_i^o\begin{bmatrix}\dot{\boldsymbol{J}}(\boldsymbol{\theta},\dot{\boldsymbol{\theta}})\dot{\boldsymbol{\theta}}\\\boldsymbol{n}(\boldsymbol{\theta},\dot{\boldsymbol{\theta}},\boldsymbol{q},\dot{\boldsymbol{q}})\\\boldsymbol{0}\end{bmatrix} \tag{2.82}$$

The second term of the previous equation depends only on the position and velocity of the independent variables and, thus, it is known. The virtual work done by the inertial forces $\delta\boldsymbol{W}^I_{inertia,i}$ and $\delta\boldsymbol{W}^{II}_{inertia,i}$ of each link can be written as

$$-\delta\boldsymbol{W}^I_{inertia,i} = \begin{bmatrix}\delta\boldsymbol{P}_{0i}^T&\delta\boldsymbol{\phi}_i^T&\delta\boldsymbol{q}^T\end{bmatrix}\boldsymbol{L}_i\begin{bmatrix}\boldsymbol{a}_{0i}\\\boldsymbol{\alpha}_i\\\ddot{\boldsymbol{q}}\end{bmatrix} \tag{2.83}$$

$$-\delta\boldsymbol{W}^I_{inertia,i} = \begin{bmatrix}\delta\boldsymbol{\theta}^T&\delta\boldsymbol{q}_d^T\end{bmatrix}\boldsymbol{N}^T\boldsymbol{V}_i^{oT}\boldsymbol{L}_i\left(\boldsymbol{V}_i^o\boldsymbol{N}\begin{bmatrix}\ddot{\boldsymbol{\theta}}\\\ddot{\boldsymbol{q}}_{\boldsymbol{d}}\end{bmatrix} + \boldsymbol{V}_i^o\begin{bmatrix}\dot{\boldsymbol{J}}(\boldsymbol{\theta},\dot{\boldsymbol{\theta}})\dot{\boldsymbol{\theta}}\\\boldsymbol{n}(\boldsymbol{\theta},\dot{\boldsymbol{\theta}},\boldsymbol{q},\dot{\boldsymbol{q}})\\\boldsymbol{0}\end{bmatrix}\right) \tag{2.84}$$

where the $\boldsymbol{L}_i$ matrix contains all the terms not depending on virtual displacements and accelerations.

The term $\delta \boldsymbol{W}^{II}_{inertia,i}$ can be rewritten as

$$\delta \boldsymbol{W}^{II}_{inertia,i} = \begin{bmatrix} \delta \boldsymbol{P}_{0i}^T & \delta \boldsymbol{\phi}_i^T & \delta \boldsymbol{q}^T \end{bmatrix} \boldsymbol{l}_i = \begin{bmatrix} \delta \boldsymbol{\theta}^T & \delta \boldsymbol{q}_d^T \end{bmatrix} \boldsymbol{N}^T \boldsymbol{V}_i^{oT} \boldsymbol{l}_i \tag{2.85}$$

All the other terms such as the variation of the elastic energy $\delta \boldsymbol{H}$, gravity $\delta \boldsymbol{W}_g$ and the resultant generalized forces $\delta \boldsymbol{W}_f$ do not depend on accelerations. Then, they can be gathered into a unique term $\tilde{\boldsymbol{l}}_{\boldsymbol{i}}$. By naming $\delta \boldsymbol{W}_i$ the term with all the contributions not depending on accelerations, we can obtain

$$\delta \boldsymbol{W}_i = \begin{bmatrix} \delta \boldsymbol{P}_{0i}^T & \delta \boldsymbol{\phi}_i^T & \delta \boldsymbol{q}^T \end{bmatrix} \tilde{\boldsymbol{l}}_{\boldsymbol{i}} = \begin{bmatrix} \delta \boldsymbol{\theta}^T & \delta \boldsymbol{q}_d^T \end{bmatrix} \boldsymbol{N}^T \boldsymbol{V}_i^{oT} \tilde{\boldsymbol{l}}_{\boldsymbol{i}} \tag{2.86}$$

All the links contributions can be added to obtain the final formulation:

$$\begin{aligned} &- \delta \boldsymbol{W}^{I}_{inertia} = \\ &\sum_{i=1}^{N} \begin{bmatrix} \delta \boldsymbol{\theta}^T & \delta \boldsymbol{q}_d^T \end{bmatrix} \boldsymbol{N}^T \boldsymbol{V}_i^{oT} \boldsymbol{L}_i \left(\boldsymbol{V}_i^o \boldsymbol{N} \begin{bmatrix} \ddot{\boldsymbol{\theta}} \\ \ddot{\boldsymbol{q}}_{\boldsymbol{d}} \end{bmatrix} + \boldsymbol{V}_i^o \begin{bmatrix} \dot{\boldsymbol{J}}(\boldsymbol{\theta}, \dot{\boldsymbol{\theta}}) \dot{\boldsymbol{\theta}} \\ \boldsymbol{n}(\boldsymbol{\theta}, \dot{\boldsymbol{\theta}}, \boldsymbol{q}, \dot{\boldsymbol{q}}) \\ \boldsymbol{0} \end{bmatrix} \right) = \\ &= \delta \boldsymbol{W} = \sum_{i=1}^{N} \begin{bmatrix} \delta \boldsymbol{\theta}^T & \delta \boldsymbol{q}_d^T \end{bmatrix} \boldsymbol{N}^T \boldsymbol{V}_i^{oT} \tilde{\boldsymbol{l}}_{\boldsymbol{i}} \end{aligned}$$

By naming $\boldsymbol{L} \stackrel{\text{def}}{=} \sum_{i=1}^{N} \boldsymbol{V}_i^{oT} \boldsymbol{L}_i \boldsymbol{V}_i^o$ and $\tilde{\boldsymbol{l}} \stackrel{\text{def}}{=} \sum_{i=1}^{N} \boldsymbol{V}_i^{oT} \tilde{\boldsymbol{l}}_{\boldsymbol{i}}$, and discarding the virtual displacements, the final dynamic model of the flexible multibody system results:

$$\boldsymbol{N}^T \boldsymbol{L} \boldsymbol{N} \begin{bmatrix} \ddot{\boldsymbol{\theta}} \\ \ddot{\boldsymbol{q}}_{\boldsymbol{d}} \end{bmatrix} = \boldsymbol{N}^T \left(\boldsymbol{L} \left(- \begin{bmatrix} \dot{\boldsymbol{J}}(\boldsymbol{\theta}, \dot{\boldsymbol{\theta}}) \boldsymbol{\theta} \\ \boldsymbol{n}(\boldsymbol{\theta}, \dot{\boldsymbol{\theta}}, \boldsymbol{q}, \dot{\boldsymbol{q}}) \\ \boldsymbol{0} \end{bmatrix} \right) + \tilde{\boldsymbol{l}} \right) \tag{2.87}$$

2.6 Differences between ERLS and FFR formulations

In this section the differences between the Equivalent Rigid-Link System and the Floating Frame of Reference formulations are briefly recalled.

- The ERLS approach deals directly with a classical Denavith-Hartenberg [54] formulation as well as coping with the flexible-link robot as if it were a rigid-link one.

- In the FFR formulation the i-th deformed body does not represent rigid displacements with respect to the i-th link, in the sense that there are not rigid motions of the deformed body with respect to the local reference frame. On the other hand, the rigid displacements are required for the ERLS approach: they are defined by the values of the rigid-body modal coordinates.

- In the FFR, the joint parameters and deformation modal values are couple in the *kinematic equations*. Indeed, the constraint equations depend on both the elastic

deformations and on the reference motion of the elastic bodies.

In the ERLS formulation, the *kinematic equations* just contain the joint parameters, since the deformation modal values are present in the compatibility conditions at the joints. This means that *the kinematic equations of the ERLS are decoupled from the compatibility equations of the displacement at the joints* [37] [50] [51].

- As a consequence of the previous point, if a closed-form solution of the *kinematic equations* is available, it can be employed without resorting to iterative algorithm procedures.
- Moreover, for the ERLS approach the choice of independent variables is not problematic as it is, on the other hand, for the FFR formulation, as stated by Shabana in [26].

Chapter 3

Comparison between the ERLS-FEM and the ERLS-CMS approaches

In this chapter, two different approaches for the modeling of 3D flexible multibody system using an Equivalent Rigid-Link System are compared through numerical simulations. The first formulation is based on a Finite Element Method approach (ERLS-FEM), recalled in Chapter 1, whereas the second deals with the extension of the model through a modal approach, i.e. the Component Mode Synthesis technique (ERLS-CMS), described in Chapter 2. The two methodologies are compared in terms of accuracy in time and frequency domains and computational time. A flexible L-shaped manipulator has been chosen as a benchmark mechanism and its dynamic behavior has been simulated under different input conditions. The effects of the beam discretization and the number of considered modes have been taken into account and discussed.

Part of the work described in this chapter has been published in [2].

3.1 Introduction

As described in Chapter 1, the Equivalent Rigid-Link formulation has been firstly developed in combination with a Finite Element Method approach. The main drawback of this method is that the discretization of the beam elements (i.e. the number of nodes of the mesh) has to be kept low if a low computational time is required. In particular, a fast resolution of the dynamic equations and, therefore, a fast computational time is needed if the model has to be employed for real-time control systems or simulations.

For these reason, in recent years, a novel formulation based on a modal approach has been developed (Chapter 2). The modal formulation (ERLS-CMS) allows to keep the number of degrees of freedom low but, at the same time, to maintain a good accuracy in the simulated dynamic behavior of the mechanism.

Section 3.2 presents a theoretical comparison between the ERLS-FEM and CMS approaches, Section 3.3 describes the numerical implementation and simulation, Section

3.4 reports the results and Section 3.5 the conclusions of the chapter.

3.2 Theoretical comparison

In the following, the main differences between the theoretical models Equivalent Rigid-Link System - Finite Element Method and the Component Mode Synthesis are highlighted. With respect to the ERLS-FEM formulation, the ERLS-CMS:

- takes into account all the terms without simplifications and/or neglecting some, even if with a small contribution, inertia coupling terms. Indeed, in the virtual displacement formulation of the ERLS-FEM approach, the terms with lower-order magnitude are usually neglected [51];
- allows to work with whatsoever flexible or rigid-link shape and finite elements thanks to the modal representation; the Equivalent Rigid-Link System - Finite Element Method usually deals with flexible beam type links, in which the node discretization is easier to apply;
- allows, as already explained, to reduce the complexity of the model and possibly maintain a number of degrees of freedom that can be handled by a processor when a fine discretization is needed;
- allows the choice of a specific number of equations, which globally describes the dynamic behavior of the flexible system;
- allows to avoid ill-conditioned problems that often affect large dimensional models;
- allows to operate with lower computational resources on equal computing time, as it will be presented in this chapter;
- can be very useful for real-time simulation purposes, control, estimation and optimization algorithms;
- allows to retain only the interior modes of interest (e.g. by using the Craig-Bampton approach [55] or different Model Order Reduction techniques, as it is explained in Chapter 4).

3.3 Numerical implementation and simulation

The Equivalent Rigid-Link System - Finite Element Method and Component Mode Synthesis dynamic models have been implemented in Matlab^{TM} environment to test their accuracy and computational effort.

In the recent years, different benchmark mechanisms for flexible multibody systems have been proposed in the Literature, such as single-link, planar, closed loop and spatial

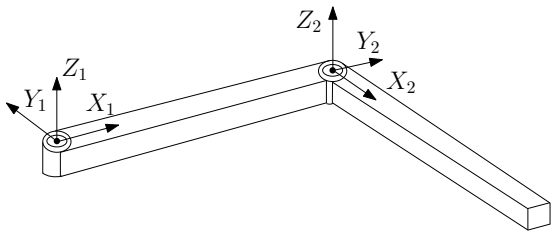

Figure 3.1: Double pendulum.

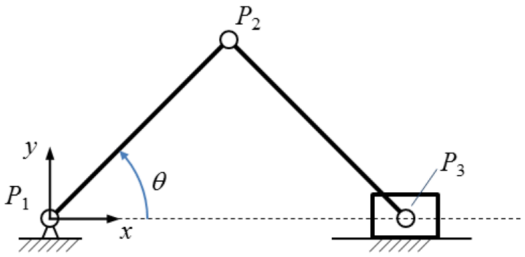

Figure 3.2: Slider-crank linkage mechanism.

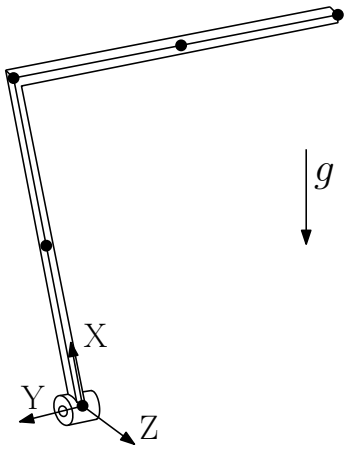

Figure 3.3: L-shaped manipulator: reference frame and possible node discretization.

manipulators (e.g. [56, 37, 57, 58, 59, 60]). In Figures 3.1 and 3.2 a double-pendulum and a slider-crank linkage mechanisms are reported as examples.

In this work, looking at a 3-D motion and excitation, a L-shaped mechanism, already employed in [12], has been chosen. An image of the manipulator and a possible node discretization is shown in Fig. 3.3. The L-shape mechanism is basically made of two flexible rods and it allows to induce motion and vibrations in different directions. For the ERLS-CMS model, the link flexibility has been imported through a special file, i.e. the modal neutral file, generated in Ansys^{TM} and based on the Craig-Bampton reduction. In Chapter 4 other different Model Order Reduction techniques are taken into account and compared.

The L-shaped system has one rigid rotational degree of freedom and, in these tests, it has been modeled with two and four Euler-Bernoulli beams - Finite Elements - in Ansys^{TM}. Figure 3.4 reports an image of the Euler-Bernoulli beams of the L-shaped manipulator in Ansys^{TM} for the case with 4 beam elements. Even if a low number of finite elements is considered, a good representation of its dynamic behavior can be obtained [12, 39, 57, 61]. Each Euler-Bernoulli beam has two nodes and six degrees of freedom: the two-elements system has a total of 18 DOF, whereas the four-elements one has a total of 30 DOF.

The geometrical and mechanical parameters of the benchmark mechanism are reported in Tab. 3.1.

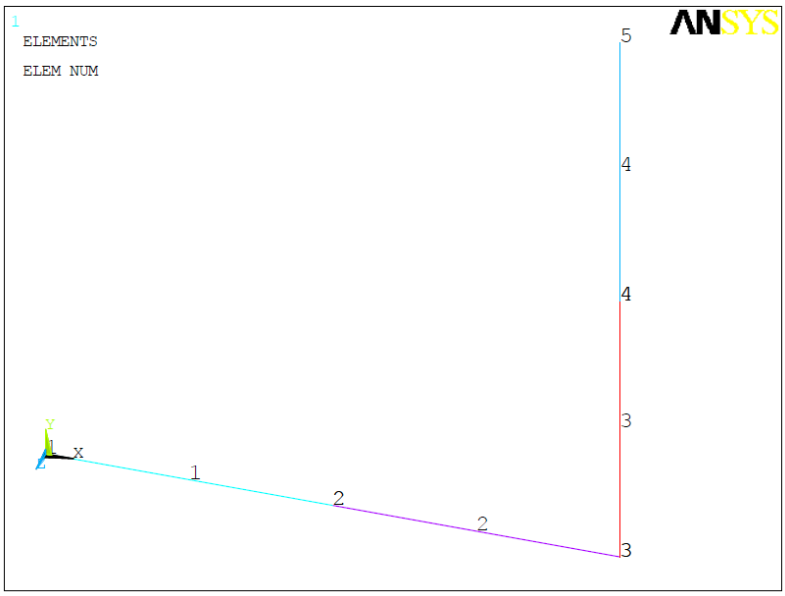

Figure 3.4: Euler-Bernoulli beams of the L-shaped manipulator in Ansys^{TM} (case with 4 beam elements).

Table 3.1: Geometrical and mechanical parameters of the L-shaped manipulator.

Rod	Material	Length [m]	Depth [m]	Width [m]	Density [kg/m^3]	Poisson's ratio	Young's module [N/m^2]
1^{st}	Aluminum	0.5	0.008	0.008	2700	0.33	7e^{10}
2^{nd}	Aluminum	0.5	0.008	0.008	2700	0.33	7e^{10}

To compare the two formulations, the responses of the mechanism under different inputs have been evaluated. In particular, as it was done in other works [12, 37, 58, 59], gravitational force and torque inputs have been considered and the results compared. Gravity vector is reported in Fig. 3.3, whereas the torque input signal is shown in Fig. 3.5. Gravitational force has been chosen as a natural way to excite the system, whereas the step torque input allows to properly excite the 3-D mechanism upon a wider range of frequencies.

The torque input signal allows, from a statically balanced configuration at 135°, to fast accelerate and decelerate the L-shaped system. In order to simulate the realistic mechanical behavior, a motor inertia I_m, a shrink disc inertia I_c and an elbow articulation concentrated mass m_e have been added to the model. The chosen values are $I_m = 0.0043\ Kg\ m^2$, $I_c = 0.001269\ Kg\ m^2$ and $m_e = 0.017\ Kg$, respectively.

The number of exported vibrational modes is defined in Ansys^{TM} when creating the *.mnf* file for Adams^{TM}, that exploits the Craig-Bampton modal reduction. In the 2-elements case, all available modes have been exported, whereas in the 4-elements case two different files with 18 and 30, over the 30 available modes, have been created. In Table 3.2, the exported natural frequencies are reported. The first 6 values of modes are not present in

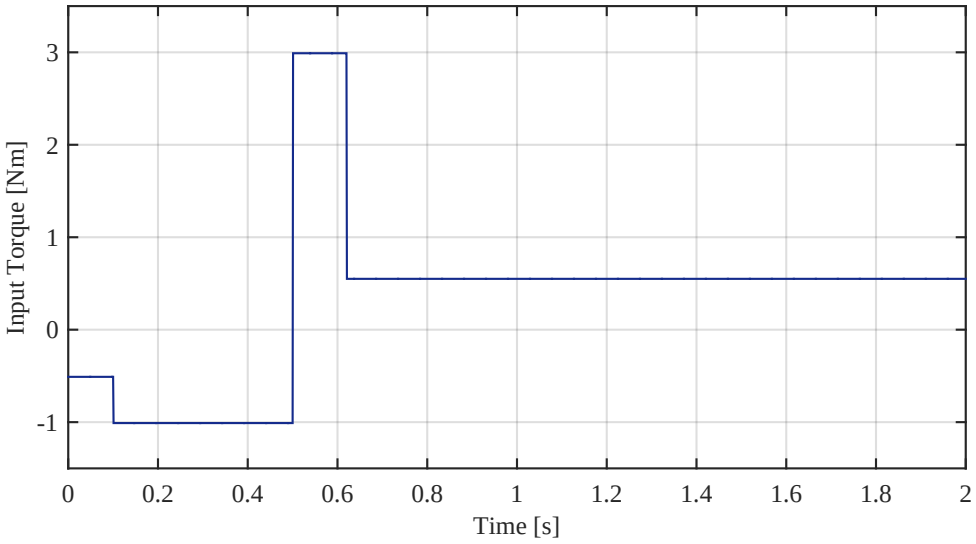

Figure 3.5: Input torque signal.

Table 3.2: Natural frequencies $[Hz]$ obtained by Adams^{TM} report files.

Mode	2 el. (18 m.)	4 el. (18 m.)	4 el. (30 m.)	Mode	4 el. (30 m.)
7	23.33	28.19	28.19	19	5466.76
8	37.56	34.42	34.42	20	6104.64
9	1171.02	103.24	103.25	21	6104.64
10	1273.62	106.16	106.16	22	6483.02
11	2519.98	187.01	186.90	23	7991.92
12	2729.22	234.08	234.08	24	11313.76
13	2729.22	1434.45	1344.65	25	14071.89
14	3241.51	1463.87	1371.12	26	18313.23
15	5427.78	3761.82	3360.82	27	19697.79
16	9207.15	6368.74	3379.20	28	23294.27
17	10398.16	7310.70	3507.58	29	23651.84
18	12610.60	12023.24	3508.01	30	25068.96

the table since they are equal to zero representing rigid-body modes.

Table 3.3: Hardware used for the numerical simulations.

Computer	HP Pavillon dv6
Processor	Intel® Core^{TM} 2 Duo CPU T6400 @ 2.00 GHz 2.00 GHz
Installed memory (RAM)	4.00 GB
System type	64-bit Operating System, x64-based processor
Windows edition	Windows 10 Pro

For each subdivision of the L-shaped manipulator in beam elements, different numerical simulations have been run, by varying the number of considered modes. The dynamics of the robotic system has been simulated for a time equal to 2 seconds and by adopting the variable step *ode45* solver in Matlab, based on an explicit Runge-Kutta formulation.

For each number of considered modes, three simulations have been run in order to obtain a correct average value of computational time. The properties of the laptop used for the numerical simulations are reported in Table 3.3.

3.4 Results and discussion

In this section, the results of the numerical simulations for the L-shaped manipulator subjected to both gravity (Subsection 3.4.1) and torque inputs (Subsection 3.4.2) are presented.

The dynamic simulations of the mechanism under gravity are intended to highlight the L-shaped system frequency response over a large frequency domain, whereas simulations with torque input highlight the behavior of the system under a forced condition, in a way more similar to a real application.

Four significant cases have been highlighted:

- the 2- and 4-elements models without reduction equivalent to the ERLS-FEM 2- and 4-beam elements model, i.e. 2 el. 18/18 modes and 4 el. 30/30 modes;
- the 4-elements model exported from Ansys^{TM} with 18 modes, i.e. 4 el. 18/18 modes;
- the model obtained by the full 30/30 reduced choosing only the first 18 modes, i.e. 4 el. 18/30 modes.

For the four cases and for the two input conditions (gravity and step torque), the position signals of the tip of the mechanism over the x, y and z axis and the z-coordinate acceleration signal of the L-shaped manipulator in both time and frequency domains have been analyzed. Moreover, the average computational times have been acquired and compared. For both the two input conditions, at the beginning of the excitation, the manipulator is in a static balanced position at 135°.

3.4.1 Mechanism under gravitational force

To better appreciate the differences between Finite Element Method and Component Mode Synthesis model results, the x, y and z coordinates position signals are reported in Figures 3.6, 3.7 and 3.8, respectively. The tip z-coordinate acceleration signal of the L-shaped manipulator under gravity both in the time and frequency domains are reported in Figures 3.9(a) and 3.9(b). For the acceleration comparison, the z-coordinate has been chosen since it is the one that is heavily excited due to the considered external forces acting on the L-shaped mechanism and, therefore, allows a better comparison of the results.

By considering the position signals, the 4-elements 18-modes and the 4-elements 30-modes signals overlap almost perfectly in all x, y and z coordinates, whereas the 2-elements signal shows a consistent difference.

By considering the acceleration signal, the 4-elements 18-modes and the 4-elements 30-modes signals have a largely overlapping behavior, whereas, as it can be expected, the

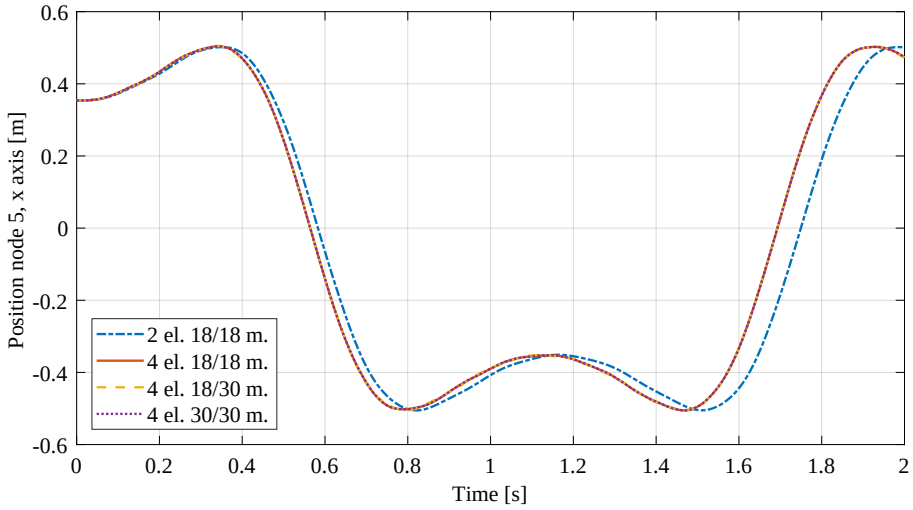

Figure 3.6: Comparison of the tip x-coordinate position of the L-shaped mechanism under gravity force.

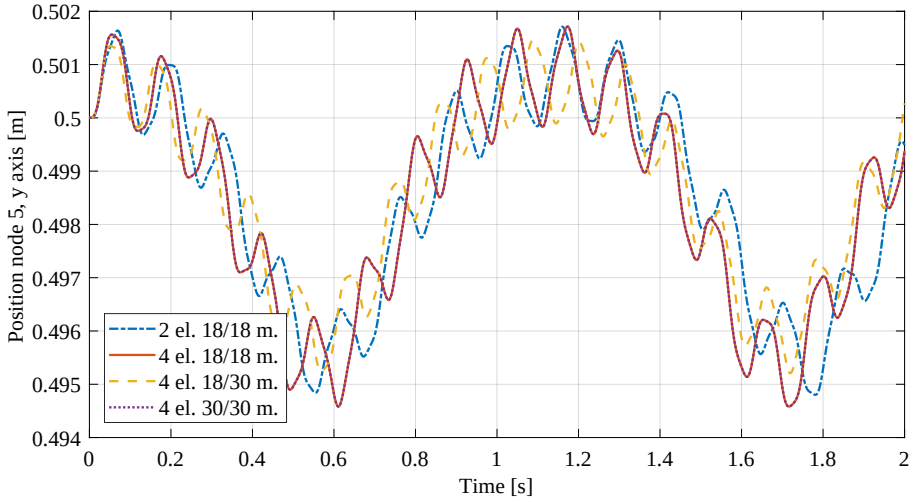

Figure 3.7: Comparison of the tip y-coordinate position of the L-shaped mechanism under gravity force.

2-elements signal shows a good agreement only at low frequencies. Small differences can be observed for the 4 el. 18/30 modes case due to the post reduction in the mode number.

In Tab. 3.4, the resonance peaks, detected on the z-coordinate acceleration signal of the L-shaped mechanism, are reported. Only the frequencies lower than 10 kHz have been considered here.

Looking at the values of Tab. 3.4, it can be highlighted that, in both the 4-elements cases, i.e. 4 el. 18 exported modes and 4 el. 30 modes, 14 vibration modes are sufficient to obtain a very good agreement of the first 8 resonance peaks with respect to the Finite Element Method case, i.e. the full model condition. Concerning simulation results with a considered number of modes lower than 14, a good agreement can be found only with respect to the first 3 peaks. As expected, by increasing the number of considered modal

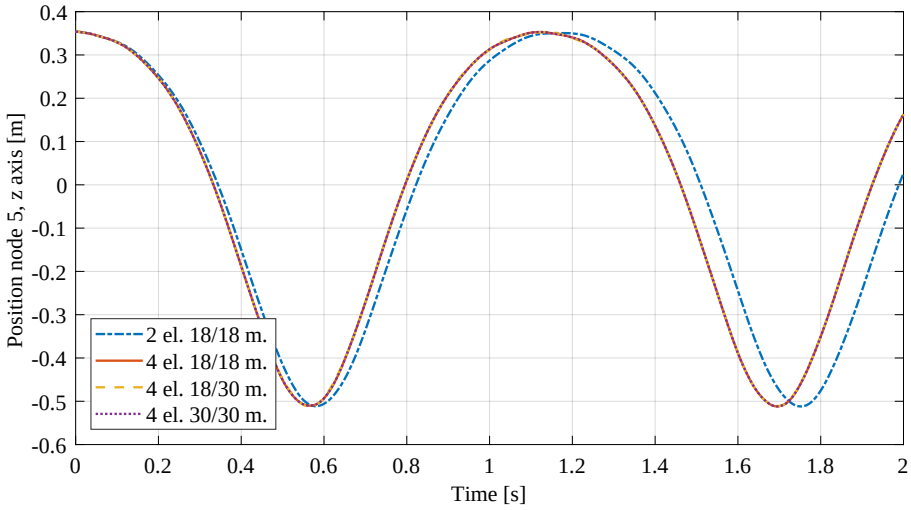

Figure 3.8: Comparison of the tip z-coordinate position of the L-shaped mechanism under gravity force.

Table 3.4: Resonance peaks $[Hz]$ with respect to beam elements and considered modes, mechanism subjected to gravity force.

Elements	Modes	Resonance peaks $[Hz]$										
		1	2	3	4	5	6	7	8	9	10	11
2 (18 m.)	18	0.5	7.5	28	31.5	1482						
4 (18 m.)	8	0.5	12	28.5								
	10	0.5	10	26.5	38							
	12	0.5	8.5	26	37.5	124.5	170					
	14	0.5	9	11.5	25.5	30.5	111.5	124	172	1464		
	16	0.5	9	11.5	25.5	30.5	111.5	124	172	2259	6163	
	18	0.5	8.5	11.5	24	30.5	111.5	117	172	265.5	2260	9334
4 (30 m.)	8	0.5	12	28.5								
	10	0.5	10	26.5	38							
	12	0.5	9.5	26	37.5	124	170					
	14	0.5	9	12	25.5	30.5	112.5	124	172	1371		
	16	0.5	9	11.5	25.5	30.5	111.5	124	172	3381		
	18	0.5	9	11.5	25.5	30.5	111.5	124	172	1918	3429	
	30	0.5	8.5	11.5	24	30.5	111.5	117	172	265.5	1767	5044

coordinates, the resonance peaks shift to lower values of frequency.

In Tab. 3.5 and Fig. 3.10 the computational time for each simulation is reported. In Tab. 3.6 the average computational time over the three simulations of each case and the percentage reduction with respect to the computational time of the FEM cases, i.e. the cases with no modal reduction, are shown.

For the 2-elements 18-modes and 4-elements 30-modes, the percentage reduction of computational effort is always greater than 50 %. An important computational time reduction can be appreciated also for the 4-elements 18-modes with respect to both 2 and 4-elements FEM cases.

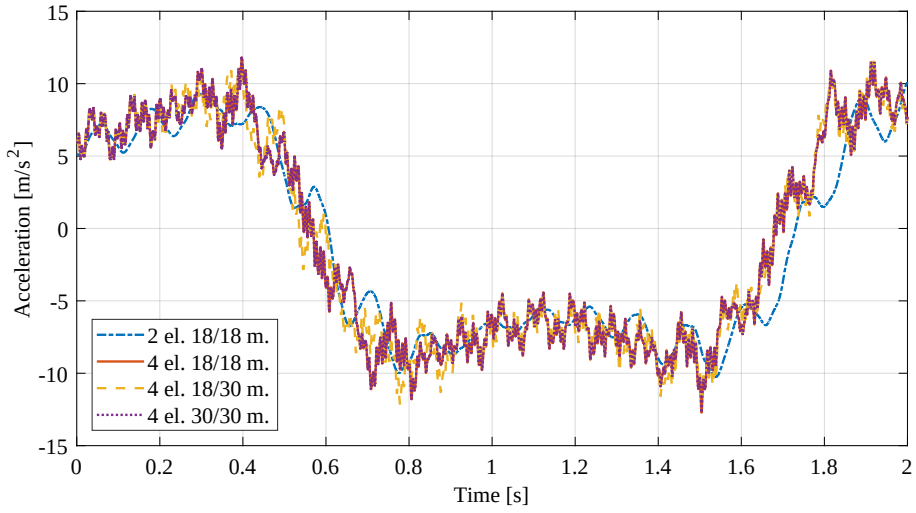

(a) Time domain.

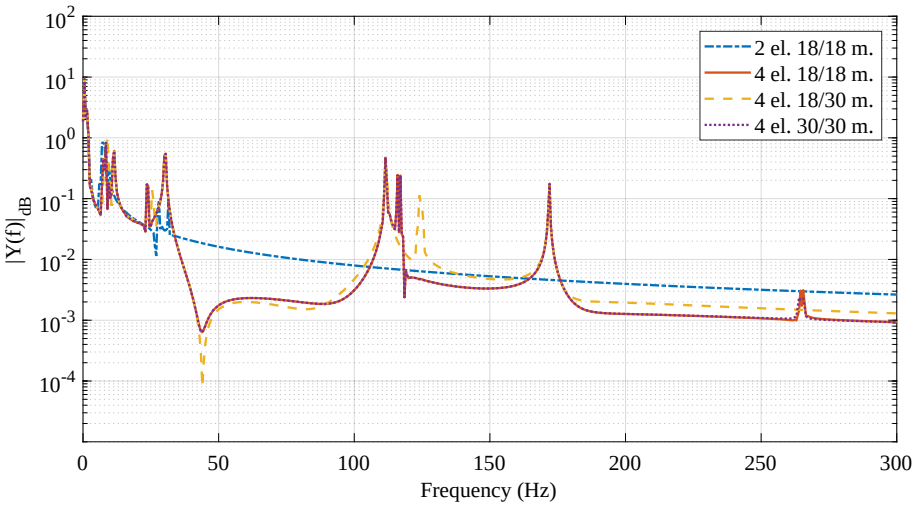

(b) Frequency domain.

Figure 3.9: Comparison of the tip z-coordinate acceleration of the L-shaped mechanism under gravity force.

By considering the four main cases previously evaluated, it can be seen that the modal reduction at 18 vibrational modes, i.e. 18 imported modes, allows a time reduction of about 22 % whereas, if 18 modes are maintained from the 4-elements 30 modes case, the time saving increases up to about 72 %.

If the 14 modes condition is evaluated, i.e. the one that allows to have an agreement on the first 8 resonance peaks, it can be appreciated that the reduction in time is always greater than 88 %, thus allowing to highlight the better performances of the ERLS-CMS approach with respect to the ERLS-FEM one.

Table 3.5: Computational time [s], mechanism under gravity.

Elements	Modes							
	6	8	10	12	14	16	18	30
2 (18 m.)	1.31	6.53	226.34	437.91	466.41	1041.23	2160.01	
	0.99	5.69	196.42	371.03	442.32	1004.10	2120.68	
	1.61	6.29	220.39	387.06	467.94	1027.24	2114.84	
4 (18 m.)	1.24	6.02	6.38	27.69	245.81	1128.18	1667.27	
	0.99	5.86	6.39	26.40	234.17	1046.00	1608.18	
	1.12	5.88	6.53	26.69	236.03	1085.86	1636.31	
4 (30 m.)	1.21	6.11	6.47	27.62	218.68	583.11	589.64	4969.19
	1.47	5.80	6.47	27.07	221.09	614.76	622.72	5024.79
	1.45	5.69	6.44	28.47	232.38	623.67	581.73	4974.43

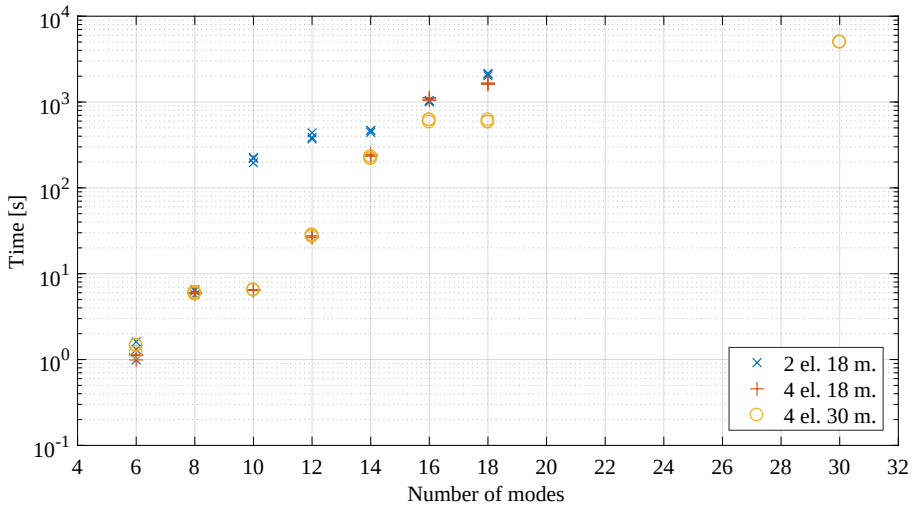

Figure 3.10: Computational time [s] in logarithmic scale, mechanism under gravity.

Table 3.6: Computational mean time [s] and reduction [%] with respect to the FEM case, mechanism under gravity.

Elements		Modes					
		10	12	14	16	18	30
2 (18 m.)	mean time [s]	214.38	398.67	458.89	1024.19	2098.84*	
	* [%]	89.79	81.01	78.14	51.20		
4 (30 m.)	mean time [s]	6.46	27.72	224.05	607.18	598.03	4989.47**
	* [%]	99.69	98.68	89.33	71.07	71.94	
	** [%]	99.87	99.44	95.51	87.83	88.01	
4 (18 m.)	mean time [s]	6.43	26.93	238.67	1086.68	1637.25	
	* [%]	99.69	98.72	88.63	48.22	21.99	
	** [%]	99.87	99.46	95.22	78.22	67.19	
Reduction with respect to		*					
Reduction with respect to		**					

3.4.2 Mechanism subjected to step torque input

In this section, the results of the simulations of the L-shaped mechanism subjected to a step torque input signal are provided. The x, y and z coordinates of the position signal of the mechanism tip (node 5 in Fig. 3.4) are reported in Figures 3.11, 3.12 and 3.13, respectively. The tip z-coordinate acceleration of the L-shaped beam under torque input is reported in Figures 3.14(a) and 3.14(b) in time and frequency domain, respectively.

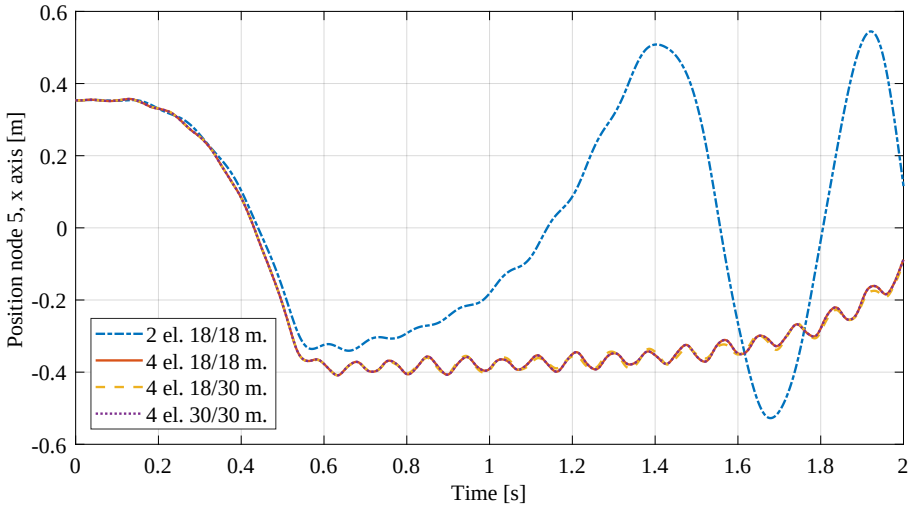

Figure 3.11: Comparison of the tip x-coordinate position of the L-shaped mechanism subjected to a step torque input.

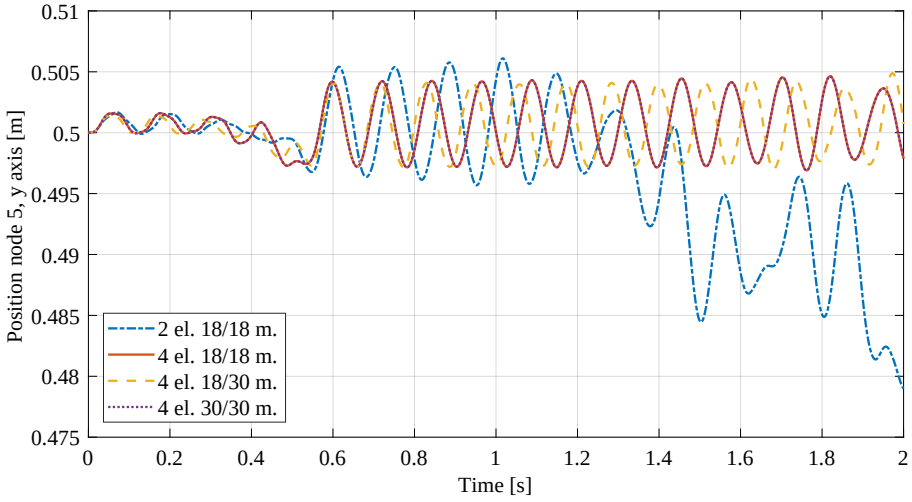

Figure 3.12: Comparison of the tip y-coordinate position of the L-shaped mechanism subjected to a step torque input.

Similarly to the gravitational force case, in the case of mechanism subjected to a step torque input, the 4-elements position and acceleration signals match each other very well, whereas the 2- elements FEM deviates from the other signal. In particular, 2- elements position coordinates show large discrepancies with respect to the 4- elements ones. By

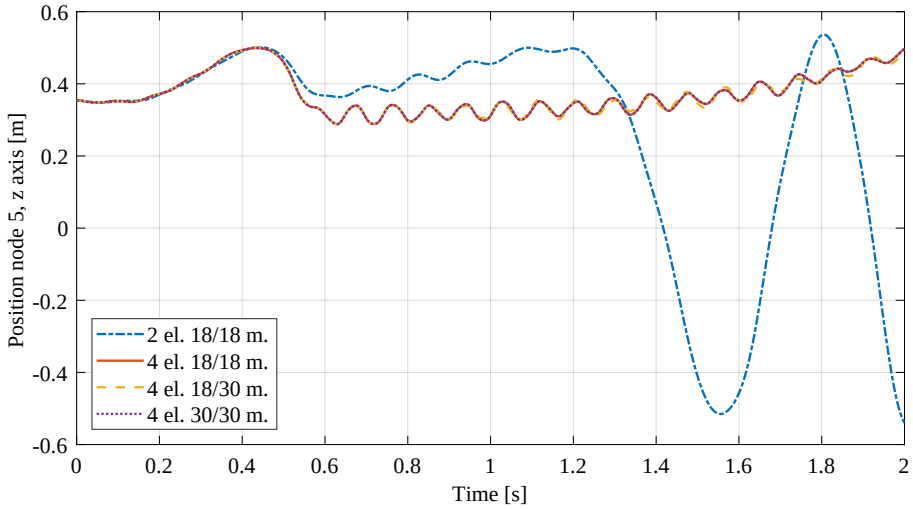

Figure 3.13: Comparison of the tip z-coordinate position of the L-shaped mechanism subjected to a step torque input.

considering the accelerations, the 2- elements captures only the low frequencies in a good manner.

Table 3.7 reports the resonance peaks of the previous acceleration signals. It can be seen that, for both 4- elements cases, only 14 modal coordinates in input are enough to identify the first 4 resonance peaks. The general trend is quite similar to the gravitational force case, since resonance peaks shift on lower frequency values by increasing the number of considered vibrational modes. With respect to the gravity case, the step torque input case shows 6 main excited frequencies.

Table 3.7: Resonance peaks $[Hz]$ with respect to beam elements and considered modes, mechanism subjected to torque input.

Elements	Modes	Resonance peaks $[Hz]$					
		1	2	3	4	5	6
2 (18 m.)	18	9.5	32.5	1491	11720		
4 (18 m.)	8	28.5					
	10	26.5	38				
	12	26.5	37.5	170			
	14	11.5	30.5	111.5	172		
	16	11	30.5	111.5	172	2271	6163
	18	11	30.5	111.5	172	2272	9345
4 (30 m.)	8	28.5					
	10	26.5	38				
	12	26.5	37.5	170			
	14	12	30.5	113	172		
	16	11	30.5	111.5	172		
	18	11	30.5	111.5	172	1929	3440
	30	11	30.5	111.5	172	1755	1778

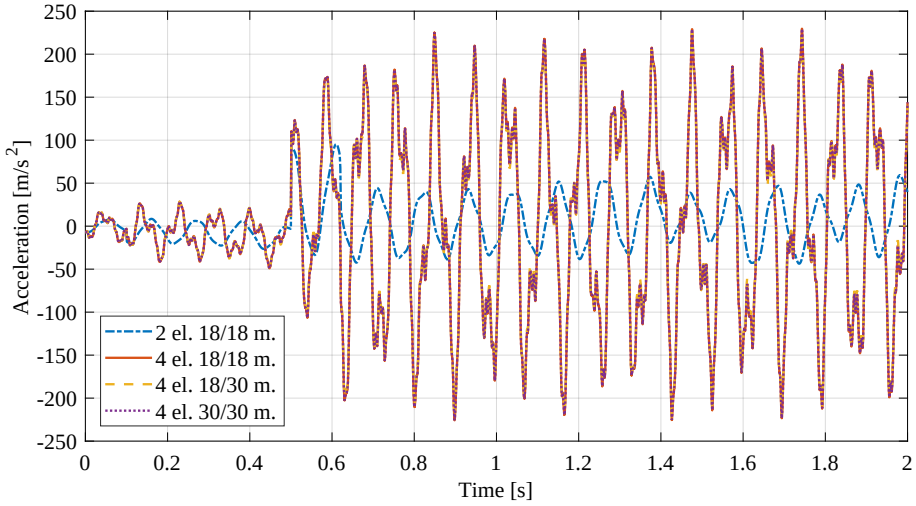

(a) Time domain.

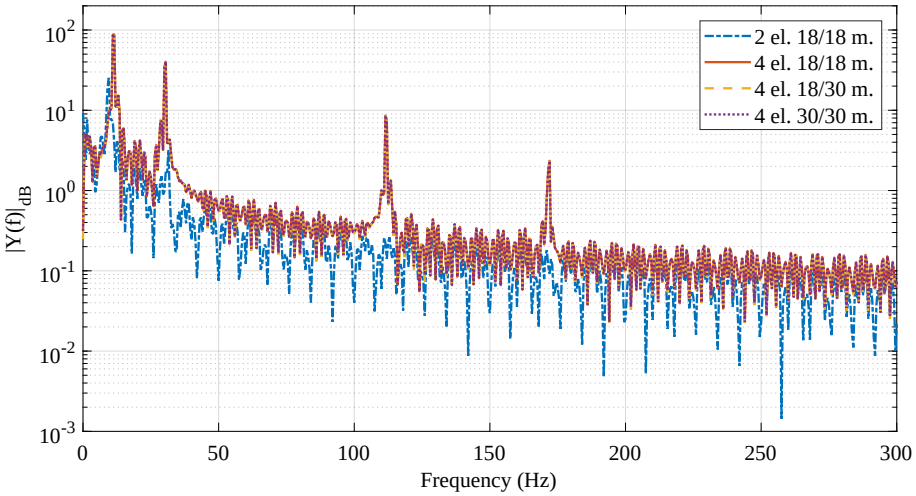

(b) Frequency domain.

Figure 3.14: Comparison of the tip z-coordinate acceleration of the L-shaped mechanism under torque input.

In Table 3.8 and in Figure 3.15 the computational time of the different simulations is reported. The values of computational time decrease by increasing the number of beam elements and the exported modes, for each number of considered modes. By increasing the beam elements and choosing the same number of modes, lower natural frequencies are considered, as it can be appreciate from Tab. 3.2. Thus, the solver is able to extend the time integration step and, therefore, the total required computational time decreases.

By considering the four main cases previously evaluated, it can be appreciated that the modal reduction at 18 modes, i.e. 18 imported modes, allows a time saving of about 20 %, whereas, if 18 modes are maintained from the 4 el. 30 modes case, the percentage time reduction increases up to about 71 %.

If the 14 modes condition is evaluated, i.e. the one that allows to have an agreement

Table 3.8: Computational time [s], mechanism subjected to torque input.

Elements	Modes							
	6	8	10	12	14	16	18	30
2 (18 m.)	1.02	5.85	203.64	387.05	454.47	1002.56	2091.69	
	1.37	6.35	213.72	374.69	445.70	1021.75	2105.60	
	1.42	5.62	198.73	378.21	448.13	986.64	2055.80	
4 (18 m.)	1.09	5.38	5.85	30.23	255.47	1070.51	1678.88	
	1.06	5.15	5.81	29.13	244.35	1053.85	1625.22	
	1.19	5.32	6.13	31.08	259.08	1087.85	1721.40	
4 (30 m.)	1.23	5.41	6.18	29.31	219.46	578.43	591.33	5137.08
	1.33	5.31	6.16	30.27	219.47	573.86	591.82	5127.65
	1.41	5.56	6.51	30.44	229.45	590.09	635.96	5087.46

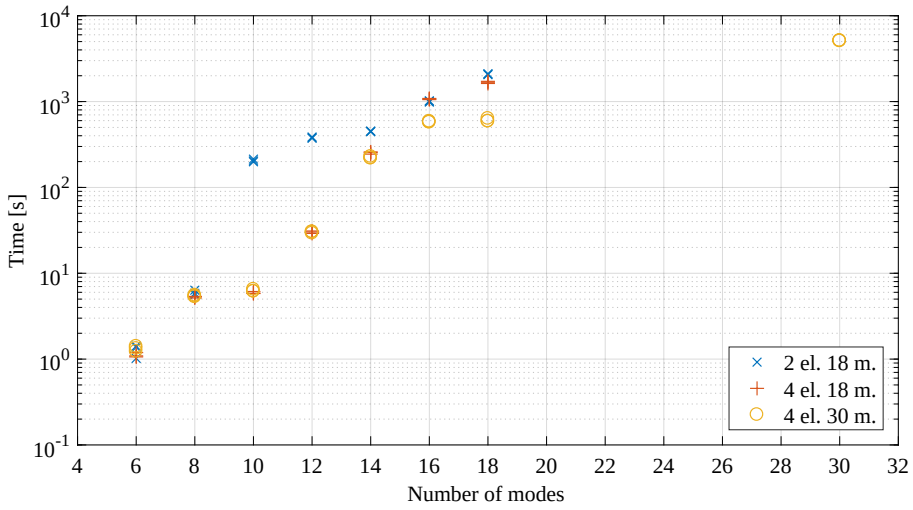

Figure 3.15: Computational time [s] in logarithmic scale, mechanism subjected to torque input.

on the first 4 resonance peaks, the time reduction is again always greater than 88 %, thus allowing to highlight the better performances of the modal approach (ERLS-CMS) with respect to the ERLS-FEM one.

Similarly to the gravitational force case, in the simulations of the mechanism subjected to a torque input it can be affirmed that the ERLS-CMS model with a number of modes lower than the maximum one allows a reduction of computational effort of great significance.

It has to be noticed that the results presented in this chapter have been obtained with a model suitable for small displacements and small elastic deformations. By considering longer rods or by increasing the stiffness of the material, a more flexibility would be introduced. This fact could lead to large elastic deformations. In such a condition, the Equivalent Rigid-Link System formulation could not be adopted any more being the approach not suitable to cope with large elastic deformations of the system.

Table 3.9: Computational mean time [s] and reduction [%] with respect to the FEM case, mechanism subjected to torque input.

Elements		Modes					
		10	12	14	16	18	30
2 (18 m.)	mean time [s]	205.36	379.98	449.43	1003.65	2084.36*	
	* [%]	90.15	81.77	78.44	51.85		
4 (30 m.)	mean time [s]	6.28	30.01	222.79	580.79	606.37	5117.40**
	* [%]	99.70	98.56	89.31	72.14	70.91	
	** [%]	99.88	99.41	95.65	88.65	88.15	
4 (18 m.)	mean time [s]	5.93	30.15	252.97	1070.74	1675.17	
	* [%]	99.72	98.55	87.86	48.63	19.63	
	** [%]	99.88	99.41	95.06	79.08	67.27	
Reduction with respect to		*					
Reduction with respect to		**					

3.5 Conclusions

In this chapter, a comparison between the Finite Element Method and the Component Mode Synthesis approaches, based on an Equivalent Rigid-Link System 3-D dynamic formulation, have been presented.

With respect to the kinematics and dynamics equations recalled in Chapters 1 and 2, a theoretical comparison between the two approaches has been discussed. The two models have been numerically implemented in Matlab^{TM} environment, by choosing a L-shape manipulator as a benchmark system. Different numerical simulations have been run by varying the discretization of the beams and the number of considered modes, adopting the gravitational force and a step torque as input signals. The performance of the models have been evaluated by comparing the position and acceleration signals in both time and frequency domain, as well as the average computational time and percentage time reduction with respect to the complete models.

Results show that, with respect to the Equivalent Rigid-Link System - Finite Element Method implementation, given the fact that the modal formulation allows to reduce the number of degrees of freedom of the system, the computational time required for the simulations decreases.

As demonstrated, the Equivalent Rigid-Link System - Component Mode Synthesis approach allows to keep both the gross and the fine motion of the robotic system. Since the choice of the selected modes could be made in different manners, in the next Chapter, different Model Order Reduction strategies are applied and evaluated to increase the performance of the ERLS-CMS approach.

Chapter 4

Comparison of Model Order Reduction Techniques

In this chapter, a comparison of different Model Order Reduction techniques for flexible multibody dynamics is presented. In particular, the modal formulation based on the Equivalent Rigid-Link System presented in Chapter 2 is adopted and implemented in combination with different reduction techniques, i.e. Craig-Bampton, Interior Mode Ranking (IMR), Guyan, Least Square Model Reduction (LSMR) and Mode Displacement Method (MDM). These techniques allow to reduce the computational time required by the dynamic model to be simulated, while maintaining a good accuracy in the description of the dynamic behavior of the system.

In order to assess the advantages and disadvantages of the different methodologies, these techniques are applied to a L-shaped benchmark mechanism under two different input conditions: gravitational force and a step torque. The accuracy of each reduced model is numerically estimated by means of vector correlation methods, i.e. the Modal Assurance Criterion (MAC), the Cross-Orthogonality (CO) and the Normalized Cross-Orthogonality (NCO), the behavior in frequency domain and through the comparison of computational time.

Part of the work described in this chapter has been previously published in [3].

4.1 Introduction

In multibody dynamics, the classical approach to take the flexibility of elastic robotic systems into account is based on the rigid-body dynamic model of the system and then the elastic deformations are introduced. The elastic deformations of the bodies affect the rigid motion and vice versa. It results in a highly non-linear dynamic formulation described by a coupled set of partial differential equations. As mentioned in Chapter 1, two main methodologies can be found in the Literature to derive a set of ordinary differential equations: the nodal approach (i.e. the Finite Element Method, FEM) and the modal one [15]. However, since a high number of degrees of freedom is introduced by the discretization of the flexible bodies, proper reduction methods should be applied in

order to allow an efficient numerical simulation of the multibody system, while keeping an accurate description of the predominant dynamic behavior.

Model Order Reduction techniques can be classified in physical coordinates techniques, generalized coordinates (i.e. modal coordinates) and hybrid methods, such as the Component Mode Synthesis (CMS). A review of Model Order Reduction techniques for structural dynamics, numerical mathematics and system and control is proposed in [62], whereas in [63], [64] and [65] reduced order modeling strategies are applied in dynamics sub-structuring. An example of model reduction can be found in [66], in which an elastic rod is considered. Furthermore, in the field of multibody systems, an overview of the basic approaches to model elastic multibody systems using the Floating Frame of Reference formulation in given by [67]. Recently, a novel ranking method (Interior Mode Ranking, IMR), that allows the selection of interior normal modes in the Craig-Bampton technique [68], has been proposed in [69].

In this Chapter, the Equivalent Rigid-Link System formulation for modeling the dynamics of flexible multibody systems is considered in its recent extension to a modal approach, i.e. the Component Mode Synthesis, presented in Chapter 2. As described in Chapter 3, this formulation, compared to the original ERLS-FEM, allows to achieve a more flexible solution based on a reduced-order system of equations. In particular, the classical Craig-Bampton approach has been adopted to select the internal vibrational modes of interest [12]. However, this reduction is not the only technique capable of reducing the number of degrees of freedom of a flexible multibody system.

For this reason, in this chapter different Model Order Reduction techniques are implemented and the results compared. In particular, the advantages and disadvantages of the different techniques are evaluated by simulating the dynamics of a L-shaped benchmark mechanism under different input conditions: the effects of gravity only and a certain torque signal. The FEM models of the benchmark mechanism are developed in Ansys® with different refinements of discretization, whereas dynamics and post-processing are evaluated in Matlab™. The reduced model accuracy is evaluated through the comparison of the computational time, the accuracy in frequency domain and by means of modal vector correlation parameters: the Modal Assurance Criterion [70] [71] [65], the Cross-Orthogonality [70] and the Normalized Cross-Orthogonality [72] [69] [73].

The remaining of the chapter is organized as follows: in Section 4.2 the Model Order Reduction techniques that have been implemented and tested on the ERLS dynamic model are briefly recalled; Section 4.3 shows the numerical implementation of the model on a benchmark mechanism, whereas in Section 4.4 the numerical results are presented and discussed. Finally, Section 4.5 highlights the conclusions of this work.

4.2 Model Order Reduction Techniques

In this section, the techniques that have been implemented for the Model Order Reduction (MOR) of the ERLS dynamic model are briefly recalled.

The generic equation of the dynamic equilibrium is considered

$$\boldsymbol{M}\ddot{\boldsymbol{X}}(t) + \boldsymbol{C}\dot{\boldsymbol{X}}(t) + \boldsymbol{K}\boldsymbol{X}(t) = \boldsymbol{F}(t) \tag{4.1}$$

where $\boldsymbol{M}$, $\boldsymbol{C}$, $\boldsymbol{K} \in \mathbb{R}^{n\times n}$ are the mass, dumping and stiffness matrices of the complete model, respectively, $\boldsymbol{X} \in \mathbb{R}^n$ is the independent coordinates vector, $\boldsymbol{F} \in \mathbb{R}^n$ is the force vector acting on the system, and n the number of DOF of the complete model. Starting from (4.1), several Model Order Reduction techniques assume the form of a coordinate transformation such as

$$\boldsymbol{X}(t) = \boldsymbol{T}\boldsymbol{Z}(t) \tag{4.2}$$

where $\boldsymbol{T} \in \mathbb{R}^{n\times m}$ is the transformation matrix that transforms the reduced model coordinates $\boldsymbol{Z} \in \mathbb{R}^m$ in the complete model ones $\boldsymbol{X}$, being m the number of DOF of the reduced model. Since the transformation matrix is generally time-dependent, the following equations can be written

$$\begin{aligned} \dot{\boldsymbol{X}}(t) &= \boldsymbol{T}\dot{\boldsymbol{Z}}(\boldsymbol{t}) \\ \ddot{\boldsymbol{X}}(t) &= \boldsymbol{T}\ddot{\boldsymbol{Z}}(\boldsymbol{t}) \end{aligned} \tag{4.3}$$

By substituting the previous expressions into (4.1) and by multiplying by matrix $\boldsymbol{T}^T$, the final dynamic equilibrium equation for the reduced model can be obtained

$$\boldsymbol{M}_r\ddot{\boldsymbol{Z}}(t) + \boldsymbol{C}_r\dot{\boldsymbol{Z}}(t) + \boldsymbol{K}_r\boldsymbol{Z}(t) = \boldsymbol{F}_r(t) \tag{4.4}$$

where $\boldsymbol{M}_r$, $\boldsymbol{C}_r$, $\boldsymbol{K}_r \in \mathbb{R}^{m\times m}$ are the mass, dumping and stiffness matrices of the reduced model, whereas $\boldsymbol{F}_r \in \mathbb{R}^m$ represents the force vector acting on the system. The reduced model matrices have been obtained as

$$\boldsymbol{M}_r = \boldsymbol{T}^T\boldsymbol{M}\boldsymbol{T}, \quad \boldsymbol{C}_r = \boldsymbol{T}^T\boldsymbol{C}\boldsymbol{T}, \quad \boldsymbol{K}_r = \boldsymbol{T}^T\boldsymbol{K}\boldsymbol{T}, \quad \boldsymbol{F}_r = \boldsymbol{T}^T\boldsymbol{F} \tag{4.5}$$

In the following of this section, the Model Order Reduction techniques for flexible multibody dynamics that have been implemented together with the ERLS-CMS formulation are briefly recalled and described. In particular, Craig-Bampton, Interior Mode Ranking, Guyan's reduction, Least Square Model Reduction and Mode Displacement Method have been considered.

4.2.1 Craig-Bampton

Craig-Bampton is the classical modal reduction technique in flexible multibody dynamics [68] [65]. It is a hybrid fixed-interface method that belongs to the Component Mode Synthesis techniques. The formulation of the method assumes the form reported in (4.2). The degrees of freedom are divided into two sets:

- the boundary DOF, indicated with B, where the reduced link is connected with other components of the mechanical structure;

- the interior DOF, indicated with I.

The dynamic equation for a link of the system, without considering the contribution of the damping, can be written as

$$\begin{bmatrix} \boldsymbol{M}_{BB} & \boldsymbol{M}_{BI} \\ \boldsymbol{M}_{IB} & \boldsymbol{M}_{II} \end{bmatrix} \begin{Bmatrix} \ddot{\boldsymbol{X}}_B \\ \ddot{\boldsymbol{X}}_I \end{Bmatrix} + \begin{bmatrix} \boldsymbol{K}_{BB} & \boldsymbol{K}_{BI} \\ \boldsymbol{K}_{IB} & \boldsymbol{K}_{II} \end{bmatrix} \begin{Bmatrix} \boldsymbol{X}_B \\ \boldsymbol{X}_I \end{Bmatrix} = \begin{Bmatrix} \boldsymbol{F}_B \\ \boldsymbol{F}_I \end{Bmatrix} \tag{4.6}$$

The transformation matrix $\boldsymbol{T}_{CB}$, between physical and Craig-Bampton coordinates, assumes the following form

$$\boldsymbol{X} = \begin{Bmatrix} \boldsymbol{X}_B \\ \boldsymbol{X}_I \end{Bmatrix} = \begin{bmatrix} \boldsymbol{I} & \boldsymbol{0} \\ \boldsymbol{\varphi}_C & \boldsymbol{\varphi}_N \end{bmatrix} \begin{Bmatrix} \boldsymbol{q}_C \\ \boldsymbol{q}_N \end{Bmatrix} = \boldsymbol{T}_{CB} \begin{Bmatrix} \boldsymbol{q}_C \\ \boldsymbol{q}_N \end{Bmatrix} \tag{4.7}$$

In the transformation matrix the first column partition is related to the constraint modes, which describe the motion of the system when each boundary degree of freedom undergoes a unit displacement, while holding the other boundary degrees of freedom fixed. The second column partition is related to the fixed-boundary modes, that can be described as the interior DOF motion when the interface is fixed. The number of fixed-interface modes can be reduced in order to decrease the total number of DOF. Finally, $\boldsymbol{q}_C$ and $\boldsymbol{q}_N$ are the reduced model coordinates corresponding to the constraint and to the fixed-boundary normal modes, respectively.

4.2.2 Interior Mode Ranking

The Interior Mode Ranking (IMR) [69] technique was developed for the selection of the interior normal modes in the Craig-Bampton reduction. The IMR method allows an analytical ranking of the interior modes by comparing their single contributions to the dynamics of interest of the complete system, given the actual boundary conditions. In the IMR method (see [69] for the complete formulation) a weighted participation coefficient γ is defined for each considered interior mode ζ

$$\gamma_{\Lambda,\zeta} = \sum_{i \in \Lambda} \frac{|\gamma_{i,\zeta}|}{||\boldsymbol{\gamma}_i||} \alpha_i \qquad \zeta = 1, ..., s \tag{4.8}$$

where Λ represents the set of the full system vibrational modes to be represented and $\boldsymbol{\gamma}_i$ is the vector whose entries are the coefficients $\gamma_{i,\zeta}$.

Furthermore, α_i is a normalized weighting coefficient referring to the i-th mode, employed to define the level of importance of each mode with respect to the reduced model. The α_i have to be designed in such a way that

$$\sum_{i \in \Lambda} \alpha_i = 1 \tag{4.9}$$

The larger the value of the coefficients $\gamma_{\Lambda,\zeta}$, the more the dynamics of the ζ-th interior mode affects the full system. The retained modes are those with the largest values of the

weighted participation coefficients. In the IMR reduction here adopted, the number of interior modes to be retained is defined in advance and an equal weighting coefficient is assigned to all of them.

4.2.3 Guyan's reduction

Another Model Order Reduction technique that has been taken into account is Guyan's reduction. It is a physical-type technique which is based on the assumption that the effect of inertial forces on the eliminated physical coordinates is negligible [74] [75].

The degrees of freedom corresponding to master (denoted by subscript m) and slave (subscript s) are divided into two groups and, then, the equation of motion can be expressed as follows

$$\begin{bmatrix} \boldsymbol{M}_{mm} & \boldsymbol{M}_{ms} \\ \boldsymbol{M}_{sm} & \boldsymbol{M}_{ss} \end{bmatrix} \begin{Bmatrix} \ddot{\boldsymbol{X}}_m \\ \ddot{\boldsymbol{X}}_s \end{Bmatrix} + \begin{bmatrix} \boldsymbol{K}_{mm} & \boldsymbol{K}_{ms} \\ \boldsymbol{K}_{sm} & \boldsymbol{K}_{ss} \end{bmatrix} \begin{Bmatrix} \boldsymbol{X}_m \\ \boldsymbol{X}_s \end{Bmatrix} = \begin{Bmatrix} \boldsymbol{F}_m \\ \boldsymbol{0} \end{Bmatrix} \tag{4.10}$$

Neglecting the inertia associated with the slave degrees of freedom, the following expression can be obtained

$$\boldsymbol{X}_s = -\boldsymbol{K}_{ss}^{-1} \boldsymbol{K}_{sm} \boldsymbol{X}_m \tag{4.11}$$

Finally, eliminating $\boldsymbol{X}_s$ from (4.10), the transformation matrix $\boldsymbol{T}_G$ can be written as

$$\boldsymbol{T}_G = \begin{bmatrix} \boldsymbol{I} \\ -\boldsymbol{K}_{ss}^{-1} \boldsymbol{K}_{sm} \end{bmatrix} \tag{4.12}$$

4.2.4 Least Square Model Reduction

The Least Square Model Reduction (LSMR) [76] is a physical coordinates reduction technique. It is based on the subdivision of the eigenvectors into master m and slave s components, depending on their reference to master or slave degrees of freedom. Starting from (4.1), the displacement vector $\boldsymbol{X}(t)$ can be expressed as

$$\boldsymbol{X}(t) = \boldsymbol{\Phi}\, \boldsymbol{q}(t) \tag{4.13}$$

where $\boldsymbol{\Phi}$ is the complete eigenvector matrix of the full model, whereas $\boldsymbol{q}$ is the modal coordinates vector. If a modal truncation is applied in order to reduce the computation of the complete eigenvector matrix and only p eigenvectors of the full model are retained, (4.13) assumes the following form

$$\boldsymbol{X}(t) = \boldsymbol{\Phi}_p\, \boldsymbol{q}_p(t) \tag{4.14}$$

Furthermore, the previous matrix equation can be partitioned as

$$\boldsymbol{X}(t) = \begin{Bmatrix} \boldsymbol{X}_m(t) \\ \boldsymbol{X}_s(t) \end{Bmatrix} = \begin{Bmatrix} \boldsymbol{\Phi}_{mp} \\ \boldsymbol{\Phi}_{sp} \end{Bmatrix} \boldsymbol{q}_p(t) \tag{4.15}$$

Finally, the transformation matrix $\boldsymbol{T}_{LSMR}$ for the LSMR technique is given by

$$\boldsymbol{T}_{LSMR} = \begin{bmatrix} \boldsymbol{I} \\ \boldsymbol{\Phi}_{sp}\boldsymbol{\Phi}_{mp}^{+} \end{bmatrix} \tag{4.16}$$

4.2.5 Mode Displacement Method

The Mode Displacement Method (MDM) [62] is a modal coordinates reduction technique, that consists in a truncation of high frequency vibrational modes.

In the case of maintaining m modes among the n of the full model, it holds

$$\boldsymbol{X} = \sum_{j=1}^{m} \boldsymbol{\Phi}_j \boldsymbol{q}_j + \sum_{j_r=m+1}^{n} \boldsymbol{\Phi}_{j_r} \boldsymbol{q}_{j_r} \tag{4.17}$$

where the second contribution of the right side of the equation corresponds to the deleted vibration modes. The final coordinate transformation is given by

$$\boldsymbol{X} = \boldsymbol{\Phi}_m \, \boldsymbol{q}_m \tag{4.18}$$

where the subscript m indicates, in this case, the order of the reduced model.

4.3 Simulations on a benchmark mechanism

The Equivalent Rigid-Link System modal formulation, in combination with the Model Order Reduction techniques presented in Sect. 4.2, have been implemented in Matlab™ environment, using a L-shaped mechanism as a benchmark [12]. An image of the mechanism, described in Chapter 3, is reported in Fig. 3.3 and its geometrical and mechanical parameters in Tab. 3.1.

The 1-DOF system has been modeled in Ansys® Mechanical ADPL with 4, 8 and 16 *beam188* finite elements, i.e. 2, 4 and 8 elements for each of the two flexible rods that compose the L-shaped system. It results a number of degrees of freedom for each subdivision equal to 30, 54 and 102, respectively. The mass M and stiffness K matrices of the complete models have been exported from Ansys® for each discretization in Euler-Bernoulli beam elements and imported in Matlab™, where the reduction techniques have been applied. Then, the dynamics of the robotic system has been numerically evaluated under two different input conditions: gravitational force and step torque signal (reported in Fig. 3.5), in a way similar to Chapter 3. Figure 4.1 reports a graphical overview on the numerical simulations.

For each subdivision of the mechanism in beam elements and for each model order reduction technique, different simulations have been run, by varying the number of considered vibrational modes. In this way, the influence of the beam discretization, the reduction strategy and the number of modal variables can be evaluated.

The numerical simulations provided the dynamics of the system for a time equal to 2 seconds. The *ode45* variable-step solver, based on a Runge-Kutta integration scheme, has

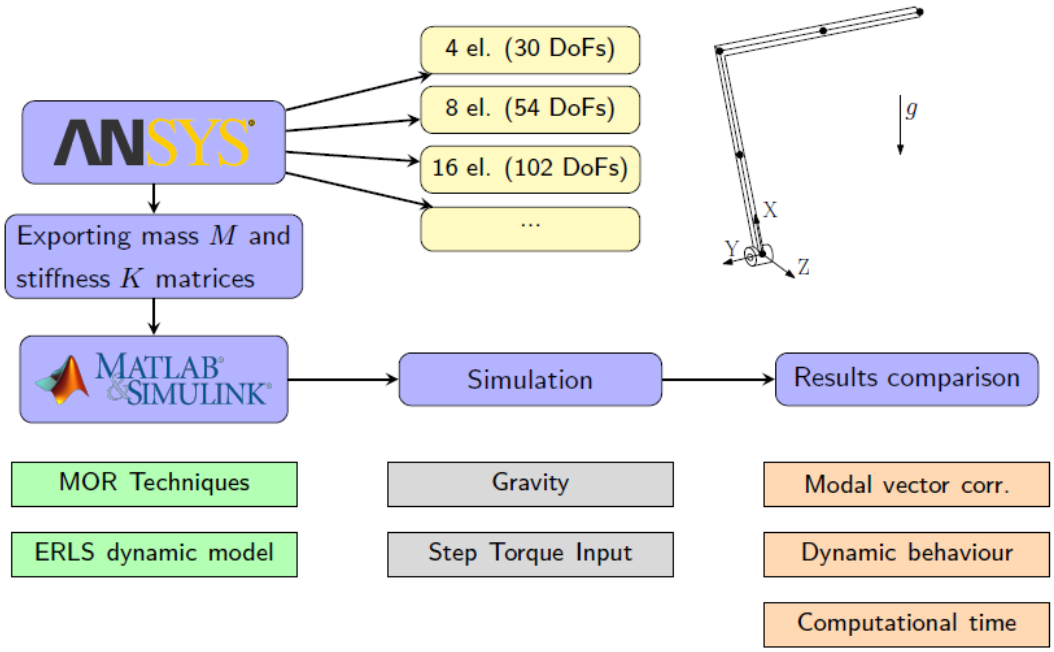

Figure 4.1: Graphical overview on the numerical simulations.

been adopted. Each simulation has been run three times in order to obtain an average value of computational time. For the numerical simulations, a laptop running Windows 10 64 bit with an Intel® Core™ i7-4710HQ CPU @2.50 GHz and a 8 GB DDR3 installed RAM has been adopted.

4.4 Results and discussion

In this section, the results of the numerical simulations presented in Section 4.2 are reported and discussed. Firstly, the different Model Order Reduction techniques have been compared through the Modal Vector Correlation Parameters (Subsection 4.4.1), then the dynamic behavior has been evaluated in the cases of mechanism subjected to gravitational force (Subsection 4.4.2) and step torque input (Subsection 4.4.3).

4.4.1 Modal Vector Correlation Parameters

In order to evaluate the accuracy of the reduced models in matching the mode frequencies and shapes of the full order models, three modal vector correlation parameters have been adopted: the Modal Assurance Criterion (MAC) [70] [71] [65], the Normal Cross-Orthogonality (NCO) [72] [69] [73] and the Cross-Orthogonality (CO) [70]. The three modal vector correlation parameters are defined as follows

$$\boldsymbol{MAC}_{i,j} = \frac{(\phi_i^T \phi_{r,j})^2}{(\phi_i^T \phi_i)(\phi_{r,j}^T \phi_{r,j})} \qquad \boldsymbol{NCO}_{i,j} = \frac{(\phi_i^T \boldsymbol{M} \phi_{r,j})^2}{(\phi_i^T \boldsymbol{M} \phi_i)(\phi_{r,j}^T \boldsymbol{M} \phi_{r,j})} \qquad \boldsymbol{CO}_{i,j} = \phi_i^T \boldsymbol{M} \phi_{r,j} \tag{4.19}$$

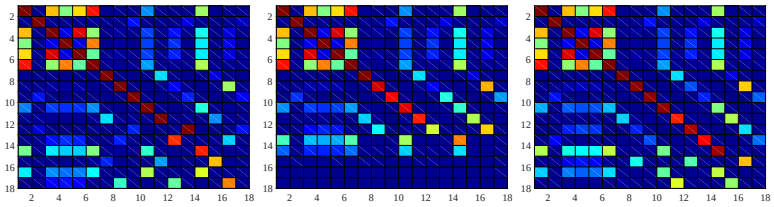

(a) MAC: Craig-Bampton. (b) MAC: IMR. (c) MAC: Guyan.

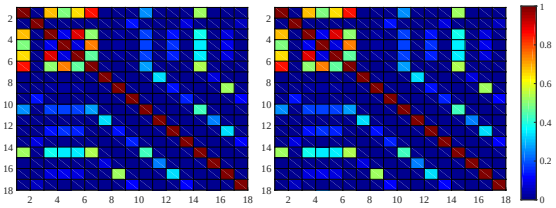

(d) MAC: LSMR. (e) MAC: MDM.

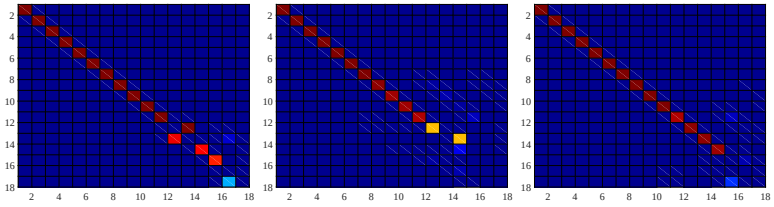

(g) NCO: Craig-Bampton. (h) NCO: IMR. (i) NCO: Guyan.

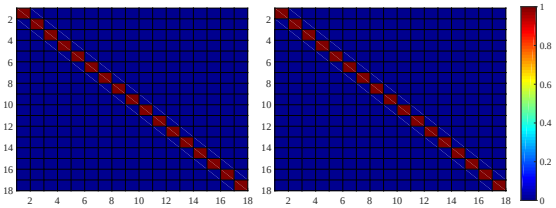

(j) NCO: LSMR. (k) NCO: MDM.

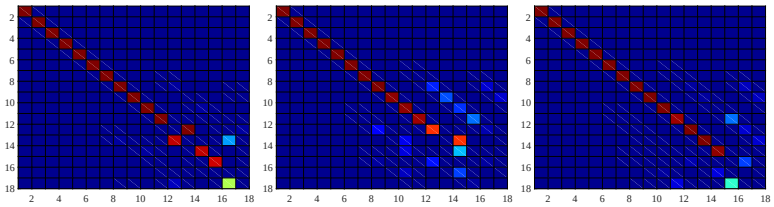

(m) CO: Craig-Bampton. (n) CO: IMR. (o) CO: Guyan.

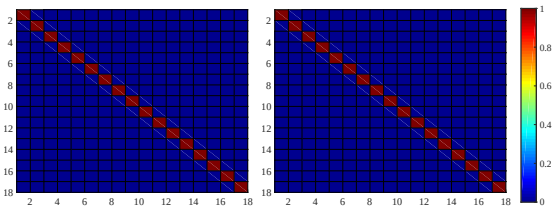

(p) CO: LSMR. (q) CO: MDM.

Figure 4.2: MAC, NCO and CO for the different methods, case with 16 elements and 18 considered modes.

where ϕ_i is the i-th eigenvector of the complete model, $\phi_{r,j}$ is the j-th eigenvector of the reduced model and $\boldsymbol{M}$ is the mass matrix of the reduced model. By varying the indexes i and j, the modal vector parameters constitute a matrix, that assumes values close to a identity matrix if the reduction is well-designed. In particular, the reduction can be considered well-performed if the diagonal and extra diagonal elements assume the following values [70]:

- diagonal elements > 0.9
- extra diagonal elements < 0.1

Table 4.1: Modal vector correlation parameter MAC, case with 16 el. and 18 retained modes.

	MAC				
	diagonal			extra diagonal	
	min	mean	< 0.9	max	mean
CB	0	.6952	12°	.9989	.0792
IMR	0	.6340	9°	.8609	.0643
Guyan	0	.7511	11°	.8136	.0784
LSMR	1	1	-	.6672	.0667
MDM	1	1	-	.8540	.0701

Table 4.2: Modal vector correlation parameters NCO and CO, case with 16 el. and 18 retained modes.

	NCO					**CO**				
	diagonal			extra diagonal		diagonal			extra diagonal	
	min	mean	< 0.9	max	mean	min	mean	< 0.9	max	mean
CB	0	.7057	12°	.9996	.0111	0	.7136	12°	.9998	.0148
IMR	0	.6449	12°	.6790	.0030	0	.6694	12°	.8240	.0094
Guyan	0	.7685	15°	.1656	.0014	0	.7731	15°	.4069	.0063
LSMR	1	1	-	0	0	1	1	-	0	0
MDM	1	1	-	0	0	1	1	-	0	0

In Figure 4.2, the graphical representations of the resultant matrices for the three parameters and the different reduction methods, in the case with 16 elements and 18 retained modes, are reported. In particular, in the techniques here implemented, the internal modes that have been chosen are those neither corresponding to the constrained end nor to the tip of the mechanism.

Tables 4.1 and 4.2 reports the values of MAC, NCO and CO for diagonal and off diagonal elements, in the different reduction strategies, in the case with 16 elements and 18 considered modes. In particular, for the diagonal elements the minimum, the mean and the index of the first element greater than 0.9 are considered; for the extra-diagonal the maximum and the mean values. As it can be seen from Figure 4.2 and from Tables 4.1 and 4.2, in the Craig-Bampton, IMR and Guyan the choice of internal and secondary modes is

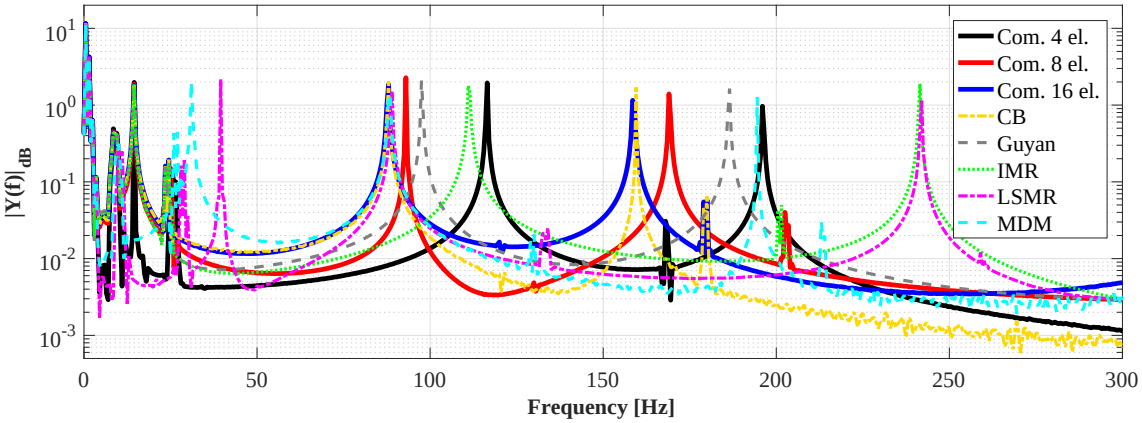

Figure 4.3: Comparison of the tip z-coordinate acceleration, case with 16 el. and 18 considered modes, mechanism under gravity.

fundamental for a good reduction, whereas the LSMR and MDM methods show a higher correspondence (i.e. values closer to an identity matrix) since they are based on a modal truncation approach.

4.4.2 Mechanism under gravitational force

In the following, the results of the different Modal Order Reduction techniques for the mechanism subjected to gravitational force are described. In particular, the accuracy in the frequency domain and the computational time are taken into account and compared between the different techniques.

Accuracy

Figure 4.3 reports the tip z-coordinate acceleration of the L-shaped mechanism subjected to gravitational force in the frequency domain, whereas in Table 4.3 the resonance peaks for the case with 16 elements and 18 retained modes are reported. Only the frequencies lower than 300 Hz have been reported. In particular, the case with 16 elements and 18 retained modes is considered.

A good agreement between the different reduction techniques and the complete model in the first resonance peaks can be found. By considering the second, third and fourth peaks, only Craig-Bampton, IMR and Guyan are capable of tracking the complete model signal in with good accuracy. Moreover, with respect to the model with 16 elements (blue line), Craig-Bampton (dotted-dashed yellow line) tracks also the last three peaks with adequate precision.

Computational time

In Tables 4.4 and 4.5 the average computational times for the mechanism under gravity force are reported for the complete and reduced models, respectively. Figure 4.4 reports

Table 4.3: Resonance peaks [Hz] of the tip z-coordinate acceleration, case with 16 el. and 18 retained modes, mechanism under gravity.

Peaks	1	2	3	4	5	6	7	8
Complete 4 el.	0.5	8.5	14.5	25.5	116.5	168	196	
Complete 8 el.	0.5	8.5	14.5	24	93	169	202.5	
Complete 16 el.	0.5	8.5	14.5	24.5	88	158.5	180	
CB	0.5	8.5	14.5	24.5	88	159.5	180	
IMR	0.5	8.5	14.5	24.5	111	201.5	241.5	
Guyan	0.5	8.5	14.5	24.5	97.5	186.5		
LSMR	0.5	10	29	39.5	89	134	242	
MDM	0.5	10	26	31	88	130	194.5	213

a 3D representation of the computational times for the different techniques, by varying the number of retained vibrational modes and the number of elements considered in the discretization. As expected, the computational time steeply increases by increasing the number of retained modes. On the other hand, the number of elements seems to have the opposite trend with respect to computational time: by increasing the number of elements at constant number of retained modes, lower frequencies are taken into account and, therefore, the variable-step solver can increase the time-step used in the simulation.

Table 4.4: Average computational time [s], complete models, mechanism under gravity.

4 el. (30 m.)	8 el. (54 m.)	16 el. (102 m.)
1602,14	4046,99	16102,97

Table 4.5: Average computational time [s], reduced models, mechanism under gravity.

Method	Elements	Modes					
		8	10	12	14	16	18
Craig-Bampton	4	2,58	5,96	9,02	169,23	571,00	902,21
	8	3,12	5,13	13,49	32,38	51,20	89,75
	16	3,20	4,70	11,55	26,71	46,74	79,76
IMR	4	2,58	6,10	9,05	453,90	469,97	1079,11
	8	3,15	5,30	21,44	63,87	76,50	189,87
	16	1,85	5,82	13,60	176,38	322,75	502,47
Guyan	4	3,64	6,34	9,63	173,44	417,39	459,74
	8	2,55	5,74	18,87	28,04	94,64	297,22
	16	3,40	5,42	18,48	23,31	100,36	305,73
LSMR	4	2,59	6,04	9,18	181,77	255,96	421,53
	8	3,17	5,14	16,28	23,16	474,67	517,33
	16	3,22	4,80	15,02	19,77	629,20	1158,22
MDM	4	2,60	5,84	9,60	178,36	251,26	515,40
	8	3,08	5,02	16,26	23,50	28,45	74,06
	16	3,20	4,78	14,18	18,33	37,01	48,60

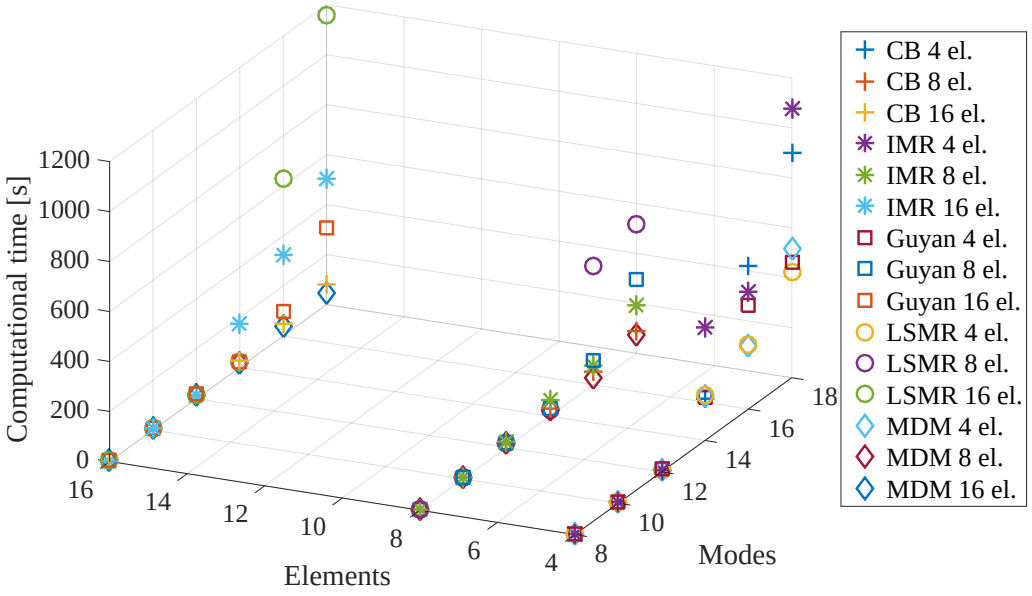

Figure 4.4: Average computational time [s], mechanism under gravity.

Table 4.6: Time reduction with respect to complete model, case 18 retained modes, mechanism under gravity.

	4 el. (30 m.)	8 el. (54 m.)	16 el. (102 m.)
Complete model	1602,14 s	4046,99 s	16102,97 s
CB	43.69 %	97.78 %	99.50 %
IMR	32.65 %	95.31 %	96.88 %
Guyan	71.30 %	92.66 %	98.10 %
LSMR	73.69 %	87.22 %	92.81 %
MDM	67.83 %	98.17 %	99.70 %

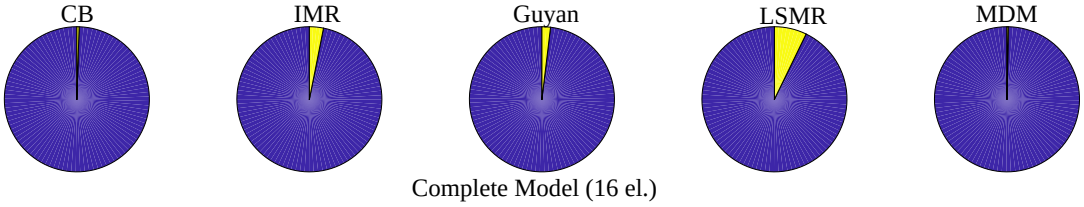

Figure 4.5: Pie charts of time reduction with respect to complete model, case with 16 el. and 18 retained modes, mechanism under gravity.

In Table 4.6, the time reduction with respect to the complete models, in the cases with 18 maintained modes, are described. For the 4 elements case, LSMR and Guyan are the techniques that allows the highest percentage of time reduction. For the 8 elements case, MDM and Craig-Bampton allows the best reduction rate; the same trend can be found for the 16 elements case (with 103 DOF in total).

To better visualize the percentage of time reduction with respect to the complete model,

the pie charts related to the 16 elements cases are shown in Figure 4.5. As it can be seen, MDM and Craig-Bampton are the ones that allows higher values of percentage time reduction, followed by Guyan, IMR and, finally, LSMR.

4.4.3 Mechanism subjected to step torque input

Accuracy

Figure 4.6 shows the Fast Fourier Transform of the z-coordinate of the mechanism tip for the different reduction techniques in the case of step torque input, whereas Table 4.7 reports the values of the resonance peaks for the frequencies lower than 300 Hz.

From the graph and the table it can be seen that a good agreement between the complete model signal and the reduced ones can be appreciated in the first two resonance peaks, whereas Craig-Bampton seems to be the method that best matches the behavior of the full model (16 elements). As expected, the two techniques based on a modal vector truncation, LSMR and MDM, are the ones that present the less accurate results in the description of the dynamic behavior of the L-shaped mechanism.

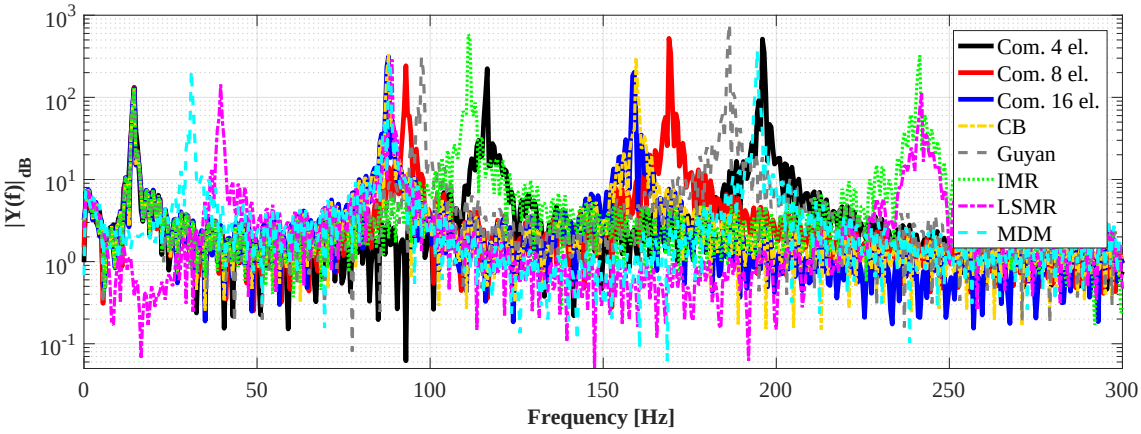

Figure 4.6: Comparison of the tip z-coordinate acceleration, case with 16 el. and 18 considered modes, mechanism subjected to a torque input.

Table 4.7: Resonance peaks [Hz] of the tip z-coordinate acceleration, case with 16 el. and 18 retained modes, mechanism subjected to a torque input.

Peaks	1	2	3
Complete 4 el.	14.5	116.5	196
Complete 8 el.	14.5	93	169
Complete 16 el.	14.5	88	159
CB	14.5	88	159.5
IMR	14.5	111	241.5
Guyan	14.5	97.5	186.5
LSMR	39.5	89	242
MDM	31	88.5	194.5

Computational time

Computational times are reported in Tables 4.8 and 4.9 for the complete and the reduced models respectively. Figure 4.7 depicts a 3D representation of computational times for the different numerical simulations that have been run. As expected, a time reduction can be noticed by increasing the number of model elements at constant number of retained modes, since lower frequencies are, in general, taken into account and the variable-step solver can adopt larger intervals for the numerical integration.

Table 4.8: Average computational time [s], complete models, mechanism subjected to a torque input.

4 el. (30 m.)	8 el. (54 m.)	16 el. (102 m.)
1703,26	4110,21	17754,19

Table 4.9: Average computational time [s], reduced models, mechanism subjected to a torque input.

Method	Elements	Modes					
		8	10	12	14	16	18
Craig-Bampton	4	3,40	6,10	11,34	167,59	574,99	919,16
	8	3,30	4,39	13,00	33,73	50,71	89,66
	16	3,34	4,49	11,66	28,89	47,63	80,72
IMR	4	3,41	6,08	10,97	459,32	482,43	1092,52
	8	3,30	4,87	24,74	66,13	107,50	184,80
	16	2,69	5,83	15,14	171,01	316,48	510,80
Guyan	4	3,64	6,11	11,23	172,24	436,26	465,36
	8	3,41	5,16	20,70	30,67	98,44	292,73
	16	3,40	5,40	21,42	29,57	110,34	301,42
LSMR	4	3,33	6,10	11,33	184,68	229,75	408,88
	8	3,45	4,57	18,61	22,43	498,42	555,91
	16	3,44	4,43	16,56	20,03	637,77	1176,80
MDM	4	3,33	6,02	11,31	180,71	230,76	554,30
	8	3,39	4,60	18,89	24,11	31,09	80,87
	16	3,45	4,24	16,43	19,59	39,99	47,31

By considering the values reported in Table 4.10, it can be notice that LSMR and Guyan are the fastest methods for the case with 4 elements. By considering the 8 elements case, the fastest technique is Craig-Bampton, followed by MDM and IMR. In the 16 elements case, Craig-Bampton and MDM appear to be the methods that reduce at best the computational time.

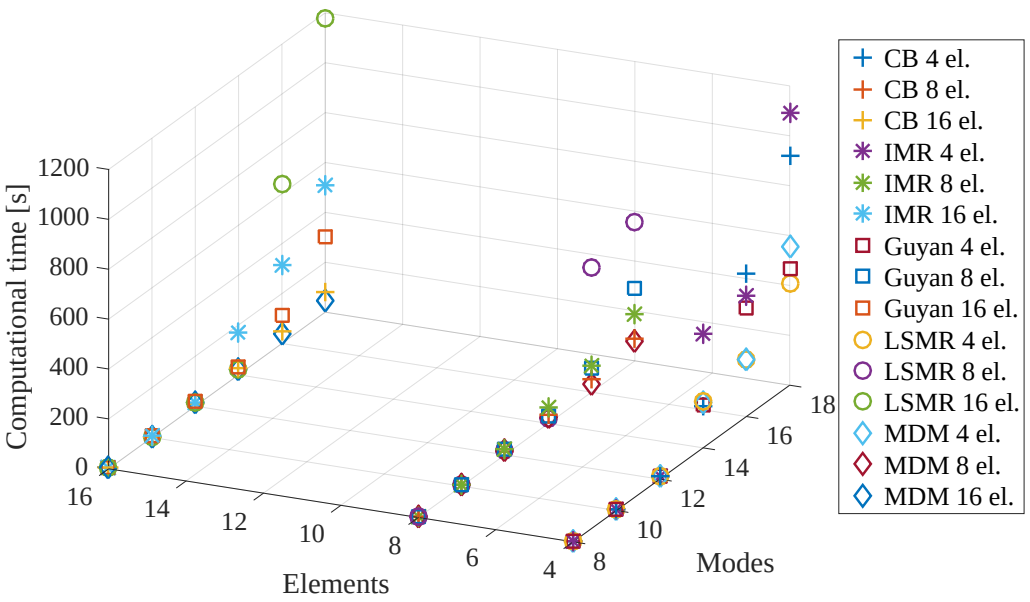

Figure 4.7: Average computational time [s], mechanism subjected to a torque input.

Table 4.10: Time reduction with respect to complete model (case 18 retained modes), mechanism subjected to a torque input.

	4 el. (30 m.)	8 el. (54 m.)	16 el. (102 m.)
Complete model	1703,26 s	4110,21 s	17754,19 s
CB	46.04 %	98.82 %	99.55 %
IMR	35.86 %	95.50 %	97.12 %
Guyan	72.68 %	92.88 %	98.30 %
LSMR	75.99 %	86.47 %	93.37 %
MDM	67.46 %	98.03 %	99.73 %

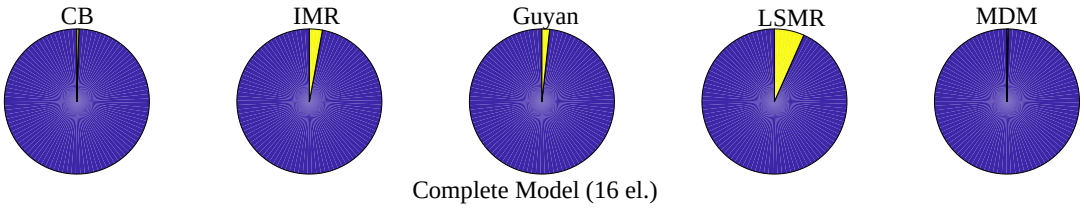

Figure 4.8: Pie charts of time reduction with respect to complete model, case with 16 el. and 18 retained modes, mechanism subjected to a torque input.

Table 4.11: Comparison of Model Order Reduction techniques.

	Modal Vector Parameters	Dynamics	Comp. Time
CB	✗	✓ ✓ ✓	✓ ✓ ✓
IMR	✗	✓	✓ ✓
Guyan	✓	✓	✓ ✓
LSMR	✓ ✓ ✓	✗	✗
MDM	✓ ✓ ✓	✗	✓ ✓ ✓

4.5 Conclusions

In this chapter, a first comparison of different model order reduction techniques using the ERLS modal formulation has been presented. Several Model Order Reduction techniques for flexible multibody dynamics (i.e. Craig-Bampton, Interior Mode Ranking, Guyan's reduction, Least Square Model Reduction and Mode Displacement Method) have been implemented in Matlab using a L-shape deformable system with one rigid degree of freedom as a benchmark mechanism.

Several numerical simulations have been performed in order to evaluate the accuracy of the different methodologies in the frequency domain and their performances in computational time. In particular, two different conditions have been used to excite the mechanical system: the natural gravitational force and an input torque signal, which represent a case closer to a possible real application. Furthermore, the model order reduction techniques have been compared by using three vector correlation parameters: the Modal Assurance Criterion, the Normal Cross-Orthogonality and the Cross-Orthogonality.

Table 4.11 reports a comprehensive and general overview on the techniques discussed in this chapter. In particular, Craig-Bampton, IMR and Guyan show good performances in the description of the dynamic behavior and in the percentage reduction of computational time, but not good results in the evaluation of modal vector correlation parameters. This is because in these techniques the choice of internal vibrational modes is fundamental for a good modal reduction. On the other hand, LSMR and MDM show a high correspondence in the modal vector parameters but a lower accuracy in the dynamic behavior and, in particular, in matching the resonance peaks of the complete models.

In further developments of this work, the model order reduction techniques here presented will be applied to other flexible multibody systems with two (or more) degrees of freedom and different subdivisions in finite element. Furthermore, more techniques will be considered and a deeper analysis of the choice of internal modes will be performed and analyzed.

Chapter 5

Cable-Driven Robotic Systems

Cable-driven robots are a special class of flexible-link systems in which flexible cables, rather than rigid links, are used to actuate the end-effector. Cables can find applications in both rigid-link structures, where they are employed to drive serial and parallel kinematic chains, and in the control of suspended mobile manipulators.

This chapter presents an introduction on cable-driven robotic systems. First, a brief overview on traditional designs of robots that employ tendon-based elements is presented, highlighting the advantages and disadvantages of this class of manipulators with respect to their rigid-link counterparts. Then, the concepts of cable-based parallel robots and of cable-suspended parallel robots are recalled and described by introducing an analysis of the state of the art with the last developments and applications in this field.

5.1 Cable-driven robots

In the last decades, several researchers have studied and analyzed cable-based systems, which are an open field of investigation in both industry and academia. Advantages of this class of manipulators over conventional ones are that cable-based robots can have a larger workspace [77], they can easily be made to be reconfigurable [78] and modular [79], they are lighter than their rigid-links counterparts, they can be easily transported and their end-effector can achieve high accelerations and velocities. Disadvantages of cable-based robotic system include redundancy (as cables can carry load in tension but not in compression) and interference between the cables and the environment. For these reasons, cable-driven systems have received attention, different kind or cable-based robots have been investigated and several researches have been conducted over the years, especially for control purposes, dynamic modeling, trajectory planning and tracking [80, 81, 82, 83, 84].

Some of the most common requirements that designers has to take into account when designing new robotic systems are: cost-effectiveness, force capability, dimensions of the workspace, dynamic performances, repeatability and safety [85]. In the following part of this section, these requirements are analyzed and a comparison between cable-robots and traditional manipulators is carried out.

The main contribution to the cost of a robotic device is given by actuators and

(a) (b)

(c)

Figure 5.1: Crane devices: mobile crane (a), tower crane (b) and gantry cranes (c).

manufacturing. Therefore, a *cost-effective design* can be obtained by adopting a structure composed of few components, to be realized with simple mechanical processes. On the other hand, the requirements of a more complex control architecture has usually limited impact on the design costs, since, in the recent years, powerful control systems are made available in the market at relatively low prices. In the next future, a trend towards mechanically simple but computationally demanding systems may be expected. By considering cable-driven devices, their mechanical architecture is usually simpler and more cost-effective with respect to traditional robots, even if the controller architecture could be more sophisticated and complex.

Payload-to-weight ratio is another feature that has to be taken into account while designing novel robotic devices. Moving large loads is, indeed, a common task in several production and industrial environments. Unfortunately, traditional robots with serial architecture, often characterized by cumbersome and heavy structures, do not allow to carry high payloads. This is due to the fact that each motor has to carry the weight and the inertial forces produced by the following links and by the load. Moreover, link cross sections are usually determined by the low stiffness of the serial structures. In this context,

cable-robots usually show high values of the payload-to-weight ratio, since their structure is lighter and the overall force can be split between several actuators.

One of the most important advantage of cable-driven robots with respect to conventional ones is the capability of working over a larger *workspace*. The concept of workspace of a cable-driven system can be defined as the set of end-effector poses in which the system is *manipulable* [86]. A cable-robot can be defined as *manipulable* at a given configuration if any wrench can be exerted with only positive tensions of the cables [85].

The feature of having a large workspace is typical of crane-type structures. For example, mobile cranes (Fig. 5.1(a)) and tower cranes (Fig. 5.1(b)) are employed in construction sites, whereas gantry cranes (Fig. 5.1(c)) are typical of the shipbuilding industry and for the loading and unloading of containers and supplies from trains and ships. Mobile and tower cranes are composed of a serial structure, whereas gantry cranes use parallel rigid-link design. In all these cases, the rigid structure provides further degrees of freedom to the cables carrying the load. Since cranes are under-constrained systems, it is hard to implement a completely automatic control system; in the majority of the cases such devices are operated in quasi-static conditions, to avoid the sway motion of the load. On the contrary, cable-robots (Fig. 5.2) allow the implementation of automatic controllers even when they need to operate in large or huge workspaces.

Since cables are low-weight elements, these devices are usually characterized by *low inertia loads* and their end-effector could reach higher velocities and accelerations. Therefore, cable-based devices can be employed for several different tasks where a high speed is demanded, such as pick-and-place.

Repeatability indicates the positional deviation of the system from the average of displacements, as measured in different trials having the same target and conducted in the same conditions. It is a fundamental feature in several robotic tasks, where either the goal pose or target continuous trajectories have to be reached with high accuracy. Cable-driven devices can hardly achieve high levels of accuracy and repeatability, because of the elasticity and flexibility of cables, which are usually hard to compensate by control. A solution to compute good estimates of the end-effector pose is to adopt kinematic redundancy.

Final, but not less important, *safety* is a main concern in machine design, especially when human operators can be present in the robot workspace. By considering cable-robots, cable redundancy can be implemented and safety systems can be installed, as well as strategies to recover the end-effector in case of cable failure [87].

The main drawback of cable-robots is the *unilateral actuation*, since cables can only carry tension forces but not compression ones [88, 89]. This feature has some important implications, in particular in the choice of the number of actuators and their locations in the kinematic structure of the mechanism. Indeed, the unilateral actuation forces the majority of cable-driven robots to have a number of actuators greater than the number of degrees of freedom and, therefore, a feasible tension distribution for any given wrench has to be found. Moreover, unlike traditional rigid-link manipulators, the extension of the workspace not only depends on the geometrical constraints but also on the cables configuration and on the feasible range of cable tensions.

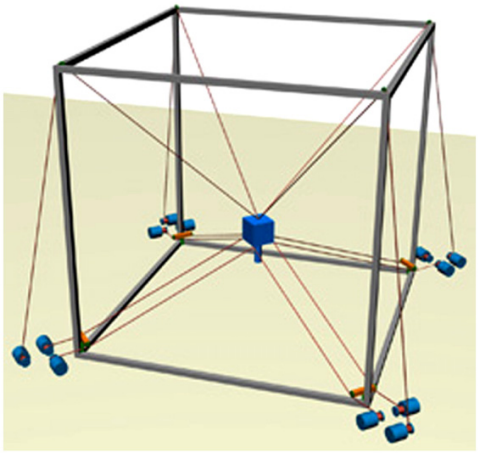

Figure 5.2: Example of fully-constrained parallel robot [90].

In the past years, several designs of cable-based manipulators have been developed in robotics. Two main families of cable-based devices can be found: the first is represented by robots in which cables work in conjunction with a rigid-link structure to actuate the kinematic chain, the second is composed of robots in which flexible cables substitute traditional rigid-link structures, by directly acting on the moving platform or end-effector. In both these two families of cable-based manipulators, the actuators (i.e. the electric motors) may be mounted on the base of the manipulator, in order to reduce the loads on the frame of the systems.

Examples of cable-driven manipulators with a rigid-link structure can be found in [91], where a 2-DOF cable-driven planar mechanism is studied, and in [92], where the design of a mobile, inexpensive cable-driven device for upper extremity rehabilitation is presented. Examples of cable-direct-driven robots with passive serial-link support can be found in [93, 94, 95]. Prototypes of this class of robotic systems have been employed especially in the field of rehabilitation [96]. An example of parallel rigid-link chain driven by cables can be found in [97], where a two-DOF planar haptic interface based on a closed 5-bar linkage mechanism is presented.

Another application of cable-based devices with a serial-link support is surgery. Indeed, in recent years, flexible cables have also been employed in surgical robots to reduce surgeon fatigue and facilitate supervised tele-surgery. An interesting example is given by [98], where an autonomous multilateral system using the Raven, an open-architecture surgical robot with two cable-driven 7-DOF arms, is described. Real-time control and enhancing of tracking performances in cable-driven surgical robots can be found in [99] and in [100], whereas in [101] a tendon sheath analysis for estimation of force and elongation in surgical cable-driven robots is presented.

The following part of this thesis is focused in cable-driven parallel robots, i.e. devices where the moving platform or end.effector is directly supported by cables, as it is described in the next section.

(a) (b)

Figure 5.3: The Skycam [110] (a) and the NIST Robocrane [111] (b).

5.2 Cable-driven parallel robots

Cable-Driven Parallel Robots (CDPRs) consist of a moving platform supported in-parallel by cables that are actuated by tensioning motors [85, 102]. An example of cable-driven manipulator is reported in Fig. 5.2. Usually, each cable of the robot is reeled on a pulley that is mounted on the robot frame and is actuated by an electric motor. The other extremity of the cable is fixed to an attaching point of the common moving platform. Idle pulleys could also be interposed between the extremities of each cable, to measure cable tensions (see Chapters 6 and 7), or to achieve particular kinematic designs.

As it can be seen in the following, applications of cable-driven parallel robots can be found in several different fields, spanning from heavy load and large scale manipulation [90, 103, 104], building tasks [105, 106], to rescue operations [107] and upper limbs rehabilitation [108, 109].

One of the first example of cable-driven parallel robot is given by the Skycam, an aerial robotic camera system used in large areas, such as a stadium or an arena [110]. An image of the system is reported in Fig. 5.3(a). Another classical example of CDPR is given by the NIST Robocrane, a 6-DOF suspended manipulator designed to improve the stability of crane loads and to control position, velocity and force of machinery for cutting or excavating tasks (Fig. 5.3(b)). CDPRs can also be employed for very large applications, such as the Arecibo Radio Telescope in Puerto Rico [112] (Fig. 5.4(a)) and the Five-hundred meter Aperture Spherical Radio Telescope in the Pingtang County, China [113] (Fig. 5.4(b)).

Several prototypes of CDPRs have been investigated in the last decades. In [114], Holland and Cannon first patented a cable-driven suspended system for manipulating and handling materials over large workspaces. An interesting example of large-scale cable-driven parallel robot is the CableRobot simulator, developed by the Max Planck Institute for Biological Cybernetics in cooperation with the Fraunhofer Institute for Manufacturing Engineering and Automation IPA [115, 116]. The system, shown in Fig. 5.6(a), represents the first cable-driven simulator capable of transporting humans for studies in the field of

(a) (b)

Figure 5.4: The Arecibo Radio Telescope (a) and the Chinese Five-hundred meter Aperture Spherical Radio Telescope, FAST (b).

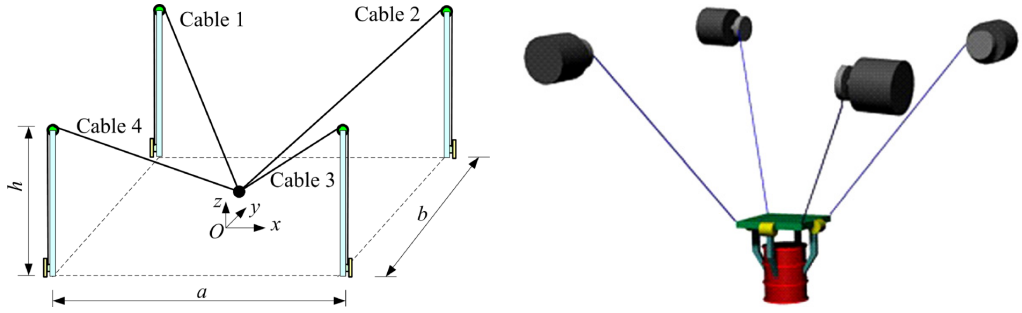

(a) (b)

Figure 5.5: Examples of under-constrained cable-driven parallel robots [90].

human perception research and virtual reality applications. Moreover, a large-dimension reconfigurable suspended cable-driven parallel robots to carry workers in an airplane maintenance workshop was presented in [117].

Applications of cable-driven robot are in the field of rehabilitation, especially for upper limbs neuro-rehabilitation of post-stroke patients. An example is given by Feriba3, a 4-cables planar mechanism composed of a circular end-effector that can be moved on a square workspace [86]. The cables can generate 3 generalized forces on the end-effector, that can be used to perceive feedback from real or virtual environments as an haptic device. In [118], the authors presented PiRoGa5, a cable-driven haptic system for robotic assisted spine surgery, in which six cables are attached to a pen-like shaped end-effector that allows the surgeon to be guided by haptic feedback.

A wire-based robot for neuro-rehabilitation (NeReBot) was described in [119, 120]. The robot, shown in Fig. 5.7(a), consists of a set of 3 cables connected to the patient upper limb by means of a splint and independently controlled by 3 motors. By controlling wire length, the rehabilitation treatment, based on the passive or active-assistive spatial motion of the limb, can be delivered over a wide workspace. MariBot, shown in Fig. 5.7(b), is the evolution of NeReBot and consists of a 5-DOF cable-robot for rehabilitation [108]. Its working space is much larger with respect to the NeReBot and covers nearly every

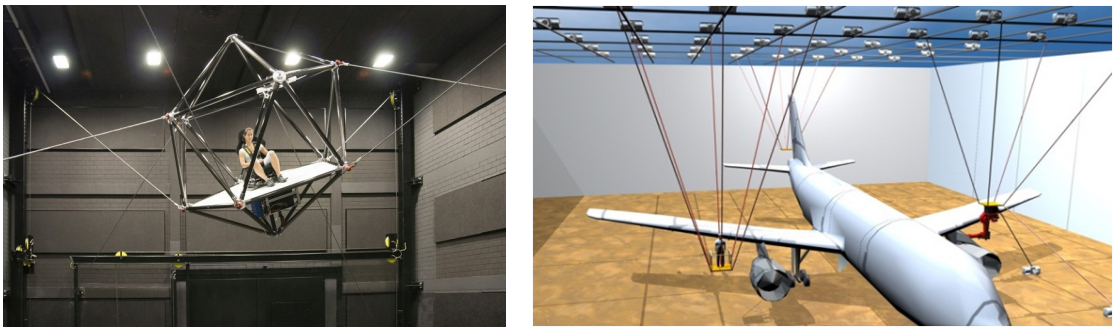

(a) (b)

Figure 5.6: The CableRobot simulator [116] (a), CDPR for airplane maintenance [117] (b).

movement of the upper limb.

Another example of cable-driven parallel robot for rehabilitation is given by CAREX, a Cable-Driven Arm Exoskeleton in which rigid links of the exoskeleton are replaced with lightweight cuffs fixed to the moving limb segments of the human arm. Cables are routed through these cuffs, which are driven by motors, to move the limb segments relative to each other in order to achieve desired forces on the hand, i.e., both pull and push, in any direction as required in neural training [121].

Cable-driven parallel robots can be classified as *fully constrained* or *under-constrained*, based on the degree to which the cables determine the pose of the manipulator [122, 123]. In fully constrained manipulators (Fig. 5.2), the pose of the end-effector is completely determined given the current length of the cables. On the other hand, under-constrained systems (Fig. 5.5) rely on the presence of gravity to determine the resulting position and orientation of the common moving platform.

In the following section, we will focus on cable-suspended parallel robots, which are a typical example of under-constrained systems.

5.3 Cable-suspended parallel robots

Cable-Suspended Parallel Robots (CSPRs) are under-constrained system, which rely on gravity to maintain the cables taut. Several cable-suspended parallel robots have been studied and implemented in the recent years. Examples can be found in [124, 125, 126].

Dealing with cable-suspended parallel robots, one topic of interest that has been investigated in recent years is the planning of feasible trajectories that extend beyond the static workspace, thus enabling novel applications for this class of flexible-link mechanisms. By dynamically controlling the moving platform, the workspace of these robots can be extended. The dynamic workspace [127] was first defined by G. Barrette and C. Gosselin as the set of poses that the end-effector can reach with at least one kinematic state.

Controlling a cable-suspended parallel robot in its dynamic workspace can be very challenging. In [128], C. Gosselin *et al.* presented a dynamic trajectory planning approach

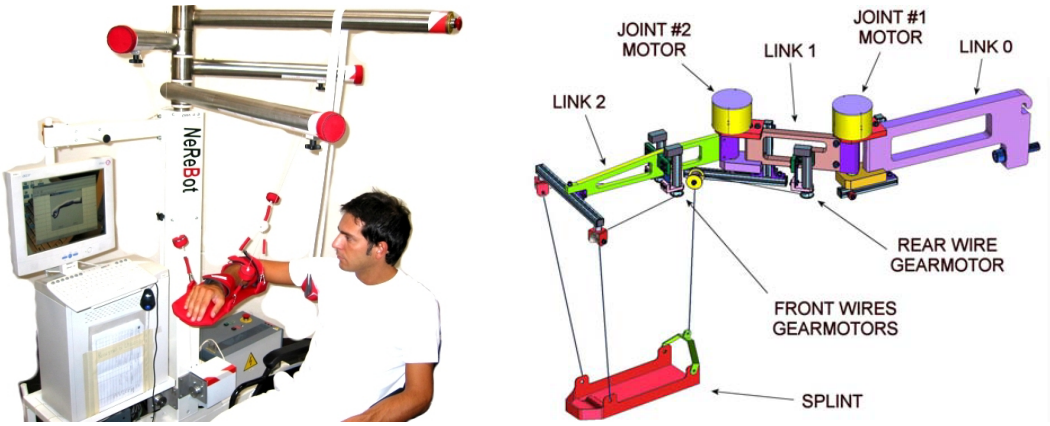

(a) (b)

Figure 5.7: Examples of cable-driven robots for rehabilitation: NeReBot [119] (a) and MariBot [108] (b).

for a 2-DOF CSPR with point-mass end-effector. The work was then extended to a spatial robot in [129]. The approach is based on parametric Cartesian trajectories and guarantees that all cables remain in tension throughout the trajectory. The dynamic trajectory planning of CSPRs was applied to the point-to-point motion of a 2-DOF mechanism [130] and a 3-DOF robot [131].

A spatial robot with point-mass end-effector was studied in [132], whereas the static to dynamic transitions for a planar and a spatial cable-suspended point-mass mechanism were presented in [133]. The trajectory connects an initial point at rest to a final point in the dynamic workspace to be reached with zero velocity but non-zero acceleration.

In [134], the authors investigated elliptical trajectories for a point-mass end-effector suspended by means of three cables. Furthermore, in [135], a novel method to perform static to dynamic transitions for fully constrained 3-DOF CSPRs from an initial state of rest to an elliptical trajectory was presented. In [136], the periodic trajectory planning beyond the static workspace was extended to a 6-DOF CSPRs, whereas in [137], a dynamic point-to-point trajectory planning technique that ensures zero translational and rotational velocity at the end-points of each trajectory segment was proposed. Recently, in [138], P. Dion-Gauvin and C. Gosselin studied the dynamic point-to-point trajectories of a 3-DOF cable-suspended robot based on a hypo-cycloid curve.

Other examples of trajectory planning for under-actuated cable-suspended robots can be found in [139], where spatial point-to-point motions were defined for a 3-DOF cable-suspended parallel robot, and in [140], where a randomized kino-dynamic planning technique was adopted to design dynamic motions. In [141], the authors investigated the optimal control of an under-actuated cable-driven micro-macro robot, by applying the *differential flatness* framework to make the system controllable for point-to-point movements.

Moreover, in [142] and [143] dynamic recovery trajectories after a cable failure were analyzed, whereas in [144] a robust trajectory planning method for under-actuated non-linear

systems in point-to-point motions was presented and experimentally evaluated through a double-pendulum system.

In the next chapters, two examples of cable-suspended parallel robots are presented and analyzed. In Chapter 6, a novel design of CSPRs based on variable radius drums is investigated. The device, named Cable-Based Robotic Crane, is capable of moving a load through a planar working area using just two actuated degrees of freedom, in a way similar to a traveling crane. An experimental prototype is presented and validated showing good performances and accuracy. The design of robotic crane can find applications in the loading and unloading of materials in large workspaces, such as in industrial of naval fields.

Chapter 7 presents a particular class of cable-suspended parallel robots, which is given by pendulum-like robots [145, 146, 147, 5]. These kind of manipulators consists of a cable-suspended passive robotic arm, whose oscillation in its dynamic workspace can be modulated by actively controlled the length of the cables or the orientation of the end-effector. The device studied in Chapter 7 is capable of performing point-to-point motion beyond its static workspace, using two actuated joints only and employing parametric excitation to pump to or subtract energy from the systems akin to playground swings. The device find applications for pick-and-place repetitive tasks.

Chapter 6

Cable-Driven Robotic Cranes based on Variable Radius Drums

In this chapter, the modeling and validation of a novel design of Cable-Suspended Parallel Robot (CSPR) based on variable radius drums, is presented. A Variable Radius Drum (VRD) is characterized by the variation of the spool radius along its profile. This kind of device is used, in this context, for the development of a cable-driven mechanism, which can support and move a load through a planar working area with just two actuated degrees of freedom, similar to overhead traveling cranes. The device is named Cable-Based Robotic Crane (CBRC). Instead of using several actuators to wind or unwind each cable connecting the end-effector to the frame of the robot, the proposed design is based on the coupling of the winding/unwinding of several cables, allowing to use only one actuator for this task.

After a brief introduction about devices based on variable radius drums, the kinematic analysis and the synthesis of the geometry of the VRD profile are developed. Then, the schema of a bi-dimensional horizontal moving mechanism, based on the VRD theory, and an experimental prototype of a three-dimensional CBRC, are presented. The features of this cable-based overhead traveling crane and an analysis of cables tensions are discussed. Finally, the performances of this robotic system are evaluated, showing a deviation between the end-effector and the nominal planar surface of less than 1% throughout the whole working area. The prototype presented in this chapter has been developed at the Robotics Laboratory of the Department of Engineering and Architecture, University of Trieste (Italy). Part of the work described in this chapter has been previously published in [4].

6.1 Introduction

One of the most common application of cable-suspended parallel robots is the manipulation of loads in large workspaces. In the majority of the cases, especially in industrial plants, shipyards and production sites in general, this task is performed using traditional overhead cranes, which consist of parallel runways with a traveling bridge spanning the gap. A hoist, the lifting component of a crane, travels along the bridge. An image on a traditional overhead crane is reported in Fig. 6.1(a).

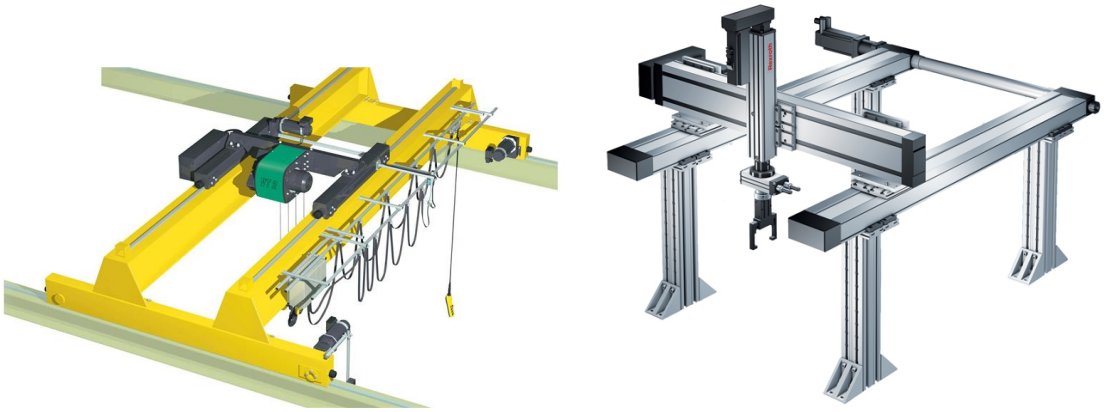

(a) (b)

Figure 6.1: A traditional overhead traveling crane (a) and a Cartesian robot.

The structure of a traditional overhead traveling crane is usually heavy, it requires linear guides along the whole work area and it can not be easily disassembled or re-positioned. Nowadays, the main research area of traditional overhead cranes is the dynamical modeling and control, in order to eliminate swing effects and ensure system stability. Examples can be found in [103, 148, 149, 150, 151].

With respect to traditionally overhead cranes, the design of the cable-suspended parallel robot presented here, called Cable-Based Robotic Crane, do not require rails or linear guides along the whole span of the system since they are essentially composed of a series of pulleys, drums and cables. For this reason, their frame is lighter and can be easily disassembled. Furthermore, they are modular and their accuracy only depends on the positioning of the pulleys supports in the set-up phase.

A comparison between Cartesian robots and the device presented here can also be introduced. Cartesian robots (Fig. 6.1(b)) are characterized by a high stiffness and are employed in the handling of small workspaces, where they are extremely accurate for high precision pick-and-place tasks. On the contrary, the device described in this chapter is meant for the handling of large amount of materials in very large workspaces, where the weight of the structure can be an issue. One possible application could be the loading and unloading of materials and supplies for general tasks in the naval field, where the workspace is large, the infrastructures have to be light and the accuracy is much less demanding. Furthermore, the proposed mechanism could also be deployed as a 2D aerial overhear conveyor for industrial or even mining application, where vertical motion is not required. On the other hand, it has to be noticed that, in the cases in which a movement of the load in the vertical direction is needed (such as for pick-and-place tasks), a winch could be mounted on the end-effector of the robotic crane.

Since cables are used in power transmissions, drive systems and load handling, drums and pulleys have been used in different kind of applications. A drum, or spool, consists of a spindle with flanges, around which a cable is wrapped (Figures 6.2(a), 6.2(b)). The cylindrical surface of an ordinary drum has a constant radius [152]. A typical device, in

(a)

(b)

(c)

Figure 6.2: Traditional constant radius drum (a), sailboat winch (b), winch with ratchet and pawl (c).

which an ordinary drum is employed, is a winch [153]. It essentially consists of a movable drum around which a cable is wrapped, so that the rotation of the drum produces a drawing force at the end of the cable. Winches are usually equipped with a ratchet wheel and a pawl to prevent slippage of the load [154] (Fig. 6.2(c)). Examples of research studies in cable-drum systems can be found in [155], where a cable mechanism is used as a linear motion sensor, in [156], where a study on the prediction of slip in cable-drum system is proposed, and in [152], where the transmission backlash of a precise cable drive system is analyzed and experimentally measured.

While traditionally drums and winches are characterized by a constant radius, in this chapter the use of variable radius drum (VRD), a mechanical device consisting in a drum with a radius that changes along its profile, is proposed. The concept of variable radius drum has been firstly presented by Seriani and Gallina in [157]. As the VRD is rotated by an angle α, a correspondent length of cable is released or wound. This length can be expressed by a non-linear function $g = g(\alpha)$, which depends on the VRD profile and on the angular position.

With respect to constant radius drums (CRDs) with radius r, in which the length of the released cable is given by the linear function $g = \alpha\, r$, VRDs present the following advantages:

- in a VRD it is possible to synthesize a specific profile shape in order to obtain the desired relationship $g = g(\alpha)$;
- in a VRD, a specific profile shape can be defined in order to modify the value of the torque generated by the cable on the VRD itself [158].

A Variable Radius Drum Mechanism (VRDM) is a mechanism (i.e. a linkage mechanism, or a cable-driven robot) which contains at least one VRD.

Several examples of VRD can be found in the present Literature. Endo *et al.* proposed a new weight compensation mechanical system with a non-circular pulley and a springs [159]. Kilic *et al.* used a wrapping cams mechanism in the synthesis of non-linear torsional spring [160], whereas a similar methodology has been used by Schmit and Okada to develop a non-linear rotational spring [161]. Furthermore, a non-constant radius pulley for antagonistic springs was proposed by Kim and Deshpande [162]. Shin *et al.* developed a methodology to synthesize variable radius pulleys to improve joint torque capacity in pneumatic artificial muscles, used as actuators for the Stanford Human-Friendly Robot [163]. An application of VRD in locomotion is given by Kljuno *et al.*, who developed the quadruped cable-driven robot RoboCat [164]. From a kinematic point of view, the synthesis of a variable radius drum was approached by Gallina on a particular case of rocker-belt mechanisms [165].

In recent years, another example of mechanisms based on variable radius drums can be found in [166], where the convexity of the VRD is taken into account as a condition for the design of the VRD. This approach was verified through its use in the static balancing of a one-degree-of-freedom robot arm and of a one-degree-of-freedom cable-driven parallel robot. In [167], the authors proposed a mechanism consisting of a pair of non-circular pulleys with a constant-length cable that allows to generate non-monotonic motions. This property was illustrated through two examples, namely trajectory guiding and static balancing. Finally, a low-cost variable stiffness joint design using translational variable radius pulleys was presented in [168].

The remaining of this chapter is organized as follows: Section 6.2 gives a general description of a Cable-Based Robotic Crane, Section 6.3 presents the direct kinematic analysis as well as the synthesis of a variable radius drum, whereas in Section 6.4 a bi-dimensional horizontal moving mechanism, based on a VRD, is proposed. Section 6.5 reports the inverse kinematic and dynamics of the CBRC, whereas Section 6.6 an analysis of cable tensions. The experimental prototype of the three-dimensional CBRC, developed at the Robotics Laboratory of the Department of Engineering and Architecture, University of Trieste (Italy) is presented in Section 6.7. Section 6.8 reports an analysis of the error sources in the experimental prototype. In Section 6.9, the experimental results and the performance of this mechanism in moving the end-effector through a planar workspace with high accuracy are presented, whereas Section 6.10 concludes the chapter and outlines some possible future developments of this work.

6.2 Description of the CBRC

In this section, the description of a Cable-Based Robotic Crane is presented. A graphic representation of this three-dimensional overhead traveling crane based on variable radius drums is reported in Fig. 6.3.

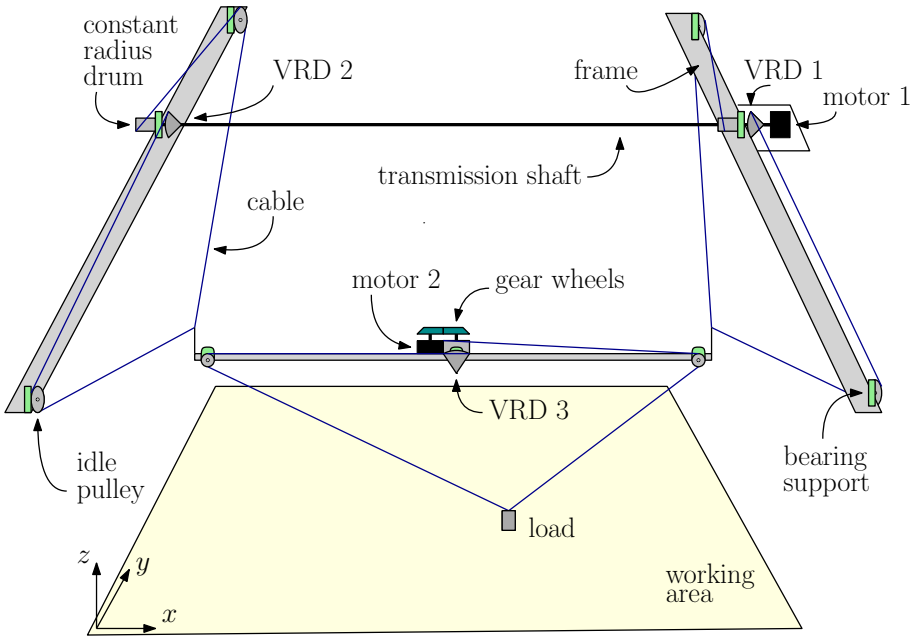

Figure 6.3: Graphic representation of a Cable-Based Robotic Crane.

The cable-suspended robot is composed of three Horizontal Moving Cable-Mechanisms (HMCMs) identical in size, that allow the motion of a load within a planar working area. The two upper mechanisms, identified by VRD 1 and 2, are located at the same vertical height in a parallel position. The end-effector of each of this two upper systems is then connected to one edge of the frame of the third HMCM. Thereby, the lower frame, identified by VRD 3, can be shifted horizontally through y axis. HMCMs 1 and 2 are connected by means of a rigid transmission shaft, which guarantees that they have the same angular position α. The third HMCM is located on the lower frame and allows the motion of the load through x axis. In this way, the 2-DOF CBRC allows the motion of a load through the rectangular working area indicated in yellow in Figure 6.3.

The cable-based robotic crane is actuated by two motors: the first is directly connected to the upper transmission shaft and ensures the motion through y axis, whereas the second, which ensures the motion along x axis, is located on the shifting frame and transmits the torque to the VRD 3 by means of two gear wheels.

6.3 Kinematic analysis and synthesis

In this section, the kinematic analysis of a variable radius drum for each HMCM is briefly summarize. In Figure 6.4 a graphical representation of the VRD is reported. On the left,

the VRD is constrained in point $\boldsymbol{O}$ by means of a rotational joint, whereas, on the right, an idle pulley is fixed in point $\boldsymbol{P}_b$ with another joint of the same type. The cable is fixed at one end of the VRD in point $\boldsymbol{F}$, it is wound around the drum profile and, initially, it is separated from the VRD in the tangent point $\boldsymbol{P}_t$. At initial conditions, this tangent point fixed at the VRD is defined $\boldsymbol{A}$, as shown in Fig. 6.4(a). The cable is then wrapped around the idle pulley and it is tangent to its surface in points E and $\boldsymbol{C}_0$. A marker is located on the VRD in order to easily identify the angular rotation of the drum with respect to the reference frame, given by angle α, which is assumed to be positive in the clockwise direction.

In order to describe the parameters that characterize the kinematic analysis of the VRD, two different configurations of the drum are taken into account: the case with $\alpha = 0$ and the one with $\alpha > 0$, reported in Fig.s 6.4(a) and 6.4(b), respectively.

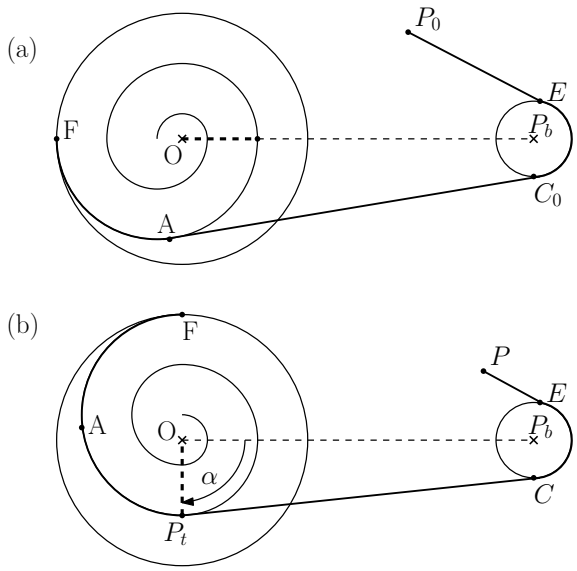

Figure 6.4: Kinematic Analysis of a Variable Radius Drum.

Case $\alpha = 0$

In this configuration, the system is assumed to be in a stable equilibrium point. A proper torque acts on the VRD along the counter-clockwise direction and a force pulls the cable to balance the torque action.
When $\alpha = 0$, the total length of the free cable, not wound around the drum, from point $\boldsymbol{P}_0$ to the tangent point $\boldsymbol{A}$ is defined l_0. The length of l_0 is given by

$$l_0 = ||\boldsymbol{AC}_0|| + \widehat{\boldsymbol{C}_0\boldsymbol{E}} + ||\boldsymbol{EP}_0|| \tag{6.1}$$

The symbol $\widehat{*}$ indicates arcs as well as curved segments on the variable radius drum.

Case $\alpha > 0$

In this configuration, the drum is rotated in clockwise direction of an angle $\alpha > 0$ and a segment of cable length $\widehat{\boldsymbol{AP}_t}$ is wound around the variable radius drum. The length of the segment $\boldsymbol{PE}$ is now changed with respect to the previous configuration: in particular, the length of $\boldsymbol{PE}$ is a function of α and of the shape of the VRD.

It can be easily obtained that

$$||\boldsymbol{P}_t\boldsymbol{C}|| + \widehat{\boldsymbol{CE}} + ||\boldsymbol{EP}|| = l_0 - \widehat{\boldsymbol{AP}_t} \tag{6.2}$$

The length of cable wound by the VRD during its rotation is a function of angular position. This function is defined $g(\alpha)$

$$g(\alpha) := ||\boldsymbol{EP}_0|| - ||\boldsymbol{EP}|| \tag{6.3}$$

By replacing (7.1) and (7.2) into (7.3), $g(\alpha)$ can be written as

$$g(\alpha) = (||\boldsymbol{P}_t\boldsymbol{C}|| - ||\boldsymbol{AC}_0||) + (\widehat{\boldsymbol{CE}} - \widehat{\boldsymbol{C}_0\boldsymbol{E}}) + \widehat{\boldsymbol{AP}_t} \tag{6.4}$$

Three addends contribute in (7.4):

- $(||\boldsymbol{P}_t\boldsymbol{C}|| - ||\boldsymbol{AC}_0||)$ is the difference between the length of the cable tangent to the variable radius drum and the idle pulley in case $\alpha = 0$ and $\alpha > 0$;
- $(\widehat{\boldsymbol{CE}} - \widehat{\boldsymbol{C}_0\boldsymbol{E}})$ is the difference between arcs on the idle pulley when $\alpha = 0$ and $\alpha > 0$;
- $\widehat{\boldsymbol{AP}_t}$ is the curved profile of the VRD on which the cable is wound.

6.3.1 Direct kinematic analysis

The Direct Kinematic Analysis of the VRD calculates the relationship between the function of wound cable $g(\alpha)$ and the angular position of the variable radius drum α, by knowing the geometry of the VRD profile. In order to do this, the angle of the tangent point P_t with respect to horizontal line is defined as $\phi = \phi(\alpha)$ and it is considered positive in clockwise direction (see Fig. 6.5). The profile of the VRD geometry in polar coordinates can be expressed as $\rho = \rho(\beta_r)$. The angle β_r is assumed to be positive in the counter-clockwise direction with respect to the relative reference frame fixed to the VRD. Then, the direct kinematic analysis can be developed by solving the integral of the VRD curve

$$g(\alpha) = (||\boldsymbol{P}_t\boldsymbol{C}|| - ||\boldsymbol{AC}_0||) + (\widehat{\boldsymbol{CE}} - \widehat{\boldsymbol{C}_0\boldsymbol{E}}) + \int_{-\phi(0))}^{\alpha-\phi(\alpha)} \sqrt{\rho^2 + (d\rho/d\beta_r)^2}\, d\beta_r \tag{6.5}$$

In (7.5), both the addends $(||\boldsymbol{P}_t\boldsymbol{C}|| - ||\boldsymbol{AC}_0||)$ and $(\widehat{\boldsymbol{CE}} - \widehat{\boldsymbol{C}_0\boldsymbol{E}})$ are non-linear functions of the angular position α. Their calculation depends on the function $\rho(\beta_r)$ and it has to be analyzed case by case.

6.3.2 Variable Radius Drum synthesis

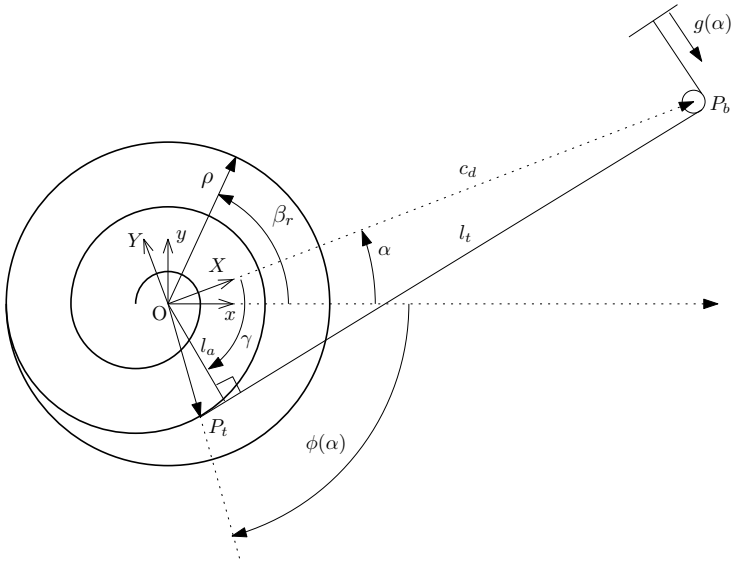

Figure 6.5: Variable radius drum parameters in case of point-like idle pulley and neglected cable thickness.

In Fig. 6.5, it can be seen that, as the VDR rotates in clockwise direction, an observer on the drum notes the idle pulley rotating in the counter-clockwise direction of the same angle. The unit vectors $\boldsymbol{x}$ and $\boldsymbol{y}$ define the reference frame of the VRD, whereas the unit vectors $\boldsymbol{X}$ and $\boldsymbol{Y}$ define the inertial reference frame, with respect to the VRD, fixed to the idle pulley center $\boldsymbol{P}_b$. In this initial approach to the problem, the idle pulley is assumed to be point-like, with a radius equal to zero. In this configuration, the distance between the idle pulley and the center of the VRD can be defined as c_d, the distance between tangent point $\boldsymbol{P}_t$ and the idle pulley center as l_t, the angle between the segment $\boldsymbol{OP}_b$ and the minimum distance between the cable and the center $\boldsymbol{O}$ of the VRD as γ. The synthesis aims at calculating the profile of the VRD by knowing the wound cable length function $g(\alpha)$.

In local coordinates, the tangent point $\boldsymbol{P}_t$ can be written as a sum of two vectors: the first from $\boldsymbol{O}$ and $\boldsymbol{P}_b$, $\{c_d \;\; 0\}^T$, the second from $\boldsymbol{P}_b$ and $\boldsymbol{P}_t$, $\{l_t \;\; 0\}^T$

$$\boldsymbol{P}_t = \boldsymbol{T}(\alpha) \begin{Bmatrix} c_d \\ 0 \end{Bmatrix} + \boldsymbol{T}(\alpha)\boldsymbol{T}(-\gamma)\boldsymbol{T}\left(-\frac{\pi}{2}\right) \begin{Bmatrix} l_t \\ 0 \end{Bmatrix} \tag{6.6}$$

where the operator $\boldsymbol{T}(x)$ is the rotation matrix between two reference frames rotated by an angle x. The whole mathematical derivations to obtain the VRD profile synthesis are reported in Appendix B.1.

Finally, the geometry of VRD profile, in Cartesian coordinates, is given by the following equation (Eq. (B.5) in Appendix B.1)

$$c_d \, sin(-\gamma) + \left(1 - \frac{d\gamma}{d\alpha}\right) l_t = 0 \tag{6.7}$$

where l_t is equal to

$$l_t = \frac{c_d sin\gamma}{1 + \frac{\frac{d^2 g}{d\alpha^2}}{\sqrt{c_d^2 - \left(\frac{dg}{d\alpha}\right)^2}}} \tag{6.8}$$

and γ can be written as

$$\gamma = cos^{-1}\left(\frac{1}{c_d}\frac{dg}{d\alpha}\right) \tag{6.9}$$

The necessary conditions for the existence of a solution for the VRD synthesis problem is the continuity of $g(\alpha)$ and its derivative. Furthermore, from (6.8) it has to be noticed that it is necessary that $dg/d\alpha < c_d$. This fact suggests that the idle pulley has to be located at a proper distance from the variable radius drum.

In Appendix B.2, the extended synthesis of the variable radius drum by considering the radius of the idle pulley and the cable thickness is reported.

6.4 Horizontal Moving Cable-Mechanism

Before presenting the prototype of a Cable-Based Robotic Crane, which is illustrated in Section 6.7, the schema of a bi-dimensional HMCM based on a variable radius drum, developed by applying the theory developed in Section 6.3, is proposed.

A horizontal moving cable-mechanism (Fig. 6.6), which is a module of the crane, is capable of moving a load along a linear path, parallel to the x axis. For the development of the cable-based device only pulling cables, revolute joints, a regular drum and a variable radius drum are needed. It has to be noticed that, differently from traditional overhead cranes, no prismatic joints are required in this type of mechanisms.

Conventional planar cable-based robots or mechanisms, which operate in the vertical plane and are subjected to gravitational force, are, in general, 2 degree-of-freedom systems. The most common configuration of this kind of mechanisms is in the form of a triangle and a load is suspended through two (or more) cables between the related motor-drums. The actuators need to be correctly controlled, if, for example, the load has to be carried through a linear path and a trajectory parallel to the ground has to be followed. Hence, the control architecture of such systems has to cope with a 2 (or more)-DOF system. On the contrary, the cable-driven robot presented here is capable of reaching the same target using just one degree of freedom, by coupling the winding and unwinding of two cables and allowing the use of a single actuator for this task.

The HMCM, proposed in Fig. 6.6, is composed of a VRD, a constant radius pulley (which radius is r_1 and it is represented in grey), two idle pulleys (that rotate around points $\boldsymbol{P}_{b1}$ and $\boldsymbol{P}_{b2}$ and have each one radius equal to r), and the load. The latter, represented by a little grey rectangle, is assumed to have mass m at point $\boldsymbol{L}$. m is the third HMCM load for the first two modules, whereas the load of the end-effector for the third horizontal moving cable mechanism. The system operates in the vertical plane and, therefore, gravity force is acting on the mass, which is connected by two cables at point $\boldsymbol{L}$. In this context, cables are modeled with null thickness and infinite stiffness. The left cable goes around the

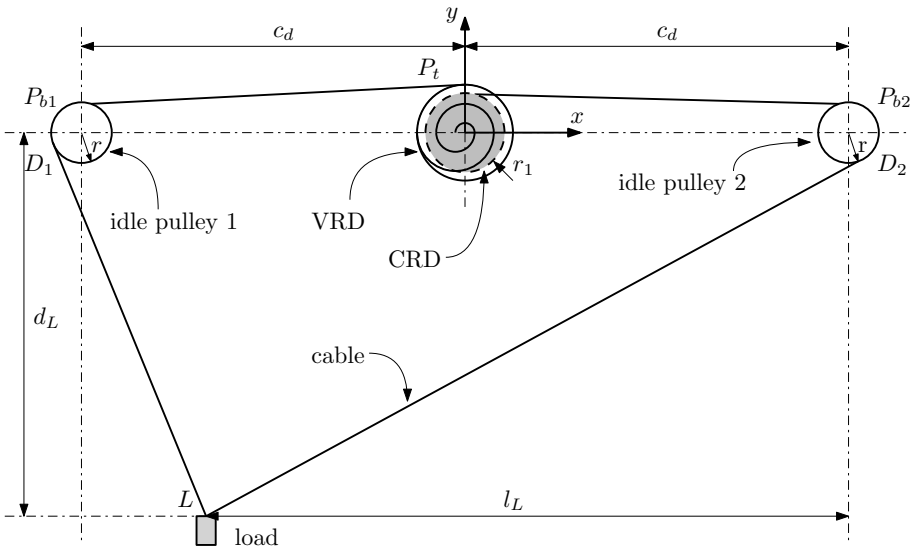

Figure 6.6: Graphical representation of a horizontal moving cable-mechanism based on a variable radius pulley.

idle pulley, constrained in $\boldsymbol{P}_{b1}$, and it is then wound around the variable radius pulley. On the contrary, the right cable goes around the idle pulley, fixed in $\boldsymbol{P}_{b2}$, and then it is wound around the constant radius pulley. It has to be noticed that the VRD and the CRD are connected to the same shaft and, therefore, they have the same angular position α.

In Fig. 6.6, c_d indicates the distance between the centers of the lateral pulleys and the center of the variable and constant radius drums, whereas d_L is the distance between the horizontal linear path of the load and the x axis. Finally, l_L indicates the horizontal distance between point $\boldsymbol{L}$ of the load and the vertical segment intersecting the center of the right idle pulley $\boldsymbol{P}_{b2}$. The angular position α of the VRD is considered positive in the clockwise direction and it is assumed to be null when the load is on the right.

In order to apply the theory developed in Section 6.3, the horizontal moving mechanism is considered in its initial position ($\alpha = 0$, $l_L = 0$). In this configuration, the point $\boldsymbol{L}$ of the load has coordinates $\{c_d, -d_L\}^T$. When the shaft of the VRD and CRD rotates in clockwise direction, a segment of the left cable is wound around the variable radius profile whereas, simultaneously, the right cable is released.

By indicating with $\boldsymbol{D}_1$ and $\boldsymbol{D}_2$ the tangency points on the idle pulleys, the synthesis of the variable radius drum profile can be obtained by the following relationship

$$g(\alpha) = \boldsymbol{D}_1\widehat{(0)\boldsymbol{D}_1}(\alpha) + (||\boldsymbol{L}(0) - \boldsymbol{D}_1(0)|| - ||\boldsymbol{L}(\alpha) - \boldsymbol{D}_1(\alpha)||) \tag{6.10}$$

where

$$||\boldsymbol{L}(0) - \boldsymbol{D}_1(0)|| = \sqrt{||\boldsymbol{L}(0) - \boldsymbol{P}_b||^2 - r^2} = \sqrt{(2c_d)^2 + d_L^2 - r^2} \tag{6.11}$$

and

$$||\boldsymbol{L}(\alpha) - \boldsymbol{D}_1(\alpha)|| = \sqrt{(2c_d - l_l(\alpha))^2 + d_L^2 - r^2} \tag{6.12}$$

The function $l_L(\alpha)$ formulates the correlation between the VRD angular position and the horizontal translation of the load $\boldsymbol{L}$. It can be written in the following form

$$l_L(\alpha) = \sqrt{||\boldsymbol{L}(\alpha) - \boldsymbol{P}_b||^2 - d_L^2} = \sqrt{||\boldsymbol{L}(\alpha) - \boldsymbol{D}_2(\alpha)||^2 + r^2 - d_L^2} \tag{6.13}$$

where $||\boldsymbol{L}(\alpha) - \boldsymbol{D}_2(\alpha)||$ can be expressed by

$$\begin{aligned} ||\boldsymbol{L}(\alpha) - \boldsymbol{D}_2(\alpha)|| &= ||\boldsymbol{L}(0) - \boldsymbol{D}_2(0)|| + r_1\alpha + \boldsymbol{D}_2\widehat{(0)\boldsymbol{D}_2}(\alpha) \\ &= \sqrt{d_L^2 - r^2} + r_1\alpha - \boldsymbol{D}_2\widehat{(0)\boldsymbol{D}_2}(\alpha) \end{aligned} \tag{6.14}$$

For the sake of simplicity, the arcs $\boldsymbol{D}_1\widehat{(0)\boldsymbol{D}_1}(\alpha)$ as well as $\boldsymbol{D}_2\widehat{(0)\boldsymbol{D}_2}(\alpha)$ can be considered equal to zero in the numeric implementation. Finally, the analytical function for the synthesis of the VRD profile can be obtained by backward replacing (6.14), (6.13), (6.12) and (6.11) into (6.10).

A 3D model of the variable radius drums was realized in SolidWorks® by implementing the analytical profile. An image of the model is reported in Fig. 6.7(a), whereas an image of a 3D printed prototype is shown in Fig. 6.7(b).

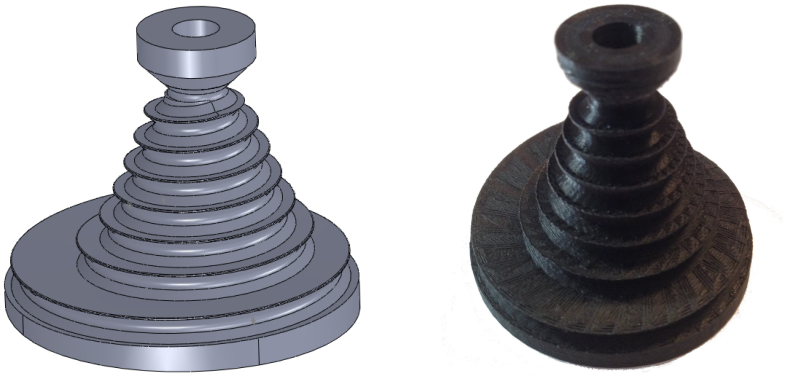

(a) (b)

Figure 6.7: Variable radius drum: 3D model (a) and 3D printed plastic prototype (b).

6.5 Inverse kinematics and dynamics

The inverse kinematic analysis and the reduced inertia of the CBRC are here presented. With reference to Fig. 6.8, the function $l_L(\alpha)$ can be expressed as $l_L(\alpha) = c_d - x$, where x is the position of the end-effector in the Cartesian space. With simple trigonometric considerations and by knowing that $\boldsymbol{LP}_{b2} = \sqrt{{l_L}^2 + {d_L}^2}$, it is possible to find the values of angles ε_1, ε_2 and ε_3 as follows

$$\varepsilon_1 = atan\left(\frac{l_L}{d_L}\right)$$

$$\begin{aligned}\varepsilon_2 &= \frac{\pi}{2} - asin\left(\frac{r}{\boldsymbol{LP}_{b2}}\right) - \varepsilon_1 \\ \varepsilon_3 &= \frac{\pi}{2} - asin\left(\frac{r}{d_L}\right) - \varepsilon_2\end{aligned} \tag{6.15}$$

For a given value of the free coordinate α, the length of an unrolled segment of cable can be easily calculated with the following equation

$$\begin{aligned}\alpha\, r_1 &= ||\boldsymbol{L}(\alpha) - \boldsymbol{D}_2(\alpha)|| + \widehat{\boldsymbol{D}_2(\alpha)\boldsymbol{D}_2}(0) - ||\boldsymbol{L}(0) - \boldsymbol{D}_2(0)|| \\ &= \sqrt{{l_L}^2 + {d_L}^2 - r^2} + \varepsilon_3\, r - \sqrt{{d_L}^2 - r^2}\end{aligned} \tag{6.16}$$

The equation of inverse kinematic $\alpha = \tilde{f}(x)$ is straightforward

$$\alpha = \frac{1}{r}\left(\sqrt{{l_L}^2 + {d_L}^2 - r^2} - \sqrt{{d_L}^2 - r^2} + \varepsilon_3\, r\right) \tag{6.17}$$

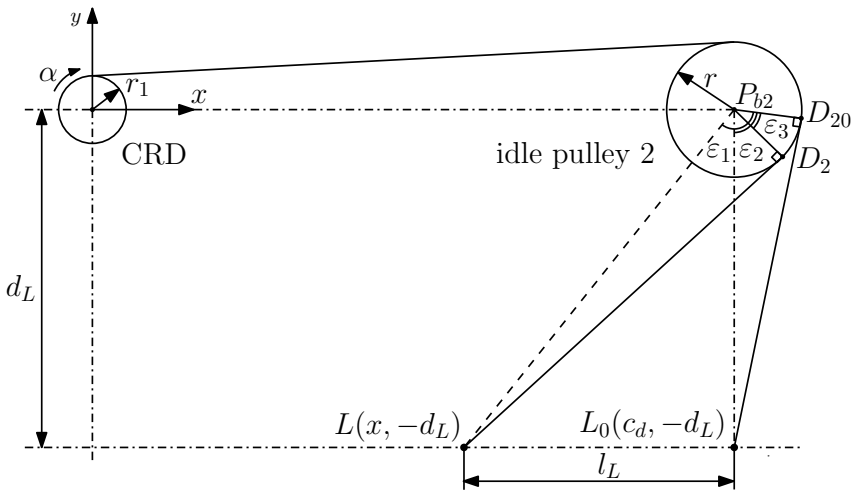

Figure 6.8: Inverse kinematic analysis of the HMCM.

As far as dynamics is concerned, the reduced inertia I related to the shaft of the variable radius drum can be calculated as

$$I = I_{VRD} + I_P\, {\tau_{\alpha,\theta_2}}^2 + I_P\, {\tau_{\alpha,\theta_1}}^2 + m\, {\tau_{\alpha,x}}^2 \tag{6.18}$$

where I_{VRD} is the inertia of the variable radius drum, I_P the inertia of the idle pulley and m the mass of the load. Furthermore, τ_{α,θ_2}, τ_{α,θ_1} and $\tau_{\alpha,x}$ indicate the transmission ratios between the VRD shaft (which rotates of an angle α) and the pulley on the right (θ_2), the pulley on the left (θ_1) and the end-effector (x), respectively. The contributions of the different transmission ratios can be expressed as

$$\tau_{\alpha,\theta_2} = \frac{\dot{\theta}_2}{\dot{\alpha}} = \frac{r_1}{r}$$

$$\begin{aligned}\tau_{\alpha,x} &= \frac{\dot{x}}{\dot{\alpha}} = \frac{\mathrm{d}\,\tilde{f}^{-1}(\alpha)}{\mathrm{d}\,\alpha} \\ \tau_{\alpha,\theta_1} &= \frac{\dot{\theta}_1}{\dot{\alpha}}\end{aligned} \tag{6.19}$$

By taking into account that

$$\theta_2 = \frac{r_1}{r}\,\alpha = \frac{r_1}{r}\,\tilde{f}(x) \tag{6.20}$$

for symmetry the expression of θ_1 in function of angle α can be obtained and written as

$$\theta_1 = -\frac{r_1}{r}\,\tilde{f}(-x) = -\frac{r_1}{r}\,\tilde{f}(-\tilde{f}^{-1}(\alpha)) \tag{6.21}$$

where the direct kinematic equation $x = \tilde{f}^{-1}(\alpha)$ has been taken into account.
Finally, by calculating the derivative function with respect to α, the expression of the transmission ratio between the VRD and the idle pulley 1 can be obtained

$$\tau_{\alpha,\theta_1} = \frac{\dot{\theta}_1}{\dot{\alpha}} = \frac{r_1}{r}\frac{\tilde{f}'(-x)}{\tilde{f}'(x)} = \frac{r_1}{r}\frac{\tilde{f}'(-\tilde{f}^{-1}(\alpha))}{\tilde{f}'(\tilde{f}^{-1}(\alpha))} \tag{6.22}$$

6.6 Cable tension analysis

In this section, an analysis of cable tensions in the CBRC is presented. For the sake of simplicity, the bi-dimensional horizontal moving mechanism presented in Section 6.2 is considered. In Fig. 6.9, a graphical representation of cable tensions $\boldsymbol{T}_1$ and $\boldsymbol{T}_2$ in the robotic crane is shown. $\boldsymbol{L}$ is the weight force, whereas θ_1 and θ_2 are the angles between the cables and the vertical plane. It has to be noticed that, in this analysis, the idle pulleys, the VRD and the CRD are considered to be point-like.

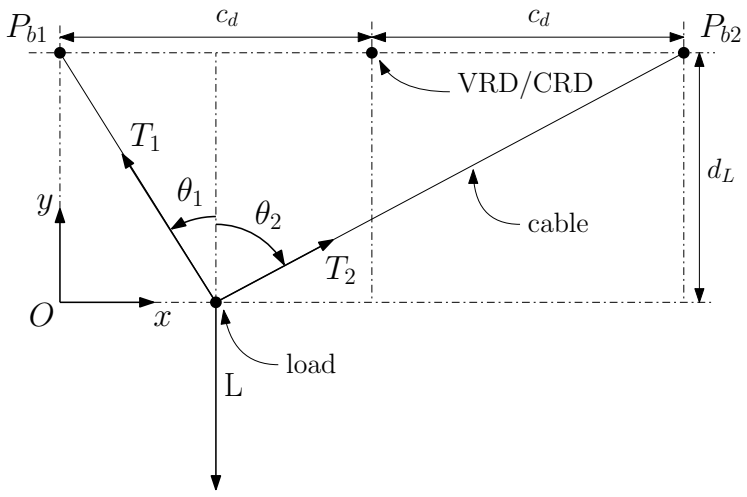

Figure 6.9: Graphical representation of cable tensions in the HMCM.

By solving the horizontal and vertical equilibrium equations system, the two tensions

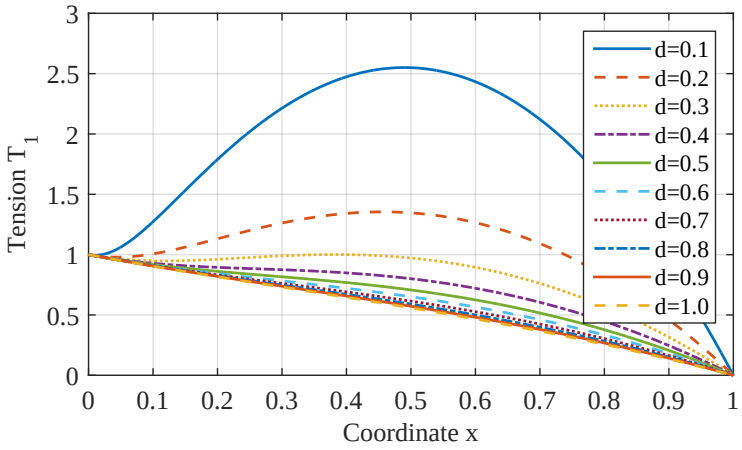

Figure 6.10: Tension $\boldsymbol{T}_1$ over the x axis, for different values of parameter d.

$\boldsymbol{T}_1$ and $\boldsymbol{T}_2$ can be easily obtained

$$\begin{aligned} \boldsymbol{T}_2 &= \frac{\boldsymbol{L}}{sin(\theta_2)\frac{cos(\theta_1)}{sin(\theta_1)} + cos(\theta_2)} \\ \boldsymbol{T}_1 &= \boldsymbol{T}_2 \frac{sin(\theta_2)}{sin(\theta_1)} \end{aligned} \tag{6.23}$$

In order to make the examination independent from distance d_L and from inter-axle spacing c_d, the parameter d, defined as $d := d_L/2\,c_d$, is introduced. Moreover, the tensions $\boldsymbol{T}_1$ and $\boldsymbol{T}_2$ are divided by the weight force mg, and the x coordinate by the distance $2\,c_d$.

In Fig. 6.10, the trend of tension $\boldsymbol{T}_1$ over the x axis, for different values of the parameter d, is reported. It has to be noticed that only tension $\boldsymbol{T}_1$ has been reported, since the two tensions are symmetric with respect to the central vertical axis of the mechanism, corresponding to a value of $x = 0.5$.

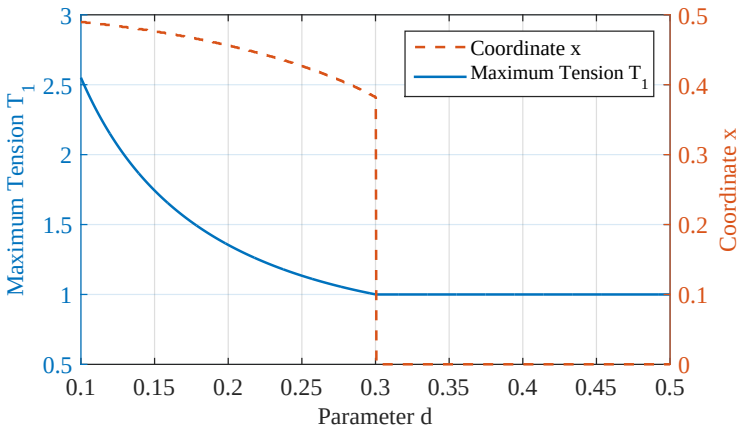

Figure 6.11: Maximum tension $\boldsymbol{T}_1$ and its position on x axis with respect to d.

In Fig. 6.11, the maximum tension $\boldsymbol{T}_1$ and its position on the x axis with respect to parameter d are reported. For $d = 0.3$ a discontinuity point occurs in the position of the x

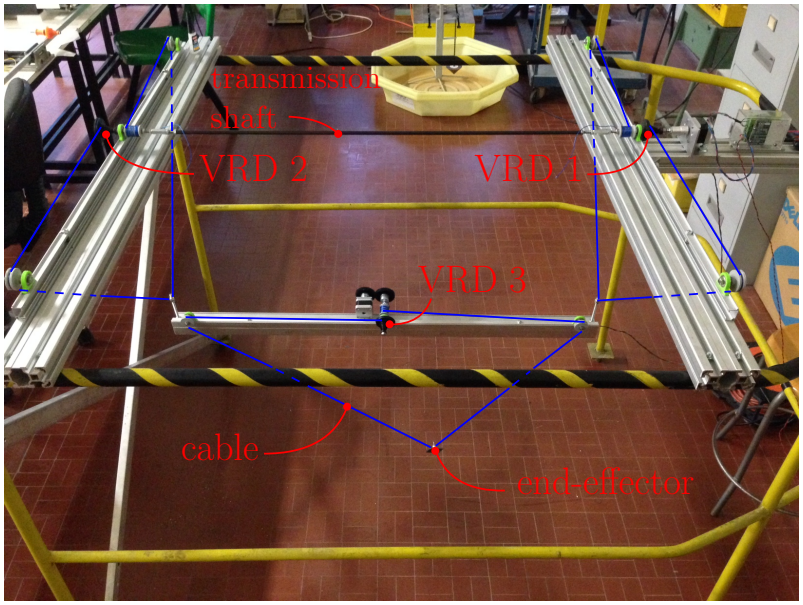

Figure 6.12: Experimental prototype of the Cable-Based Robotic Crane.

coordinate and, for values of d greater than this, the maximum tension in the cable equals the weight force. This analysis can be applied in the first stage of the design of a real CBRC, when the vertical distance of the end-effector with respect to the pulleys horizontal height has to be designed. Additionally, it has to be underlined that the torque required to maintain the load in an equilibrium point is null. This is because the potential energy is constant since the load moves along a linear horizontal path.

6.7 Prototype of the Cable-Based Robotic Crane

Item	Specifications
Step Angle	1.8°
Step Angle Accuracy	±5% (full step, no load)
Resistance Accuracy	±10%
Inductance Accuracy	±20%
Temperatru Rise	80°CMax. (rated current,2 phase on)
Ambient Temperatuar	–20°C~+50°C
Insulation Resistance	100M?Min.,500VDC
Dielectric Strength	500VAC/ for one minute
Shaft Radial Play	0.02Max. (450 g–load)
Shaft Axial Play	0.08Max. (450 g–load)
Max. radial force	28N (20mm foom the flange)
Max.axial force	10N

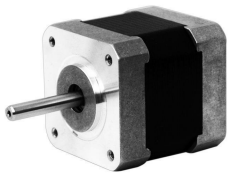

42MM Hybrid Stepping Motor Specificatiors

Model No	Rated Voltage	Current /Phase	Resistance /Phase	Inductance /Phase	Holding Torque	# of Leads	Rotor Inertia	Weinght	Detent Torque	Length
XY42STH34-0354A	V	A	Ω	mH	Kg–cm		g–cm²	kg	g–cm	mm
	12	0.35	34	33	1.6	4	35	0.22	120	34

Figure 6.13: Specifications of Stepper Motor Nema 17.

An experimental prototype of the Cable-Based Robotic Crane was fabricated at the Robotics Laboratory of the Department of Engineering and Architecture, University of

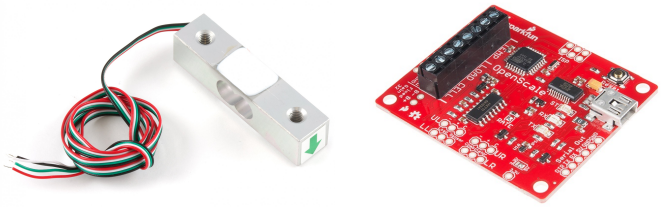

(a) (b)

Figure 6.14: Phidgets load cell (a), SparkFun OpenScale board (b).

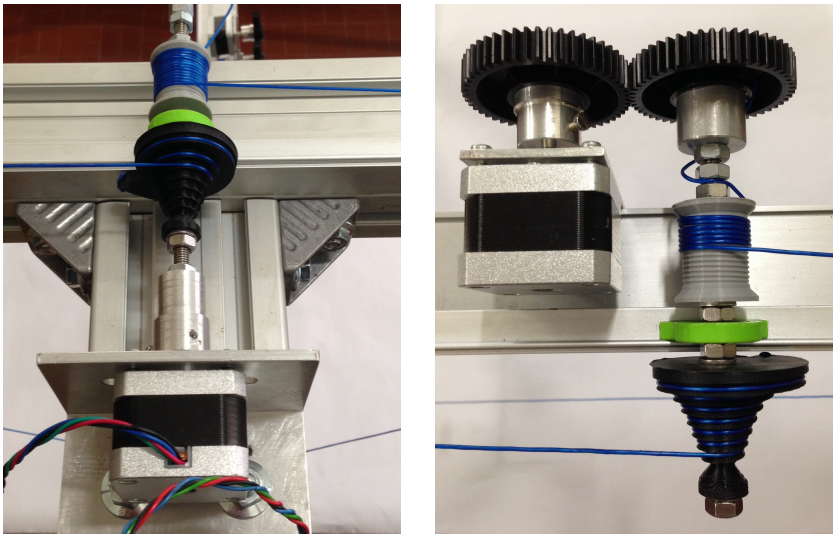

(a) (b)

Figure 6.15: Actuator system of the VRD 1 and 2 (a), gear wheels and VRD 3 (b).

Trieste (Italy). A general overview of the experimental device is reported in Fig. 6.12.

Before describing the features of the experimental system, it is necessary to underline that the fabrication of a variable radius drum is a critical aspect, since its shape can not be easily obtained by means of traditional manufacturing processes. To obtain a working prototype, the 3D printing fused deposition modeling (FDM) technology has been used. This technique allows the creation of free-form shapes by means of a 3D modeling software. Not only the variable radius drums, but also the constant radius drums, the idle pulleys and the supports for the bearings have been produced with 3D printing technology in PLA, using an Ultimaker 2+ 3D printer. The upper and lower frames of the CBRC have been realized with aluminum profile shapes, whereas the transmission shaft has been built in carbon, in order to ensure a light weight but also a proper torque resistance.

With reference to Fig. 6.6, the geometrical parameters for each of the three single HMCM that composes the experimental CBRC are: $c_d = 500\ mm$, $d_L = 500\ mm$, $r = 15\ mm$ and $r_1 = 10\ mm$. In this prototype, a load with a mass equal to $m = 0.550\ Kg$ has been chosen. As actuators, two 12 V powered NEMA 17 stepper motors (Fig. 6.13) have been

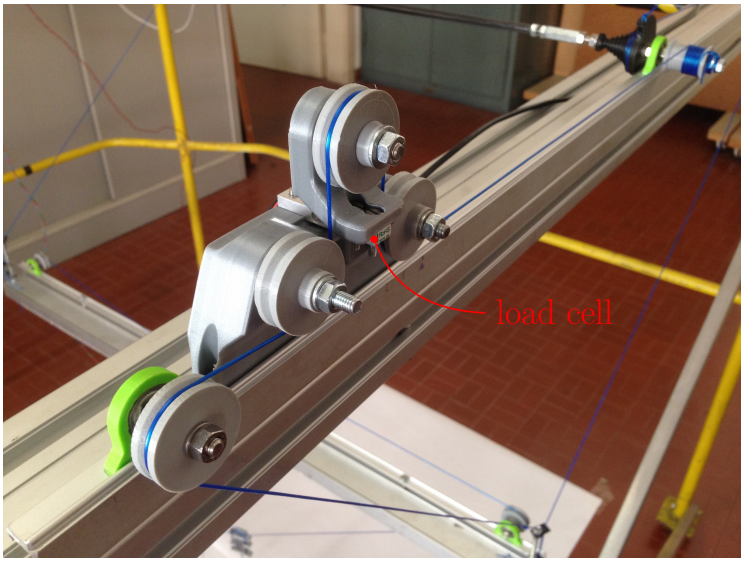

Figure 6.16: Cable tension measurement system.

adopted. Those electric motors have been chosen for the compact shape, lightweight and output torque properties. The motors are driven by two L293D drivers directly controlled by an Arduino® UNO rev.3 micro-controller board, equipped with the ATmega 328P. Figures 6.15(a) and (b) show the actuator system for the two upper mechanisms, and for the variable radius drum 3, respectively.

In order to measure the cable tensions, a proper measurement system, reported in Figure 6.16, has been designed and implemented. It consists in three 3D printed idle pulleys and a Phidgets micro load cell (Fig. 6.14(a)), that allows to measure the cable tension in the vertical direction. The load cell has been calibrated and the data have been acquired by means of a SparkFun OpenScale board (Fig. 6.14(b)).

6.8 Error sources in the experimental prototype

From Figures 6.12 and 6.15 it can be noticed that the variable radius drums and the constant radius drums are not planar, but they are in the form of a helical cone and a cylinder, respectively. Indeed, except in the cases when the spiral angle is less then 360 degrees, purely planar VRDs and CRDs are impossible to build. This fact introduces an error with respect to the mathematical model developed in Section 6.2 and 6.3, which is inherent to purely planar mechanisms.

Furthermore, the idle pulleys and the drums are not coplanar. In fact, as the bearings supports (printed in green plastic) for both idle pulleys and drums shafts are mounted on the same plane, a small offset between the tangent point of the cable on the drums and the tangent point of the cable on the pulleys is present. This deviation produces an error source with respect to the nominal behavior of the mechanism but, for the sake of simplicity, it has been neglected in this context.

The most important error sources that affect the CBRC can be summarized in the

following list:

- manufacturing errors;
- mathematical approximation in the VRD synthesis (6.14), namely

$$\boldsymbol{D}_1\widehat{(0)\boldsymbol{D}_1}(\alpha) \simeq 0 \tag{6.24}$$

  as well as

$$\boldsymbol{D}_2\widehat{(0)\boldsymbol{D}_2}(\alpha) \simeq 0 \tag{6.25}$$

- non-planarity of the idle pulleys and drums;
- geometrical errors;
- misalignment of the pulleys and drums axis;
- cables elongation and elasticity [103, 101, 169];

  Cables elongation Δx with respect to the nominal length x_0 can be calculated with the following equation

$$\Delta x = \frac{T(x)}{AE}\, x_0 \tag{6.26}$$

  where $T(x)$ is the cable tension, A is the cross-sectional area of the cable, whereas E the Young's modulus. In the plastic cable employed in our prototype $EA \simeq 13\ kN$.

  In particular, with respect to Fig. 6.9, the accuracy errors Λ_x and Λ_y in x and y directions, due the cable elasticity and relative to the payload, can be evaluated as follows

$$\Lambda_x = \frac{|x_E - x_L|}{mg} \quad \Lambda_y = \frac{|y_E - y_L|}{mg} \tag{6.27}$$

  where (x_L, y_L) and (x_E, y_E) are the end-effector coordinates in nominal position and the ones affected by cable elongations, calculated with (6.23) and (6.26). Figure 6.17 reports the trend of these errors along the x axis.

- scale errors;

  The scale error e_x for a single horizontal moving cable mechanism (Fig. 6.9) affects the measure on the end-effector position along the x axis, resulting in the following error

$$e_x = \frac{(K_1^2 - 1)l_1^2(\alpha) - (K_2^2 - 1)l_2^2(\alpha)}{2L^2} \tag{6.28}$$

  where K_1 and K_2 are the scale factors on idle pulleys 1 and 2 respectively, $l_1(\alpha)$ and $l_2(\alpha)$ are the length of the free-cables 1 and 2 in function of the free-coordinate α and $L = 2\,c_d$.

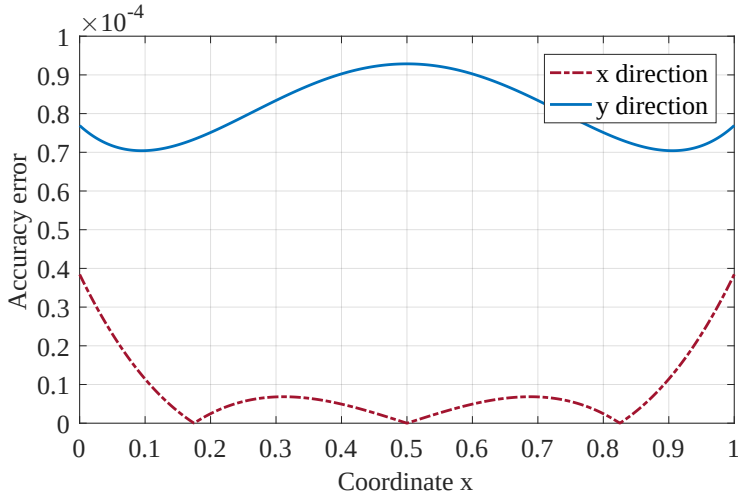

Figure 6.17: Accuracy errors Λ_x and Λ_y, relative to the payload, over the x axis ($d = 0.5$).

6.9 Experimental results

The performance of the Cable-Based Robotic Crane presented in this chapter can be evaluated by measuring the deviation of the end-effector from a nominal planar surface. A grid has been marked out on the working area of the overhead traveling crane and the height of the load has been measured, in static conditions, by means of a vertical caliper through the surface in both x and y directions. On the working area a sampling interval of $\Delta x = 50\ mm$ and $\Delta y = 50\ mm$, starting from ($x = 0$, $y = 0$) till ($x = 700\ mm$, $y = 700\ mm$), has been chosen.

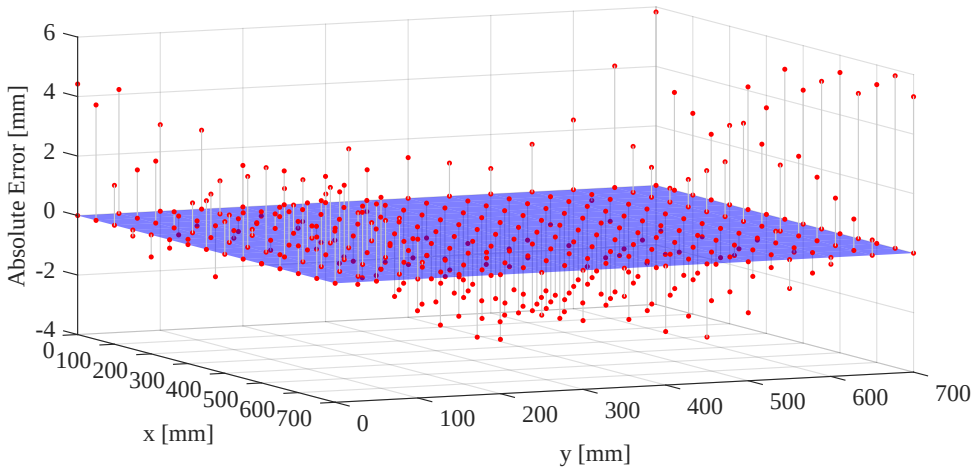

Figure 6.18: Absolute experimental error with reference to nominal planar surface.

In Fig. 6.18, the experimental results are shown. The red dots indicate the measure points, whereas the blue planar surface is the nominal plane. The maximum deviation from the theoretic path is actually really small and equal to 5.8 mm. At this value corresponds a maximum relative error of 0.83% to the total length of the path in one direction (700 mm). The relative error is very small and lower than 1% throughout the whole planar workspace.

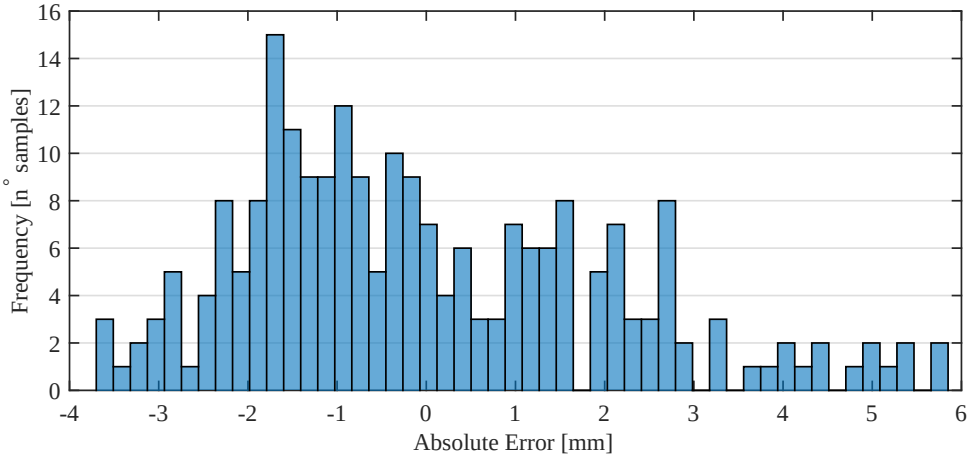

Figure 6.19: Histogram of the absolute experimental errors with respect to the nominal planar surface.

In Fig. 6.19 an histogram of the absolute experimental errors with respect to the nominal planar surface is reported.

Furthermore, the errors along x and y axis have been evaluated in order to provide the positional accuracy of the upper and lower HMCMs separately. In particular, errors in the x direction have been evaluated by fixing the upper HMCMs and moving only the lower HMCM. In the same manner, y errors refer to the center of the frame of the lower HMCM, when only the two upper mechanisms are activated. Measures in x and y directions have been acquired in static conditions, with the same approach used for the evaluation of vertical accuracy. In fact, measurements have been taken after the dynamic oscillations became negligible. In Figures 6.20 and 6.21, the absolute experimental errors in x and y directions are reported. Table 6.1 summarizes the statistical analysis of the absolute errors in the three directions. The Kolmogorov-Smirnov test has been applied to the distribution of the errors in order to verify the normality of data.

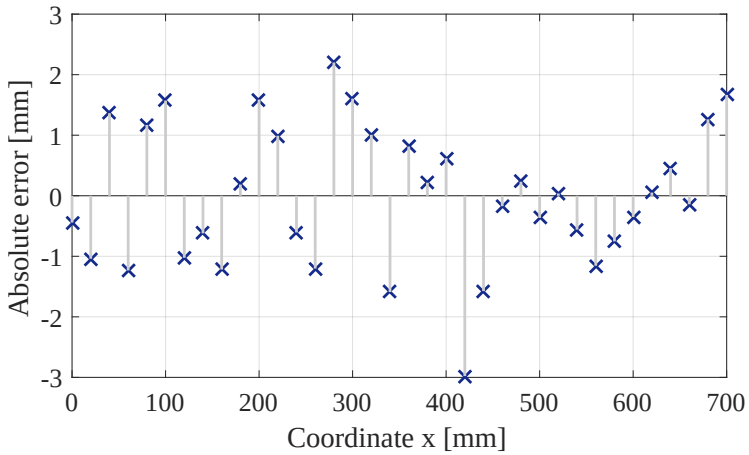

Figure 6.20: Absolute experimental error in x axis.

These results show that the experimental prototype, even in this early stages of

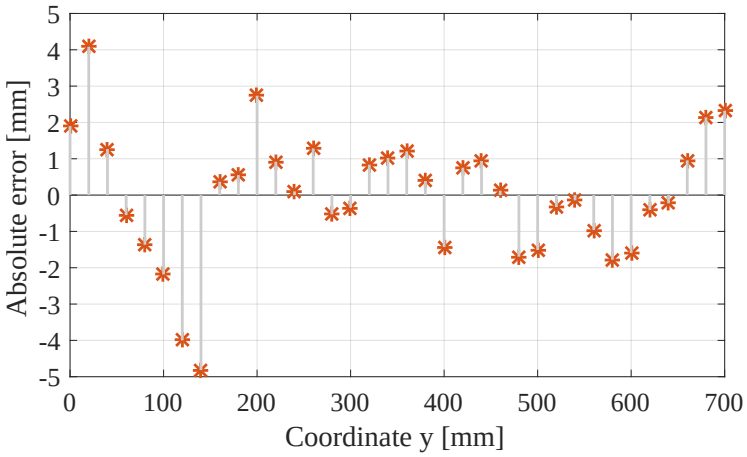

Figure 6.21: Absolute experimental error in y axis.

Table 6.1: Statistical analysis of absolute errors [%].

Axis	Max	Mean	St. Dev.	p-value (K.-S. test)
x	0.4254	0.1352	0.0938	< 0.05
y	0.6880	0.1895	0.1626	< 0.05
z	0.8326	1.6858	1.1992	< 0.05

development, can achieve its task with acceptable accuracy and precision. Moreover, the offset of the drums does not produce a worrying effect on the performance of the global mechanism. The deviation error could be further reduced by using more accurate manufacturing technologies for the VRD and the pulleys, with respect to 3D printing technique, e.g. milling machine manufacturing.

Table 6.2: Experimental cable tension errors in function of x position with respect to theoretical data ($d = 0.5$).

x-coord. [mm]	Max	Mean	St. Dev.
150	0.0556	0.0336	0.0181
250	0.0427	0.0237	0.0173
350	0.0402	0.0237	0.0172
450	0.0421	0.0231	0.0183
550	0.0415	0.0189	0.0191
650	0.0334	0.0159	0.0131
750	0.0224	0.0130	0.0058
850	0.0268	0.0130	0.0095

Finally, the cable tensions of the presented prototype have been measured in order to compare them with those previously computed in Section 6.6 (case $d = 0.5$ in Fig. 6.10). The results are reported in Fig. 6.22. For each point, 6 different measures have been acquired and the statistical analysis of the data is reported in Tab. 6.2. The results have been divided by mg, where m is the mass of the load used in the measures, in order to

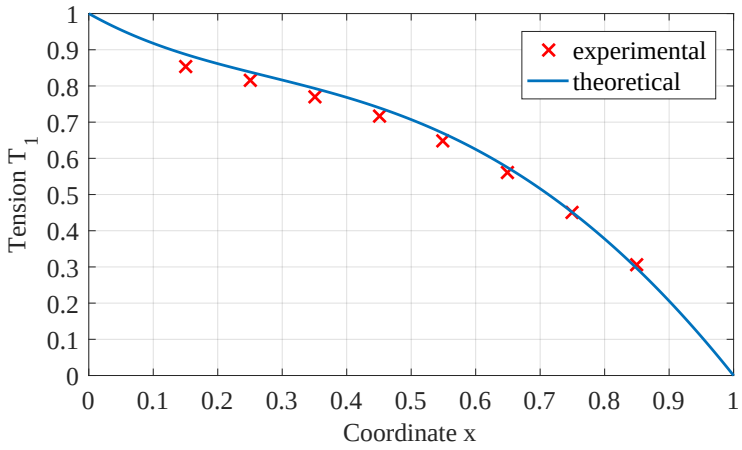

Figure 6.22: Tension T_1 over the x axis, comparison between theoretical and experimental data ($d = 0.5$).

compare them with the predicted data. A good agreement between the theoretical curve and the experimental results can be found.

6.10 Conclusions

Cable-suspended parallel robots can be guided through a predefined trajectory using non-circular pulleys or drums. In this chapter, after a brief introduction about devices based on non circular pulleys and drums, a novel design of overhead traveling crane, based on variable drums and named Cable-Based Robotic Crane, was presented. The direct kinematic analysis and the synthesis of the geometry of a variable radius drum were proposed. The VRD theory was applied firstly on a bi-dimensional horizontal moving mechanism and, then, to a three-dimensional overhead crane. An experimental prototype of a CBRC, produced using 3D printing technology, was developed at the Robotics Laboratory of the Department of Engineering and Architecture, University of Trieste, Italy.

The performance of the mechanism were evaluated and a deviation of the end-effector from the nominal position of less than 1%, throughout the whole working area in both x, y and z directions, was found. Furthermore, the cable tensions have been measured and compared with the theoretical values.

The presented prototype of Cable-Based Robotic Crane highlights the advantages of using variable radius drums with respect to traditional constant radius drums, the first and foremost being the simplicity in the required actuation system. In fact, it is well known that it would need several constant radius drums with a coupled actuation system to drive them in a synchronous manner in order to make the end-effector moving along a linear path on a planar surface. The device presented in this chapter is based on the coupling of the winding and unwinding of the cable and it allows the motion of the end-effector through a planar workspace by using 2-DOF only. Additionally, the VRD requires only to compensate the variation of the radius in order to produce a demanded speed or torque output.

Moreover, the cable-driven robot described in this chapter is characterized by a lighter weight with respect to traditional overhead traveling cranes, it is reconfigurable and modular. In this preliminary prototype, the effects of oscillations and vibrations might occur during the end-effector motion. Even if this problem arises also in traditional overhead traveling cranes, in the presented experimental system the cables flexibility as well as the pendulum phenomena might introduce negative issues during the movement of the load. From a practical perspective, where stiffness might be required by several applications, this aspect need to be further investigate, e.g. by implementing anti-swing as well vibration-suppression control strategies [83]. Furthermore, the maximum speed of the system depends on the size of the cables and their tensions, as well as its acceleration is limited by the cables stability, since they support traction forces but no compression ones. Such problems have been addressed in other cable robots, where gravity forces are involved [95].

In future developments of this work, several improvements could be introduced in the manufacturing of the complex shapes of VRDs profiles. Furthermore, a complete sensitivity analysis of CBRC kinematics would be useful to evaluate potential issues before providing interesting real applications. Finally, the safety of the system in the case of cable failure [87] can be analyzed and the elongation of the cables [101] can be examined.

Chapter 7

Under-Actuated, Pendulum-Like, Cable-Driven Robots

In this chapter, the design and experimental validation of a 3-degree-of-freedom, under-actuated, pendulum-like, cable-driven robot is presented. The end-effector of the mechanism is capable of performing point-to-point motions, from a starting pose to a goal one in the dynamic workspace of the robot, to be reached with zero angular and linear speed, by means of two actuators only. The device uses parametric excitation to control the oscillations of a variable-length pendulum, akin to a playground swing. Feedback linearization allows the dynamics of the variable-length pendulum to be decoupled from the orientation of the end-effector. A pool of Adaptive Frequency Oscillators provides smooth estimations of the current phase of the oscillation in real-time and without delay to inform the parametric excitation controller. Experimental results demonstrate feasibility of the proposed design and control approach.

The work presented in this chapter has been developed at the Wearable Robotic Systems (Lab), Department of Mechanical Engineering, Stevens Institute of Technology (Hoboken, NJ, USA) during the visiting period that I spent abroad in the first part of the third year of my Ph.D.

Part of the work described in this chapter has been presented in [5] (paper under review).

7.1 Introduction

Pendulum-like cable-driven robots are a special class of cable-suspended parallel robots. These flexible-link manipulators consist of a cable-suspended passive robotic arm, whose oscillations can be modulated by actively controlling the lengths of the cables or the orientation of the end-effector. If the end-effector is regarded as a lumped mass, the system can be modeled as a variable-length pendulum (Lorentz's pendulum [170]), whose swing-up motion can be assimilated to the one provided by children on playground swings [171, 172, 173]. Several theoretical studies deal with the process of pumping and subtracting energy in the variable-length pendulum. In 1970, J. A. Burns proved that lengthening the

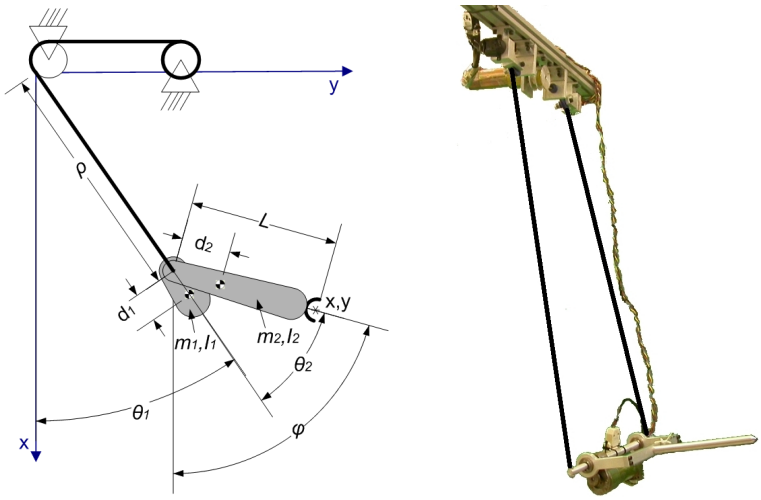

(a) (b)

Figure 7.1: The 3-DOF under-actuated cable-driven robot presented in [145]: kinematic diagram (a) and experimental prototype (b).

cable when the pendulum reaches the maximum angular amplitude and shortening it when the amplitude is zero increases the energy of the system [174]. Furthermore, the dynamic modeling of the playground swing was studied by J. Case in [175, 176], by approximating the swing to a linear harmonic oscillator with driving and parametric terms.

An example of robotic system that uses parametric self-excitation is given by the WinchBot [177], a 2-DOF under-actuated robot capable of moving a point-mass end-effector over arbitrary paths using parametric self-excitation. Other authors have studied 3-DOF pendulum-like robots, capable of performing point-to-point motions using two actuated joints only. In particular, not only the position but also the orientation of the end-effector of these systems can be controlled during a motion that extends beyond the static workspace.

A 3-DOF pendulum-like under-actuated cable-driven robot was presented in [145]: the robot consists of an end-effector with an actuated arm suspended on a cable wound on a reel. The kinematic diagram and an image of the experimental prototype are reported in Fig. 7.1. A novel design for a 3-DOF under-actuated, pendulum-like robot was proposed by D. Zanotto *et al.* in [146]. Figure 7.2 reports the kinematic diagram of the flexible-link manipulator. The control system is based on feedback linearization to decouple the dynamics of the system into two simple single-input single-output systems. The robot enables point-to-point trajectories using two actuators only. However, no experimental validation was presented in that work.

In [147], another example of 3-degree-of-freedom cable-suspended robot was presented. The system (Fig. 7.3) is similar to the one described in [146] and does not require an actuator to be mounted on the end-effector. However, its dynamics are more complex and the control system is based on heuristic characterization.

In [178], the dynamic behavior of a pendulum with periodical variable-length was analyzed by comparing analytical results obtained with an approximate model to the ones

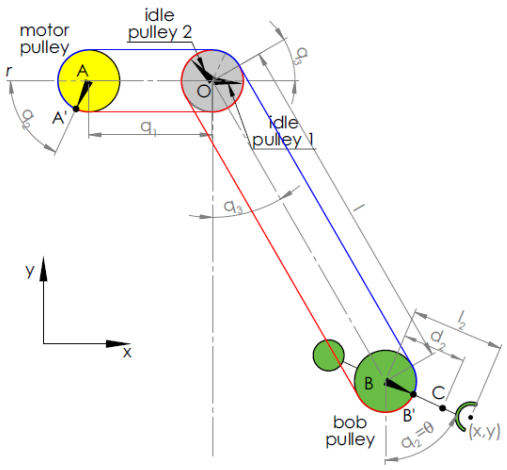

Figure 7.2: The 3-DOF under-actuated cable-driven robot presented in [146].

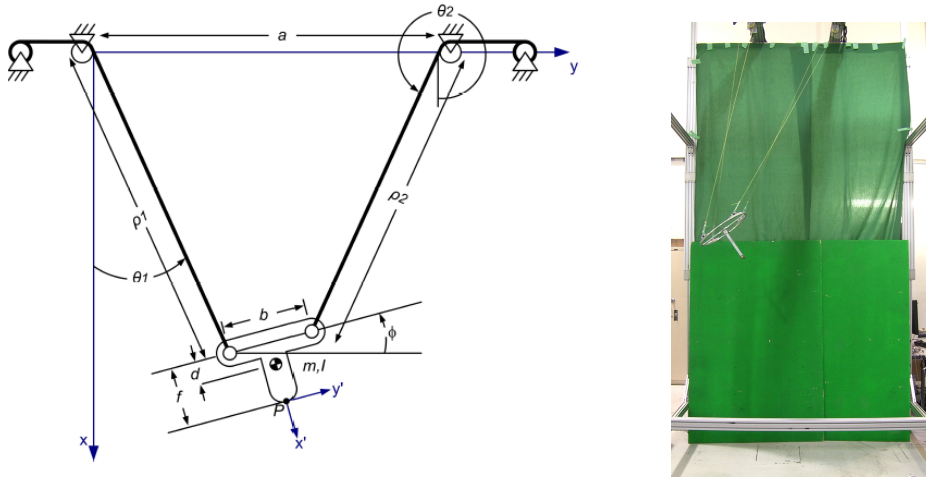

(a) (b)

Figure 7.3: The 3-DOF under-actuated cable-driven robot presented in [147]: kinematic diagram (a) and experimental prototype (b).

derived by means of non-approximate equations solved numerically. In [179], the control of angular oscillations of a variable-length pendulum using mass reconfiguration was proposed, whereas a time optimal control of a swing was presented in [180].

In this chapter, the modeling and non-linear control of a 3-DOF, under-actuated, pendulum-like, cable-driven robot is presented. The end-effector of the mechanism is capable of completing planar point-to-point motions from a starting pose $[x_S, y_S, \theta_S]^T$ to a goal one $[x_G, y_G, \theta_G]^T$, reached with zero angular and linear speed, by means of two actuated winches only. Not only the position but also the orientation of the end-effector is controlled during a motion that extends beyond the static workspace. Similar to [146], the proposed controller uses feedback linearization to turn the complex coupled dynamics of the system into those of two decoupled subsystems: a variable-length pendulum and a linear

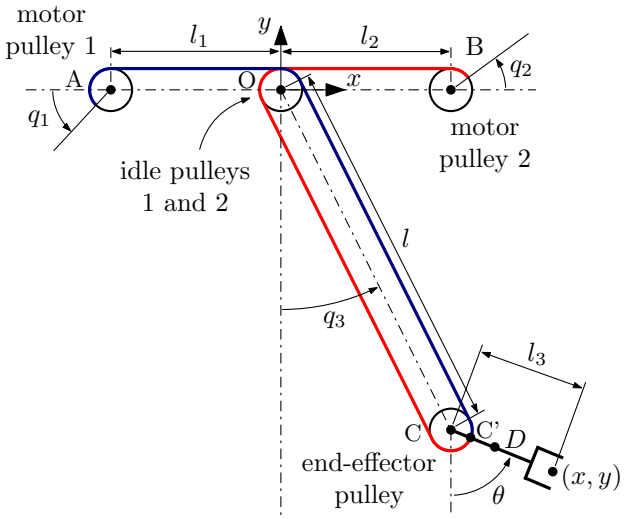

Figure 7.4: Kinematic diagram of the pendulum-like manipulator.

controllable system. A pool of oscillators (Adaptive Frequency Oscillators, AFO) estimate the phase of the pendulum-robot in real-time and phase-locked parametric excitation is employed to modulate the amplitude of the oscillations.

The novel contributions of this work can be summarized as follows:

1. the development of a novel design for a pendulum-robot, which is functionally equivalent but structurally simpler than the one described in [146];

2. the introduction of Adaptive Frequency Oscillators to provide smooth estimates of the pendulum phase, which inform the parametric excitation controller;

3. the experimental validation of the pendulum-like robot.

The remaining of the chapter is organized as follows: in Section 7.2 the kinematic and dynamic models of the pendulum robot are presented, in Section 7.3 the trajectory planning and control system are analyzed, whereas in Section 7.4 the experimental prototype is described. Section 7.5 reports the experimental results. Finally, the conclusions and some possible future developments of this work are discussed in Section 7.6.

7.2 Kinematic and dynamic modeling

The kinematic diagram of the cable-driven robot presented in this chapter is shown in Fig. 7.4. It is composed of two actuated revolute joints, namely q_1 and q_2, that allow to control the length of the pendulum l and the absolute orientation of the end-effector θ. The robotic arm, whose center of mass is indicated as D, is suspended by means of two cables that are connected to the same point C' of the end-effector pulley. The two cables are wrapped around two co-axial, independent idle pulleys, whose axis is indicated by point O, and then fixed to the motor pulleys 1 and 2. The third degree of freedom of the flexible-link manipulator is the passive angle of oscillation q_3. By means of the two actuated joints,

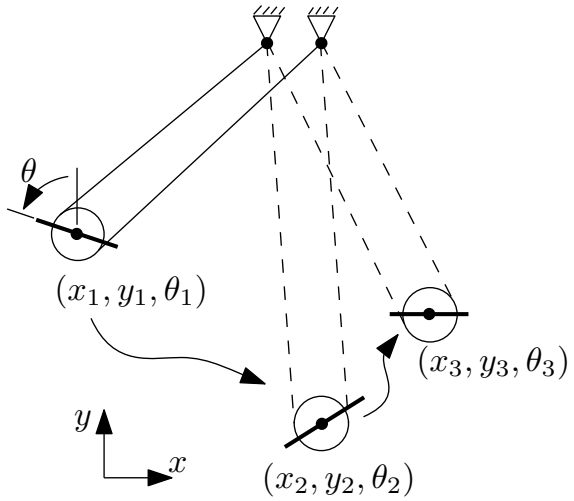

Figure 7.5: Dynamic motion beyond the static workspace.

the end-effector can reach a desired pose $[x_G, y_G, \theta_G]^T$ with zero angular and linear speed. Since the configurations of the robot with $q_3 \neq 0$ are not included in the static workspace of the manipulator, they do not correspond to stable equilibrium points and the system cannot be indefinitely steady for those values of the passive degree of freedom. In Fig. 7.5 a representation of the dynamic motion of the manipulator beyond its static workspace is reported.

The inputs to the forward kinematics are the actuated joint variables q_1 and q_2 and the passive swing angle of the pendulum q_3. While the first two variables are derived from the encoders mounted on the motors, the swing angle can be estimated using a custom follower (see Sec. 7.4).

With reference to the kinematic diagram reported in Fig. 7.4, the total cable lengths L_1 and L_2 can be expressed as functions of the joint variables

$$\begin{aligned} L_1 &= \left(\frac{\pi}{2} + q_1\right) r + l_1 + \left(\frac{\pi}{2} - q_3\right) r + l + \left(\frac{\pi}{2} - \theta + q_3\right) r = \\ &= \frac{3\pi}{2} r + q_1 r + l_1 + l - \theta r \\ L_2 &= \left(\frac{\pi}{2} - q_2\right) r + l_2 + \left(\frac{\pi}{2} + q_3\right) r + l + \left(\frac{\pi}{2} + \theta - q_3\right) r = \\ &= \frac{3\pi}{2} r - q_2 r + l_2 + l + \theta r \end{aligned} \tag{7.1}$$

where r indicates the radius of the actuated pulleys, of the idle pulleys and of the end-effector pulley. From (7.1) it can be seen that the total length of the pendulum l only depends on the actuated joint variables

$$l = L_0 + \left(\frac{q_2 - q_1}{2}\right) r \tag{7.2}$$

where L_0 is a known constant parameter. The pose of the end-effector $[x\ y\ \theta]^T$ can be

computed as:

$$\begin{bmatrix} x \\ y \\ \theta \end{bmatrix} = \begin{bmatrix} l\,\sin(q_3) + l_3\,\sin(\frac{q_1+q_2}{2}) \\ -l\,\cos(q_3) - l_3\,\cos(\frac{q_1+q_2}{2}) \\ \frac{q_1+q_2}{2} \end{bmatrix} \tag{7.3}$$

Given the Cartesian pose of the end-effector, the corresponding joint variables can be computed as

$$\begin{bmatrix} q_1 \\ q_2 \\ q_3 \end{bmatrix} = \begin{bmatrix} \theta + \sqrt{\bar{x}^2 + \bar{y}^2} \\ \theta - \sqrt{\bar{x}^2 + \bar{y}^2} \\ \arctan(-\bar{x}/\bar{y}) \end{bmatrix} \tag{7.4}$$

where

$$\begin{bmatrix} \bar{x} \\ \bar{y} \end{bmatrix} = \begin{bmatrix} x \\ y \end{bmatrix} - l_3 \begin{bmatrix} \sin\,\theta \\ -\cos\,\theta \end{bmatrix} \tag{7.5}$$

It should be noticed that the absolute orientation of the end-effector θ is constrained between $\pm\pi/2$.

The dynamics equations can be derived by applying the Newton-Euler approach to the free body diagram shown in Fig. 7.6. In the following, both friction forces and aerodynamics effects are neglected and the cables are modeled as massless bodies with infinite stiffness. Under these assumptions, the equations of motion are

$$\begin{cases} \ddot{l} = \dfrac{d_2 \sin\beta(r\tau_2 - d_2\tau_1 \sin\beta)}{J_{EE}} + d_2\dot{\theta}^2\cos\beta + g\cos q_3 + l\dot{q_3}^2 - \dfrac{\tau_1}{m_{EE}} \\ \ddot{q_3} = \dfrac{{d_2}^2\tau_1 \sin\beta\cos\beta - d_2 r\tau_2\cos\beta}{J_{EE}\,l} + \dfrac{d_2\dot{\theta}^2\sin\beta - g\sin q_3 - 2\dot{l}\dot{q_3}}{l} \\ \ddot{\theta} = \dfrac{r\tau_2 - d_2\tau_1\sin\beta}{J_{EE}} \end{cases} \tag{7.6}$$

where

$$\begin{aligned} \tau_1 &= T_1 + T_2 \\ \tau_2 &= T_1 - T_2 \\ \beta &= \theta - q_3 \end{aligned} \tag{7.7}$$

T_1 and T_2 are the tensions measured on the cables; m_{EE} and J_{EE} are the mass and the

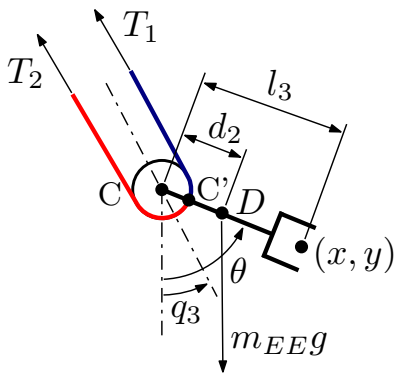

Figure 7.6: Free body diagram for the end-effector.

barycentric moment of inertia of the end-effector, respectively.

By means of the following *input-space transformation*

$$\begin{cases} \tau_1 = m_{EE}\left(-v_1 + g\,\cos q_3 + d_2 v_2\,\sin\beta + d_2\dot{\theta}^2\,\cos\beta + l\dot{q_3}^2\right) \\ \tau_2 = \dfrac{1}{r}(J_{EE}v_2 + d_2 m_{EE}\,\sin\beta(-v_1 + g\,\cos q_3 + d_2 v_2\,\sin\beta) + \\ \qquad + d_2 m_{EE}\,\sin\beta(d_2\dot{\theta}^2\,\cos\beta + l\dot{q_3}^2)) \end{cases} \tag{7.8}$$

the equations of motion (7.6) can be rewritten as

$$\begin{cases} \ddot{l} = v_1 & \text{(7.9a)} \\ \ddot{q_3} = -\dfrac{d_2 v_2\,\cos\beta}{l} - \dfrac{g\,\sin q_3 - d_2\dot{\theta}^2\,\sin\beta + 2\dot{l}\dot{q_3}}{l} & \text{(7.9b)} \\ \ddot{\theta} = v_2 & \text{(7.9c)} \end{cases}$$

where v_1 and v_2 are the new control variables. In (7.9b), the first term represents the driving excitation, whereas the second term controls the parametric excitation of the pendulum-robot.

The state-space form of the dynamic system can be obtained by introducing this change of variables: $x_1 = l$, $x_2 = q_3$, $x_3 = \theta$, $x_4 = \dot{l}$, $x_5 = \dot{q_3}$, $x_6 = \dot{\theta}$, which yields the following expression

$$\dot{\boldsymbol{x}} = \begin{bmatrix} x_4 \\ x_5 \\ x_6 \\ 0 \\ -\frac{g\,\sin(x_2) - d_2 x_6^2\,\sin(x_3 - x_2) + 2x_4 x_5}{x_1} \\ 0 \end{bmatrix} + \begin{bmatrix} 0 & 0 \\ 0 & 0 \\ 0 & 0 \\ 1 & 0 \\ 0 & -\frac{d_2\,\cos(x_3 - x_2)}{x_1} \\ 0 & 1 \end{bmatrix} \begin{bmatrix} v_1 \\ v_2 \end{bmatrix} \tag{7.10}$$

This system can be decoupled into two independent single-input subsystems:

- a variable-length pendulum (x_1, x_2, x_4, x_5), which is not linearizable (see Appendix C.1);
- a linear controllable system (x_3, x_6), which corresponds to the absolute rotation of the end-effector.

This decoupling holds if (i) the end-effector is balanced (i.e., $d_2 = 0$) or (ii) the absolute orientation of the end-effector is fixed (i.e., $\ddot{\theta} = 0$ and $\dot{\theta} = 0$, which also implies $v_2 = 0$). In the following, it is assumed that $d_2 = 0$.

7.3 Control system

In this section, the control system that allows to steer the robot from a starting pose $[l_S, q_{3S}, \theta_S]^T$ to a goal pose $[l_G, q_{3G}, \theta_G]^T$ is described. It is assumed that both the starting and the goal pose are reached with zero velocity (but non-zero acceleration) in the dynamic

workspace of the pendulum-robot. The decoupling of the system allows to develop two independent planners, one for the pendulum length and one for the end-effector orientation.

7.3.1 Adaptive Frequency Oscillators

The pendulum length planner relies on the real-time estimation of the pendulum phase. To obtain smooth, lag-free estimates of the phase of the pendulum-robot a pool of Adaptive Frequency Oscillators (AFO) has been implemented. The Adaptive Frequency Oscillators were first introduced by L. Righetti *et al.* [181, 182] and have later been applied to the estimation of human cyclical movements, e.g. in elbow and gait assistance [183, 184, 185]. The AFO estimates a quasi-periodic signal $q_3(t)$ as a combination of M oscillators. The estimation $\hat{q_3}(t)$ is given by

$$\hat{q_3}(t) = q_{30} + \sum_{1}^{M} a_i \sin(\tilde{\varphi}_i(t)) \tag{7.11}$$

where $\tilde{\varphi}_i$ and a_i are the phase and the amplitude of the i-th harmonic component, respectively, and q_{30} is a constant term. The dynamics of the M oscillators are described, for $i = 1, ..., M$, by the following equations

$$\dot{\tilde{\varphi}}_i(t) = i\omega + \varepsilon F(t)\cos(\tilde{\varphi}_i(t)) \tag{7.12a}$$
$$\dot{\omega}(t) = \varepsilon F(t)\cos(\tilde{\varphi}_1(t)) \tag{7.12b}$$
$$\dot{a_i}(t) = \nu F(t)\sin(\tilde{\varphi}_i(t)) \tag{7.12c}$$
$$\dot{q_{30}}(t) = \nu F(t) \tag{7.12d}$$

where ω is the fundamental frequency and the estimation error can be calculated as

$$F(t) = q_3(t) - \hat{q_3}(t) \tag{7.13}$$

The phase of the fundamental harmonic is stored in $\tilde{\varphi}_1$. The gains ε and ν are the coupling strength and the learning factor, respectively, and can be tuned to adjust the learning rate of the phase and amplitude. To estimate the phase of the pendulum-robot $M = 4$ oscillators have been chosen, whereas the coupling strength and the gain factor have been set to $\varepsilon = 12$ and $\nu = 0.5$, respectively.

A smooth phase correction term similar to [185] was introduced to lock the phase estimate to a particular event of the pendulum motion, such that the beginning of each semi-oscillation corresponds to a null phase. Let indicate with t_k the time instant at which the k-th semi-oscillation is completed, and with $P_e(t_k)$ the phase error at the end of the k-th semi-oscillation. An additional state variable $\varphi_e(t)$ is introduced to gradually learn $P_e(t_k)$:

$$\dot{\varphi_e}(t) = \epsilon_\varphi(t_k)\omega(t)e^{-\omega(t)(t-t_k)} \tag{7.14}$$

In the previous equation, $\epsilon_\varphi(t_k) = k_\epsilon[P_e(t_k) - \varphi_e(t_k)]$ and k_ϵ is a proportional gain. Assuming $\omega(t)$ constant over one semi-oscillation, $\dot{\varphi_e}(t)$ is a first-order system filtering a

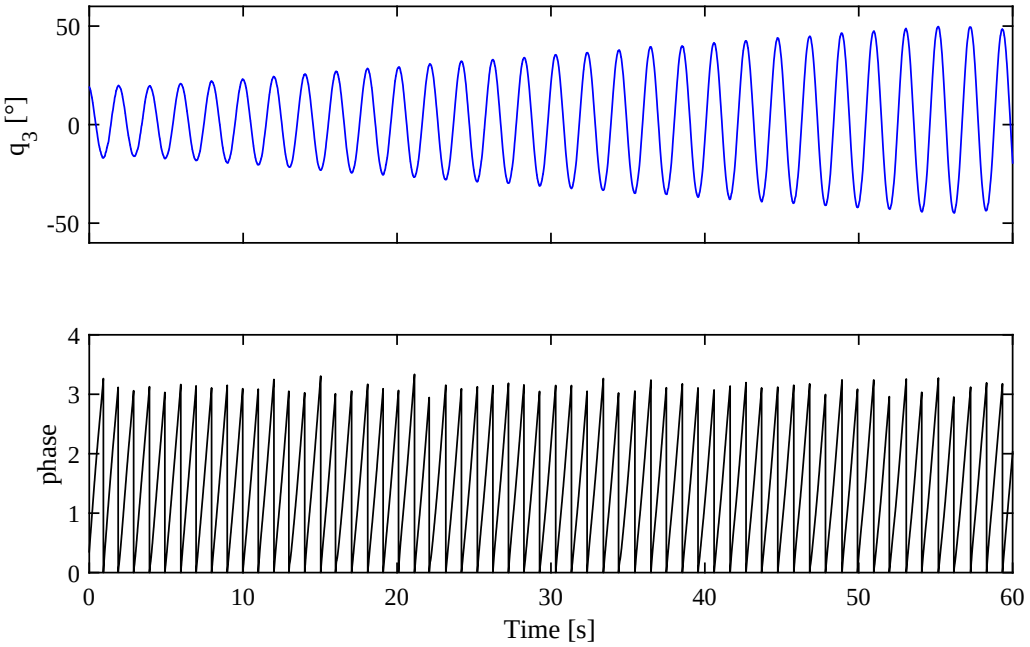

Figure 7.7: Oscillation q_3 of the pendulum and phase φ estimated in real-time with the Adaptive Frequency Oscillators.

fraction of $P_e(t_k)$ at each semi-oscillation. The corrected phase φ is obtained by summing $\varphi_e(t)$ to the original AFO phase $\tilde{\varphi}_1(t)$ and by applying a modulo operation to bound the estimated phase between 0 and π:

$$\varphi = \text{mod}(\tilde{\varphi}_1 + \varphi_e, \pi) \tag{7.15}$$

An example of the oscillation q_3 of the pendulum (with increasing energy) and of the phase φ estimated in real-time with the Adaptive Frequency Oscillators is reported in Figure 7.7.

7.3.2 Pendulum length planner

The dynamics of the variable-length pendulum are described by (7.9a) and (7.9b), in which the input force is applied by the two motors acting on the cables. In this work, it has been considered that $d_2 = 0$, therefore the model is a pure parametric oscillator capable of pumping and subtracting energy by appropriately modulating the length of the pendulum-robot [176, 146]. To pump energy into the system, the end-effector is lifted as it passes through the lowest point of the oscillation ($q_3 = 0$), whereas it is lowered as the bob reaches the highest point ($\dot{q_3} = 0$). The opposite method is applied to subtract energy from the pendulum. The theoretical time-optimal trajectory for the length $l(t)$ is a square-wave whose frequency is twice that of the pendulum [180]. A representation of this ideal trajectory for pumping and subtracting energy is reported in Fig. 7.8.

In a real pendulum, the cable length cannot be varied instantaneously. Therefore, a

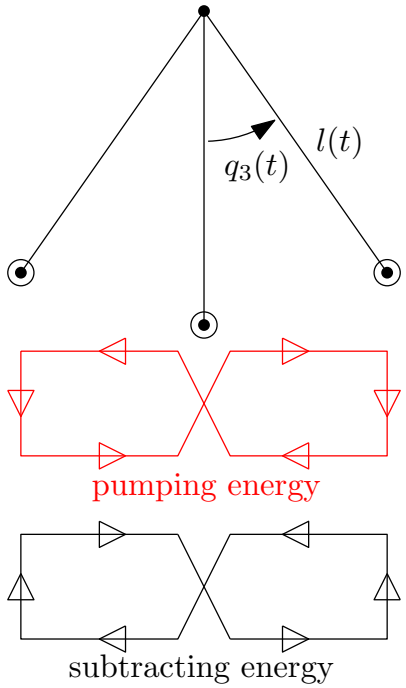

Figure 7.8: Theoretical trajectories of the pendulum length to pump and subtract energy.

sinusoidal law is chosen for the cable length planner instead of a square wave:

$$l_d(\varphi) = A \sin(2\varphi) \tag{7.16}$$

In (7.16), $l_d(\varphi)$ is the desired length of the pendulum, $\varphi \in [0; \pi)$ is the phase and A is a constant parameter controlling the rate of change of the pendulum amplitude during energy pumping ($A < 0$) or subtracting ($A > 0$). To control *both* the amplitude of the oscillation *and* the length of the pendulum, (7.16) is modified as follows:

$$l_d(\varphi) = \left[l_i + \frac{(l_f - l_i)\varphi}{\pi} \right] + A \sin(2\varphi) \tag{7.17}$$

Thus, the desired trajectory is composed of a linear term, driving the system from the length at the beginning of the current semi-oscillation l_i to the final length for the current semi-oscillation l_f, and a periodic term designed to increase or decrease the energy of the system. The periodic term is the truncated Fourier series expansion of an odd periodic function with zero mean value. The desired trajectory satisfies the boundary constraints on the position: $l(0) = l_i$ and $l(\pi) = l_f$.

The free parameter A, which is constant within each semi-oscillation, must be optimized at every semi-oscillation to bring the pendulum as close as possible to the desired amplitude q_{3f}, as detailed in the following subsection.

The length l_i and the velocity $\dot{l}_i$ are derived from the encoder readings (7.2), whereas

l_f and $\dot{l}_f$ are chosen as follows

$$l_f = l_i + \Delta l, \qquad \Delta l = \begin{cases} (l_G - l_i) \quad if \quad |l_G - l_i| < \Delta l_{max} \\ \text{sgn}(l_G - l_i)\Delta l_{max} \quad otherwise \end{cases} \tag{7.18}$$

$$\dot{l}_f = \begin{cases} 0 \quad if \quad (|l_G - l_i| < \Delta l_{max}) \wedge (q_{3P} = q_{3G}) \\ 2\dot{\varphi}A \quad otherwise \end{cases} \tag{7.19}$$

where Δl_{max} is the maximum variation of the length within a semi-oscillation, which is a constant parameter that depends on the maximum performance of the system (see Tab. 7.1). q_{3P} is the estimate of $q_3(\pi)$, i.e., the oscillation amplitude at the end of the current semi-oscillation. This value is predicted on-line using numerical integration, as described in the next subsection. If the system reaches the goal amplitude at the end of the current semi-period, $\dot{l}_f$ is set to zero for a soft landing, otherwise, the value $2\dot{\varphi}A$ is imposed to obtain a smoother trajectory.

7.3.3 Optimization

The free parameter A is optimized at every semi-oscillation in order to drive the angle from its current value q_3 to the desired one q_{3f} at the end of the current semi-oscillation. This optimization is aimed at minimizing the error function $|q_{3f} - q_{3P}|$.

Two alternative approaches are proposed to choose the value of q_{3f} for the current semi-oscillation:

1. The first one is based on the maximum variation of the amplitude Δq_{3max} within the semi-oscillation and, similarly to $\Delta l_{\max}$, is related to the maximum performance of the system (see Tab. 7.1). By following this approach, the amplitude of the oscillation is modified (increased or decreased) using the following law

$$\begin{aligned} q_{3f} &= -q_{3f,prev} + \Delta q_3, \\ \Delta q_3 &= \begin{cases} (q_{3G} - q_3) \quad if \quad |q_{3G} - q_3| < \Delta q_{3max} \\ \text{sgn}(q_{3G} - q_3)\Delta q_{3max} \quad otherwise \end{cases} \end{aligned} \tag{7.20}$$

   where $q_{3f,prev}$ is the value of q_{3f} at the previous semi-oscillation.

2. The second approach, firstly proposed in [146], is based on the specific energy e of the pendulum sub-system:

$$e = \frac{1}{2}\left(\dot{l}^2 + l^2\dot{q}_3^{\,2}\right) - gl\cos q_3 \tag{7.21}$$

   The variation of the specific energy is imposed to be proportional to the variation of the pendulum length, which leads to the following expression for the desired

amplitude [146]

$$|q_{3f}| = \arccos\left[c_0\frac{\dot{l}_f}{l_f} + c_1 + \frac{c_2}{l_f}\right] \tag{7.22}$$

where c_0, c_1 and c_2 are constant parameters that depend on l_i, $\dot{l}_i$ and on the overall variations of energy $\Delta e = e_G - e_S$ and length of the pendulum $\Delta L = l_G - l_S$:

$$c_0 = \frac{1}{2g}, \quad c_1 = -\frac{\Delta e}{g\Delta L}, \quad c_2 = -\frac{\dot{l}_i}{2g} + \frac{\Delta e l_i}{g\Delta L} + l_i \cos q_{3S} \tag{7.23}$$

A suitable value for A can be estimated on-line using numerical optimization. For this purpose, the bisection method was selected because it inherently accounts for constraints in the optimization variable, it does not require explicit knowledge of the function to be optimized and has relatively low computational cost. First, (7.9b) is rewritten in terms of phase φ by using the variable transformation $\varphi = \omega t$. Then, at each iteration of the bisection method, numerical integration is performed with the Runge-Kutta method, using the states at the beginning of the current semi-oscillation (i.e., $\varphi = 0$) as initial conditions, and imposing the stopping condition $\varphi = \pi$. A diagram of the real-time optimization is reported in Fig. 7.9.

The number of integration steps is limited to $N = 20$ ($\Delta\varphi = \pi/N$), which yields a good trade-off between accuracy and computational time. The cost function is defined as the deviation $err = q_{3f} - q_{3P}$. The maximum number of iterations for the bisection method is limited to $M = 50$ and the estimates of A are continuously fed to the planner (7.17) after the 4-th bisection operation, in order to smoothly change the parameter A between one semi-oscillation and the next one.

7.3.4 End-effector orientation planner

A minimum-jerk trajectory is designed for the orientation of the end-effector $\theta_d(t)$

$$\theta_d(t) = a_5 t^5 + a_4 t^4 + a_3 t^3 + a_2 t^2 + a_1 t + a_0 \tag{7.24}$$

where the coefficients of the fifth-order polynomial assume the following values

$$\begin{aligned} &a_0 = \theta_S, \quad a_1 = 0, \quad a_2 = 0, \\ &a_3 = \frac{6(\theta_G - \theta_S)}{t_{\theta,max}^5}, \quad a_4 = \frac{15(\theta_S - \theta_G)}{t_{\theta,max}^4}, \quad a_5 = \frac{10(\theta_G - \theta_S)}{t_{\theta,max}^3} \end{aligned} \tag{7.25}$$

and they are chosen to satisfy the boundary conditions on the orientation at the beginning and at the end of each trajectory: $\dot{\theta}_S = 0$, $\ddot{\theta}_S = 0$, $\dot{\theta}_G = 0$, $\ddot{\theta}_G = 0$. The maximum time $t_{\theta,max}$ was manually tuned in order to respect the physical limitations of the prototype (see Tab. 7.1).

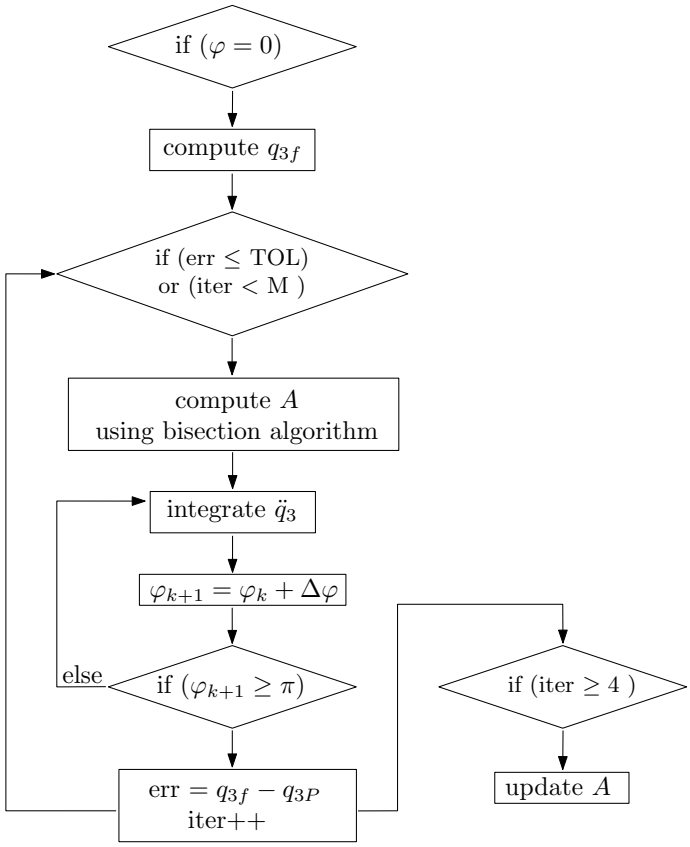

Figure 7.9: Real-time optimization of A.

7.3.5 Controller architecture

The architecture of the control system is illustrated in Fig. 7.10. The trajectory planning relies on the phase of the oscillation, which is estimated by the AFO and corrected based on the measured q_3. The corrected phase φ is fed into the planner, where the desired length l_d and orientation θ_d (and their time derivatives) are computed. The following control laws (linear PD block) are implemented to track the desired trajectory

$$\begin{cases} v_1 = \ddot{l_d} - k_{l1}\dot{e}_l - k_{l0}e_l \\ v_2 = \ddot{\theta_d} - k_{\theta 1}\dot{e}_\theta - k_{\theta 0}e_\theta \end{cases} \tag{7.26}$$

where $e_l(t) = l(t) - l_d(t)$, $e_\theta(t) = \theta(t) - \theta_d(t)$ and the coefficients k_{*1} and k_{*0} are defined such that the corresponding Hurwitz polynomials have both the roots in the stable half plane.

The input-space transformation (7.8) is then applied to compute τ_1 and τ_2, from which the corresponding cable tensions T_{1fl} and T_{2fl} are derived using (7.7). Since in a real prototype unmodeled dynamics, noise and disturbances may draw the robotic system away from its ideal behavior, the contributes of a simple PID controller (PID_L block) are added

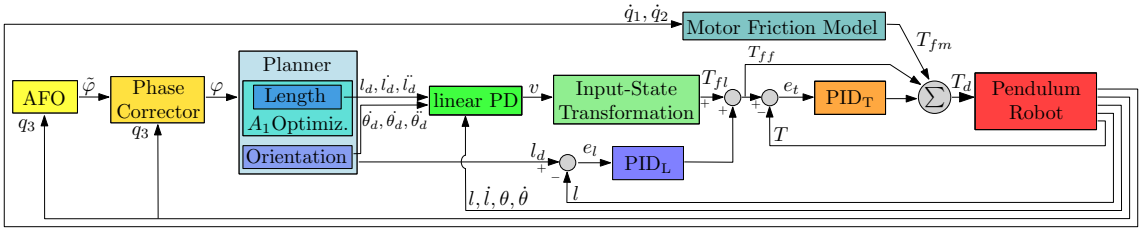

Figure 7.10: Architecture of the control system.

to the ideal cable tensions T_{1fl} and T_{2fl}. For example, the tension for cable 1 is

$$T_{1ff} = T_{1fl} + k_{l,P} e_l + k_{l,I} \int_{\hat{t}}^{t} e_l dt + k_{l,D} \dot{e}_l \tag{7.27}$$

where $\hat{t}$ is the time instant when the current trajectory started. The gains of the length PID controller have been manually tuned and set to the following values: $k_{l,P} = 291.0$, $k_{l,I} = 0.08$, $k_{l,D} = 0.08$.

The desired lengths l_{1d} and l_{2d} are computed using (7.2) and (7.3):

$$\begin{aligned} l_{1d} &= l_d - r\theta_d \\ l_{2d} &= l_d + r\theta_d \end{aligned} \tag{7.28}$$

Furthermore, a low-level PID controller for the cable tensions (PID$_T$ block) is implemented to reduce disturbances. As a result, the commanded tension for cable 1, which is fed to the motor driver, takes the following form

$$T_{1d} = T_{1ff} + T_{1fm} + k_{t,P} e_t + k_{t,I} \int_{\hat{t}}^{t} e_t dt + k_{t,D} \dot{e}_t \tag{7.29}$$

where T_{1fm} is the contribution given by the motor friction model and T_{1ff} is the contribution (7.27). A similar control law is implemented for cable 2. The gains for the tension PID control system have been manually tuned in order to ensure a good overlap between the desired signal and the values measured from the load cells (Section 7.4). The following values have been adopted: $k_{t,P} = 0.70$, $k_{t,I} = 0.04$ and $k_{t,D} = 0.00$.

7.4 Experimental prototype

An experimental prototype of the 3-DOF pendulum-like manipulator has been developed at the Wearable Robotic System (WRS) Laboratory, Department of Mechanical Engineering, Stevens Institute of Technology (Hoboken, NJ, USA). In the following of this section, the mechanical and the electronic hardware are described.

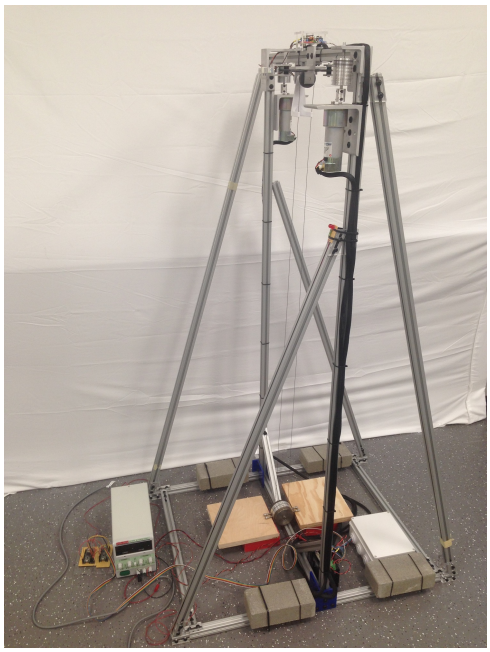

(a)

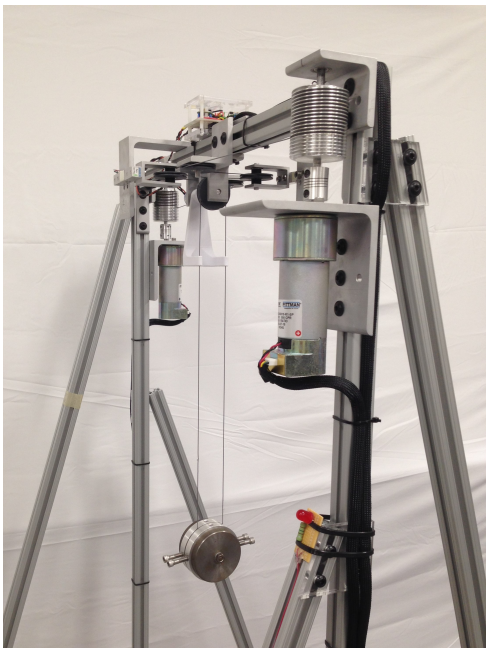

(b)

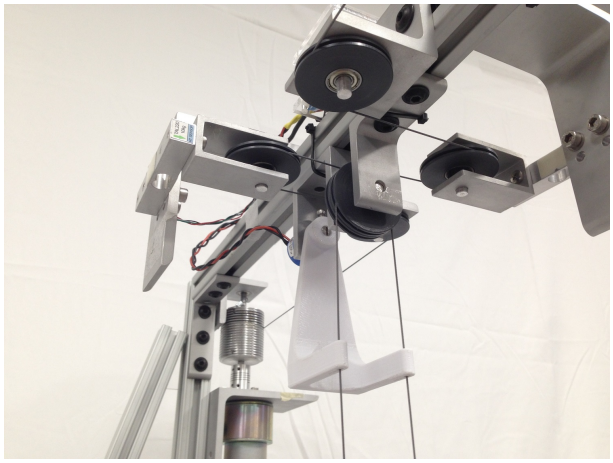

(c)

Figure 7.11: Prototype of pendulum-like cable-driven robot developed in the WRS Laboratory at Stevens Institute of Technology (a) and (b); close-up on the custom pulley system and 3D-printed follower (b).

7.4.1 Mechanical hardware

The experimental setup is shown in Fig. 7.11. It is composed of an aluminum frame on which the two actuators are mounted. The motors are brushed 24 V Pittman gear-motors, model GM9236S0 15-R1-SP. Each motor is powered by an Advanced Motion Control 12A8-QDI analog driver and can retract or release the cable by means of a custom spool. Figures 7.12 and 7.13 report an image of a motor connected to a custom spool and of the drivers, respectively. The analog drivers have been manually calibrated in order to

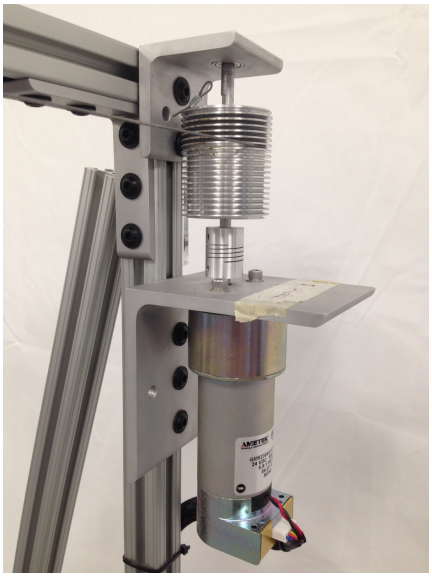

Figure 7.12: Brushed DC gear-motor (Pittman GM9236S0 15-R1-SP) and custom spool.

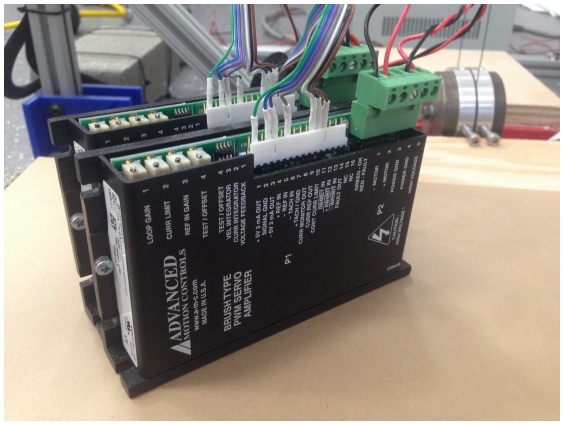

Figure 7.13: AMC-12A8 analog drivers.

limit the maximum output current and to employ the whole voltage range provided by the DAC ($\pm 10\ V$) that converts the digital signal of the micro-controller in an analogue one from the driver (Subsection 7.4.2). Furthermore, in the early stage of development of the prototype, the motor friction has been characterized, in order to obtain the relationship between current I and angular speed ω, that is used as feed-forward contribution in the control system (Figure 7.10).

Motor encoders are used to measure cable lengths, while the oscillations of the pendulum-robot are tracked by means of a custom-designed PTA 3D printed follower connected to a rotary potentiometer (Bourns), shown in Fig. 7.11(b). Prior to start the tests, its range has been characterized by connecting an encoder to its shaft in order to derive the relationship between Volt and radiants.

The end-effector of the pendulum-like robot consists of a custom pulley mounted between four metal disks that ensure the balancing of the bob; two screws on each side

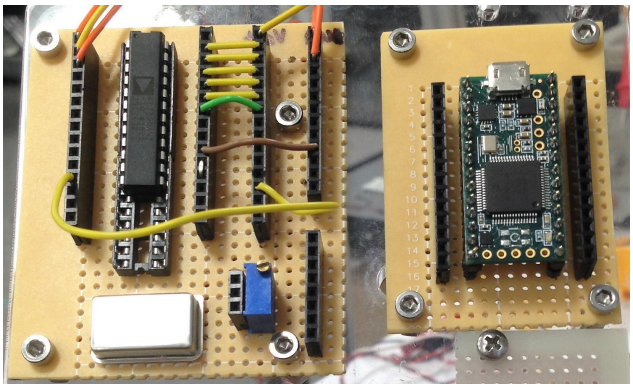

(a) Circuit for the 12-bit ADC (right), Teensy 3.2 (left).

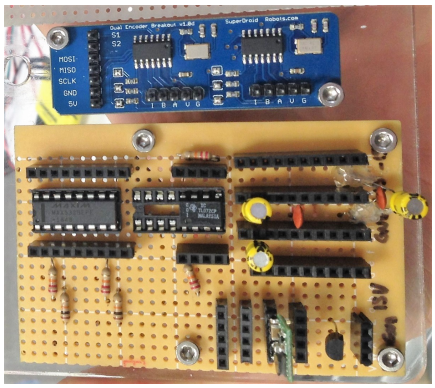

(b) Dual Encoder Breakout board (top), circuit for the 12-bit DAC (bottom).

Figure 7.14: Electronic boards for data acquisition and control.

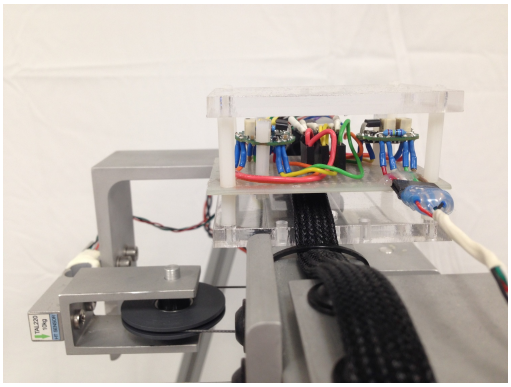

(a)

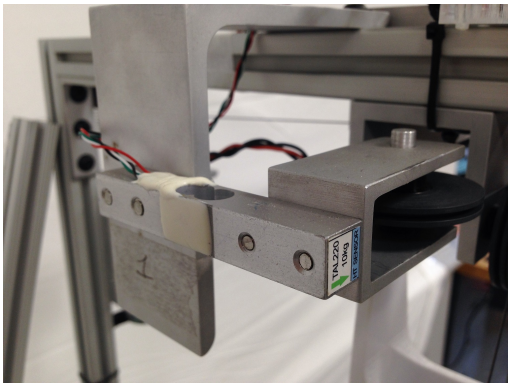

(b)

Figure 7.15: Load cell amplifiers (a), close-up on one load cell TAL220 (b).

are used to indicate the orientation. A system of idle pulleys, shown in Fig. 7.11(c), was designed to route the cables from the spools to the end-effector, following the kinematic diagram in Fig. 7.4 and to allow the measurement of cable tensions by means of two cantilever-type load cells (TAL220). The load cells have been adequately calibrated with known weights in the set-up phase of the work. The cable adopted in the experimental prototype is a 0.032" diameter stainless steel wire with a nylon coating.

7.4.2 Electronic hardware

The control architecture of the pendulum-robot was designed to ensure reliable performance at relatively low cost. Data acquisition was implemented on a Teensy 3.2 micro-controller, equipped with a 32 bit, 72 MHz ARM Cortex-M4 microprocessor. An image of the micro-controller is reported in Fig. 7.14(a).

The signal acquired from the load cells is amplified with a custom board (Fig. 7.15) and, together with the signal of the potentiometer, sampled at 5 kHz using a multichannel

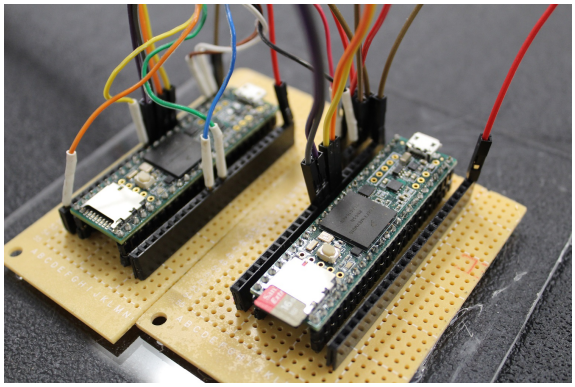

Figure 7.16: Teensy 3.5 (left) and Teensy 3.6 with microSD card (right).

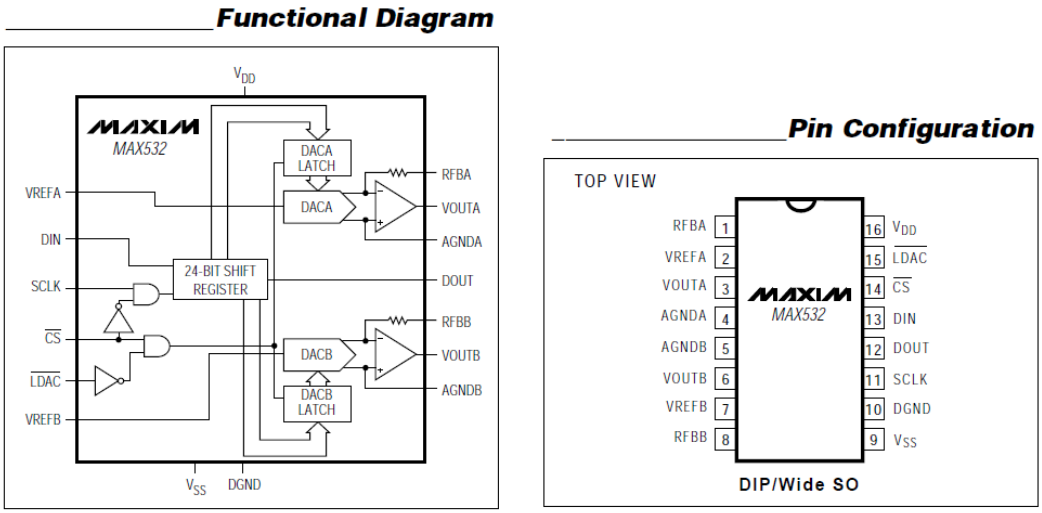

Figure 7.17: 12-bit DAC (MAX532) functional diagram and pin configuration.

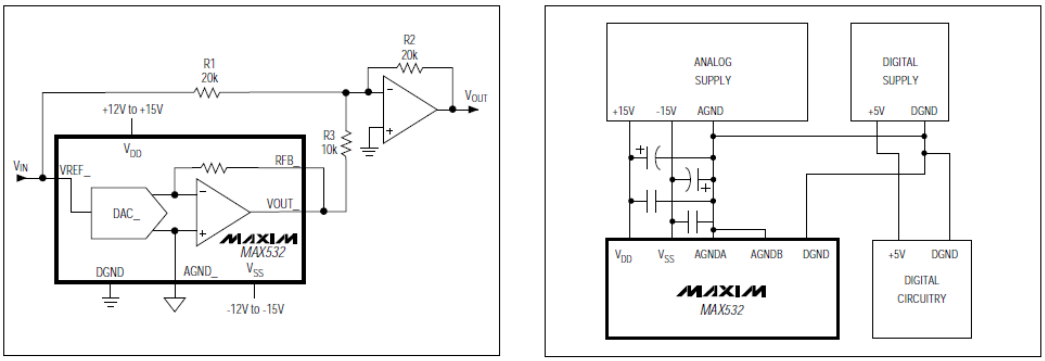

Figure 7.18: DAC MAX532 bipolar operation configuration and power supply grounding.

12-bit ADC, model AD7890. The signal from the encoders is acquired in SPI by means of a Dual Encoder Breakout board (Fig. 7.14(b)) at 2 kHz. Then, the signal from load cells and potentiometer is low-pass filtered with a Butterworth, 2nd order, 12 Hz passband filter, in Teensy 3.2, and sent to the main controller, along with encoders data, at a rate of 1

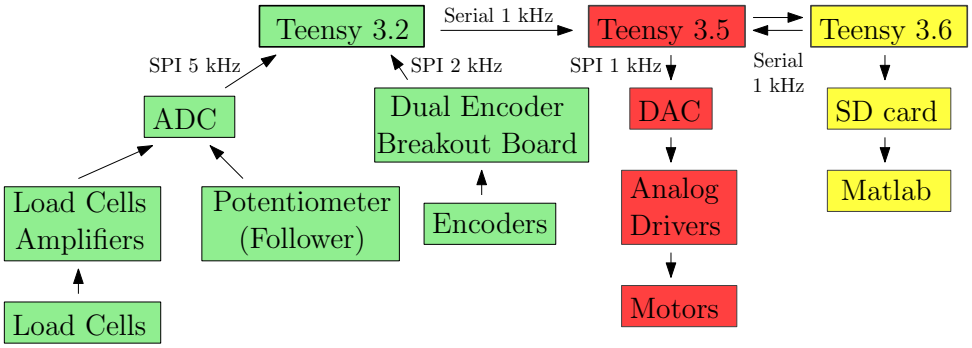

Figure 7.19: Overview on the electronic hardware and connections: data acquisition (green), dynamic model and control system (red), data logging (yellow).

kHz. The custom circuit that has been designed, built and tested for the ADC is reported in Fig. 7.14(a).

The dynamic model and the control system have been implemented on a Teensy 3.5 micro-controller (32 bit, 120 MHz ARM Cortex-M4), which runs both the high and the low-level algorithms described in Section 7.3 and directly controls the motor drivers by means of a 12-bit DAC (MAX 532). The frequency of the control loop is 1 kHz. A custom board has been designed and developed for the DAC MAX532. An image of the board is reported in Fig. 7.14(b), whereas the functional diagram and pin configuration of the chip are shown in Fig. 7.17. The DAC has been integrated in the circuit in bipolar operation configuration (Fig. 7.18), using a 2-channels operational amplifier TL072CP. A DC/DC converter CUI INC, series PYB30 has been adopted for the 5V digital power supply.

An auxiliary Teensy 3.6 micro-controller (32 bit, 180 MHz ARM Cortex-M4) logs all data to a microSD card at 1 kHz for the post-processing in Matlab. Furthermore, to better handle the computational power of the micro-controllers, the optimization of parameter A is also run on the Teensy 3.6 and the optimized data is sent back to the main controller at 1 kHz. Figure 7.16 reports an image of Teensy 3.5 and Teensy 3.6.

In Figure 7.19, an overview on the electronic hardware connections and signals is reported: data acquisition is represented in green, the controller in red and the data logging in yellow. For the software implementation the open-source Arduino IDE has been adopted, on a laptop running Windows 10 64 bit with an Intel® Core™ i5 CPU M480 @2.67 GHz and 4.00 GB installed RAM.

7.5 Experimental results

In this section, the experimental validation of the under-actuated, pendulum-like, cable-driven robot is presented. Firstly, a preliminary amplitude controller is proposed, then experimental tests on the point-to-point motion are illustrated. The nominal parameters of the prototype, including geometrical characteristics, robot limits and tolerances for the point-to-point motion, are reported in Tab. 7.1.

Table 7.1: Parameters of the experimental prototype.

Geometrical Parameters		Prototype Limits		Tolerances	
L_0	$1.420\ m$	ΔL_{max}	$0.020\ m$	L	$0.005\ m$
r	$0.019\ m$	Δq_{3max}	$0.60°$	q_3	$2.00°$
m_{EE}	$1.037\ Kg$	$t_{\theta,max}$	$5.00\ s$	θ	$4.00°$
J_{EE}	$6.410 \cdot 10^{-4}\ Kg/m^2$	θ_{max}	$\pm 90°$		
d_2	$0.000\ m$	T_{max}	$15.00\ N$		
l_3	$0.000\ m$				

7.5.1 Amplitude control

Figure 7.20 reports the coordinate q_3 and the specific energy in the case of free oscillation of the pendulum-robot, with the motors blocked and, therefore, a constant length of the pendulum. Figure 7.21 shows an energy pumping/subtracting test, performed using the planner described in (7.16). In this case, A is constant and its sign determines whether energy is added to or subtracted from the pendulum. In the test of Fig. 7.21 the constant value of A is equal to 0.125. The same test is reported in Fig. 7.22, with $A = 0.250$. It can be sees that, by increasing the parameter A, the time needed to pump and subtract energy decreases.

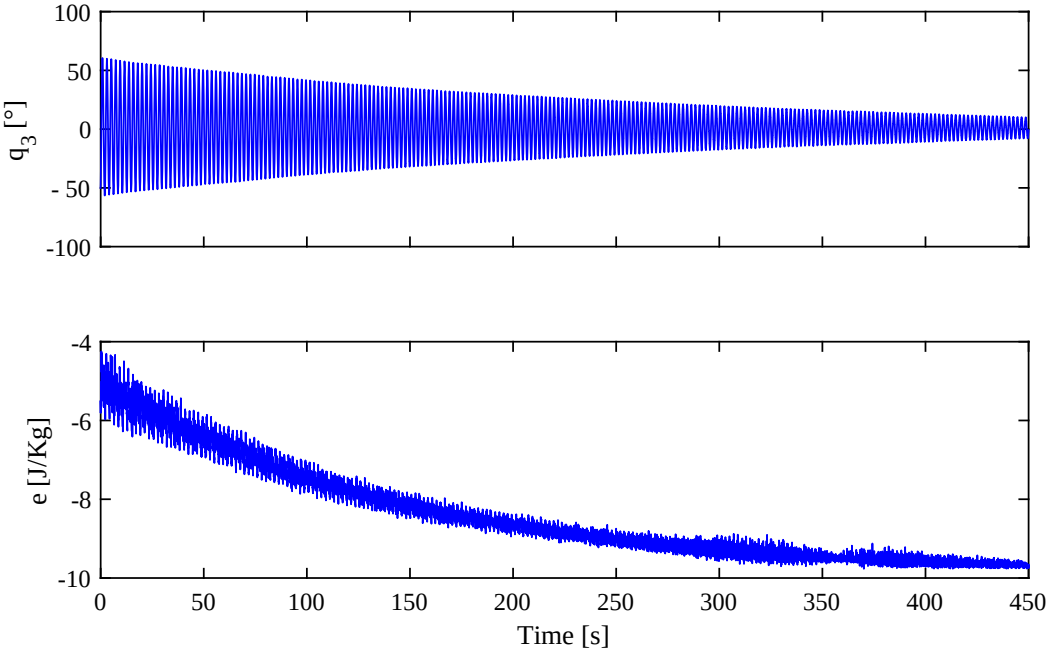

Figure 7.20: Free oscillation of the pendulum-robot.

With respect to Fig. 7.20, it can be appreciated that in both tests of Figures 7.21 and 7.22, the rate of decreasing amplitude is higher than in the free-oscillation case.

An amplitude control test was also conducted in which the parameter A in (7.16) was optimized at each semi-oscillation to linearly increase (or decrease) the oscillation angle q_3 of the pendulum-robot, as shown in Fig. 7.23.

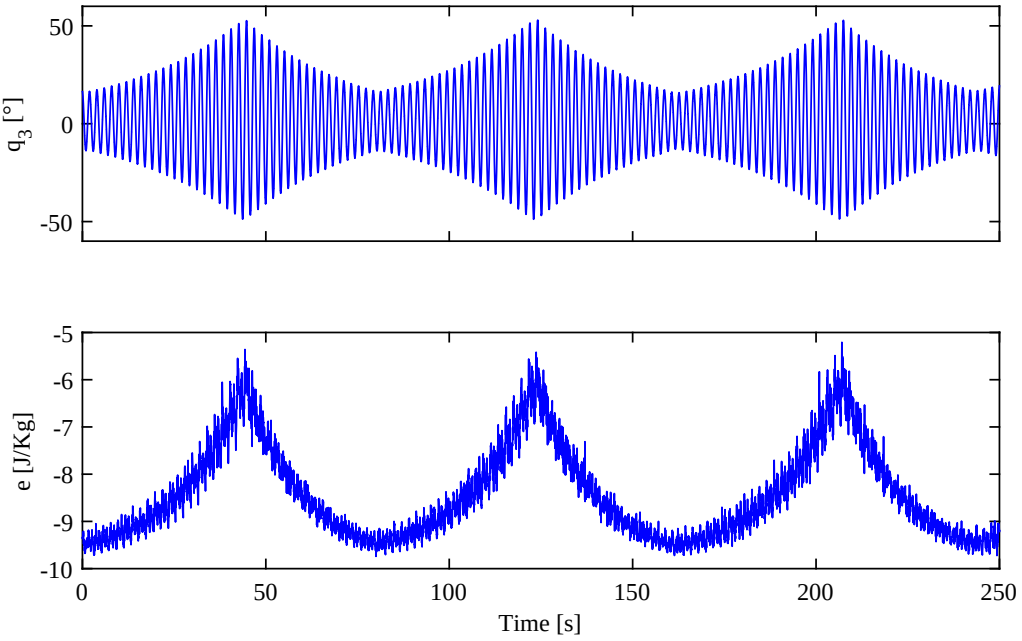

Figure 7.21: Pumping and subtracting energy with $A = 0.125$.

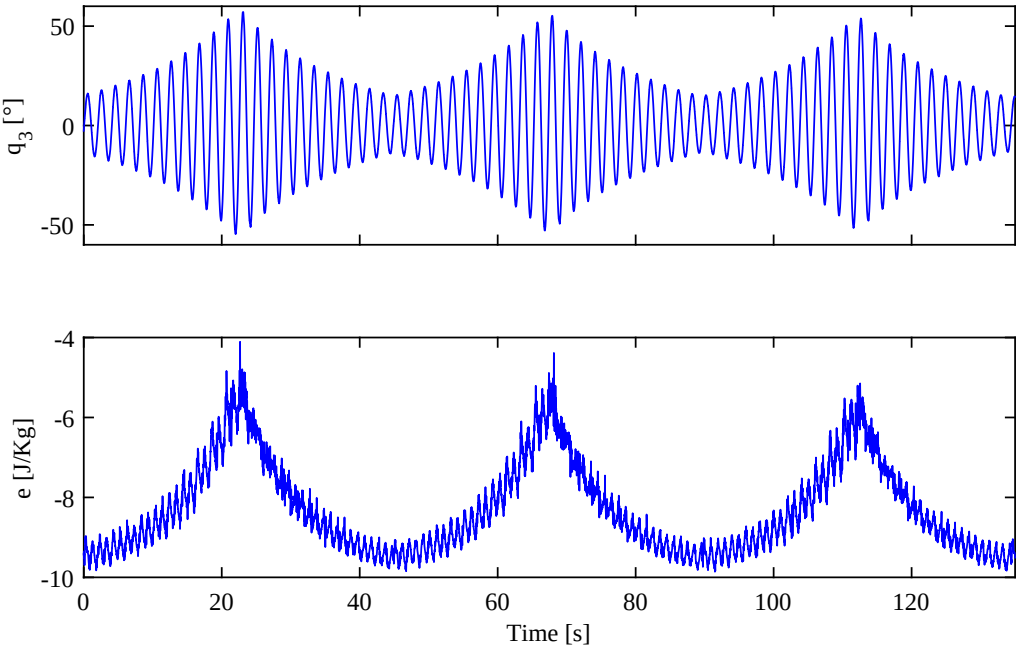

Figure 7.22: Pumping and subtracting energy with $A = 0.250$.

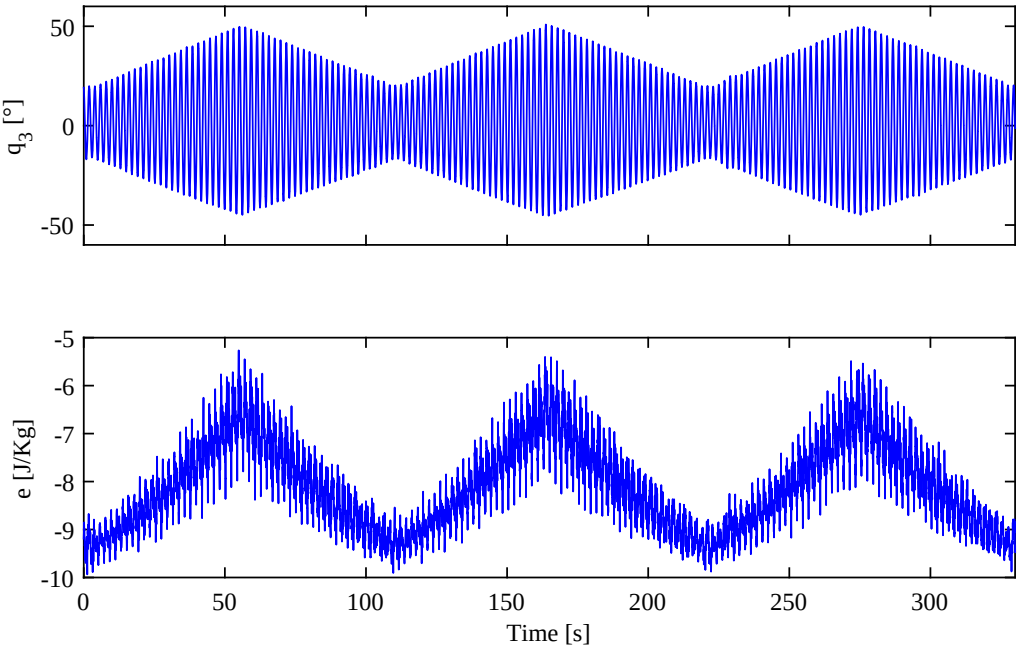

Figure 7.23: Linear amplitude control with A optimized at each semi-oscillation.

7.5.2 Point-to-point motion

In order to evaluate the performances of the point-to-point trajectory planning and of the control system, a sequence of target Cartesian poses $[x, y, \theta]^T$ for the end-effector was tested. This sequence, reported in Table 7.2, was chosen to include variations in length, amplitude and orientation.

Table 7.2: Sequence of target points $[l_G, q_{3G}, \theta_G]^T$.

Position variable	Unit	1	2	3	4	5
l_G	$[m]$	1.00	0.50	0.50	1.00	1.00
q_{3G}	$[^\circ]$	20	20	47	34	20
θ_G	$[^\circ]$	0	40	17	-11	0

Figure 7.24 illustrates an example of point-to-point motion using the linear approach for increasing and decreasing the amplitude q_3 described in (B.7). The four plots represent the length, amplitude, orientation and specific energy of the pendulum-robot over time. In the graph of q_3 the green segments are the predicted values q_{3P}. It can be noticed that both the measured length and the oscillation angle track the desired values very well. The differences between the desired and predicted values of q_3 are due to the tolerance set for the numerical optimization, whereas the differences between measured and predicted q_3 are due to modeling errors (e.g., friction, aerodynamics effects, noise, and vibrations).

Figure 7.25 shows another point-to-point motion test during which the end-effector is driven through the same sequence of via-points, this time using the energy approach (B.9) to determine the desired amplitude of the current semi-oscillation. As it can be seen, when

the length of the pendulum is increased or decreased, the angle q_3 is modulated to force the variation of specific energy to be proportional to the variation of the length. As in the previous case, the system tracks the desired length and oscillation angle very well.

In both tests, however, the tracking performance for the orientation θ were less desirable. This was probably due to the friction forces generated by the cable wrapping and unwrapping around the end-effector pulley, and to unmodeled off-plane oscillations originating from small vibrations in the robot frame.

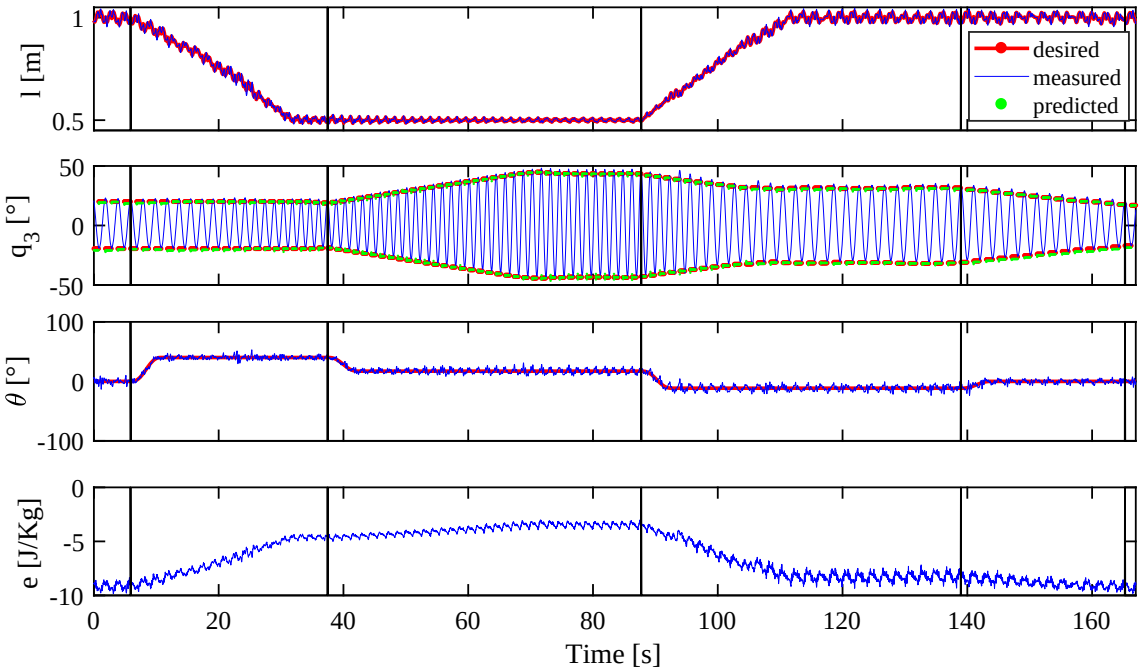

Figure 7.24: Position variables (length l, amplitude q_3, orientation of the end-effector θ) and specific energy e for a point-to-point motion test with linear variations of q_3. Vertical solid lines indicate target achievements.

7.6 Conclusions

In this chapter, a novel design of a 3-DOF under-actuated, pendulum-like, cable driven robot was presented and experimentally validated. The end-effector of the mechanism is capable of performing point-to-point motions in the dynamic workspace of the robot, from a starting pose to a goal one, reached with zero angular and linear speed, using two actuated joints only. Feedback linearization allows to decouple the dynamics of the variable-length pendulum from the dynamics of the rotation of the end-effector. The device leverages parametric excitation to control the oscillation of the variable-length pendulum, similar to a playground swing.

With respect to previous works published in the Literature, in this chapter a novel design of pendulum-like robot was described and a pool of Adaptive Frequency Oscillators was introduced, to obtain lag-free, smooth estimations of the current phase of the oscillation in real-time. These smooth estimates allow the on-line trajectory planner to integrate the

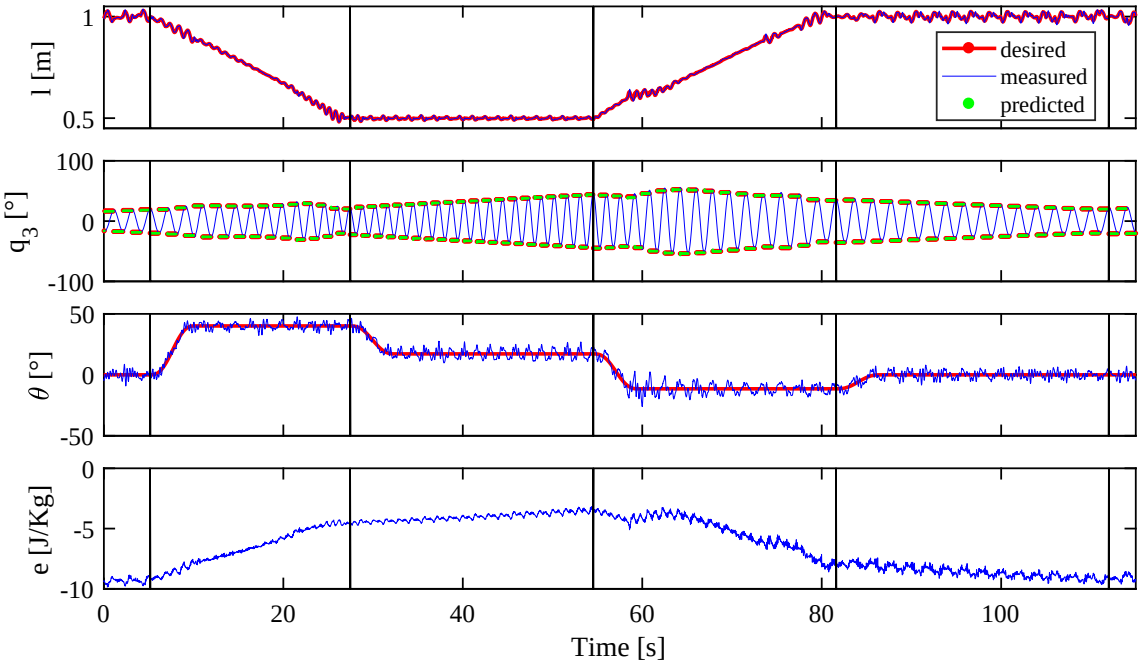

Figure 7.25: Position variables (length l, amplitude q_3, orientation of the end-effector θ) and specific energy e for a point-to-point motion test with energy method variation for q_3. Vertical solid lines indicate target achievements.

equation of motion of the variable-length pendulum directly in the phase domain, without the discontinuities that would result from using other techniques that are based on event detection [145, 146]. The proposed control approach is not computationally demanding and therefore can be implemented on micro-controllers. Furthermore, this approach is based on the real-time optimization of only one parameter during each semi-oscillation. The optimization is not approximated and it is not based on heuristic relationships based on previous experimental data [147].

The ability of the pendulum-robot to modulate the amplitude of the oscillations using parametric self-excitation was experimentally validated with good results. Further, two alternative criteria to select the target oscillation amplitude at each semi-oscillation during arbitrary point-to-point motions were presented and experimentally tested, yielding satisfactory performance.

The tracking performance were less desirable for the pendulum orientation than they were for its length and oscillation angle. To reduce off-plane oscillations that might have contributed to this effect, a future version of the end-effector will feature an on-board spinning mass, which will stabilize the oscillation plane using the gyroscopic effect.

Future work will also include extending the proposed controller to the case of non-balanced end-effector (that is, $d_2 \neq 0$). In this case, the end-effector of the current prototype will be equipped with a non-centered additional mass that could be used to excite the system with a driving term, in a way similar to children moving their legs on a playground swing [175, 176]. A systematic comparison between the effectiveness of the driving and parametric terms (and combination thereof) will then be conducted.

Chapter 8

Conclusions

The research activity presented in this Ph.D. thesis has been focused on the kinematic and dynamic modeling, simulation and control of flexible-link robotic systems. Flexible multibody dynamics is an open field of investigation in both industry and academia, since the industrial demand of high performance operation with high speed and precision has highlighted the need to study and develop lightweight manipulators, in which the effects of elasticity arise. Therefore, while modeling and control this particular class of robotic systems, the dynamics effects of structural flexibility has to be taken into account.

In Chapter 1, an overview on flexible multibody dynamics has been presented. In particular, a formulation based on an Equivalent Rigid-Link System has been recalled and described in its evolution through the last two decades [1]. The ERLS concept, firstly proposed in combination with a Finite Element Method approach, allows the kinematic equations of motion of the equivalent rigid-link system to be decoupled from the compatibility equations of the displacements at the joints.

Chapter 2 recalled a recent formulation of the ERLS concept through a modal approach, in particular a Component Mode Synthesis technique [12]. This novel approach allows to obtain a more flexible solution based upon a reduced-order system of equations. The kinematic equations have been recalled and the equation of motion derived for a generic flexible-link mechanism.

In Chapter 3, a comparison between the ERLS-FEM and the ERLS-CMS approaches have been presented and described. A L-shaped benchmark mechanism has been implemented in Matlab and numerically simulated through different input conditions: gravitational force and a torque input. Results have been compared in terms of accuracy in the time and frequency domains, and by means of the computational time required by the simulations. Using the modal approach (ERLS-CMS) an important reduction of computational time has been highlighted, while maintaining a good accuracy in simulating both the fine and gross motion of the benchmark system [2].

In the CMS approach, a classical Craig-Bampton reduction technique has been initially employed. However, this is not the only Model Order Reduction strategy capable of selecting the vibrational modes to be retained to keep the model dimension at a minimum while preserving the accuracy of the system response. For this reason, in Chapter 4,

different Model Order Reduction techniques (i.e. Craig-Bampton, Interior Mode Ranking (IMR), Guyan, Least Square Model Reduction (LSMR) and Mode Displacement Method (MDM)) have been applied, in combination with the ERLS modal approach, to a benchmark mechanism under different input conditions. The accuracy of each reduced model has been numerically evaluated through the comparison of computational time, the behavior in frequency domain and by means of vector correlation methods, i.e. the Modal Assurance Criterion (MAC), the Cross-Orthogonality (CO) and the Normalized Cross-Orthogonality (NCO) [3].

In the second part of my Ph.D. thesis, I have studied cable-driven robots, which are a special class of flexible-link manipulators, in which flexible cables, rather than rigid links, are used to drive the end-effector.

Advantages of this class of manipulators are the possibility of operating in large workspaces, their reconfigurability and modularity. With respect to manipulators composed of rigid links, cable-driven robotic systems can be easily transported, present a higher payload-to-weight ratio and their end-effector can usually achieve higher velocities and accelerations. Disadvantages include redundancy (as cables can be used in tension but not in compression) and the interference between the cables and the surrounding environment.

Cable-driven robots have been adopted to several different tasks, including loading and large-scale manipulation, construction systems, pick-and-place, building tasks as well in rehabilitation and surgery.

In Chapter 5, an introduction about cable-robots has been presented. In Chapters 6 and 7, a special class of cable-robots has been analyzed: cable-suspended parallel robots. These manipulators are typical examples of under-constrained systems, which rely on gravitational force to determine the resulting pose of the end-effector.

In Chapter 6, a novel design of a 2-DOF cable-suspended parallel robot based on variable radius drums has been presented. This kind of manipulator can be used as an overhead traveling crane and, therefore, it has been called Cable-Based Robotic Crane. A variable radius drum is a device characterized by the variation of the spool radius along its profile, allowing highly flexible input-output relationship with respect to more conventional mechanisms. In particular, the device that has been proposed allows to move the end-effector through a planar working area, with just two actuated joints. The kinematic analysis and the synthesis of the profile of the variable radius drum has been presented. Then, the design of an horizontal moving cable-mechanism, which constitutes a module of the CBRC, has been described and analyzed.

A working prototype of a three-dimensional cable-based overhead traveling crane has been developed at the Robotics Laboratory, Department of Engineering and Architecture, University of Trieste (Italy). The experimental device has been validated, demonstrating the feasibility of the proposed approach in moving the end-effector through a planar surface with high accuracy. Furthermore, the cable tensions have been analyzed and compared with the ones predicted by the theoretical model [4].

Chapter 7 dealt with another class of cable-suspended robots: pendulum-like manipulators. These mechanisms rely on gravity to maintain the cables taut and, due to their

specific design, constantly operate outside their static workspace. They are composed of a cable-suspended robotic arm, whose oscillation can be modulated by actively controlling the lengths of the cables or the orientation of the robotic arm. A novel design of a 3-DOF pendulum-like, cable-driven robot has been presented and experimentally validated. The robot can steer the end-effector through a point-to-point motion from a start pose to a goal one, to be reached with zero angular and linear speed. The device is based on parametric excitation and it relies on two actuated degrees of freedom only. The control system is based on a feedback linearization that allows to decouple the dynamics of the variable-length pendulum, to the dynamics of the rotation of the end-effector. Adaptive Frequency Oscillators have been introduced to estimate the phase of the pendulum in real-time and without delay. A prototype of the pendulum-robot has been fabricated at the Wearable Robotic System (WRS) Laboratory, Department of Mechanical Engineering, Stevens Institute of Technology (Hoboken, NJ, USA). The prototype and the control system have been designed to ensure reliable performance using open-source software and relatively low-cost hardware. The experimental device has been validated, showing the feasibility of the proposed approach for steering the robot through a point-to-point motion in its dynamic workspace [5].

The dynamic modeling and control of flexible-link robotic systems is still an open area of investigation. By considering the work presented in the first part of this thesis, future works will be devoted to further investigate Model Order Reduction techniques through the implementation of other benchmark mechanisms with at least two degrees of freedom. Closed-chain mechanical systems could be also taken into account. In future developments, the reduced order models obtained with the modal reduction could be adopted in control system for the suppression of vibrations in robotic systems with deformable links.

The field of cable-driven robots, and in particular of cable-suspended parallel robots, can as well offer several possible interesting and challenging developments. With reference to the work presented in this thesis, the prototype described in Chapter 6 and fabricated at University of Trieste (Italy) could be further enhanced, by improving the mechanical hardware and implementing a sway-suppression control system. The 2-DOF cable-based robotic crane could in future be applied in a real environment, e.g. in the naval or construction fields. Furthermore, different applications of variable-radius drums in the field of cable-suspended robots could be investigated.

By considering the prototype of pendulum-robot developed at Stevens Institute of Technology, further development of the work could include a future version of the end-effector, to reduce off-plane oscillation using the gyroscopic effect by means of an on-board spinning mass. Furthermore, the control architecture could be extended to the case with a non-balanced end-effector, which will introduce a non-null driving term, that can be used for the self-excitation of the pendulum in addition to the parametric one. A comparison between the two approaches of excitation (parametric and driving) could as well be investigated.

Appendix A

A.1 Nomenclature

$\boldsymbol{\alpha}$	angular acceleration vector
$\bar{\boldsymbol{\Omega}}$	matrix of angular speeds for the whole mechanism
$\bar{\boldsymbol{R}}$	local-to-global rotation matrix for the whole mechanism
$\boldsymbol{\epsilon}$	strain vector
$\boldsymbol{\Gamma}$	diagonal matrix of the squares of natural frequencies of each link
$\hat{\boldsymbol{B}}$	matrix of relationships between the linear velocities of three non-aligned nodes with respect to the velocity of the first one
$\hat{\boldsymbol{I}}$	matrix of $\hat{\boldsymbol{i}}$ components
$\boldsymbol{\Omega}$	skew-symmetric matrix of absolute angular velocities
$\boldsymbol{\omega}$	absolute angular velocity
$\boldsymbol{\Phi}$	matrix of absolute rotational displacements
$\boldsymbol{\phi}$	angular virtual terms vector
$\boldsymbol{\phi}$	vector of virtual rotational displacements
$\boldsymbol{\theta}$	independent generalized coordinates vector
$\tilde{\boldsymbol{l}}$	sub-matrix of $\boldsymbol{l}$ elements independent from accelerations for the whole mechanism
$\boldsymbol{A}$	Skew-symmetric matrix of absolute angular accelerations
$\boldsymbol{a}$	linear acceleration vector
$\boldsymbol{C}$	compatibility matrix
$\boldsymbol{C}_d$	elastic terms compatibility matrix
$\boldsymbol{C}_r$	rigid terms compatibility matrix
$\boldsymbol{D}$	matrix of relationships between vibrational modal coordinates and rigid-body modal coordinates
$\boldsymbol{E}$	vector containing the partial derivaties matrices of $\boldsymbol{C}$ with respect to the rigid degrees of freedom
$\boldsymbol{e}$	nodal position vector
$\boldsymbol{f}$	concentrated external forces and torques vector acting on each link
$\boldsymbol{f}_g$	equivalent nodal loads due to gravity

$\boldsymbol{G}$	matrix that contains the coefficients of the independent generalized coordinate acceleration
$\boldsymbol{g}$	gravity acceleration vector
$\boldsymbol{H}$	elastic energy matrix of each link
$\boldsymbol{J}$	Jacobian matrix of the ERLS
$\boldsymbol{K}$	stiffness matrix of each link
$\boldsymbol{L}$	matrix that contains all terms not depending on virtual displacements and accelerations
$\boldsymbol{L}$	selection matrix for the elements independent from virtual displacements and accelerations for the whole mechanism
$\boldsymbol{l}$	matrix that contains all terms not depending on virtual displacements
$\boldsymbol{M}$	mass matrix
$\boldsymbol{M}_C$	centrifugal stiffness terms matrix
$\boldsymbol{M}_G$	Coriolis terms matrix
$\boldsymbol{N}$	matrix that relates the vector of independent degrees of freedom with the overhall system degrees of freedom
$\boldsymbol{n}$	matrix that contains all terms not depending on both independent gereralized coordinate and modal coordinates accelerations
$\boldsymbol{P}$	linear virtual terms vector
$\boldsymbol{p}$	absolute nodal position vector
$\boldsymbol{q}$	modal coordinates vector
$\boldsymbol{q}_d$	elastic modal coordinates vector
$\boldsymbol{q}_r$	rigid modal coordinates vector
$\boldsymbol{S}$	joint displacements selector matrix
$\boldsymbol{T}$	local-to-local transformation matrix
$\boldsymbol{U}$	eigenvector
$\boldsymbol{u}$	nodal displacement vector
$\boldsymbol{U}_d$	elastic mode eigenvectors
$\boldsymbol{U}_r$	rigid-body mode eigenvectors
$\boldsymbol{V}_{\theta i}$	selection block-matrix for the rigid degrees of freedom
$\boldsymbol{V}_i^o$	selection matrix for the proper elements of the ith link
$\boldsymbol{V}_{qdi}$	selection block-matrix for the elastic modal coordinates
$\boldsymbol{V}_{qri}$	selection block-matrix for the rigid modal coordinates
$\boldsymbol{W}$	virtual work matrix
$\boldsymbol{W}_f$	generalized force work matrix
$\boldsymbol{W}_g$	gravitational force work matrix
ρ	mass density
$el.$	number of beam elements
I_c	shrink disk inertia
I_m	motor inertia
$m.$	number of modes
m_e	elbow articulation concentrated mass
AMM	Assumed Mode Method
CMS	Component Mode Synthesis
DOF	Degree of Freedom
ERLS	Equivalent Rigid-Link System
FEM	Finite Element Method

A.2 The matrix $\hat{\boldsymbol{B}}$

Using the skew-symmetric matrix definition

$$\left[\{a \quad b \quad c\}^T\right]_X = \begin{bmatrix} 0 & -c & b \\ c & 0 & -a \\ -b & a & 0 \end{bmatrix} \tag{A.1}$$

employed for the cross-product operation

$$\hat{\boldsymbol{B}} = \begin{bmatrix} \boldsymbol{I} & \boldsymbol{0} \\ \boldsymbol{I} & \left[-(\boldsymbol{P}_1 - \boldsymbol{P}_0)\right]_X \\ \boldsymbol{I} & \left[-(\boldsymbol{P}_2 - \boldsymbol{P}_0)\right]_X \end{bmatrix} \tag{A.2}$$

A.3 Development of the terms involving rotational matrices

In the following a new formulation for the terms containing the rotational matrix, namely $\delta\bar{\boldsymbol{R}}^T\bar{\boldsymbol{R}}$, $\bar{\boldsymbol{R}}^T\dot{\boldsymbol{R}}^T$ and $\bar{\boldsymbol{R}}^T\ddot{\boldsymbol{R}}^T$, is developed. Let start from the following equation

$$\boldsymbol{R}^T\boldsymbol{T} = \boldsymbol{I}, \quad \boldsymbol{R}^T\dot{\boldsymbol{R}} = \boldsymbol{\Omega} \quad \textit{and} \quad \boldsymbol{R}^T\ddot{\boldsymbol{R}} + \dot{\boldsymbol{R}}^T\dot{\boldsymbol{R}} = \boldsymbol{A} \tag{A.3}$$

where

$$\boldsymbol{\Omega} = \begin{bmatrix} 0 & -\omega_z & \omega_y \\ \omega_z & 0 & -\omega_x \\ -\omega_y & \omega_x & 0 \end{bmatrix}; \quad \boldsymbol{A} = \begin{bmatrix} 0 & -\alpha_z & \alpha_y \\ \alpha_z & 0 & -\alpha_x \\ -\alpha_y & \alpha_x & 0 \end{bmatrix} \tag{A.4}$$

are the skew-symmetric matrices referring to the absolute angular velocity and absolute angular acceleration of the link, respectively. Since $\dot{\boldsymbol{R}}^T\dot{\boldsymbol{R}} = \boldsymbol{\Omega}^T\boldsymbol{T}^T\boldsymbol{T}\boldsymbol{\Omega} = \boldsymbol{\Omega}^T\boldsymbol{\Omega}$, it yields $\boldsymbol{R}^T\ddot{\boldsymbol{R}} = \boldsymbol{A} - \boldsymbol{\Omega}^T\boldsymbol{\Omega}$. Moreover, $\dot{\boldsymbol{R}}^T = \boldsymbol{T}\boldsymbol{\Omega}$ and, $\delta\boldsymbol{T} = \boldsymbol{T}\delta\boldsymbol{\Phi}$, where

$$\delta\boldsymbol{\Phi} = \begin{bmatrix} 0 & -\delta\phi_z & \delta\phi_y \\ \delta\phi_z & 0 & -\delta\phi_x \\ -\delta\phi_y & \delta\phi_x & 0 \end{bmatrix} \tag{A.5}$$

$\delta\boldsymbol{\Phi}$ is a skew-symmetric matrix and its components are the virtual rotational displacements expressed with respect to the local frame of the link. By pre-multiplying the previous equation by $\delta\boldsymbol{T}^T$, we can obtain

$$\delta\boldsymbol{T}^T\boldsymbol{T} = \delta\boldsymbol{\Phi}^T\boldsymbol{T}^T\boldsymbol{T} = \delta\boldsymbol{\Phi}^T \tag{A.6}$$

Finally, extending the results to the matrix $\bar{\boldsymbol{R}}$, which contains on its main diagonal the single rotational matrices referred to each link, we obtain

$$\delta\bar{\boldsymbol{R}}^T\bar{\boldsymbol{R}} = \delta\bar{\boldsymbol{\Phi}}^T, \quad \bar{\boldsymbol{R}}^T\dot{\bar{\boldsymbol{R}}} = \boldsymbol{\Omega} \quad \text{and} \quad \bar{\boldsymbol{R}}^T\ddot{\bar{\boldsymbol{R}}} = \bar{\boldsymbol{A}} - \bar{\boldsymbol{\Omega}}^T\bar{\boldsymbol{\Omega}} \tag{A.7}$$

A.4 Development of the constant inertial matrices related to a link

The terms related to the inertial matrix of equations (2.60) and (2.61) can be rewritten as

$$\boldsymbol{U}^T\boldsymbol{M}\bar{\boldsymbol{A}}\boldsymbol{U} = \boldsymbol{U}^T\boldsymbol{M}(\alpha_x\bar{\boldsymbol{A}}_1 + \alpha_y\bar{\boldsymbol{A}}_2 + \alpha_z\bar{\boldsymbol{A}}_3)\boldsymbol{U} \tag{A.8}$$

where

$$\bar{\boldsymbol{A}}_1 = \begin{bmatrix} 0 & 0 & 0 \\ 0 & 0 & -1 \\ 0 & 1 & 0 \end{bmatrix}; \quad \bar{\boldsymbol{A}}_2 = \begin{bmatrix} 0 & 0 & 1 \\ 0 & 0 & 0 \\ -1 & 0 & 0 \end{bmatrix}; \quad \bar{\boldsymbol{A}}_3 = \begin{bmatrix} 0 & -1 & 0 \\ 1 & 0 & 0 \\ 0 & 0 & 0 \end{bmatrix} \tag{A.9}$$

By introducing the notation $\boldsymbol{X}_1 = \boldsymbol{U}^T\boldsymbol{M}\bar{\boldsymbol{A}}_1\boldsymbol{U}$, $\boldsymbol{X}_2 = \boldsymbol{U}^T\boldsymbol{M}\bar{\boldsymbol{A}}_2\boldsymbol{U}$ and $\boldsymbol{X}_3 = \boldsymbol{U}^T\boldsymbol{M}\bar{\boldsymbol{A}}_3\boldsymbol{U}$, it can be obtained

$$\boldsymbol{U}^T\boldsymbol{M}\bar{\boldsymbol{A}}\boldsymbol{U} = \alpha_x\boldsymbol{X}_1 + \alpha_y\boldsymbol{X}_2 + \alpha_z\boldsymbol{X}_3 \tag{A.10}$$

In the same manner, the term $\boldsymbol{U}^T\boldsymbol{M}\bar{\boldsymbol{\Omega}}\boldsymbol{U}$ of (2.61) can be rewritten as

$$\boldsymbol{U}^T\boldsymbol{M}\bar{\boldsymbol{\Omega}}\boldsymbol{U} = \omega_x\boldsymbol{X}_1 + \omega_y\boldsymbol{X}_2 + \omega_z\boldsymbol{X}_3 \tag{A.11}$$

Furthermore, since $\boldsymbol{U}^T\delta\bar{\boldsymbol{\Phi}}^T\boldsymbol{M}\boldsymbol{U} = (\boldsymbol{U}^T\boldsymbol{M}\delta\bar{\boldsymbol{\Phi}}\boldsymbol{U})^T$, we obtain

$$\boldsymbol{U}^T\delta\bar{\boldsymbol{\Phi}}^T\boldsymbol{M}\boldsymbol{U} = \delta\phi_x\boldsymbol{X}_1^T + \phi_y\boldsymbol{X}_2^T + \phi_z\boldsymbol{X}_3^T \tag{A.12}$$

The product $\boldsymbol{\Omega}^T\boldsymbol{\Omega}$ is

$$\boldsymbol{\Omega}^T\boldsymbol{\Omega} = \begin{bmatrix} (\omega_y^2+\omega_z^2) & -\omega_x\omega_y & -\omega_x\omega_z \\ -\omega_x\omega_y & (\omega_x^2+\omega_z^2) & -\omega_y\omega_z \\ -\omega_x\omega_z & -\omega_y\omega_z & (\omega_x^2+\omega_y^2) \end{bmatrix} \tag{A.13}$$

Thus, it can be rewritten as

$$\boldsymbol{\Omega}^T\boldsymbol{\Omega} = (\omega_y^2+\omega_z^2)\boldsymbol{S}_1 + (\omega_x^2+\omega_z^2)\boldsymbol{S}_2 + (\omega_x^2+\omega_y^2)\boldsymbol{S}_3 + \omega_x\omega_y\boldsymbol{S}_4 + \omega_x\omega_z\boldsymbol{S}_5 + \omega_y\omega_z\boldsymbol{S}_6 \tag{A.14}$$

where

$$\begin{aligned} \boldsymbol{S}_1 &= \begin{bmatrix} 1 & 0 & 0 \\ 0 & 0 & 0 \\ 0 & 0 & 0 \end{bmatrix}; \quad \boldsymbol{S}_2 = \begin{bmatrix} 0 & 0 & 0 \\ 0 & 1 & 0 \\ 0 & 0 & 0 \end{bmatrix}; \quad \boldsymbol{S}_3 = \begin{bmatrix} 0 & 0 & 0 \\ 0 & 0 & 0 \\ 0 & 0 & 1 \end{bmatrix} \\ \boldsymbol{S}_4 &= \begin{bmatrix} 0 & -1 & 0 \\ -1 & 0 & 0 \\ 0 & 0 & 0 \end{bmatrix}; \quad \boldsymbol{S}_5 = \begin{bmatrix} 0 & 0 & -1 \\ 0 & 0 & 0 \\ -1 & 0 & 0 \end{bmatrix}; \quad \boldsymbol{S}_6 = \begin{bmatrix} 0 & 0 & 0 \\ 0 & 0 & -1 \\ 0 & -1 & 0 \end{bmatrix} \end{aligned} \tag{A.15}$$

Introducing the variables $\boldsymbol{Y}_1 = \boldsymbol{U}^T\boldsymbol{M}\bar{\boldsymbol{S}}_1\boldsymbol{U}$, $\boldsymbol{Y}_2 = \boldsymbol{U}^T\boldsymbol{M}\bar{\boldsymbol{S}}_2\boldsymbol{U}$, $\boldsymbol{Y}_3 = \boldsymbol{U}^T\boldsymbol{M}\bar{\boldsymbol{S}}_3\boldsymbol{U}$, $\boldsymbol{Y}_4 = \boldsymbol{U}^T\boldsymbol{M}\bar{\boldsymbol{S}}_4\boldsymbol{U}$, $\boldsymbol{Y}_5 = \boldsymbol{U}^T\boldsymbol{M}\bar{\boldsymbol{S}}_5\boldsymbol{U}$ and $\boldsymbol{Y}_6 = \boldsymbol{U}^T\boldsymbol{M}\bar{\boldsymbol{S}}_6\boldsymbol{U}$, we can write

$$\boldsymbol{U}^T\boldsymbol{M}\boldsymbol{\Omega}^T\boldsymbol{\Omega}\boldsymbol{U} = (\omega_y^2+\omega_z^2)\boldsymbol{Y}_1+(\omega_x^2+\omega_z^2)\boldsymbol{Y}_2+(\omega_x^2+\omega_y^2)\boldsymbol{Y}_3+\omega_x\omega_y\boldsymbol{Y}_4+\omega_x\omega_z\boldsymbol{Y}_5+\omega_y\omega_z\boldsymbol{Y}_6 \tag{A.16}$$

With the introduction of $\bar{\boldsymbol{A}}_1$, $\bar{\boldsymbol{A}}_2$ and $\bar{\boldsymbol{A}}_3$, the previous equation can be rewritten as

$$\boldsymbol{U}^T\delta\bar{\boldsymbol{\Phi}}^T\boldsymbol{M}\bar{\boldsymbol{A}}\boldsymbol{U} = \boldsymbol{U}^T(\delta\phi_x\bar{\boldsymbol{A}}_1^T + \delta\phi_y\bar{\boldsymbol{A}}_2^T + \delta\phi_z\bar{\boldsymbol{A}}_3^T)\boldsymbol{M}(\alpha_x\bar{\boldsymbol{A}}_1^T + \alpha_y\bar{\boldsymbol{A}}_2^T + \alpha_z\bar{\boldsymbol{A}}_3^T)\boldsymbol{U} \tag{A.17}$$

and, after multiplications

$$\boldsymbol{U}^T\delta\bar{\boldsymbol{\Phi}}^T\boldsymbol{M}\bar{\boldsymbol{A}}\boldsymbol{U} = \delta\phi_x(\alpha_x\boldsymbol{Z}_11 + \alpha_y\boldsymbol{Z}_12 + \alpha_z\boldsymbol{Z}_13) + \delta\phi_y(\alpha_x\boldsymbol{Z}_21 + \alpha_y\boldsymbol{Z}_22 + \alpha_z\boldsymbol{Z}_23)+ \delta\phi_z(\alpha_x\boldsymbol{Z}_31 + \alpha_y\boldsymbol{Z}_32 + \alpha_z\boldsymbol{Z}_33) \tag{A.18}$$

in which

$$\boldsymbol{Z}_rd = \boldsymbol{U}^T\bar{\boldsymbol{A}}_r^T\boldsymbol{M}\bar{\boldsymbol{A}}_d\boldsymbol{U} \quad \text{for} \quad r = 1,2,3 \quad \text{and} \quad d = 1,2,3 \tag{A.19}$$

At the same time

$$\boldsymbol{U}^T\delta\bar{\boldsymbol{\Phi}}^T\boldsymbol{M}\bar{\boldsymbol{\Omega}}\boldsymbol{U} = \delta\phi_x(\omega_x\boldsymbol{Z}_11 + \omega_y\boldsymbol{Z}_12 + \omega_z\boldsymbol{Z}_13) + \delta\phi_y(\omega_x\boldsymbol{Z}_21 + \omega_y\boldsymbol{Z}_22 + \omega_z\boldsymbol{Z}_23)+ \delta\phi_z(\omega_x\boldsymbol{Z}_31 + \omega_y\boldsymbol{Z}_32 + \omega_z\boldsymbol{Z}_33) \tag{A.20}$$

The term

$$\boldsymbol{U}^T\delta\boldsymbol{U}\delta\bar{\boldsymbol{\Phi}}^T\boldsymbol{M}\bar{\boldsymbol{\Omega}}^T\bar{\boldsymbol{\Omega}}\boldsymbol{U} = \boldsymbol{U}^T(\delta\phi_x\bar{\boldsymbol{A}}_1^T + \delta\phi_y\bar{\boldsymbol{A}}_2^T + \delta\phi_z\bar{\boldsymbol{A}}_3^T) \times \boldsymbol{M}\left((\omega_y^2+\omega_z^2)\bar{\boldsymbol{S}}_1 + (\omega_x^2+\omega_z^2)\bar{\boldsymbol{S}}_2 + (\omega_x^2+\omega_y^2)\bar{\boldsymbol{S}}_3 + \omega_x\omega_y\bar{\boldsymbol{S}}_4 + \omega_x\omega_z\bar{\boldsymbol{S}}_5 + \omega_y\omega_z\bar{\boldsymbol{S}}_6\right)\boldsymbol{U} \tag{A.21}$$

can be written as

$$\begin{aligned}&\boldsymbol{U}^T\delta\bar{\boldsymbol{\Phi}}^T\boldsymbol{M}\bar{\boldsymbol{\Omega}}^T\bar{\boldsymbol{\Omega}}\boldsymbol{U} = \\ &\delta\phi_x\left((\omega_y^2+\omega_z^2)\boldsymbol{W}_{11} + (\omega_x^2+\omega_z^2)\boldsymbol{W}_{12} + (\omega_x^2+\omega_y^2)\boldsymbol{W}_{13} + \omega_x\omega_y\boldsymbol{W}_{14} + \omega_x\omega_z\boldsymbol{W}_{15} + \omega_y\omega_z\boldsymbol{W}_{16}\right) + \\ &\delta\phi_y\left((\omega_y^2+\omega_z^2)\boldsymbol{W}_{21} + (\omega_x^2+\omega_z^2)\boldsymbol{W}_{22} + (\omega_x^2+\omega_y^2)\boldsymbol{W}_{23} + \omega_x\omega_y\boldsymbol{W}_{24} + \omega_x\omega_z\boldsymbol{W}_{25} + \omega_y\omega_z\boldsymbol{W}_{26}\right) + \\ &\delta\phi_z\left((\omega_y^2+\omega_z^2)\boldsymbol{W}_{31} + (\omega_x^2+\omega_z^2)\boldsymbol{W}_{32} + (\omega_x^2+\omega_y^2)\boldsymbol{W}_{33} + \omega_x\omega_y\boldsymbol{W}_{34} + \omega_x\omega_z\boldsymbol{W}_{35} + \omega_y\omega_z\boldsymbol{W}_{36}\right)\end{aligned} \tag{A.22}$$

where

$$\boldsymbol{W}_{rt} = \boldsymbol{U}^T\bar{\boldsymbol{A}}_r^T\boldsymbol{M}\boldsymbol{S}_r\boldsymbol{U} \quad \text{for} \quad r = 1,2,3, \quad \textit{and} \quad t = 1,...,6 \tag{A.23}$$

A.5 Development of vectors $\hat{\boldsymbol{i}}_i$

If the nodes do not have rotational degree of freedom, only gravity force (not torques) are applied to them. In this case

$$\begin{aligned}
\hat{\boldsymbol{i}}_1 &= \begin{bmatrix} 1 & 0 & 0 & 1 & 0 & 0 & 1 & 0 & 0 & 1 & 0 & 0 & \dots \end{bmatrix}^T \\
\hat{\boldsymbol{i}}_2 &= \begin{bmatrix} 0 & 1 & 0 & 0 & 1 & 0 & 0 & 1 & 0 & 0 & 1 & 0 & \dots \end{bmatrix}^T \\
\hat{\boldsymbol{i}}_3 &= \begin{bmatrix} 0 & 0 & 1 & 0 & 0 & 1 & 0 & 0 & 1 & 0 & 0 & 1 & \dots \end{bmatrix}^T
\end{aligned} \tag{A.24}$$

It is worth to introduce the notation $\hat{\boldsymbol{I}} = \begin{bmatrix} \boldsymbol{I} & \boldsymbol{I} & \boldsymbol{I} & \boldsymbol{I} & \dots & \boldsymbol{I} \end{bmatrix}^T$ where $\boldsymbol{I}$ are 3×3 identity matrices. Conversely, if nodes have rotational degrees of freedom, $\hat{\boldsymbol{i}}$ are defined as

$$\begin{aligned}
\hat{\boldsymbol{i}}_1 &= \begin{bmatrix} 1 & 0 & 0 & 0 & 0 & 0 & 1 & 0 & 0 & 0 & 0 & 0 & \dots \end{bmatrix}^T \\
\hat{\boldsymbol{i}}_2 &= \begin{bmatrix} 0 & 1 & 0 & 0 & 0 & 0 & 0 & 1 & 0 & 0 & 0 & 0 & \dots \end{bmatrix}^T \\
\hat{\boldsymbol{i}}_3 &= \begin{bmatrix} 0 & 0 & 1 & 0 & 0 & 0 & 0 & 0 & 1 & 0 & 0 & 0 & \dots \end{bmatrix}^T
\end{aligned} \tag{A.25}$$

In this case, the matrix $\hat{\boldsymbol{I}}$ is $\hat{\boldsymbol{I}} = \begin{bmatrix} \boldsymbol{I} & \boldsymbol{0} & \boldsymbol{I} & \boldsymbol{0} & \dots & \boldsymbol{0} \end{bmatrix}^T$ where $\boldsymbol{I}$ and $\boldsymbol{0}$ are 3×3 unit and zero matrices.

The matrix $\boldsymbol{I}$ has been defined for the case where all the nodes have rotational degrees of freedom or for the opposite case, where none of them has rotational degrees of freedom. In the case where nodes with rotational degrees of freedom and nodes without are present in the same link, the development of the definition of $\boldsymbol{I}$ is straightforward.

Appendix B

B.1 Mathematical derivations of the Variable Radius Drum synthesis

In this appendix, the mathematical derivations of the VRD profile synthesis are reported. For the further calculations, it is to be noticed that

$$\frac{d\boldsymbol{T}(x)}{dx} = \boldsymbol{T}\left(x + \frac{\pi}{2}\right) \tag{B.1}$$

In particular, by differentiating (7.6) with respect to angle α, it can be obtained

$$\begin{aligned}\frac{d\boldsymbol{P}_t}{d\alpha} =& \frac{d\boldsymbol{T}(\alpha)}{d\alpha}\begin{Bmatrix} c_d \\ 0 \end{Bmatrix} + \frac{d\boldsymbol{T}(\alpha)}{d\alpha}\boldsymbol{T}(-\gamma)\boldsymbol{T}\left(-\frac{\pi}{2}\right)\begin{Bmatrix} l_t \\ 0 \end{Bmatrix} \\ & -\frac{d\gamma}{d\alpha}(\alpha)\frac{d\boldsymbol{T}(-\gamma)}{d(-\gamma)}\boldsymbol{T}(\alpha)\boldsymbol{T}\left(-\frac{\pi}{2}\right)\begin{Bmatrix} l_t \\ 0 \end{Bmatrix} \\ =& \boldsymbol{T}\left(\alpha + \frac{\pi}{2}\right)\begin{Bmatrix} c_d \\ 0 \end{Bmatrix} + \boldsymbol{T}(\alpha)\boldsymbol{T}(-\gamma)\left(1 - \frac{d\gamma}{d\alpha}\right)\begin{Bmatrix} l_t \\ 0 \end{Bmatrix}\end{aligned} \tag{B.2}$$

The unit vector normal to the VRD profile in tangent point $\boldsymbol{P}_t$ is

$$\boldsymbol{n} = \boldsymbol{T}(\alpha)\boldsymbol{T}(\boldsymbol{-\gamma})\begin{Bmatrix} 1 \\ 0 \end{Bmatrix} \tag{B.3}$$

Since $d\boldsymbol{P}_t/d\alpha$ points at any time along the tangent line $\boldsymbol{P}_t\boldsymbol{P}_b$, it is normal to unit vector $\boldsymbol{n}$. This orthogonality relationship can be written as

$$\boldsymbol{n}^T\frac{d\boldsymbol{P}_t}{d\alpha} = 0 \tag{B.4}$$

By substituting (B.2) and (B.3) into (B.4) and by using the property of orthogonal matrices

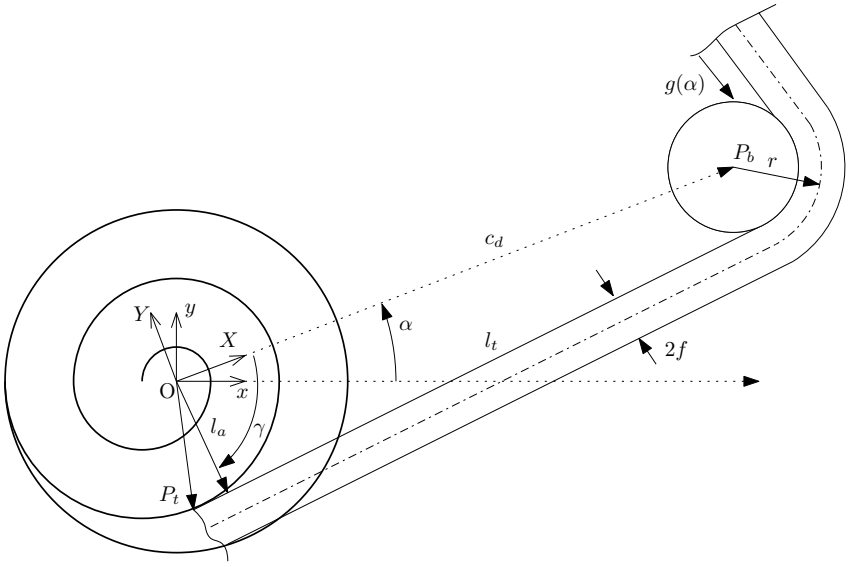

Figure B.1: Variable radius drum parameters by considering the radius of the idle pulley and the cable thickness.

$\boldsymbol{T}^T\boldsymbol{T} = \boldsymbol{I}$, it follows

$$\begin{aligned} &\begin{Bmatrix} 1 & 0 \end{Bmatrix} \boldsymbol{T}^T(-\gamma)\boldsymbol{T}\left(\frac{pi}{2}\right)\begin{Bmatrix} c_d \\ 0 \end{Bmatrix} + \left(1 - \frac{d\gamma}{d\alpha}\right)\begin{Bmatrix} 1 & 0 \end{Bmatrix}\begin{Bmatrix} l_t \\ 0 \end{Bmatrix} = 0 \\ &c_d\, sin(-\gamma) + \left(1 - \frac{d\gamma}{d\alpha}\right) l_t = 0 \end{aligned} \tag{B.5}$$

The relationship between the lever arm l_a, the unrolled cable length and the VRD rotation angle α is $l_a = dg/d\alpha$. In particular, from Fig. 6.5 it can be easily seen that $c_d cos(\gamma) = l_a$. By combining the two previous equations, it can be seen that $c_d cos(\gamma) = dg/d\alpha$. At this stage, the previous relationship can be differentiated and, by considering that $c_d\, sin(\gamma) = \sqrt{c_d^2 + l_a^2}$, it can be obtained:

$$\frac{d\gamma}{d\alpha} = -\frac{\frac{d^2g}{d\alpha^2}}{\sqrt{c_d^2 - \left(\frac{dg}{d\alpha}\right)^2}} \tag{B.6}$$

B.2 Extended synthesis of the Variable Radius Drum

In this appendix, the synthesis of the variable radius drum, by considering the radius r of the idle pulley and the thickness of the cable $2f$, is reported. The radius r includes the radius of the idle pulley and half of the cable thickness. In Fig. B.1 a graphical representation of this configuration is reported. Similarly to (7.6), the geometry of the

VRD can be now expressed as

$$\boldsymbol{P}_t = \boldsymbol{T}(\alpha) \begin{Bmatrix} c_d \\ 0 \end{Bmatrix} + \boldsymbol{T}(\alpha)\boldsymbol{T}(-\gamma)\boldsymbol{T}\left(-\frac{\pi}{2}\right) \begin{Bmatrix} l_t \\ 0 \end{Bmatrix} + \chi(\alpha) \tag{B.7}$$

where the function $\chi(\alpha)$ is equal to

$$\chi(\alpha) = \boldsymbol{T}(\alpha - \gamma) \begin{Bmatrix} r \\ 0 \end{Bmatrix} - \boldsymbol{T}(\gamma + \alpha) \begin{Bmatrix} f \\ 0 \end{Bmatrix} \tag{B.8}$$

The vector tangent to the profile in $\boldsymbol{P}_t$ can be written as

$$\begin{aligned} \frac{d\boldsymbol{P}_t}{d\alpha} =& \frac{d\boldsymbol{T}(\alpha)}{d\alpha} \begin{Bmatrix} c_d \\ 0 \end{Bmatrix} + \frac{d\boldsymbol{T}(\alpha)}{d\alpha}\boldsymbol{T}(-\gamma)\boldsymbol{T}\left(-\frac{\pi}{2}\right) \begin{Bmatrix} l_t \\ 0 \end{Bmatrix} \\ & -\frac{d\gamma}{d\alpha}(\alpha)\frac{d\boldsymbol{T}(-\gamma)}{d(-\gamma)}\boldsymbol{T}(\alpha)\boldsymbol{T}\left(-\frac{\pi}{2}\right) \begin{Bmatrix} l_t \\ 0 \end{Bmatrix} + \frac{d\chi(\alpha)}{d\alpha} \\ =& \boldsymbol{T}\left(\alpha + \frac{\pi}{2}\right) \begin{Bmatrix} c_d \\ 0 \end{Bmatrix} + \boldsymbol{T}(\alpha)\boldsymbol{T}(-\gamma)\left(1 - \frac{d\gamma}{d\alpha}\right) \begin{Bmatrix} l_t \\ 0 \end{Bmatrix} + \frac{d\chi(\alpha)}{d\alpha} \end{aligned} \tag{B.9}$$

since

$$\begin{aligned} \frac{d\chi(\alpha)}{d\alpha} =& \frac{d\boldsymbol{T}(\alpha - \gamma)}{d\alpha}\left(1 - \frac{d\gamma}{d\alpha}\right) \begin{Bmatrix} r \\ 0 \end{Bmatrix} - \frac{d\boldsymbol{T}(\alpha - \gamma)}{d\alpha}\left(1 - \frac{d\gamma}{d\alpha}\right) \begin{Bmatrix} f \\ 0 \end{Bmatrix} \\ =& \boldsymbol{T}\left(\alpha - \gamma + \frac{\pi}{2}\right)\left(1 - \frac{d\gamma}{d\alpha}\right) \begin{Bmatrix} r \\ 0 \end{Bmatrix} + \boldsymbol{T}\left(\alpha - \gamma + \frac{\pi}{2}\right)\left(1 - \frac{d\gamma}{d\alpha}\right) \begin{Bmatrix} f \\ 0 \end{Bmatrix} \end{aligned} \tag{B.10}$$

It has to be noticed that (B.9) is equal to (B.2). Consequently, the orthogonality condition of (B.4) leads to the same results of (6.8) and (6.9). In fact

$$\boldsymbol{n}^T \frac{d\chi(\alpha)}{d\alpha} = 0 \tag{B.11}$$

Finally, we obtain that the geometry of the VRD profile, in Cartesian coordinates, is given by (B.7), associated with (6.8), (6.9), and (B.8).

Appendix C

C.1 Variable-length pendulum subsystem

C.1.1 Internal dynamics

In this Appendix the internal dynamics of the variable-length pendulum is analyzed.

Let us consider the varying length pendulum subsystem, whose dynamics are described by the first two equations (7.6), reported here

$$\begin{aligned} \ddot{l} =& \frac{d_2 \sin\beta(r\tau_2 - d_2\tau_1 \sin\beta)}{J_{EE}} + d_2\dot{\theta}^2\cos\beta + g\cos q_3 + l\dot{q_3}^2 - \frac{\tau_1}{m_{EE}} \\ \ddot{q_3} =& \frac{{d_2}^2\tau_1 \sin\beta\cos\beta - d_2 r\tau_2\cos\beta}{J_{EE}l} + \frac{d_2\dot{\theta}^2\sin\beta - g\sin q_3 - 2\dot{l}\dot{q_3}}{l} \end{aligned} \tag{C.1}$$

By means of the change of variables: $x_1 = l$, $x_2 = q_3$, $x_4 = \dot{l}$, $x_5 = \dot{q}_3$, and with $d_2 = 0$, the system can be rewritten in the usual state-space form, as follows

$$\underbrace{\begin{bmatrix} \dot{x}_1 \\ \dot{x}_2 \\ \dot{x}_4 \\ \dot{x}_5 \end{bmatrix}}_{\dot{\mathbf{x}}} = \underbrace{\begin{bmatrix} x_4 \\ x_5 \\ g\ \cos x_2 + x_1 x_5^2 \\ -\frac{2x_4x_5}{x_1} - \frac{g\ \sin x_2}{x_1} \end{bmatrix}}_{\mathbf{f(x)}} + \underbrace{\begin{bmatrix} 0 \\ 0 \\ -\frac{1}{m_{EE}} \\ 0 \end{bmatrix}}_{\mathbf{g}} \tau_1 \tag{C.2}$$

It can be easily proved that the distribution $D = span\left\{\mathbf{g},\ ad_{\mathbf{f}}\mathbf{g}\ ad_{\mathbf{f}}^2\mathbf{g}\right\}$ is not involutive. Therefore the system is not linearizable by static or dynamic feedback [186].

A *partial feedback linearization* is then applied. Let inspect the internal behavior of the system [187]. First, it can be noticed that the second equation in (7.6) may be rewritten in such a way that the normalized angular momentum is exploited

$$x_1^2\dot{x}_5 + 2x_1x_4x_5 = \frac{d\left(x_1^2x_5\right)}{dt} = -gx_1\sin x_2 \tag{C.3}$$

then, the normalized angular momentum $y = x_1^2x_5$ is chosen as the output. It is straightforward to verify that its relative degree is $r = 3$. Therefore, by applying the following

diffeomorphism (which is invertible for $x_2 \neq 0$)

$$\begin{aligned} z_1 &= x_1^2 x_5 \\ z_2 &= -g\, x_1 \sin x_2 \\ z_3 &= -g\,(x_1 x_5 \cos x_2 + x_4 \sin x_2) \\ z_4 &= x_2 \end{aligned} \tag{C.4}$$

the system in (C.2) reduces to the following one

$$\begin{cases} \dot{z}_1 = z_2 \\ \dot{z}_2 = z_3 \\ \dot{z}_3 = \dfrac{g \sin z_4}{m_{EE}} \tau_1 \\ \dot{z}_4 = z_1 \left(\dfrac{g \sin z_4}{z_2} \right)^2 \end{cases} \tag{C.5}$$

where z_1, z_2 and z_3 represent the controlled dynamics, and z_4 is the internal dynamics. Therefore, as suggested by intuition, the angle q_3 represents the uncontrollable state of the system.

C.1.2 Stability of the starting and goal trajectories

Let us consider the specific energy of the pendulum subsystem, as described in (7.21). After computing its time derivative, and substituting $\ddot{l}$ and $\ddot{q}_3$ with the corresponding expressions in (7.6), the following expression can be obtained

$$\frac{de}{dt} = \dot{l}\,\ddot{l} + l\,\dot{l}\,\dot{q}_3^2 + l^2 \dot{q}_3\,\ddot{q}_3 - g\dot{l}\cos q_3 + gl \sin q_3\,\dot{q}_3 = -\frac{\dot{l}}{m_{EE}}\,\tau_1 \tag{C.6}$$

Therefore, by considering (C.6) as a Lyapunov function, we conclude that all the trajectories wherein the cable length is kept constant are bounded. Specifically, the starting and goal trajectories are bounded trajectories.

Bibliography

Author's contributions

[1] P. Boscariol, P. Gallina, A. Gasparetto, M. Giovagnoni, L. Scalera, and R. Vidoni, "Evolution of a dynamic model for flexible multibody systems," in *Advances in Italian Mechanism Science*. Springer, 2017, pp. 533–541.

[2] R. Vidoni, L. Scalera, and A. Gasparetto, "3-D ERLS based dynamic formulation for flexible-link robots: Theoretical and numerical comparison between the Finite Element Method and the Component Mode Synthesis approaches," *International Journal of Mechanics and Control*, vol. 19, no. 1, pp. 39–50, 2018.

[3] R. Vidoni, L. Scalera, A. Gasparetto, and M. Giovagnoni, "Comparison of Model Order Reduction Techniques for Flexible Multibody Dynamics using an Equivalent Rigid-Link System Approach," in *Proceedings of ECCOMAS Thematic Conference on Multibody Dynamics, June 19-22, 2017, Prague, Czech Republic*, 2017.

[4] L. Scalera, P. Gallina, S. Seriani, and A. Gasparetto, "Cable-Based Robotic Crane (CBRC): Design and Implementation of Overhead Traveling Cranes Based on Variable Radius Drums," *IEEE Transactions on Robotics*, vol. 34, no. 2, pp. 474–485, April 2018.

[5] L. Scalera, A. Gasparetto, and D. Zanotto, "Design and Experimental Validation of a 3-DOF Underactuated Pendulum-Like Robot," *IEEE/ASME Transactions on Mechatronics*, 2019, (under review).

References

[6] M. Chemnitz, G. Schreck, and J. Krüger, "Analyzing energy consumption of industrial robots," in *Emerging Technologies & Factory Automation (ETFA), 2011 IEEE 16th Conference on*. IEEE, 2011, pp. 1–4.

[7] M. Brossog, M. Bornschlegl, J. Franke *et al.*, "Reducing the energy consumption of industrial robots in manufacturing systems," *The International Journal of Advanced Manufacturing Technology*, vol. 78, no. 5-8, pp. 1315–1328, 2015.

[8] G. Carabin, E. Wehrle, and R. Vidoni, "A review on energy-saving optimization methods for robotic and automatic systems," *Robotics*, vol. 6, no. 4, p. 39, 2017.

[9] P. Boscariol and D. Richiedei, "Energy saving in redundant robotic cells: Optimal trajectory planning," in *IFToMM Symposium on Mechanism Design for Robotics*. Springer, 2018, pp. 268–275.

[10] "European union 2030 energy strategy," https://ec.europa.eu/energy/en/topics/energy-strategy-and-energy-union/2030-energy-strategy, 2014.

[11] P. Boscariol, "Dynamics and control of flexible-link mechanisms," *Ph.D. Thesis*, 2012.

[12] R. Vidoni, P. Gallina, P. Boscariol, A. Gasparetto, and M. Giovagnoni, "Modeling the vibration of spatial flexible mechanisms through an Equivalent Rigid-Link System/-Component Mode Synthesis approach," *Journal of Vibration and Control,*, vol. 23, no. 12, pp. 1890–1907, 2017.

[13] O. A. Bauchau, *Flexible Multibody Dynamics*. Springer, 2011.

[14] M. Benosman, F. Boyer, G. Vey, and D. Primautt, "Flexible links manipulators: from modelling to control," *Journal of Intelligent and Robotic Systems*, vol. 34, no. 4, pp. 381–414, August 2002.

[15] A. Shabana, "Flexible multibody dynamics: Review of past and recent developments," *Multibody System Dynamics*, vol. 1, pp. 189–222, 1997.

[16] M. Tokhi and A. Azad, *Flexible Robot Manipulators: Modeling, Simulation and Control*. Control Engineering Series, The Institution of Engineering and Technology (IET), 2008.

[17] T. M. Wasfy and A. K. Noor, "Computational strategies for flexible multibody systems," *Applied Mechanics Reviews*, vol. 56, no. 6, pp. 553–613, 2003.

[18] S. Dietz, O. Wallrapp, and S. Wiedemann, "Nodal vs. modal representation in flexible multibody system dynamics," in *Proceeding of Multibody Dynamics 2003, IDMEC/IST 2003*, Lisbon, Portugal, 2003, pp. 1–4.

[19] S. Ge, T. Lee, and G. Zhu, "Nonlinear feedback controller for a single-link flexible manipulator based on finite element model," *J. Robotic Systems*, vol. 14, no. 3, pp. 165–178, 1997.

[20] P. Kalra and A. Sharan, "Accurate modeling of flexible manipulators using finite element analysis," *Mechanism and Machine Theory*, vol. 26, pp. 299–313, 1991.

[21] J. Martins, Z. Mohamed, M. Tokhi, J. S. da Costa, and M. Botto, "Approaches for dynamic modelling of flexible manipulator systems," in *Proceedings of the IEEE Conference on Control Theory Appl.*, vol. 150, July 2003.

[22] G. Naganathan and A. Soni, "Nonlinear modeling of kinematic and flexibility effects in manipulator design," *ASME Journal of Mechanisms, Transmission and Automation in Design*, vol. 110, pp. 243–254, 1988.

[23] S. Nagarajan and D. Turcic, "Lagrangian formulation of the equations of motion for elastic mechanisms with mutual dependence between rigid body and elastic motions. part i: element level equations," *ASME Journal of Dynamic Systems, Measurements, and Control*, vol. 112, pp. 203–214, 1990.

[24] R. Theodore and A. Ghosal, "Comparison of the assumed modes method and finite element models for flexible multilink manipulators," *Int. J. Robotics Res.*, vol. 14, no. 2, pp. 91–111, 1995.

[25] D. Wang, Y. Lu, Y. Liu, and X. Li, "Dynamic model and tip trajectory tracking control for a two-link flexible robotic manipulator," in *Proceedings of the IEEE Conference on System, Man and Cybernetics*, Beijing, 1996, pp. 1020–1024.

[26] A. Shabana, *Dynamics of Multibody systems, 3rd ed.* Cambridge University press, 2005.

[27] A. A. Shabana, "An absolute nodal coordinate formulation for the large rotation and deformation analysis of flexible bodies," *Technical Report, Department of Mechanical Engineering, University of Illinois at Chicago*, 1996.

[28] ——, "Computer implementation of the absolute nodal coordinate formulation for flexible multibody dynamics," *Nonlinear Dynamics*, vol. 16, no. 3, pp. 293–306, 1998.

[29] H. A. Attia, "Dynamic analysis of spatial linkages: a recursive approach," *Meccanica*, vol. 40, no. 1, pp. 1–18, 2005.

[30] R. D. Gregorio and V. Parenti-Castelli, "On the characterization of the dynamic performances of planar manipulators," *Meccanica*, vol. 40, no. 3, pp. 267–279, 2005.

[31] L.-W. Chang and J. Hamilton, "The kinematics of robotic manipulators with flexible links using an equivalent rigid link system (erls) model," *Journal of dynamic systems, measurement, and control*, vol. 113, no. 1, pp. 48–53, 1991.

[32] D. A. Turcic and A. Midha, "Dynamic analysis of elastic mechanism systems. part i: Applications," *Journal of Dynamic Systems, Measurement, and Control*, vol. 106, no. 4, pp. 249–254, 1984.

[33] D. A. Turcic, A. Midha, and J. Bosnik, "Dynamic analysis of elastic mechanism systems. part ii: Experimental results," *Journal of dynamic systems, measurement, and control*, vol. 106, no. 4, pp. 255–260, 1984.

[34] D. A. Turcic and A. Midha, "Generalized equations of motion for the dynamic analysis of elastic mechanism systems," *Journal of Dynamic Systems, Measurement, and Control*, vol. 106, no. 4, pp. 243–248, 1984.

[35] M. Giovagnoni, H. Piccoli, and A. Rossi, "Finite elements and sensitivity coefficients in flexible planar linkage analysis," *Meccanica*, vol. 22, no. 3, pp. 157–162, 1987.

[36] M. Giovagnoni and A. Rossi, "Transient analysis of a flexible crank," *Mechanism and Machine Theory*, vol. 24, no. 4, pp. 231–243, 1989.

[37] M. Giovagnoni, "A numerical and experimental analysis of a chain of flexible bodies," *ASME Journal of Dynamic Systems, Measurement and Control*, vol. 116, pp. 73–80, 1994.

[38] A. Gasparetto, "On the modeling of flexible-link planar mechanisms: experimental validation of an accurate dynamic model," *Journal of dynamic systems, measurement, and control*, vol. 126, no. 2, pp. 365–375, 2004.

[39] ——, "Accurate modelling of a flexible-link planar mechanism by means of a linearized model in the state-space form for design of a vibration controller," *Journal of Sound and Vibration*, vol. 240, no. 2, pp. 241–262, 2001.

[40] P. Boscariol, A. Gasparetto, and V. Zanotto, "Active position and vibration control of a flexible links mechanism using model-based predictive control," *ASME Journal of Dynamic Systems, Measurement, and Control*, vol. 132, January 2010.

[41] ——, "Model predictive control of a flexible links mechanism," *Journal of Intelligent and Robotic Systems*, vol. 58, no. 2, pp. 125–147, 2010.

[42] ——, "Simultaneous position and vibration control system for flexible link mechanisms," *Meccanica*, vol. 46, no. 4, pp. 723–737, 2011.

[43] G. Boschetti, D. Richiedei, and A. Trevisani, "Delayed reference control applied to flexible link mechanisms: A scheme for effective and stable control," *Journal of dynamic systems, measurement, and control*, vol. 134, no. 1, p. 011003, 2012.

[44] R. Caracciolo, A. Gasparetto, and A. Trevisani, "Experimental validation of a dynamic model for flexible link mechanisms," *Proc. of the ASME DETC 2001*, 2001.

[45] R. Caracciolo, D. Richiedei, A. Trevisani, and V. Zanotto, "Robust mixed-norm position and vibration control of flexible link mechanisms," *Mechatronics*, vol. 15, no. 7, pp. 767–791, 2005.

[46] P. Gallina, A. Gasparetto, G. Rosati, and A. Rossi, "Design of a pid controller for a flexible five-bar closed-chain planar manipulator," in *Romansy 14*. Springer, 2002, pp. 141–150.

[47] A. Trevisani, "Feedback control of flexible four-bar linkages: a numerical and experimental investigation," *Journal of sound and vibration*, vol. 268, no. 5, pp. 947–970, 2003.

[48] A. Gasparetto and V. Zanotto, "Vibration reduction in a flexible-link mechanism through synthesis of an optimal controller," *Meccanica*, vol. 41, no. 6, pp. 611–622, 2006.

[49] V. Zanotto, A. Gasparetto, A. Lanzutti, P. Boscariol, and R. Vidoni, "Experimental validation of minimum time-jerk algorithms for industrial robots," *Journal of Intelligent & Robotic Systems*, vol. 64, no. 2, pp. 197–219, 2011.

[50] R. Vidoni, A. Gasparetto, and M. Giovagnoni, "Design and implementation of an erls-based 3-d dynamic formulation for flexible-link robots," *Robot. Comput.-Integr. Manuf.*, vol. 29, no. 2, pp. 273–282, 2013.

[51] ——, "A method for modeling three-dimensional flexible mechanisms based on an equivalent rigid-link system," *Journal of Vibration and Control*, vol. 20, no. 4, pp. 483–500, 2014.

[52] A. Gasparetto, A. K. Moosavi, P. Boscariol, and M. Giovagnoni, "Experimental validation of a dynamic model for lightweight robots," *International Journal of Advanced Robotic Systems*, vol. 10, no. 3, p. 182, 2013.

[53] A. Ben-Israel and T. N. Greville, *Generalized inverses: theory and applications*. Springer Science & Business Media, 2003, vol. 15.

[54] J. Denavit, "A kinematic notation for low pair mechanisms based on matrices," *ASME J. Appl. Mech.*, vol. 22, pp. 215–221, 1955.

[55] R. Craig and M. Bampton, "Coupling of substructures for dynamics analyses," *AIAA Journal*, vol. 6, no. 7, pp. 1313–1319, 1968.

[56] S. Dwivedy and P. Eberhard, "Dynamic analysis of flexible manipulators, a literature review," *Mechanism and Machine Theory*, vol. 41, pp. 749–777, 2006.

[57] R. Caracciolo, D. Richiedei, A. Trevisani, and V. Zanotto, "Robust mixed-norm position and vibration control of flexible link mechanisms," *Mechatronics*, vol. 15, no. 7, pp. 767–791, September 2005.

[58] C. L. Q. T. Kai Luo, Haiyan Hu, "Model order reduction of flexible multibody systems described by the ANCF," in *ECCOMAS Thematic Conference on Multibody Dynamics*, 2017.

[59] M. González, U. Lugrís, R. Gutiérrez, and J. Cuadrado, "Benchmarking of MBS simulation software," in *ASME 2005 International Design Engineering Technical Conferences and Computers and Information in Engineering Conference*. American Society of Mechanical Engineers, 2005, pp. 1885–1894.

[60] "IFToMM, International Federation for the Promotion of Mechanism and Machine Science," www.iftomm-multibody.org/benchmark/, 2017.

[61] A. Gasparetto, A. K. Moosavi, P. Boscariol, and M. Giovagnoni, "Experimental validation of a dynamic model for lightweight robots," *Int J Adv Robot Syst*, vol. 10, no. 182, 2013.

[62] B. Besselink, U. Tabak, A. Lutowska, N. Van De Wouw, H. Nijmeijer, D. Rixen, M. Hochstenbach, and W. Schilders, "A comparison of model reduction techniques from structural dynamics, numerical mathematics and systems and control," *Journal of Sound and Vibration*, vol. 332, no. 19, pp. 4403–4422, 2013.

[63] M. Allen, R. Mayes, and E. Bergman, "Experimental modal substructuring to couple and uncouple substructures with flexible fixtures and multi-point connections," *J. of Sound and Vibration*, vol. 329, no. 23, pp. 4891–4906, 2010.

[64] O. Flodén, K. Persson, and G. Sandberg, "Reduction methods for the dynamic analysis of substructure models of lightweight building structures," *Computers & Structures*, vol. 138, pp. 49–61, 2014.

[65] D. Roettgen, B. Seeger, W. Tai, S. Baek, T. Dossogne, M. Allen, R. Kuether, M. Brake, and R. Mayes, "A comparison of reduced order modeling techniques used in dynamic substructuring," in *Dynamics of Coupled Structures, Volume 4*. Springer, 2016, pp. 511–528.

[66] P. Koutsovasilis and M. Beitelschmidt, "Comparison of model reduction techniques for large mechanical systems," *Multibody System Dynamics*, vol. 20, no. 2, pp. 111–128, 2008.

[67] C. Nowakowski, J. Fehr, M. Fischer, and P. Eberhard, "Model order reduction in elastic multibody systems using the floating frame of reference formulation," *IFAC Proceedings Volumes*, vol. 45, no. 2, pp. 40–48, 2012.

[68] M. Bampton and R. Craig, JR, "Coupling of substructures for dynamic analyses." *Aiaa Journal*, vol. 6, no. 7, pp. 1313–1319, 1968.

[69] I. Palomba, D. Richiedei, and A. Trevisani, "Mode selection for reduced order modeling of mechanical systems excited at resonance," *International Journal of Mechanical Sciences*, vol. 114, pp. 268–276, 2016.

[70] G. Aglietti, S. Redi, S. Walker, and A. Kiley, "Robustness of the orthogonality checks on a satellite fem using a serep test analysis model," in *Proc. of the 24th Int. Conf. on Noise and Vibration Engineering*, 2010.

[71] M. Pastor, M. Binda, and T. Harčarik, "Modal assurance criterion," *Procedia Engineering*, vol. 48, pp. 543–548, 2012.

[72] N. Lieven and T. Waters, "Error location using normalised orthogonality," in *Proceedings-Spie The International Society For Optical Engineering*. Spie International Society For Optical, 1994, pp. 761–761.

[73] V. Zeman and M. Hajžman, "Usage of the generalized modal synthesis method in dynamics of machines," *Engineering Mechanics*, vol. 14, no. 1-2, pp. 45–54, 2007.

[74] R. Guyan, "Reduction of stiffness and mass matrices," *AIAA journal*, vol. 3, no. 2, pp. 380–380, 1965.

[75] C. Sastry, D. Mahapatra, S. Gopalakrishnan, and T. Ramamurthy, "An iterative system equivalent reduction expansion process for extraction of high frequency response from reduced order finite element model," *Computer Methods in Applied Mechanics and Engineering*, vol. 192, no. 15, pp. 1821–1840, 2003.

[76] Z. Qu, *Model order reduction techniques with applications in finite element analysis*. Springer Science & Business Media, 2013.

[77] T. Rasheed, P. Long, D. Marquez-Gamez, and S. Caro, "Tension distribution algorithm for planar mobile cable-driven parallel robots," in *Cable-Driven Parallel Robots*. Springer, 2018, pp. 268–279.

[78] L. Gagliardini, M. Gouttefarde, and S. Caro, "Design of reconfigurable cable-driven parallel robots," in *Mechatronics for Cultural Heritage and Civil Engineering*. Springer, 2018, pp. 85–113.

[79] S. Seriani, P. Gallina, and A. Wedler, "A modular cable robot for inspection and light manipulation on celestial bodies," *Acta Astronautica*, vol. 123, pp. 145–153, 2016.

[80] S.-R. Oh and S. K. Agrawal, "Cable suspended planar robots with redundant cables: controllers with positive tensions," *IEEE Transactions on Robotics*, vol. 21, no. 3, pp. 457–465, 2005.

[81] S. Oh and S. K. Agrawal, "A reference governor-based controller for a cable robot under input constraints," *IEEE transactions on control systems technology*, vol. 13, no. 4, pp. 639–645, 2005.

[82] P. Gallina and A. Trevisani, "Synthesis and experimental validation of a delayed reference controller for active vibration suppression in mechanical systems," *Journal of applied mechanics*, vol. 72, no. 4, pp. 623–627, 2005.

[83] ——, "Delayed reference control of a two-mass elastic system," *Modal Analysis*, vol. 10, no. 1, pp. 135–159, 2004.

[84] J. Gorman, K. W. Jablokow, and D. J. Cannon, "The cable array robot: Theory and experiment," in *Robotics and Automation, 2001. Proceedings 2001 ICRA. IEEE International Conference on*, vol. 3. IEEE, 2001, pp. 2804–2810.

[85] D. Zanotto, "Analysis and development of cable-driven robotic devices," *Ph.D. Thesis*, 2011.

[86] P. Gallina and G. Rosati, "Manipulability of a planar wire driven haptic device," *Mechanism and Machine Theory*, vol. 37, no. 2, pp. 215–228, 2002.

[87] G. Boschetti, C. Passarini, and A. Trevisani, "A strategy for moving cable driven robots safely in case of cable failure," in *Advances in Italian Mechanism Science*. Springer, 2017, pp. 203–211.

[88] A. Fattah and S. K. Agrawal, "On the design of cable-suspended planar parallel robots," *Journal of mechanical design*, vol. 127, no. 5, pp. 1021–1028, 2005.

[89] R. L. Williams and P. Gallina, "Planar cable-direct-driven robots: design for wrench exertion," *Journal of intelligent and robotic systems*, vol. 35, no. 2, pp. 203–219, 2002.

[90] P. Bosscher, R. L. Williams, L. S. Bryson, and D. Castro-Lacouture, "Cable-suspended robotic contour crafting system," *Automation in Construction*, vol. 17, no. 1, pp. 45–55, 2007.

[91] X. Yin and A. P. Bowling, "Dynamic performance limitations due to yielding in cable-driven robotic manipulators," *Journal of Mechanical Design*, vol. 128, no. 1, pp. 311–318, 2006.

[92] J. S. Sulzer, M. A. Peshkin, and J. L. Patton, "Design of a mobile, inexpensive device for upper extremity rehabilitation at home," in *Rehabilitation Robotics, 2007. ICORR 2007. IEEE 10th International Conference on.* IEEE, 2007, pp. 933–937.

[93] A. Trevisani, P. Gallina, and R. L. Williams, "Cable-direct-driven robot (cddr) with passive scara support: theory and simulation," *Journal of Intelligent and Robotic Systems*, vol. 46, no. 1, pp. 73–94, 2006.

[94] A. Trevisani, "Underconstrained planar cable-direct-driven robots: A trajectory planning method ensuring positive and bounded cable tensions," *Mechatronics*, vol. 20, no. 1, pp. 113–127, 2010.

[95] L. Pigani and P. Gallina, "Cable-direct-driven-robot (cddr) with a 3-link passive serial support," *Robotics and Computer-Integrated Manufacturing*, vol. 30, no. 3, pp. 265–276, 2014.

[96] J. F. Veneman, R. Kruidhof, E. E. Hekman, R. Ekkelenkamp, E. H. Van Asseldonk, and H. Van Der Kooij, "Design and evaluation of the lopes exoskeleton robot for interactive gait rehabilitation," *IEEE Transactions on Neural Systems and Rehabilitation Engineering*, vol. 15, no. 3, pp. 379–386, 2007.

[97] A. Frisoli, M. Prisco, F. Salsedo, and M. Bergamasco, "A two degrees-of-freedom planar haptic interface with high kinematic isotropy," in *Robot and Human Interaction, 1999. RO-MAN'99. 8th IEEE International Workshop on.* IEEE, 1999, pp. 297–302.

[98] B. Kehoe, G. Kahn, J. Mahler, J. Kim, A. Lee, A. Lee, K. Nakagawa, S. Patil, W. D. Boyd, P. Abbeel *et al.*, "Autonomous multilateral debridement with the raven surgical robot," in *Robotics and Automation (ICRA), 2014 IEEE International Conference on.* IEEE, 2014, pp. 1432–1439.

[99] J. Mahler, S. Krishnan, M. Laskey, S. Sen, A. Murali, B. Kehoe, S. Patil, J. Wang, M. Franklin, P. Abbeel *et al.*, "Learning accurate kinematic control of cable-driven surgical robots using data cleaning and gaussian process regression," in *Automation Science and Engineering (CASE), 2014 IEEE Int. Conf. on.* IEEE, 2014, pp. 532–539.

[100] T. Do, T. Tjahjowidodo, M. Lau, and S. Phee, "Real-time enhancement of tracking performances for cable-conduit mechanisms-driven flexible robots," *Robotics and Computer-Integrated Manufacturing*, vol. 37, pp. 197–207, 2016.

[101] L. S. Chiang, P. S. Jay, P. Valdastri, A. Menciassi, and P. Dario, "Tendon sheath analysis for estimation of distal end force and elongation," in *Advanced Intelligent Mechatronics, 2009. AIM 2009. IEEE/ASME International Conference on.* IEEE, 2009, pp. 332–337.

[102] T. Bruckmann and A. Pott, *Cable-driven parallel robots.* Springer, 2012, vol. 12.

[103] Z. N. Masoud, "Effect of hoisting cable elasticity on anti-sway controllers of quay-side container cranes," *Nonlinear Dynamics*, vol. 58, no. 1, pp. 129–140, 2009.

[104] S. Lahouar, E. Ottaviano, S. Zeghoul, L. Romdhane, and M. Ceccarelli, "Collision free path-planning for cable-driven parallel robots," *Robotics and Autonomous Systems*, vol. 57, no. 11, pp. 1083–1093, 2009.

[105] R. L. Williams, J. S. Albus, and R. V. Bostelman, "Self-contained automated construction deposition system," *Automation in Construction*, vol. 13, no. 3, pp. 393–407, 2004.

[106] J.-B. Izard, M. Gouttefarde, C. Baradat, D. Culla, and D. Sallé, "Integration of a parallel cable-driven robot on an existing building façade," in *Cable-Driven Parallel Robots.* Springer, 2013, pp. 149–164.

[107] J.-P. Merlet and D. Daney, "A portable, modular parallel wire crane for rescue operations," in *Robotics and Automation (ICRA), 2010 IEEE International Conference on.* IEEE, 2010, pp. 2834–2839.

[108] G. Rosati, P. Gallina, S. Masiero, and A. Rossi, "Design of a new 5 dof wire-based robot for rehabilitation," in *9th International Conference on Rehabilitation Robotics, 2005. ICORR 2005.* IEEE, 2005, pp. 430–433.

[109] D. Zanotto, G. Rosati, S. Minto, and A. Rossi, "Sophia-3: A semiadaptive cable-driven rehabilitation device with a tilting working plane," *IEEE Transactions on Robotics*, vol. 30, no. 4, pp. 974–979, 2014.

[110] L. L. Cone, "Skycam-an aerial robotic camera system," *Byte*, vol. 10, no. 10, p. 122, 1985.

[111] J. Albus, R. Bostelman, and N. Dagalakis, "The nist robocrane," *Journal of Field Robotics*, vol. 10, no. 5, pp. 709–724, 1993.

[112] T. C. Kavanagh and D. H. Tung, "Arecibo radar-radio telescope-design and construction," *Journal of the Construction Division*, vol. 91, no. 1, pp. 69–98, 1965.

[113] H. Li, X. Zhang, R. Yao, J. Sun, G. Pan, and W. Zhu, "Optimal force distribution based on slack rope model in the incompletely constrained cable-driven parallel mechanism of fast telescope," in *Cable-driven parallel robots*. Springer, 2013, pp. 87–102.

[114] C. S. Holland and D. J. Cannon, "Cable array robot for material handling," Nov. 30 2004, uS Patent 6,826,452.

[115] P. Miermeister and A. Pott, "Modelling and real-time dynamic simulation of the cable-driven parallel robot ipanema," in *New Trends in Mechanism Science*. Springer, 2010, pp. 353–360.

[116] P. Miermeister, M. Lächele, R. Boss, C. Masone, C. Schenk, J. Tesch, M. Kerger, H. Teufel, A. Pott, and H. H. Bülthoff, "The cablerobot simulator large scale motion platform based on cable robot technology," in *Intelligent Robots and Systems (IROS), 2016 IEEE/RSJ International Conference on*. IEEE, 2016, pp. 3024–3029.

[117] D. Q. Nguyen and M. Gouttefarde, "Study of reconfigurable suspended cable-driven parallel robots for airplane maintenance," in *Intelligent Robots and Systems (IROS 2014), 2014 IEEE/RSJ International Conference on*. IEEE, 2014, pp. 1682–1689.

[118] G. Boschetti, G. Rosati, and A. Rossi, "A haptic system for robotic assisted spine surgery," in *Control Applications, 2005. CCA 2005. Proceedings of 2005 IEEE Conference on*. IEEE, 2005, pp. 19–24.

[119] C. Fanin, P. Gallina, A. Rossi, U. Zanatta, and S. Masiero, "Nerebot: a wire-based robot for neurorehabilitation," in *ICORR'03*. HWRS-ERC, 2003, pp. 23–27.

[120] G. Rosati, P. Gallina, and S. Masiero, "Design, implementation and clinical tests of a wire-based robot for neurorehabilitation," *IEEE Transactions on Neural Systems and Rehabilitation Engineering*, vol. 15, no. 4, pp. 560–569, 2007.

[121] Y. Mao and S. K. Agrawal, "Design of a cable-driven arm exoskeleton (carex) for neural rehabilitation," *IEEE Transactions on Robotics*, vol. 28, no. 4, pp. 922–931, 2012.

[122] C. Gosselin, "Cable-driven parallel mechanisms: state of the art and perspectives," *Mechanical Engineering Reviews*, vol. 1, no. 1, pp. DSM0004–DSM0004, 2014.

[123] L. Barbazza, "Functional Design of Mechatronic Systems for Human-Robot Collaboration," *Ph.D Thesis*, 2017.

[124] M. Hiller, S. Fang, S. Mielczarek, R. Verhoeven, and D. Franitza, "Design, analysis and realization of tendon-based parallel manipulators," *Mechanism and Machine Theory*, vol. 40, no. 4, pp. 429–445, 2005.

[125] J. Pusey, A. Fattah, S. Agrawal, and E. Messina, "Design and workspace analysis of a 6–6 cable-suspended parallel robot," *Mechanism and machine theory*, vol. 39, no. 7, pp. 761–778, 2004.

[126] S.-R. Oh, K. K. Mankala, S. K. Agrawal, and J. S. Albus, "Dynamic modeling and robust controller design of a two-stage parallel cable robot," *Multibody System Dynamics*, vol. 13, no. 4, pp. 385–399, 2005.

[127] G. Barrette and C. M. Gosselin, "Determination of the dynamic workspace of cable-driven planar parallel mechanisms," *Journal of mechanical design*, vol. 127, no. 2, pp. 242–248, 2005.

[128] C. Gosselin, P. Ren, and S. Foucault, "Dynamic trajectory planning of a two-dof cable-suspended parallel robot," in *Robotics and Automation (ICRA), 2012 IEEE International Conference on*. IEEE, 2012, pp. 1476–1481.

[129] C. Gosselin, "Global planning of dynamically feasible trajectories for three-dof spatial cable-suspended parallel robots," in *Cable-Driven Parallel Robots*. Springer, 2013, pp. 3–22.

[130] C. Gosselin and S. Foucault, "Dynamic point-to-point trajectory planning of a two-dof cable-suspended parallel robot," *IEEE Transactions on Robotics*, vol. 30, no. 3, pp. 728–736, 2014.

[131] X. Jiang and C. Gosselin, "Dynamically feasible trajectories for three-dof planar cable-suspended parallel robots," in *ASME 2014 International Design Engineering Technical Conferences and Computers and Information in Engineering Conference*. American Society of Mechanical Engineers, 2014, pp. V05AT08A085–V05AT08A085.

[132] ——, "Dynamic point-to-point trajectory planning of a three-dof cable-suspended parallel robot," *IEEE Transactions on Robotics*, vol. 32, no. 6, pp. 1550–1557, 2016.

[133] P. Dion-Gauvin and C. Gosselin, "Trajectory planning for the static to dynamic transition of point-mass cable-suspended parallel mechanisms," *Mechanism and Machine Theory*, vol. 113, pp. 158–178, 2017.

[134] G. Mottola, C. Gosselin, and M. Carricato, "Dynamically feasible periodic trajectories for generic spatial three-degree-of-freedom cable-suspended parallel robots," *Journal of Mechanisms and Robotics*, vol. 10, no. 3, p. 031004, 2018.

[135] ——, "Dynamically-feasible elliptical trajectories for fully constrained 3-dof cable-suspended parallel robots," in *Cable-Driven Parallel Robots*. Springer, 2018, pp. 219–230.

[136] X. Jiang, E. Barnett, and C. Gosselin, "Periodic trajectory planning beyond the static workspace for 6-dof cable-suspended parallel robots," *IEEE Transactions on Robotics*, 2018.

[137] ——, "Dynamic point-to-point trajectory planning beyond the static workspace for six-dof cable-suspended parallel robots," *IEEE Transactions on Robotics*, 2018.

[138] P. Dion-Gauvin and C. Gosselin, "Dynamic point-to-point trajectory planning of a three-dof cable-suspended mechanism using the hypocycloid curve," *IEEE/ASME Transactions on Mechatronics*, 2018.

[139] N. Zhang, W. Shang, and S. Cong, "Geometry-based trajectory planning of a 3-3 cable-suspended parallel robot," *IEEE Transactions on Robotics*, vol. 33, no. 2, pp. 484–491, 2017.

[140] R. Bordalba, J. M. Porta, and L. Ros, "Randomized kinodynamic planning for cable-suspended parallel robots," in *Cable-Driven Parallel Robots*. Springer, 2018, pp. 195–206.

[141] L. Barbazza, D. Zanotto, G. Rosati, and S. K. Agrawal, "Design and optimal control of an underactuated cable-driven micro–macro robot," *IEEE Robotics and Automation Letters*, vol. 2, no. 2, pp. 896–903, 2017.

[142] A. Berti, M. Gouttefarde, and M. Carricato, "Dynamic recovery of cable-suspended parallel robots after a cable failure," in *Advances in Robot Kinematics 2016*. Springer, 2018, pp. 331–339.

[143] C. Passarini, D. Zanotto, and G. Boschetti, "Dynamic trajectory planning for failure recovery in cable-suspended camera systems," *ASME Journal of Mechanisms and Robotics (under review)*, 2018.

[144] P. Boscariol and D. Richiedei, "Robust point-to-point trajectory planning for nonlinear underactuated systems: Theory and experimental assessment," *Robotics and Computer-Integrated Manufacturing*, vol. 50, pp. 256–265, 2018.

[145] S. Lefrançois and C. Gosselin, "Point-to-point motion control of a pendulum-like 3-dof underactuated cable-driven robot," in *Robotics and Automation (ICRA), 2010 IEEE International Conference on*. IEEE, 2010, pp. 5187–5193.

[146] D. Zanotto, G. Rosati, and S. K. Agrawal, "Modeling and control of a 3-dof pendulum-like manipulator," in *Robotics and Automation (ICRA), 2011 IEEE International Conference on*. IEEE, 2011, pp. 3964–3969.

[147] N. Zoso and C. Gosselin, "Point-to-point motion planning of a parallel 3-dof underactuated cable-suspended robot," in *Robotics and Automation (ICRA), 2012 IEEE International Conference on*. IEEE, 2012, pp. 2325–2330.

[148] H.-H. Lee, "Modeling and control of a three-dimensional overhead crane," *Journal of Dynamic Systems, Measurement, and Control*, vol. 120, no. 4, pp. 471–476, 1998.

[149] Y. Fang, W. Dixon, D. Dawson, and E. Zergeroglu, "Nonlinear coupling control laws for an underactuated overhead crane system," *IEEE/ASME transactions on mechatronics*, vol. 8, no. 3, pp. 418–423, 2003.

[150] J. Yi, N. Yubazaki, and K. Hirota, "Anti-swing and positioning control of overhead traveling crane," *Information Sciences*, vol. 155, no. 1, pp. 19–42, 2003.

[151] S.-G. Lee, V.-H. Dang, S. Moon, B. Kim *et al.*, "Partial feedback linearization control of a three-dimensional overhead crane," *International Journal of Control, Automation and Systems*, vol. 11, no. 4, pp. 718–727, 2013.

[152] Y. Lu and D. Fan, "Transmission backlash of precise cable drive system," *Proceedings of the Institution of Mechanical Engineers, Part C: Journal of Mechanical Engineering Science*, vol. 227, no. 10, pp. 2256–2267, 2013.

[153] S.-W. Ji, S.-J. Kim, and Y.-B. Kim, "Experimental approach for mooring winch control system design," in *Control, Automation and Systems (ICCAS), 2013 13th International Conference on*. IEEE, 2013, pp. 1025–1028.

[154] J. M. Lincoln, D. L. Lucas, R. W. McKibbin, C. C. Woodward, and J. E. Bevan, "Reducing commercial fishing deck hazards with engineering solutions for winch design," *Journal of safety research*, vol. 39, no. 2, pp. 231–235, 2008.

[155] E. Kilic, M. Dolen, and A. B. Koku, "Experimental evaluation of cable-drum systems as linear motion sensors," in *2011 IEEE International Conference on Mechatronics*, 2011.

[156] E. Kilic and M. Dolen, "Prediction of slip in cable-drum systems using structured neural networks," *Proceedings of the Institution of Mechanical Engineers, Part C: Journal of Mechanical Engineering Science*, vol. 228, no. 3, pp. 441–456, 2014.

[157] S. Seriani and P. Gallina, "Variable radius drum mechanisms," *Journal of Mechanisms and Robotics*, vol. 8, no. 2, p. 021016, 2016.

[158] D. Shin, X. Yeh, and O. Khatib, "Circular pulley versus variable radius pulley: Optimal design methodologies and dynamic characteristics analysis," *IEEE Transactions on Robotics*, vol. 29, no. 3, pp. 766–774, 2013.

[159] G. Endo, H. Yamada, A. Yajima, M. Ogata, and S. Hirose, "A passive weight compensation mechanism with a non-circular pulley and a spring," in *Robotics and Automation (ICRA), 2010 IEEE International Conference on*. IEEE, 2010, pp. 3843–3848.

[160] M. Kilic, Y. Yazicioglu, and D. F. Kurtulus, "Synthesis of a torsional spring mechanism with mechanically adjustable stiffness using wrapping cams," *Mechanism and Machine Theory*, vol. 57, pp. 27–39, 2012.

[161] N. Schmit and M. Okada, "Synthesis of a non-circular cable spool to realize a nonlinear rotational spring," in *2011 IEEE/RSJ International Conference on Intelligent Robots and Systems*. IEEE, 2011, pp. 762–767.

[162] B. Kim and A. D. Deshpande, "Design of nonlinear rotational stiffness using a noncircular pulley-spring mechanism," *Journal of Mechanisms and Robotics*, vol. 6, no. 4, p. 041009, 2014.

[163] D. Shin, X. Yeh, and O. Khatib, "Variable radius pulley design methodology for pneumatic artificial muscle-based antagonistic actuation systems," in *2011 IEEE/RSJ International Conference on Intelligent Robots and Systems*. IEEE, 2011, pp. 1830–1835.

[164] E. Kljuno, J. J. Zhu, R. L. Williams, and S. M. Reilly, "A biomimetic elastic cable driven quadruped robot: The robocat," in *ASME 2011 International Mechanical Engineering Congress and Exposition*. American Society of Mechanical Engineers, 2011, pp. 759–769.

[165] P. Gallina, "A new class of rocker-belt mechanisms," *Mechanism and machine theory*, vol. 40, no. 8, pp. 963–976, 2005.

[166] M. Arsenault, "Design of convex variable radius drum mechanisms," *Mechanism and Machine Theory*, vol. 129, pp. 175–190, 2018.

[167] D. Fedorov and L. Birglen, "Differential noncircular pulleys for cable robots and static balancing," *Journal of Mechanisms and Robotics*, vol. 10, no. 6, p. 061001, 2018.

[168] C. B. Yigit, E. Bayraktar, and P. Boyraz, "Low-cost variable stiffness joint design using translational variable radius pulleys," *Mechanism and Machine Theory*, vol. 130, pp. 203–219, 2018.

[169] Y. B. Bedoustani, H. D. Taghirad, and M. M. Aref, "Dynamics analysis of a redundant parallel manipulator driven by elastic cables," in *Control, Automation, Robotics and Vision, 2008. ICARCV 2008. 10th International Conference on*. IEEE, 2008, pp. 536–542.

[170] J. Littlewood, "Lorentz's pendulum problem," Wisconsin Univ. Madison Mathematics Research Center, Tech. Rep., 1962.

[171] S. M. Curry, "How children swing," *American Journal of Physics*, vol. 44, no. 10, pp. 924–926, 1976.

[172] M. Pinsky and A. Zevin, "Oscillations of a pendulum with a periodically varying length and a model of swing," *International journal of non-linear mechanics*, vol. 34, no. 1, pp. 105–109, 1999.

[173] B. Piccoli and J. Kulkarni, "Pumping a swing by standing and squatting: do children pump time optimally?" *IEEE Control Systems*, vol. 25, no. 4, pp. 48–56, 2005.

[174] J. A. Burns, "More on pumping a swing," *American Journal of Physics*, vol. 38, no. 7, pp. 920–922, 1970.

[175] W. B. Case and M. A. Swanson, "The pumping of a swing from the seated position," *American Journal of Physics*, vol. 58, no. 5, pp. 463–467, 1990.

[176] W. B. Case, "The pumping of a swing from the standing position," *American Journal of Physics*, vol. 64, no. 3, pp. 215–220, 1996.

[177] D. Cunningham and H. H. Asada, "The winch-bot: A cable-suspended, under-actuated robot utilizing parametric self-excitation," in *Robotics and Automation, 2009. ICRA'09. IEEE International Conference on.* IEEE, 2009, pp. 1844–1850.

[178] A. O. Belyakov, A. P. Seyranian, and A. Luongo, "Dynamics of the pendulum with periodically varying length," *Physica D: Nonlinear Phenomena*, vol. 238, no. 16, pp. 1589–1597, 2009.

[179] D. S. Stilling and W. Szyszkowski, "Controlling angular oscillations through mass reconfiguration: a variable length pendulum case," *International Journal of Non-Linear Mechanics*, vol. 37, no. 1, pp. 89–99, 2002.

[180] J. E. Kulkarni, "Time-optimal control of a swing," in *Decision and Control, 2003. Proceedings. 42nd IEEE Conference on*, vol. 2. IEEE, 2003, pp. 1729–1733.

[181] L. Righetti, J. Buchli, and A. J. Ijspeert, "Dynamic Hebbian learning in adaptive frequency oscillators," *Physica D: Nonlinear Phenomena*, vol. 216, no. 2, pp. 269–281, 2006.

[182] ——, "Adaptive frequency oscillators and applications," *The Open Cybernetics and Systemics Journal*, vol. 3, pp. 64–69, 2009.

[183] R. Ronsse, N. Vitiello, T. Lenzi, J. van den Kieboom, M. C. Carrozza, and A. J. Ijspeert, "Human–robot synchrony: flexible assistance using adaptive oscillators," *IEEE Transactions on Biomedical Engineering*, vol. 58, no. 4, pp. 1001–1012, 2011.

[184] D. Zanotto, P. Stegall, and S. K. Agrawal, "Adaptive assist-as-needed controller to improve gait symmetry in robot-assisted gait training," in *Robotics and Automation (ICRA), 2014 IEEE International Conference on.* IEEE, 2014, pp. 724–729.

[185] T. Yan, A. Parri, V. R. Garate, M. Cempini, R. Ronsse, and N. Vitiello, "An oscillator-based smooth real-time estimate of gait phase for wearable robotics," *Autonomous Robots*, vol. 41, no. 3, pp. 759–774, 2017.

[186] B. Charlet, J. Levine, and R. Marino, "On dynamic feedback linearization," *Systems & Control Letters*, vol. 13, no. 2, pp. 143 – 151, 1989.

[187] A. Isidori, *Nonlinear Control Systems. Third edition. Communications and Control Engineering Series*, M. Thoma, E. D. Sontag, B. W. Dickinson, A. Fettweis, and J. L. M. J. W. Modestino, Eds. Springer-Verlag New York, Inc. Secaucus, NJ, USA, 1995.

Acknowledgments

These three years of Ph.D. program have been a challenging and life-changing experience for me, which would not have been possible without the help, the support and the guidance I received from many people.

The wide range of research activities presented in this thesis have been carried out at the Polytechnic Department of Engineering and Architecture (DPIA), University of Udine (Italy), partially, at the Department of Engineering and Architecture (DIA), University of Trieste (Italy), and at the Wearable Robotic Systems (WRS) Laboratory, Department of Mechanical Engineering, Stevens Institute of Technology (Hoboken, NJ, USA).

First and foremost, I would like to express my gratitude to my supervisor, Prof. Alessandro Gasparetto, for his constant and stimulating presence and for his confidence in me. It was thanks to him that I could start this growth and learning path with good prospects for the future. I also had the chance to experiment a wide range of scientific experiences, to participate at international conferences and to spend a visiting period abroad.

I am deeply grateful to Prof. Paolo Gallina, who has been a reference point with his suggestions and support. It was thanks to him that I decided to start doing research.

I would like to thank Prof. Renato Vidoni for his help to develop the results presented in the first part of this thesis and for his constructive comments and valuable stimuli he gave me during my Ph.D.

I would like to acknowledge Prof. Damiano Zanotto for his hospitality at the Wearable Robotic Systems Laboratory and for the help he provided in the design and validation of the pendulum-robot. I am also thankful for the example he has provided as a researcher.

I would like to thank Stefano Seriani, for his contagious curiosity, for his help and ideas, and Paolo Boscariol for his precious suggestions and the motivation he gave me.

I gratefully acknowledge the support from the *Industrial and Information Engineering Ph.D. Program* (IIE-Ph.D.) of University of Udine, who partially funded my research period in the US.

Furthermore, I would like to thank all the Ph.D. candidates at the DPIA department, in particular Tommaso, Roberto, Giovanni and Andrea. Special thanks to my colleagues and friends at University of Trieste, in particular Gabriele, Thomas, Riccardo and Martino.

I would like to thank Edi Zanzaro for his contribution in the comparison of model order reduction techniques.

My time in Hoboken and New York was made enjoyable in large part due to many

colleagues and friends that have been my reference frame, in particular to Yufeng, Ton, Jennifer, Arun, Sierra, Valentina, Corey and Aaron.

A special thank to Alessandro and Martina for all the great moments spent together.

Finally, I would like to thank my mum Nadia, Paolo, my grandma Mercedes, my uncle Tarcisio and Alessandro for their constant encouragement and support.